



IntechOpen

Strength of Materials

*Edited by Héctor Jaramillo S.,
Julian Arnaldo Avila and Can Chen*



Strength of Materials

*Edited by Héctor Jaramillo S., Julian
Arnaldo Avila and Can Chen*

Published in London, United Kingdom



IntechOpen





Supporting open minds since 2005



Strength of Materials

<http://dx.doi.org/10.5772/intechopen.83265>

Edited by Héctor Jaramillo S. , Julian Arnaldo Avila and Can Chen

Contributors

Ayobami Busari, Williams Kupolati, Loto Tolulope Roland, Sadiku Rotimi Emmanuel, Jacques Snyman, Ndambuki Julius, Galina Slavcheva, Olga Artamonova, Evgeny Chernishov, Makno Basoeiki, Raphael Goncalves, Carla Maciel, Cassius Ruchert, Waldek Wladimir Bose Filho, Julian Arnaldo Avila, Haroldo Cavalcanti Pinto, Mohammad Masoumi, Fabio Faria Conde, Hector Enrique Jaramillo S. , Juan Pablo Arango Fierro, Jose Luis Arango Fierro, Kai Zhang, Zhenquan Wang, Deguo Wang, Qiang Xu, Zhongyu Lu, Go Yamamoto, Keita Koizumi, Tomonaga Okabe, Xiaofeng Qin

© The Editor(s) and the Author(s) 2020

The rights of the editor(s) and the author(s) have been asserted in accordance with the Copyright, Designs and Patents Act 1988. All rights to the book as a whole are reserved by INTECHOPEN LIMITED. The book as a whole (compilation) cannot be reproduced, distributed or used for commercial or non-commercial purposes without INTECHOPEN LIMITED's written permission. Enquiries concerning the use of the book should be directed to INTECHOPEN LIMITED rights and permissions department (permissions@intechopen.com).

Violations are liable to prosecution under the governing Copyright Law.



Individual chapters of this publication are distributed under the terms of the Creative Commons Attribution 3.0 Unported License which permits commercial use, distribution and reproduction of the individual chapters, provided the original author(s) and source publication are appropriately acknowledged. If so indicated, certain images may not be included under the Creative Commons license. In such cases users will need to obtain permission from the license holder to reproduce the material. More details and guidelines concerning content reuse and adaptation can be found at <http://www.intechopen.com/copyright-policy.html>.

Notice

Statements and opinions expressed in the chapters are these of the individual contributors and not necessarily those of the editors or publisher. No responsibility is accepted for the accuracy of information contained in the published chapters. The publisher assumes no responsibility for any damage or injury to persons or property arising out of the use of any materials, instructions, methods or ideas contained in the book.

First published in London, United Kingdom, 2020 by IntechOpen

IntechOpen is the global imprint of INTECHOPEN LIMITED, registered in England and Wales, registration number: 11086078, 7th floor, 10 Lower Thames Street, London, EC3R 6AF, United Kingdom

Printed in Croatia

British Library Cataloguing-in-Publication Data

A catalogue record for this book is available from the British Library

Additional hard and PDF copies can be obtained from orders@intechopen.com

Strength of Materials

Edited by Héctor Jaramillo S. , Julian Arnaldo Avila and Can Chen

p. cm.

Print ISBN 978-1-78985-993-5

Online ISBN 978-1-78985-994-2

eBook (PDF) ISBN 978-1-83880-143-4

We are IntechOpen, the world's leading publisher of Open Access books Built by scientists, for scientists

4,700+

Open access books available

121,000+

International authors and editors

135M+

Downloads

151

Countries delivered to

Our authors are among the
Top 1%

most cited scientists

12.2%

Contributors from top 500 universities



WEB OF SCIENCE™

Selection of our books indexed in the Book Citation Index
in Web of Science™ Core Collection (BKCI)

Interested in publishing with us?
Contact book.department@intechopen.com

Numbers displayed above are based on latest data collected.
For more information visit www.intechopen.com



Meet the editors



Héctor E. Jaramillo S. is a full-time professor-researcher of the Autónoma de Occidente University (Cali, Colombia). He has a PhD from the Universidad del Valle with an emphasis in the mechanics of solids. The PhD dissertation was about the design and development of a finite element model of the L4-L5-S1 segment of the human spine and the experimental characterization was made in the Orthopaedic Bioengineering Research Laboratory of the Colorado State University. He has vast experience in finite element analysis using no linear, orthotropic, and hyperelastic materials. He has a masters degree in civil engineering (2004), and a BSc in Mechanical Engineering (1992). His topics of interest are the mechanics of solids, fatigue fracture mechanics, mechanical engineering design, and finite element analysis.



Dr Julian Avila has been an Assistant Professor at the São Paulo State University – UNESP, Brazil, since 2017. He has conducted research in additive manufacturing, welding and joining, materials characterization, and mechanical testing of metallic materials, such as aluminum and magnesium alloys, high strength low alloy steels, and Maraging steels. Regarding microstructural characterization, he has been developing knowledge using X-ray diffraction from conventional and synchrotron sources, SEM/EBSD, and magnetic Barkhausen noise. Related to mechanical testing, he is researching the effect of hydrogenating environments in steels, aluminum, and magnesium alloys on fracture toughness and fatigue. Currently, he is working with the mechanical and microstructural assessment of steel processed by additive manufacturing, FSW, and conformation processes.



Dr Chen is a senior engineer specializing in the field of pavement and construction materials engineering. He led several research projects for New Mexico, Iowa, and California Department of Transportation. Dr Chen's work has led to publications in prestigious journals and conferences. He also serves as committee member and referee for multiple peer-reviewed journals and international conferences. Dr Chen performs extensive research on epoxy-modified asphalt, design of ultra-high strength concrete (UHPC), and bridge pavement material monitoring and evaluation. He has research collaboration with the National Center for Asphalt Technology, FHWA Fairbank Highway Research Center, New Zealand Transport Agency, and other research institutes in China.

Contents

Preface	XIII
Section 1 Traditional Materials	1
Chapter 1 Tensile Strength of Unidirectional Carbon Fiber-Reinforced Plastic Composites <i>by Go Yamamoto, Keita Koizumi and Tomonaga Okabe</i>	3
Chapter 2 Research Progress of the Drill String Hardbanding Materials <i>by Kai Zhang, Zhenquan Wang and Deguo Wang</i>	15
Chapter 3 Effect of Textures and Microstructures on the Occurrence of Delamination during and after Fracture Toughness Tests of API X80 Steel Plates <i>by Fabio Faria Conde, Haroldo Cavalcanti Pinto, Mohammad Masoumi and Julian Arnaldo Avila</i>	27
Chapter 4 Contact Strength of Material <i>by Xiaofeng Qin</i>	53
Chapter 5 Corrosion Fatigue of Aluminum-Copper-Lithium Alloy 2050-T84 Submitted at Salt Spray and Aqueous Saline Solution <i>by Maciel Carla Isabel dos Santos, Bose Filho Waldek Wladimir and Ruchert Cassius Olívio Figueiredo Terra</i>	65
Chapter 6 Dynamic Effect in Fatigue on High-Deflection Structures <i>by Raphael Paulino Goncalves</i>	81
Chapter 7 Modeling of Creep Deformation and Creep Fracture <i>by Qiang Xu and Zhongyu Lu</i>	95

Section 2	
Sustainable Materials	117
Chapter 8	119
Structural Evaluation of Bamboo Bike Frames: Experimental and Numerical Analysis	
<i>by Juan P. Arango Fierro, Jose L. Arango Fierro and Héctor E. Jaramillo Suárez</i>	
Chapter 9	139
Use of Sustainable Materials in Self-Healing Concrete	
<i>by Busari Ayobami Adebola, Kupolati Williams Kehinde, Loto Tolulope Roland, Sadiku Rotimi Emmanuel, Jacques Snyman and Ndambuki Julius</i>	
Chapter 10	151
Nano-Modification of Building Composite Structures	
<i>by Evgeny Chernishov, Olga Artamonova and Galina Slavcheva</i>	
Chapter 11	169
Bioconc-Based Green Concrete Quality Treatment for Mass Concrete's Low Heat Concrete	
<i>by Makno Basoeki</i>	

Preface

Since time immemorial, man has needed to protect himself from the inclemency of nature; this justified the construction of a living place. Constructions that were erected based on empirical rules, which were transmitted from generation to generation verbally and, for which there was no scientific treatise or research that defined a study of the behavior of the materials used in its construction. Great structures carried out in different cultures can be mentioned; the Egyptians built great temples, pyramids (2778-2160 BC) and obelisks; the Chinese built the Great Wall of China (3rd century BC) and fortified cities, and the Aztecs created their great cities.

The Greeks advanced the art of construction, known as the study of the “determination of the centers of gravity” by Archimedes (287-212 BC), whose theory was used for the transport and lifting of the columns of the Temple of Diana of Ephesus. With the birth and development of the Roman Empire, the Romans became great builders, as a result, we have the great coliseums and the famous Pont du Gard in southern France. The Greeks and Romans accumulated experience for many years in the art of structural engineering, which had a little boom during the Middle Ages and was only expressed strongly during the Renaissance. The Italian architect Fontana (1543-1607), who built the Vatican obelisk at the request of Pope Sixtus V, is famous from this time.

During the renaissance, the contributions made by Leonardo Da Vinci (1452-1519) are highlighted in his notes “Testing the strength of iron wires of various lengths” and apparently performed research about column loads, which stated that “the load varies inversely with the length and directly with the cross-section.” Also, Leonardo was the first to draw the catenary and propose a study using a discrete model, which was a great contribution to the resistance of materials. Galileo Galilei in his book “Discorsi e dimostrazioni matematiche intorno a due nuove scienze”, shows methods applied to the analysis of stresses where he presents a logical sequence of analysis. The “two new sciences” that the Galilean text alludes to are the “Strength of Materials”, which he addresses in the first two chapters of the book. The other science is that of the “Local Movement”, developed in the third and fourth chapters. This represents the beginning of the Strength of Materials as a science.

It is necessary to clarify that Galileo’s approaches did not have the weight of a structured theory, but it was a guide to the researchers and scientists who succeeded him, so for example and in chronological order after Galileo arrived, Euler (1707-1783), Coulomb (1736-1806), Poisson (1781-1840), Navier (1785-1836), Cauchy (1789-1857), and Airy (1801-1892) among others, who laid the foundation for the theory of the Strength of Materials. Theoretical bases that govern the structural design, which today allows us to have homes, machines, and equipment with greater degrees of reliability in its design, which make the life of today’s man more comfortable.

The development of Strength of Materials, the application of mathematics, and the help of computers, has allowed for the creation of advanced techniques in the determination of stresses and strain on structural elements, under different conditions of load, temperature, etc., in a few minutes and even seconds.

The book *Strength of Materials* contains eleven peer-reviewed chapters organized in two sections. Section 1 is focused on the strength of metal and composites materials, in other words on traditional materials used in engineering projects. Chapter 1 predicted the tensile strengths of unidirectionally aligned carbon-fiber-reinforced plastic (UD-CFRP) using a spring element model. The model takes into account a stress concentration acting on an intact fiber surface from a fracture site in a neighboring fiber. The surface stress concentration was experimentally investigated by implementing multi-fiber fragmentation testing in combination with the spring element model simulation. On the other hand, Chapter 2 reviews the research history and status quo of the hardbanding materials in tool joints. The authors show the advantages and disadvantages of several kinds of wear-resisting materials.

Chapter 3 presents the study on the microstructural features, fracture toughness, and delamination occurrence of two X80 grade steel plates with different processing routes and chemical composition. A schematic model was proposed, showing the source of delamination and the reason for the lowest toughness for 45° to the rolling direction. Chapter 4 compares the classic static strength theory and fatigue strength theory of materials; due to the static contact strength being the limiting condition of contact fatigue strength.

Chapter 5 justifies the application of the aluminum-copper-lithium alloy 2050-T84 as a structural component of aircrafts, substituting aluminum alloys used at the present time, due to the possibility of reduction of density, an increase of stiffness, high fracture toughness, greater resistance to the propagation of cracks by fatigue, and greater resistance to corrosion. Chapter 6 studies the fatigue behavior of two generic components; a classical structure and a structure-mechanism, using three different methods of calculation; load history (static), transient modal superposition (dynamic), and frequency domain modal superposition (dynamic). The objective was to demonstrate the differences between each calculation methodology due to the different ways each considers the dynamic effect.

Finally, Section 1 ends with Chapter 7. This chapter analyzes the recent advances in the development of a modified hyperbolic sine law able to depict the minimum creep strain rate over a wider range of stress levels; the development of the creep fracture criterion and model based on the cavity area fraction along grain boundary calibrated with the most representative and comprehensive cavitation data obtained from x-ray synchrotron investigation, and the development of the mesoscopic composite approach modeling of creep deformation and creep damage.

Section 2 contains chapters on the strength of sustainable materials or non-conventional materials. Chapter 8 describes the evaluation and simulation of the mechanical behavior of bike-frames made out of bamboo. Included are some technical values of bamboo bike-frames and these will allow them to define the technical characteristics of the product and guarantee their operating conditions.

This is followed by Chapter 9, which assessed the use of self-healing technology on concrete using sustainable material as an active method of healing cracks, in order to improve the stability, strength, and sustainability of civil infrastructure. The outcome of the review showed three prominent methods used in self-healing technology, which include autogenous healing, encapsulation of polymeric material, and microbial production of calcium-carbonate (biotechnological approaches). The review also revealed that calcium carbonate is a versatile material that can be used in crack healing for the filling of voids and improve the porosity of the concrete.

Chapter 10 reviews the theoretical framework of nanomodification principles of building composites and experimental verification of these principles and, the concepts of nanomodification of building composite structures. The chapter also suggests the conceptual model of the nanomodification from the point of view of the evolutionary model of a solid phase formation depending on the kinetics of heterogeneous processes.

Section 2 and the book are closed with Chapter 11, which describes the research started with a laboratory-scale trial mix, using a Low Heat Concrete Bioconc based concrete Job Mix, from cement content reduction 20%, 25%, 30%, and 40%. The result showed the optimum job mix to be Low Heat Concrete Bioconc based concrete Job Mix on 40% cement as binder content reduction.

The eleven chapters in this book each focus on a particular aspect of the Strength of Materials, but are able to provide a general idea of the direction of current efforts on the use of Strength of Materials as a science. Within each chapter, the reader will come into contact not only with different topics in Strength of Materials, but also with several techniques of synthesis, characterization, and interpretation of results, which can be useful to synthesize and investigate other materials.

Dear reader, with this book you will have access to important subjects on the engineering and Strength of Materials. Chapters can be read in sequence as they are presented or in any sequence that the reader deems appropriate, due to each chapter being independent of the others. This is an excellent book that contains several recent topics at the frontier of knowledge on Strength of Materials, which can be consulted not only by experienced researchers but also by students to understand how vast this science can be.

Dr Héctor Enrique Jaramillo Suárez
Science and Engineering of Materials Research Group,
Energetic and Mechanical Department,
Engineering Faculty,
Autónoma de Occidente University,
Cali, Colombia

Dr Julian Arnaldo Avila
Assistant Professor,
Sao Paulo State University,
Brazil

Dr Can Chen, Ph.D., P.E.
ChemCo Systems,
USA

Section 1

Traditional Materials

Tensile Strength of Unidirectional Carbon Fiber-Reinforced Plastic Composites

Go Yamamoto, Keita Koizumi and Tomonaga Okabe

Abstract

The tensile strengths of unidirectionally aligned carbon fiber-reinforced plastic (UD-CFRP) were predicted by implementing a spring element model (SEM) that takes into account a stress concentration acting on an intact fiber surface originated from a fracture site in an neighboring fiber. The surface stress concentration was experimentally investigated by implementing multi-fiber fragmentation testing in combination with the SEM simulation. Four types of epoxy materials were selected to explore the effects of matrix polymer properties on the surface stress concentration. The size scaling results, coupled with the results of the SEM simulation, designed to take into account the surface stress concentration, were reasonably consistent with the experimentally obtained data on the tensile strengths of the UD-CFRP composites, irrespective of the differences in the matrix mechanical characteristics. The possible mechanisms by which additional stress concentration is generated on an intact fiber surface were analyzed numerically using the finite element method.

Keywords: carbon fiber-reinforced plastic (CFRP), tensile strength prediction, fiber fragmentation, stress concentrations, finite element analysis

1. Introduction

Tensile strength prediction of unidirectional carbon fiber-reinforced plastic (UD-CFRP) composites had been one of the major topics of CFRP composite research since the 1950s. Many attempts had been conducted to predict tensile strength, including the early pioneering work by Cox [1], Rosen [2], and Kelly and Tyson [3]. In recent years the studies using enhanced computer simulations have deepened the understanding of failure processes of a UD-CFRP composite, and these studies have enabled greatly increased understanding of the failure of the composite structures [4, 5]. More recently the work by Swolfs and colleagues showed observations of individual fiber breaks occurring leading to the creation of clusters of breaks in UD-CFRP composites using high-resolution synchrotron tomography, leading to an experimental proof of critical cluster size [4]. The work by Thionnet and colleagues has used a 3D multi-scale simulation coupled with experimental results which has allowed a detailed understanding of failure in UD-CFRP composites including the kinetics of fiber breaks not only in monotonic tests but also in long-term steady load tests [5]. Moreover, improved computer

techniques have enriched the understanding of the failure processes of UD-CFRP composites [4–7].

According to the above-mentioned previous reports, the failure mechanisms of UD-CFRP composites can be described as follows: no load perturbation resulting from a fiber break is uniformly distributed among the surviving fibers because it is more heavily applied to the next fibers. Therefore, when a fiber breaks, the load that it is carrying is transferred to the surviving neighbors, increasing the degree of concentrated stress on these fibers relative to more distant fibers and increasing the probability of failure at this position. This consequently leads to the constitution of broken fiber clusters and subsequent failure of the UD-CFRP composites. Considering such fracture processes, although a large number of studies have only addressed the load redistribution caused by fiber breakage, several studies that have implemented fragmentation tests have reported that a matrix crack or damage to a matrix comes from around a fiber break point. Although the concentrated stress on an intact fiber surface neighboring a fiber break point has been widely acknowledged as a critical factor determining the ultimate tensile strength of UD-CFRP composites, the strength prediction of such composite considering the stress concentration owing to the fiber failure is so far from satisfactory.

Here we considered the stress concentration acting on an intact fiber surface caused by a fracture site in a neighboring broken fiber into our prediction of the ultimate tensile strengths of the UD-CFRP composites. The concentrated stress acting on the intact fiber surface was investigated by utilizing a double-fiber fragmentation testing in combination with a SEM simulation. The acquired stress concentration factors were then implemented to access the tensile strength of the UD-CFRP composites. The double-fiber fragmentation composites and the UD-CFRP composites were elaborated with a T1100G-type carbon fiber and epoxy material and tested to validate the proposed prediction method. The size scaling results obtained in conjunction with the results obtained from the SEM simulation were reasonably consistent with the experimental data on the tensile strengths of the UD-CFRP composites. We have also systematically investigated a possible scenario on the origin of stress concentrations generated on an intact fiber surface which is investigated through a numerical analysis based on the finite element method.

2. Experimental method

2.1 Sample preparation and mechanical characterization

T1100G-type carbon fiber and four types of bisphenol-A-epoxy resin materials were used to elaborate multi-fiber and UD-CFRP composites. The four types of preheated and degassed epoxy resins were separately poured into a preheated glass mold, then cured in an air oven at 160°C for 5 h followed by post-curing at 180°C for 2 h. The specimens were cut into a dumbbell shape (gauge length = 30 mm; width narrow parallel portion = 5 mm; thickness = 1 mm) according to the JIS-K7161-2 standard. The mechanical properties were measured by uniaxial tensile loading tests performed on a servohydraulic testing machine (i.e., MTS Landmark) with a loading cell of 50 kN under atmospheric conditions at room temperature. The load application was performed at a crosshead speed of 4.17 $\mu\text{m/s}$ (0.25 mm/min). Two strain gauges were mounted along the longitudinal and transverse directions on the sample. **Figure 1** indicates that tensile loading experiments performed herein revealed that the four types of epoxy materials exhibited different mechanical characteristics. Therefore, the epoxy materials are hereafter referred to as

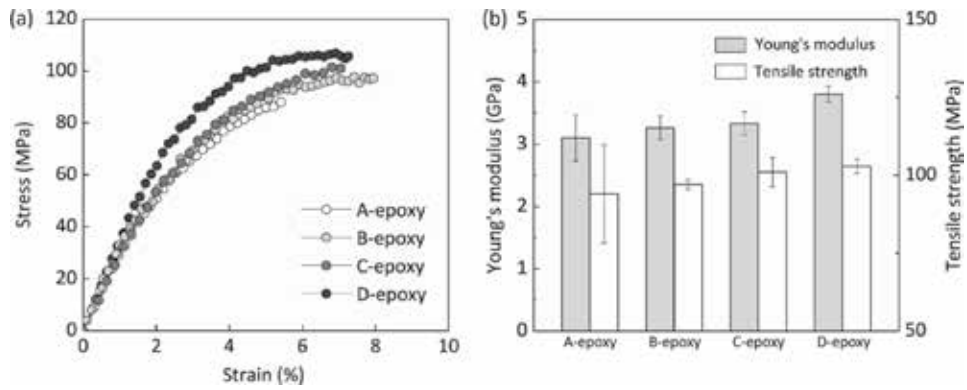


Figure 1. Summary of the (a) stress–strain curves and (b) mechanical properties for the four types of epoxy materials.

“A-epoxy,” “B-epoxy,” “C-epoxy,” and “D-epoxy,” with the order of the names indicating the magnitude of the elastic modulus.

Multi-fiber fragmentation specimens were elaborated by positioning two to four fibers parallel to the loading direction, implementing an interfiber spacing of approximately one-half to four fiber diameters (i.e., approximately 3.5–20.0 μm). The details of sample preparation can be found in [8]. Multi-fiber fragmentation tests were conducted to facilitate the derivation of a quantitative description of fiber failure mechanisms by using a polarized light microscope equipped with a four-point bending machine. A strain gauge was used to monitor the tensile strain applied to the fibers. The tensile strain was increased in 0.1% steps until a maximum of 5.0% strain was applied and kept constant during the measurement of both the number and positions of the broken fibers. The number of fractured fibers observed under the pure bending conditions was measured using the microscope. The strain applied to the fiber ε_f was calculated as follows:

$$\varepsilon_f = \varepsilon_c \times \frac{2.0}{\kappa} \times \left(\frac{t - 2d}{t} \right) - \varepsilon_f^r, \quad (1)$$

where ε_c is the acquired composite strain, κ is the gauge factor ($=2.13$), t is the thickness of the multi-fiber specimens (≈ 2 mm), d is the embedded fiber depth (≈ 60 μm), and ε_f^r is the indirectly applied strain that comes from the included residual strain on the fiber caused by the thermal expansion mismatch between them. The tensile strengths of the UD-CFRP composites were investigated to validate the accuracy of the predicted tensile strength. The composites were elaborated via conventional technique to prepare the laminate structure of $[0_6]$. The volume fraction of the fiber and the density of the UD-CFRP composites were 57% and 1.79 Mg/m^3 , respectively. The tensile strength of the composites was measured via tensile loading tests under ambient conditions. The crosshead speed and the gauge length were 21.2 $\mu\text{m/s}$ (1.27 mm/min) and 127 mm, respectively.

2.2 Model preparation

Monte Carlo methods were mounted in the SEM simulation to investigate the SCF on the intact fiber surface next to the fiber break points. The details of model preparation and simulation procedures can be found in [8]. In brief, a simulation model consisted of longitudinal and transverse spring in a 3D hexagonal arrangement. In this analysis, the longitudinal elements behave as carbon fibers that exclusively sustain the tensile load, while the transverse elements work as a matrix that

only carries the shearing load. The stiffness matrices of the fiber matrix elements are separately calculated as follows:

$$\mathbf{K}_L^e = \pi R^2 \int_0^l \mathbf{B}_L^{eT} E_f \mathbf{B}_L^e dz, \quad (2)$$

$$\mathbf{K}_T^e = \frac{\pi R l}{3} \int_0^l \mathbf{B}_T^{eT} G_m \mathbf{B}_T^e dr, \quad (3)$$

$$\mathbf{B}_L^e = \begin{bmatrix} \frac{1}{l} & -\frac{1}{l} \end{bmatrix}, \quad (4)$$

$$\mathbf{B}_T^e = \begin{bmatrix} \frac{1}{d} & -\frac{1}{d} \end{bmatrix}, \quad (5)$$

where \mathbf{K}_L^e and \mathbf{K}_T^e are the stiffness matrices of the fiber and matrix elements, respectively. Subscripts L and T represent the longitudinal and transverse spring elements, respectively, E_f is the Young's modulus of the fiber ($=324$ GPa), G_m is the shear modulus of a matrix ($=1.4$ GPa), R is the radius of the fiber ($=2.7$ μm), and l and d are the element lengths along the longitudinal and transverse directions, respectively. The length of the transverse spring d can be obtained as follows:

$$d = \begin{cases} 0.01 & (f \leq 4) \\ R \left(\sqrt{\frac{2\pi}{\sqrt{3}V_f}} - 2 \right) & (f > 4) \end{cases}, \quad (6)$$

where V_f and f are the volume fraction of the fiber ($=57\%$) and the number of fibers in the SEM, respectively. The experimentally acquired average interfiber spacing in the multi-fiber fragmentation specimens was ~ 0.01 mm. Therefore, d was set to 0.01 to examine the results of the multi-fiber fragmentation tests conducted under the condition that the maximum number of fibers in the model is four. A hexagonal close-packed structure was assumed for the analysis of the full composite model. In the SEM having two to four fibers, the longitudinal elements other than the fibers are assigned as a matrix; therefore, the stiffness of a matrix is implemented in the longitudinal elements.

With the aim of simplicity, the SEM model considers exclusively the effect of plastic deformation of the matrix. The axial stress σ_s in the broken fiber when plastic deformation occurs in the matrix close to the fiber breaking point or the fiber edge is expressed as a function of distance D_s from those positions as follows:

$$\sigma_s = \frac{2\tau_s D_s}{R}, \quad (7)$$

where τ_s is the interfacial shear stress and is postulated to be constant; the matrix behaves as an elasto-perfectly plastic body, and the equilibrium equation to represent the entire system is given as follows:

$$\left[\sum_{e=1}^{N_f - N_b - N_p} \mathbf{K}_L^e - \sum_{e=1}^{N_m} \mathbf{K}_T^e \right] \mathbf{u} + \sum_{e=1}^{N_p} \pi R^2 \int_0^l \mathbf{B}_L^{eT} \sigma_s dz = \mathbf{f}, \quad (8)$$

where N_f and N_m are the number of spring elements for the fiber and matrix, respectively, N_b is the number of fractured fibers, and N_p is the number of fiber spring elements in the plastic deformation region. We considered herein the

situation where the fiber failure is assumed to take place at the fiber surface, based on the fact that almost all fibers were broken by surface flaws [9]. Therefore, the probability of fiber breakage $P_f(\sigma)$ under the condition that the fiber is subjected to stress σ at the surface area $S_f (= 2\pi RL_f)$ is given as follows:

$$P_f(\sigma) = 1 - \exp \left\{ -\frac{S_f}{S_{f,0}} \left(\frac{\sigma}{\sigma_{01}} \right)^{m_1} - \frac{S_f}{S_{f,0}} \left(\frac{\sigma}{\sigma_{02}} \right)^{m_2} \right\}, \quad (9)$$

where $S_{f,0} (= 2\pi RL_{f,0})$ is the fiber surface area ($L_{f,0} = 10$ mm), L_f is the gauge length, $\sigma_{01} (=7.7)$ and $\sigma_{02} (=9.1)$ are the Weibull scale parameters, and $m_1 (=4.5)$ and $m_2 (=13.0)$ are the Weibull shape parameters. The details of the Weibull parameter determination procedures can be found in [10, 11]. Fibers are hexagonally arranged in the model; thus, the fiber surface can be divided into six parts. Thus, taking into account the contribution of concentrated stress acting on an intact fiber surface, the probability of fiber breakage $P_{f,i}(\sigma)$ can be rewritten as follows:

$$P_{f,i}(\sigma) = 1 - \exp \left\{ -\frac{S_{f,i}}{S_{f,0}} \left(\frac{\alpha_i \sigma}{\sigma_{01}} \right)^{m_1} - \frac{S_{f,i}}{S_{f,0}} \left(\frac{\alpha_i \sigma}{\sigma_{02}} \right)^{m_2} \right\}, \quad (10)$$

where $S_{f,i}$ is the i -th fiber segment of the surface area ($S_{f,i} = \pi RL_{f,0}/3$). The SEM does not represent the matrix aside from the shear load directly. Thus, the additional stress concentration is applied in an ad hoc manner to illustrate the experimentally observed correlations in fiber failures. The strength of the n -th fiber segment is determined by choosing a random number R_n ranging from 0 to 1 and solving equation $R_n = P_{f,n}(\sigma)$. The longitudinal spring element was removed from the simulation model when the stress applied to a fiber at the n -th fiber segment achieved the statistical distribution of the strength of the fiber σ_n .

The surface SCFs α of an intact fiber were investigated by implementing the SEM to investigate the α value, with the purpose of ensuring that it was equivalent to the coordinated fracture percentage, which is defined as a failure occurring at the elements adjacent to a broken element in the same horizontal plane of the broken fiber element that was determined via multi-fiber-fiber fragmentation testing. Thus, the two to four longitudinal elements in the center of the SEM were assigned to the fibers, and the remaining were assigned to the matrix. In the study, the bimodal Weibull distribution was implemented as the statistical distribution of fiber strength. The full composite model comprised 1024 fibers measuring 3 mm in length that were divided into 300 segments. Prior to comparing the simulated results to the experimental data, the simulated strengths were subjected to size scaling [12].

3. Results and discussion

First, the UD-CFRP composites made with four types of matrix polymers were elaborated and then employed with tensile loading tests to investigate their mechanical properties along the direction of the fiber axis. As shown in **Figure 2**, all composites tested in this study demonstrated catastrophic failure after reaching a maximum load, exhibiting a stress-strain relationship that is typically observed in conventional UD-CFRP composites; no clear difference was noted between the Young's modulus values, whereas, for example, the composite fabricated with the D-epoxy demonstrated strength enhanced by a factor of about 1.2 compared to the composite prepared with the A-epoxy.

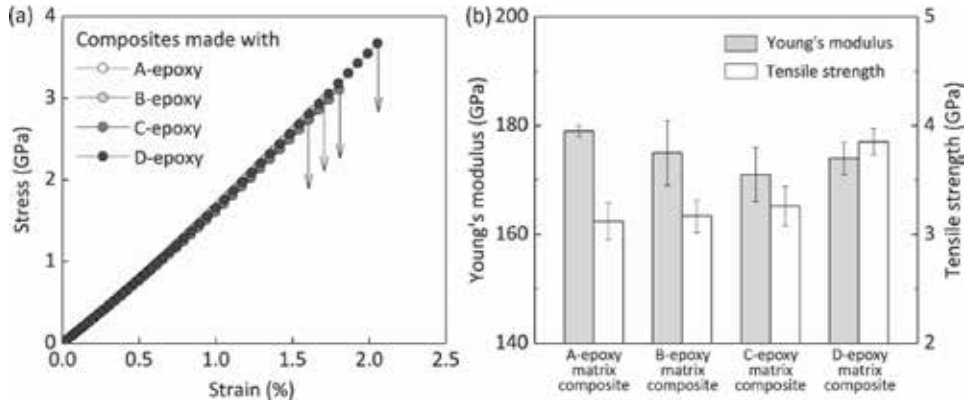


Figure 2.

Summary of the (a) stress–strain curves and (b) mechanical properties for the four types of UD-CFRP composites.

As previously mentioned, the fibers next to a broken fiber were applied to enhanced concentrated stress, leading to the increased of the failure probability. Thus, the understanding of the failure processes of the above-mentioned fiber is a requirement for the tensile strength prediction of UD-CFRP composites. A double-fiber fragmentation testing was conducted in order to investigate the effects of the interfiber spacing on the failure processes of such fibers. First, the B-epoxy was used in the specimen preparation. It was found from the double-fiber fragmentation testing that a large number of fiber underwent failure at similar positions, suggesting that the concentrated stress generated by fiber failure was sufficiently high to cause the next fiber to fracture, which nullifies the influence of randomly distributed flaws along the fiber on the fiber strength. The percentages of coordinate fractures observed for the double-fiber composites with interfiber spacings of 3.6, 9.9, and 20.0 μm were 73, 57, and 60%, respectively. Even though some flocculation has been observed for the percentages of coordinate fractures, the acquired percentages appeared to be higher than those observed for fiber failure that was governed by the statistical strength distribution of fibers [13]. This indicates that for an interfiber spacing of one-half to four fiber diameters, the failure processes of the fiber were governed by the fiber-fiber interactions.

Next, the fiber fracture behavior of the multi-fiber fragmentation specimens having up to four fibers was investigated to determine the surface SCFs. The microscopy observation revealed that matrix cracks and the coordination of fractures in neighboring fibers have been observed in multi-fiber fragmentation specimens, irrespective of the number of fibers. The coordinated fracture percentages in the double-fiber specimens tended to increase as the number of fibers was increased. At 3.2% fiber strain (i.e., ϵ_f calculated via Eq. (1) for a composite strain ϵ_c of 5.0%), the coordinated fracture percentages in the double-, triple-, and quadruple-fiber specimens were calculated to be 48.3% ($\pm 14.1\%$), 33.3% ($\pm 17.8\%$), and 15.8% ($\pm 5.8\%$), respectively.

A quantitative determination of the surface SCFs α on an intact fiber next to a fiber break point was achieved by implementing the SEM to investigate the α . **Figure 3a** shows the relationship between the SCF and the coordinated fracture percentages for each fragmentation specimen, which was determined by systematically sweeping α in the SEM simulation. The simulation results demonstrated that the percentages increased with an increased SCF and decreased in response to an increase in the number of fibers. By comparing the simulated coordinated fracture percentages to the experimentally obtained data, the surface SCF on an intact fiber

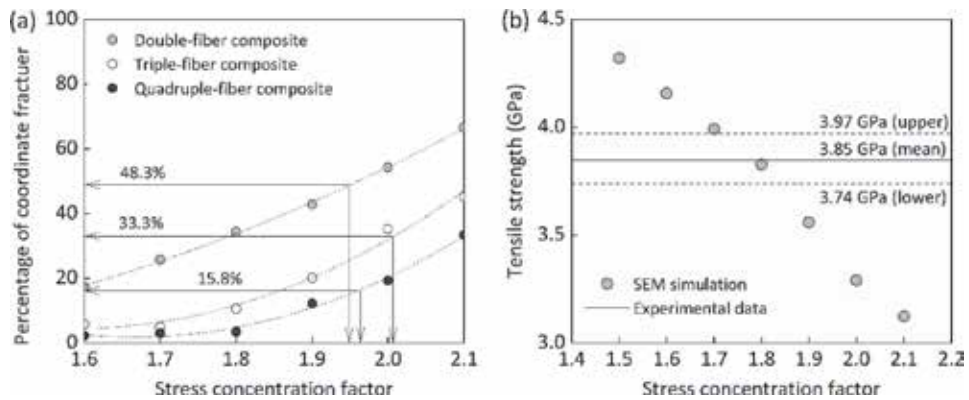


Figure 3.
 (a) Relationship between the stress concentration factors and the percentage of coordinated fractures. (b) Experimental and simulated results for the UD-CFRP composites.

appeared to be ~ 2.0 . Furthermore, no fiber number significantly affects the surface SCF, suggesting that for the UD-CFRP composites elaborated with the B-epoxy, the stress concentration acting on the fiber surface was approximately twice as much as the fiber stress with no additional surface stress concentration. **Figure 3b** depicts a comparison of the simulated experimental results for the UD-CFRP composites prepared with the B-epoxy. As indicated in **Figure 3b**, the measured tensile strengths of the B-epoxy matrix composites are 3.05–3.32 GPa (mean, 3.17 GPa). The simulated data that acquired no consideration of the added concentrated stress were incongruent with the experimental data, whereas the predictions incorporating an SCF of 2.0 were reasonably consistent with the experimental data, indicating that the prediction method proposed herein yields a reasonably accurate tensile strength prediction when the matrix crack-induced surface stress concentration of fibers is appropriately considered.

We implemented the above-mentioned strength prediction method into the UD-CFRP composites elaborated with the “A-epoxy,” “C-epoxy,” and “D-epoxy.” The surface SCF on intact fibers was acquired via the double-fiber fragmentation testing taking into account of the fact that for the B-epoxy matrix composites, no fibers number influence the SCFs. The SCFs were calculated as ~ 2.15 for the A-epoxy material, ~ 1.93 for the C-epoxy material, and ~ 1.75 for the D-epoxy material. Thus, surface SCFs were implemented to access the tensile strength of the three types of the UD-CFRP composite materials. In one example, as shown in **Figure 2b**, the measured tensile strengths of the D-epoxy matrix composites ranged from 3.74 to 3.97 GPa (mean, 3.85 GPa). The estimated tensile strength simulated under the condition of $\alpha = 1.75$ was ~ 3.9 GPa. Consequently, the results demonstrate that, even if the mechanical properties of the matrix materials vary, the proposed method can yield a reasonable prediction of the tensile strength of the UD-CFRP composites.

The possible mechanisms by which the additional concentrated stress occurs is not clear so far; moreover it is unclear why the SCF varies depending on the matrix mechanical properties. A numerical analysis using the FEM was performed to understand possible mechanisms by which significant stress occurred on the intact fiber surface next to the fiber break point. The details of model preparation and material properties can be found in [8]. In brief, a hexagonal fiber arrangement was used in this study, and only one-half of the composite structure was modeled and analyzed due to reasons of structural symmetry. The plasticity-free layer model, referred to as the SSV model [10], an elastic layer with a thickness of 50 nm, was

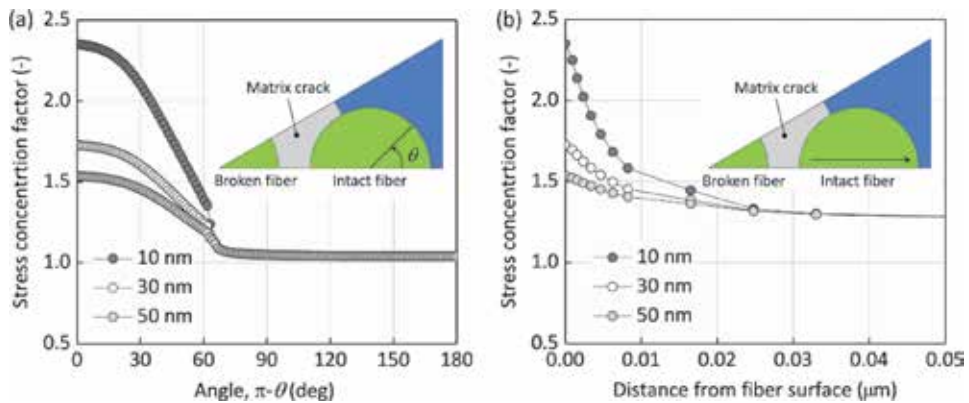


Figure 4. Positional dependence of the SCF in the (a) circumferential direction and (b) diameter direction of the intact fiber.

applied around the matrix crack using the same elastic properties as the D-epoxy material. No matrix crack was assumed to reach the intact fiber surface, and there was a gap between the crack tip and the intact fiber surface. In this analysis, the gap was changed to 10, 30, and 50 nm. The elastic stiffnesses of the T1100G-type carbon fiber are listed in [11].

It was demonstrated that an SCF of $\alpha = \sim 1.7$, as observed for the D-epoxy matrix composite with the gap of 30 nm, was indeed on the surface of the intact fiber. Here, the SCF was defined as the ratio of the stress of an outermost surface element of the intact fiber to the stress in an element sufficiently away from the fiber break point. Note that the stress recovery behavior in the broken fiber was reasonably consistent with that obtained from the SEM simulation under the SCF condition of $\alpha = 1$. **Figure 4a** shows the effects of the gap on the SCF in the circumferential direction of the intact fiber; the SCF decreases with the increase in the measurement angle, and the SCF reaches almost 1, regardless of the differences in the gaps. **Figure 4b** summarizes the effects of the gap on the SCF in the diameter direction of the intact fiber; the SCF decreases with the increase in the distance from fiber surface, indicating that a significantly higher stress concentration is generated on the outermost surface area, and the degree of stress concentration is going to be small rapidly inside the fiber. The averaged SCF subjecting on the full cross-sectional area of the intact fiber next to a broken fiber at the plane of fracture was calculated to be approximately 1.1. This “averaged SCF” is reasonably consistent with the previously reported averaged SCF around a broken fiber in a UD-CFRP composite [14–17].

4. Conclusions

Four types of UD-CFRP composite materials with different mechanical characteristics were elaborated in this study. The tensile strengths of the fabricated composites were predicted via a SEM simulation based on the results obtained from multi-fiber fragmentation experiments. The primary aim of this study was to explore the effects of matrix polymer properties on the stress concentrated on the fiber surface. It was revealed that the extent of concentrated stress acting on the intact fiber surface can be changed by modifying the mechanical properties of the matrix polymer. By employing an epoxy matrix having a higher Young’s modulus

and increased tensile strength in the composite preparation reduced the SCF from a ~ 2.15 to ~ 1.75 . We have also shown a numerical scenario on the origin of the stress concentrations that are generated on the intact fiber surface by implementing the SSV model and employing the rehardening characteristics of epoxy materials. Finally, we confirmed that employing the measured SCFs and bimodal Weibull distribution to determine how strength is statistically distributed throughout the fiber yields the predicted strengths of the four types of UD-CFRP composites that are reasonably consistent with the experimental data, thereby demonstrating the validity of the proposed prediction method.

Acknowledgements

This work was partly supported by Toray Industries, Inc., and JSPS KAKENHI with grant number 18K04721.

Author details

Go Yamamoto*, Keita Koizumi and Tomonaga Okabe
Department of Aerospace Engineering, Tohoku University, Sendai, Japan

*Address all correspondence to: yamamoto@plum.mech.tohoku.ac.jp

IntechOpen

© 2019 The Author(s). Licensee IntechOpen. This chapter is distributed under the terms of the Creative Commons Attribution License (<http://creativecommons.org/licenses/by/3.0>), which permits unrestricted use, distribution, and reproduction in any medium, provided the original work is properly cited. 

References

- [1] Cox HL. The elasticity and strength of paper and other fibrous materials. *British Journal of Applied Physics*. 1952; **3**(3):72-79. DOI: 10.1088/0508-3443/3/3/302
- [2] Rosen BW. Tensile failure of fibrous composites. *AIAA Journal*. 1964;2(11): 1985-1991. DOI: 10.2514/3.2699
- [3] Kelly A, Tyson W. Tensile properties of fibre-reinforced metals: Copper/tungsten and copper/molybdenum. *Journal of the Mechanics and Physics of Solids*. 1965;13(6):329-350
- [4] Swolfs Y, Morton H, Scott AE, Gorbatikh L, Reed PAS, Sinclair I, et al. Synchrotron radiation computed tomography for experimental validation of a tensile strength model for unidirectional fibre-reinforced composites. *Composites Part A Applied Science and Manufacturing*. 2015;77(6): 106-113. DOI: 10.1016/j.compositesa.2015.06.018
- [5] Thionnet A, Chou HY, Bunsell A. Fiber break processes in unidirectional composites. *Composites Part A Applied Science and Manufacturing*. 2014;65: 148-160. DOI: 10.1016/j.compositesa.2014.06.009
- [6] Chou HY, Bunsell AR, Mair G, Thionnet A. Effect of the loading rate on ultimate strength of composites. Application: Pressure vessel slow burst test. *Composite Structures*. 2013;104: 144-153. DOI: 10.1016/j.compstruct.2013.04.003
- [7] Tavares RP, Otero F, Turon A, Camanho PP. Effective simulation of the mechanics of longitudinal tensile failure of unidirectional polymer composites. *International Journal of Fracture*. 2017; **208**(1-2):269-285. DOI: 10.1007/s10704-017-0252-9
- [8] Yamamoto G, Onodera M, Koizumi K, Watanabe J, Okuda H, Tanaka F, et al. Considering the stress concentration of fiber surfaces in the prediction of the tensile strength of unidirectional carbon fiber-reinforced plastic composites. *Composites Part A Applied Science and Manufacturing*. 2019;121:499-509. DOI: 10.1016/j.compositesa.2019.04.011
- [9] Watanabe J, Tanaka F, Higuchi R, Matsutani H, Okuda H, Okabe T. A study of stress concentrations around fiber breaks in unidirectional CF/epoxy composites using double-fiber fragmentation tests. *Advanced Composite Materials*. 2018;27(6): 575-587. DOI: 10.1080/09243046.2017.1416567
- [10] Suo Z, Shih CF, Varias AG. A theory for cleavage cracking in the presence of plastic flow. *Acta Metallurgica et Materialia*. 1993;41(5):1551-1557. DOI: 10.1016/0956-7151(93)90263-R
- [11] Tane M, Okuda H, Tanaka F. Nanocomposite microstructures dominating anisotropic elastic modulus in carbon fibers. *Acta Materialia*. 2019; **166**:75-84. DOI: 10.1016/j.actamat.2018.12.029
- [12] Okabe T, Takeda N. Size effect on tensile strength of unidirectional CFRP composites experiment and simulation. *Composites Science and Technology*. 2002;62(15):2053-2064. DOI: 10.1016/S0266-3538(02)00146-X
- [13] Van Den Heuvel PWJ, Van Der Bruggen YJW, Peijs T. Failure phenomena in multi-fibre model composites: Part 1. An experimental investigation into the influence of fibre spacing and fibre-matrix adhesion. *Composites Part A Applied Science and Manufacturing*. 1996;27(9):855-859. DOI: 10.1016/1359-835X(96)00023-1
- [14] Van Dyke P, Hedgpeeth JM. Stress concentrations from single-filament

failures in composite materials. *Textile Research Journal*. 1969;**39**(7):618-626.
DOI: 10.1177/004051756903900702

[15] Nedele MR, Wisnom MR. Stress concentration factors around a broken fibre in a unidirectional carbon fibre-reinforced epoxy. *Composites*. 1994;**25**(7):549-557. DOI: 10.1016/0010-4361(94)90183-X

[16] Nedele MR, Wisnom MR. Three-dimensional finite element analysis of the stress concentration at a single fibre break. *Composites Science and Technology*. 1994;**51**(4):517-524. DOI: 10.1016/0266-3538(94)90084-1

[17] Wisnom MR, Green D. Tensile failure due to interaction between fibre breaks. *Composites*. 1995;**26**(7):499-508. DOI: 10.1016/0010-4361(95)96807-I

Research Progress of the Drill String Hardbanding Materials

Kai Zhang, Zhenquan Wang and Deguo Wang

Abstract

Among anti-wear technologies, hardbanding is the most effective measure to reduce the wear of drill pipe and casing. Many new hardbanding materials are introduced constantly, and the varieties of hardbandings are becoming more and more abundant. In this paper, the research history and status quo of the hardbanding materials in tool joint are reviewed. And the advantages and disadvantages of all kinds of wear-resisting materials are introduced. Finally, the development orientation in hardbanding materials in drill joint was pointed out.

Keywords: drill string, hardbanding, casing wear, anti-friction, anti-wear

1. Introduction

The drill pipe joint is an important part of drill pipe, which is used to connect the drill pipe to form a drilling string. It always adopts a larger wall thickness and larger outer diameter, which can increase the drill string strength and protect drill pipe. In the process of drilling, when the inclination of the well is larger or the drill string is subjected to larger lateral force, the drill pipe joint will contact with the borehole wall or the inner wall of the casing, which can cause both the serious drill string wear and the heavy casing wear.

At present, there are lots of anti-wear technologies of the drill pipe joint, such as drill string hardbanding, rubber drill pipe protector, casing pipe blast joint, etc. Among them, hardbanding is the process of bonding the hardbanding alloy with the parent steel of the drill pipe (**Figure 1**), which has the advantages of stable performance, simple operation, and easy maintenance [2]. At the moment, hardbanding is the most effective measure to reduce the wear of drill pipe and casing among these anti-wear technologies [3]. However, with the development of oil and gas exploration and drilling technology, complex well structures, such as deep well, extended reach well, horizontal well, and highly-deviated well, are being used more and more widely. In addition, the formation structures, such as strong abrasive formation, fractured formation, etc., are becoming more and more complex in the process of oil drilling. All of these put forward higher requirements for anti-wear and anti-friction characteristics of hardbandings, so the development of new hardbanding materials has already been the task of top priority [4–6].

With the gradual solution of the problems in the field application of hardbanding materials, many new hardbanding materials are introduced constantly, and the varieties of hardbandings are becoming more and more abundant. For this paper, the development and application of hardbanding materials for drill pipe joints were reviewed. Furthermore, the development of a new hardbanding material



Figure 1.
Hardbanding welding process and morphology after welding [1].

independently developed by our team was reviewed. Finally, the weaknesses and development orientation of hardbanding materials were pointed out.

2. Development status of hardbanding materials

The development process of the hardbanding material is divided into two stages: the first stage is the cemented carbide material stage (from the 1930s to the early 1990s); the second stage is the “casing-friendly” material stage (from the 1990s to the present) [7].

2.1 Cemented carbide material stage

The cemented carbide hardbanding material was invented and marketed by Hughes Tool Company in the 1930s, which was designed to prevent the abrasive wear of drill pipe joints in the open hole section and improve the service life of drill pipe. This hardbanding material is composed of low carbon steel matrix and carbide particles, which is a very effective method of protecting drill pipe joints in shallow wells (<1500 m) and vertical wells (well deviation below 2°) [8, 9].

But as wells become more complex, the depth of the well is getting deeper, and the angle of the well is getting larger. The casing failures caused by the hardbanding of cemented carbide became more and more serious, which had aroused wide concern [10]. A lot of experimental studies have shown that during rotary drilling and tripping, the cemented carbide particles embedded in it will be soon exposed, because of the relatively soft base alloy of this wear-resistant belt. These exposed cemented carbide particles will cause serious abrasive wear on the casing wall and finally cause the casing failure.

In order to avoid the loss caused by casing failure, it was decided to stop using the cemented carbide hardbandings. Only the smooth drill pipes without hardbanding or other anti-wear technologies (such as rubber drill pipe protector, casing pipe blast joint, etc.) were allowed. Other anti-wear technologies could reduce casing wear to some extent but were generally faced with many problems, such as high cost, complex structure, difficult installation, low life, easy to cause downhole accidents, etc. [11].

Therefore, the major technical service companies began to develop new materials to replace the cemented carbide material. These materials are generally characterized by low friction, small wear to the casing, and high hardness, which can

protect the drill pipe joint to a certain extent. Since then, the development of drill pipe joint hardbanding material has entered the stage of “casing-friendly” material.

2.2 “Casing-friendly” material stage

“Casing-friendly” material has a low friction factor, resulting in lower casing wear. Small friction and friction heat can be produced when this hardbanding material is in contact with the inner wall of the casing. There are two main types of “casing-friendly” materials: one is the “amorphous” hardbanding material; the other one is the “crystalline” hardbanding material. The crystalline material refers to a material in which atoms follow a certain law in the arrangement. On the other hand, the material whose internal atoms are arranged in an irregular state is called the amorphous material [12, 13].

2.2.1 “Amorphous” material hardbandings

In 1990, Liquidmetal Technologies LTD developed a chromium alloy hardbanding material, named Armacor MTM. This material is an “amorphous” chromium alloy, the microstructure of which has no grain boundary and is distributed in a single atomic structure. The outstanding feature of this metal structure is that it has a very low friction factor. Therefore, the wear of the casing is very small, which can greatly reduce the wear of the casing. It is the first kind of “casing-friendly” hardbanding material, which represents a significant improvement in hardbanding technology. But because the “amorphous” hardbanding has only a very thin layer with poor abrasion performance under the high pressure, the main shortcoming of this hardbanding material is insufficient wear-resistant ability, which makes the drill pipe joint not well protected [14].

Subsequently, the Liquidmetal Technologies company has developed some new hardbanding materials, such as Armacor MStar and Armacor TMax. Till now, Armacor MStar material is their most casing-friendly material [15]. Armacor TMax material is their hardest, most wear-resistant material, which is ideal for open-hole drilling environments. In addition to this, as amorphous materials, these materials can lead to improved corrosion resistance and resistance to reactivity at elevated temperatures (oxidation, vulcanization), which are suitable for geothermal well drilling and deep well drilling.

2.2.2 “Crystalline” hardbanding materials

At the end of 1992, Arnco Technology Trust, Ltd., developed a new generation of chromium carbide hardbanding material—ARNCO 200XT™. The hardbanding can effectively reduce the wear of the casing and ensure the durability of the drill pipe joint in the open hole section, which can minimize the wear of the drill pipe joint. However, with ARNCO 200XT, it is easy to generate micro-cracks in the application and welding process. Although it has no influence in the use process, all the cracked parts should be removed during the reapplication and welding. Subsequently, the company has developed many hardbanding materials, such as ARNCO 100XT, ARNCO 300XT, ARNCO 150XT, and ARNCO 350XT, to overcome the problems existing in ARNCO 200XT [16]. The tool performances of these hardbanding materials are shown in **Figure 2**.

Arnco Technology has led the hardbanding industry since pioneering the use of casing-friendly hardbanding two decades ago. To better understand the development of “crystalline” hardbanding materials, a more detailed introduction can be found in the following:

1. ARNCO 100XT hardbanding alloy [17]. ARNCO 100XT is an iron-base alloy containing chromium, manganese, and molybdenum, which can be welded seamlessly. Because of the above 50 rockwell hardness, the drill pipe joint can be well protected. The inherent low coefficient of friction is the most significant characteristic of Arnco100 XT hardbanding alloy. In the series of products of ARNCO, its anti-friction performance is the best, which can effectively reduce the wear caused by the contact between drilling pipe string and casing to extend the service life.
1. ARNCO 300XT hardbanding alloy [18]. As the “third-generation” product of Arnco Technology, ARNCO 300XT is an iron-base alloy including nickel, boron, and niobium, which is a chrome-free metal material with little environmental pollution. ARNCO 300XT can be directly welded on the worn 100XT and 150XT hardbandings, which increases its applicability. Because of the above 60 rockwell hardness, its wear resistance is much stronger, which can be used in the open hole in extreme grinding geological structure. Besides, the wear on the casing can be reduced effectively, which can obtain the lowest radial wear on the inside-wall of the casing.
2. ARNCO 150XT hardbanding alloy [19]. As the “fourth-generation” product of Arnco Technology, ARNCO 150XT is a kind of advanced crack-free and casing-friendly hardbanding, which inherited the advantages of ARNCO 100XT and ARNCO 300XT. The wear-resistant capacity of ARNCO 150XT is between ARNCO 100XT and ARNCO 300XT, and the anti-friction capacity is higher than ARNCO 300XT and ARNCO 100XT. It’s worth mentioning that repair welding can proceed under various external conditions without any crack, which can further enhance its applicability. Specifically, it can prevent the hydrogen sulfide corrosion and withstand high torque and high temperature in severe drilling conditions in extended reach wells, deep wells, and horizontal well, because of its maintaining of a certain toughness.
3. ARNCO 350XT hardbanding alloy [20]. As the “latest-generation” product of Arnco Technology, the wear resistance of ARNCO 350XT is further enhanced (compared with the ARNCO 300 XT), and the damage to the casing is further reduced, which is at present the strongest wear-resistant performance among Arnco Company’s products. It can be easily welded to new drill pipe joints and can be directly welded to on the ARNCO 100XT, ARNCO 150XT, ARNCO 350XT, and most other crack-free hardbandings without removing the original hardbandings.
4. NonMagXT™ hardbanding [21]. The appearance of nonmagnetic drill pipes raises an even newer requirement for hardbandings. NonMagXT™ is a newly developed nonmagnetic hardbanding, which is a patent-pending iron-based alloy system. This hardbanding features clear advantages over nickel and other iron-based nonmagnetic hardband products, which can enable easy, crack-free application onto stainless steel. It can also deliver exceptional wear resistance, greater ductility, and resistance to damage while in service.

2.2.3 Other hardbanding materials

The development of new hardbanding materials with high performance has already attracted the attention of the industry. Many technical service companies have developed new materials. Major products can be found in the following:

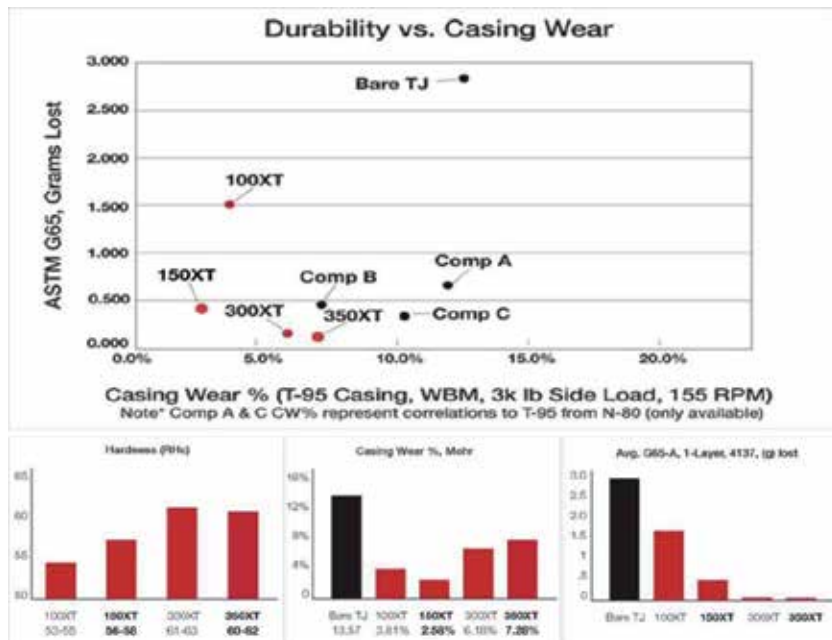


Figure 2.
 Tool performances of ARNCO hardbanding materials [16].

2.2.3.1 Postle industries hardbanding

Postle Industries has developed some new hardbanding materials, such as Duraband® NC hardbanding and Tuffband® NC hardbanding:

Duraband® NC from Hardbanding Solutions is a 100% crack-free casing-friendly hardbanding, which can provide maximum protection of the tool joint and casing as well as workstring completion tubing [22]. Duraband® NC consists of a hard but tough tool steel matrix with a high volume of tightly packed micro-constituents, which ensures a non-cracking hard band with excellent wear resistance in open hole drilling as well as being casing friendly.

Tuffband® NC is a high hardness hardbanding which can meet different application requirements [23]. When used by itself, it is especially suitable for casing-friendly hardbanding applications. When casing protection is not a factor, it can be used as a weld matrix with tungsten carbide (WC). Tuffband® NC is applied crack free and prevents spalling even under the most extreme drilling conditions and is 100% rebuildable.

2.2.3.2 TE metal works hardbanding

TE Metal Works specialize in 100% nonmagnetic applications for all directional and vertical drilling. TE NM1X hardbanding developed by TE Metal Works is an alloy which is 100% nonmagnetic and 100% crack free [24]. This hardbanding will outlast 3 times the length of non-mag welding alloys.

2.2.3.3 HBK series hardbandings

HBK series hardbandings are developed by Kooben Technology [25]. Kooben is only one company in China with the ability to research, develop, and manufacture

hardbanding. Kooben's hardbanding product line now has three grades. They are HBK 100, HBK 150, and HBK 300, which are suitable for any application. The performances of their hardbandings are similar to those of Arnco hardbandings. They can offer at the industry's most competitive prices and are compatible with all Arnco hardbandings. Besides, the client testing phase of nonmagnetic hardbanding wire has begun. In addition, Kooben is also one of the few companies in the world that have nonmagnetic hardbanding wire products.

2.2.3.4 Some hardbandings made in China

In addition to Kooben products, some "casing-friendly" materials can be occasionally reported on the Internet, and most of them imitate the foreign products. For example, Nate707J hardbanding material developed by Xi'an Nate Petroleum Technology Co., Ltd., is an iron-based amorphous hardbanding alloy, whose wear resistance is basically equivalent to that of ARMACOR Mstar and 3.8–3.9 times of that of ARNCO 100XT [26]; BoTn3000 hardbanding material produced by Shanghai BoTeng Welding Consumables Co., Ltd., is a chrome-free hardbanding material with high hardness and good wear resistance, which has reached the advanced level of similar products abroad [27]. In addition, some China units, universities, research institutes, and other institutions are studying the production of new hardbanding materials. Although China's "casing-friendly" hardbanding materials have started, some hardbanding materials have made great progress. Some properties are even better than similar foreign hardbanding materials. However, most of them are still in the research and experimental stage and have not been mass-produced and put into application [28].

3. Development status of diamond composite hardbanding materials

At present, mechanical properties and wear resistance of hardbandings have been dramatically advanced. Although such improvements have been made, hardbandings and casings still suffer from friction and wear issues. The materials of existing hardbanding products are mostly iron-base alloy materials, so the problem of wear and tear is always unavoidable because of the pairwise similarity of elements. Therefore, if nonmetallic materials with high wear resistance are used to produce hardbandings, the wear problem will be greatly solved.

Polycrystalline diamond (PCD) is widely used in oil and mining explorations due to the advantages of homogeneous hardness, good toughness, and easy processing. And furthermore, PCD has a high wear resistance and low friction coefficient. Even in a high-temperature environment, it can also maintain its excellent performance. Thus PCD is obviously an ideal hardbanding material which could accomplish the optimum balance of drill string improvement and casing wear reduction [29].

Zhang et al., of the China University of Petroleum, Beijing, has developed a new hardbanding material (shown in **Figure 3**), called PCD reinforced WC matrix composite (PCD composite for short), which is a kind of homogeneous composite material of fine property [30]. This hardbanding material has a strong resistance to wear, which can be very good to prevent the drilling pipe joint wear in the strong abrasive formation. Because of the extremely weak wear of the iron foundation material, the casing can be well protected with small friction factor and friction resistance.

In order to understand the relationship between the raw material's properties and its tool performance, the material properties and drill pipe hardbanding performance of this PCD composite were investigated [29]. We find that the

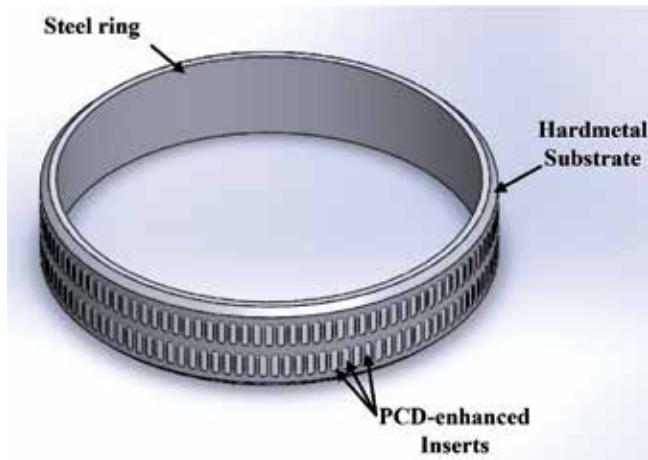


Figure 3.
Schematic description of PCD composite hardbanding.

excellent anti-friction property and reasonable hardness of this PCD composite hardbanding are the primary reasons for its enhanced tool performance. Besides, a height difference was found at the border between the PCD part and the WC matrix part, which is advantageous to form lubricant film to improve the lubricating performance. To better understand its performance, the friction and casing wear properties of PCD composite hardbanding were also investigated. The results indicate that as the applied load and sliding speed steadily increase, the friction coefficients of PCD composites decrease. In addition, the casing wear rates increase with increasing load but decline with sliding velocity. The dominant wear mechanism of the PCD composite is the micro-cutting wear, accompanied by adhesive wear [31].

Due to the poor thermal stability of PDC, the performance will be affected in high-temperature geothermal wells and deep wells [32]. In many polycrystalline diamond composites, the thermally stable polycrystalline (TSP) diamond can exhibit excellent anti-friction and good anti-abrasion, which also can be achieved in an environment of high temperature and super high pressure and thermally stable up to 1200°C. Thus, in order to improve the thermal stability, the TSP was used to replace the PCD to produce this hardbanding. By proving experimentation, TSP composites could satisfy the requirements of protecting the casing and the drill pipe at the same time when drilling deep holes. This perfect performance is dependent on the adsorbed lubricating liquid on the rubbing surface and the formation of height difference between the TSP part and the WC matrix part [33].

The overall results demonstrate that the PCD composite series hardbandings are extremely promising for drill pipe hardbanding applications.

4. Conclusions

1. At present, the research on hardbanding materials is still in the stage of “casing-friendly” materials. The hardbanding material is mainly developed to the directions of high wear resistance, high casing friendliness, and high rewelding.
2. Although more and more hardbanding products appear, ARNCO series hardbandings developed by Arnco Technology companies are still the best hard-

banding materials. The latest products ARNCO 350XT and 150XT are the best products with wear-resisting performance, which can guarantee 100% no crack.

3. In China, some “casing-friendly” hardbanding materials can be occasionally reported on the Internet, and most of them imitate the foreign products. The material performance has still a certain gap compared with mature products. Chinese research institutions should pay attention to the development of new wear-resistant belt materials to accelerate the development of a reasonable price. If the excellent performance of new wear-resistant belt material can be obtained, then China’s capacity for independent research and technology level will be enhanced.
4. PCD composite series hardbandings, which are extremely promising for drill pipe hardbanding applications. This hardbanding material has a strong resistance to wear, a good casing protected with small friction factor, and friction resistance.

Acknowledgements

This work was supported by National Key R&D Program of China (Grant No. 2016YFE0202200), the Fundamental Research Funds for the Central Universities (Grant No. 2652017070), Research Foundation of Key Laboratory of Deep Geo-drilling Technology, Ministry of Land and Resources (Grant No. PY201805), International S&T Cooperation Program of China (Grant No. 2012DFR70160), and the National Natural Science Foundation of China (No. 41672365).

Author details

Kai Zhang^{1,2*}, Zhenquan Wang³ and Deguo Wang⁴

1 School of Engineering and Technology, China University of Geosciences, Beijing, China


2 Key Laboratory on Deep Geo-Drilling Technology of the Ministry of Land and Resources, China University of Geosciences, Beijing, China

3 College of Petroleum Engineering, China University of Petroleum, Beijing, China

4 College of Mechanical and Transportation Engineering, China University of Petroleum, Beijing, China

*Address all correspondence to: zhangkai66@cugb.edu.cn

IntechOpen

© 2019 The Author(s). Licensee IntechOpen. This chapter is distributed under the terms of the Creative Commons Attribution License (<http://creativecommons.org/licenses/by/3.0>), which permits unrestricted use, distribution, and reproduction in any medium, provided the original work is properly cited. 

References

- [1] Zhang K, Wang D, Wang Z, et al. Research progress of the wear-resistant belt material in drill joint. *Oil Field Equipment*. 2016;**45**(2):94-98. DOI: 10.3969/j.issn.1001-3482.2016.02.021 (in Chinese)
- [2] Arnco Technology Trust Ltd. Hardbanding Basics [Internet]. 2015. Available from: <http://www.arncotech.com/resources/detail/hardbanding-basics/> [Accessed: 29 September 2019]
- [3] Gao DL, Sun LZ. New method for predicting casing wear in horizontal drilling. *Petroleum Science and Technology*. 2012;**30**(9):883-892. DOI: 10.1080/10916466.2010.493909
- [4] Murthy GVS, Das G, Das SK, et al. Hardbanding failure in a heavy weight drill pipe. *Engineering Failure Analysis*. 2011;**18**(5):1395-1402. DOI: 10.1016/j.engfailanal.2011.03.014
- [5] Gao D, Sun L, Lian J. Prediction of casing wear in extended-reach drilling. *Petroleum Science*. 2010;**7**(4):494-501. DOI: 10.1007/s12182-001-0098-6
- [6] Truhan J, Menon R, LeClaire F, Wallin J, Qu J, Blau P. The friction and wear of various hard-face claddings for deep-hole drilling. *Wear*. 2007;**263**(1):234-239. DOI: 10.1016/j.wear.2007.01.046
- [7] Mobley JC. Current hardbanding techniques protect pipe, casing. *Drilling Contractor*. 2005;**61**(2):21-22
- [8] Orland IJ, Bar-Matthews M, Kita NT, et al. Climate deterioration in the eastern Mediterranean as revealed by ion microprobe analysis of a speleothem that grew from 2.2 to 0.9 ka in Soreq cave, Israel. *Quaternary Research*. 2009;**71**(1):27-35. DOI: 10.1016/j.yqres.2008.08.005
- [9] Biddle JF, White JR, Teske AP, et al. Metagenomics of the subsurface Brazos-Trinity Basin (IODP site 1320): Comparison with other sediment and pyrosequenced metagenomes. *ISME Journal*. 2011;**5**(6):1038-1047. DOI: 10.1038/ismej.2010.19
- [10] Best B et al. Casing wear caused by tooljoint hardfacing. *SPE Drilling Engineering*. 1986;**1**(1):62-70. DOI: 10.2118/11992-PA
- [11] Bol GM. Effect of mud composition on wear and friction of casing and tool joints. *SPE Drilling Engineering*. 1986;**1**(05):369-376. DOI: 10.2118/13457-PA
- [12] John G. The Facts and Myths of Hardbanding [Internet]. 2000. Available from: <http://www.arncotech.cn/documents/factsandmythsofhardbanding.pdf> [Accessed: 30 October 2019]
- [13] Murthy G. Oil field drill pipes failure. In: *Handbook of Materials Failure Analysis with Case Studies from the Oil and Gas Industry*. Oxford: Butterworth-Heinemann; 2016. pp. 123-152. DOI: 10.1016/B978-0-08-100117-2.00002-9
- [14] McMicken J. Extending the life of an amorphous hardface by introduction of pellets. U.S. Patent Application 10/507,530 [12 January 2006]
- [15] Liquidmetal Coatings. OIL & GAS [Internet]. 2016. Available from: <http://www.liquidmetal-coatings.com/our-services/oil-gas/> [Accessed: 29 September 2019]
- [16] Arncon Technology Trust. Advanced Technology Backed by Unparalleled Service [Internet]. 2015. Available from: <http://www.arncotech.com/products/products-home/> [Accessed: 29 September 2019]

- [17] Arncon Technology Trust. ARNCO100XT [Internet]. 2016. Available from: <http://www.arncotech.com/products/100xt/> [Accessed: 29 September 2019]
- [18] Arncon Technology Trust. ARNCO300XT [Internet]. 2016. Available from: <http://www.arncotech.com/products/300xt/> [Accessed: 29 September 2019]
- [19] Arncon Technology Trust. ARNCO150XT [Internet]. 2016. Available from: <http://www.arncotech.com/products/150xt/> [Accessed: 29 September 2019]
- [20] Arncon Technology Trust. ARNCO350XT [Internet]. 2016. Available from: <http://www.arncotech.com/products/350xt/> [Accessed: 29 September 2019]
- [21] Arncon Technology Trust. Advanced Non-Magnetic Hardbanding [Internet]. 2016. Available from: <http://www.arncotech.com/products/arnco-nonmagxt/> [Accessed: 29 September 2019]
- [22] Postle Industries. Duraband® NC from Hardbanding Solutions 100% Crack-Free Casing Friendly Hardbanding [Internet]. 2019. Available from: <http://www.hardbandingsolutions.com/postle/duraband.php> [Accessed: 29 September 2019]
- [23] Posttazle Industries. What is Tuffband® NC? [Internet]. 2019. Available from: <http://www.hardbandingsolutions.com/postle/tuffband.php> [Accessed: 29 September 2019]
- [24] TE Metal Works. Hardbanding [Internet]. 2019. Available from: <http://temetalworks.com/hardbanding/> [Accessed: 29 September 2019]
- [25] Kooben Technology USA. Products [Internet]. 2018. Available from: <http://hardbanding.us/products/> [Accessed: 29 September 2019]
- [26] Changmao Y, Wu L. The utility model relates to an amorphous alloy type wear-resistant rod cored wire. *Hot Working Technology*. 2012;**41**(15):168-169
- [27] Youli W, Dongmei Q, Yaxin Y, et al. Study on surfacing welding technology of BoTn3000 wear-resistant belt of welding weighted drill pipe. *New Technology & New Process*. 2011;**11**:88-89. DOI: 10.3969/j.issn.1003-5311.2011.11.031 (in Chinese)
- [28] Xian S. Development and application of surfacing material for wear-resistant belt of oil drill pipe joint. *Petroleum Engineering Construction*. 2007;**4**:55-58 (in Chinese)
- [29] Zhang K, Wang D, Wang Z, et al. Material properties and tool performance of PCD reinforced WC matrix composites for hardbanding applications. *International Journal of Refractory Metals & Hard Materials*. 2015;**51**:146-152. DOI: 10.1016/j.ijrmhm.2015.03.011
- [30] Zhang K, Wang Z, Wang D, Zhao B. Processing methods and molds of the PCD composite hardbanding. Chinese Patent, Appli. NO. CN104588647 A. 2015. (in Chinese)
- [31] Zhang K, Wang Z, Wang D, Guo Y, Zhao B. Dry sliding friction and casing wear behavior of pcd reinforced wc matrix composites. *Tribology International*. 2015;**90**:84-95. DOI: 10.1016/j.triboint.2015.04.028
- [32] Zhang K, Wang ZQ, Wang DG. Friction and wear behavior of wear-resistant belts in drill joints for deep and ultra-deep wells. *Strength of Materials*. 2018;**50**(1):72-78. DOI: 10.1007/s11223-018-9944-2

[33] Zhang K, Wang Z, Wang D, et al.
Tribological behavior of TSP reinforced
WC matrix composites sliding against
N80 casing steel lubricated by
water-based drilling fluid.
International Journal of Refractory
Metals and Hard Materials.
2019;79:171-176. DOI: 10.1016/j.
ijrmhm.2018.12.005

Effect of Textures and Microstructures on the Occurrence of Delamination during and after Fracture Toughness Tests of API X80 Steel Plates

*Fabio Faria Conde, Haroldo Cavalcanti Pinto,
Mohammad Masoumi and Julian Arnaldo Avila*

Abstract

The API 5 L X80 is a high strength microalloyed steel, widely used in the gas and oil industry to fabricate pipelines. This steel presents a combination of elevated strength and toughness. In the present investigation, the microstructural features, fracture toughness and delamination occurrence of two X80 grade steel plates with different processing routes and chemical composition were studied. The first steel depicted a homogenous bainitic matrix and the second steel exhibited a banded microstructure composed of elongated ferrite grains, with macrosegregation in the mid-plane of the plates. Fracture toughness tests were conducted for both steels on 7-mm and 15-mm thick samples. The orientation distribution functions analysis revealed crystallographic intensity distribution of the austenite to ferrite transformation texture, especially the alpha-fiber ($\langle 011 \rangle \parallel$ rolling direction) which explained the anisotropy and delamination occurrences. Both processed plates of steel presented the alpha-fiber due to hot-rolling of plates. Delaminations occurrences were further investigated and attributed to a strong $\{100\} \langle 011 \rangle$ orientation presence despite microstructure homogeneity. A schematic model was proposed, showing the source of delamination and the reason for the lowest toughness for 45° to the rolling direction.

Keywords: crystallographic texture, fracture toughness, mechanical strength, microstructure characterization, TMCP, X80 plates of steel, pipeline steel

1. Introduction

The efficiency of pipeline transport systems, widely employed in the oil and gas industries, depends, to a significant extent, on increasing diameters and working pressures while reducing the wall thickness to lower the cost per transport unit [1, 2]. In this context, pipeline steels have been continuously developed toward increased strength, toughness, and formability, as well as maintaining low carbon composition to ensure adequate weldability [1, 2]. In order to achieve these goals, pipeline steels, such as API 5 L X80, X100, and X120, rely upon alloy design and

Thermo-Mechanically Controlled Processing (TMCP) to produce grain refinement by controlled deformation of austenite during rolling [3, 4]. In general, rolling of TMCP steel plates are carried out in two stages: first, rough rolling is performed in the temperature range of austenite recrystallization while alloying elements are in solution (normally above 1100°C); then, at lower temperatures (typically below 1000°C, sometimes in the intercritical range) finish rolling passes are executed, cold-working the matrix [4–6]. At these lower temperatures, the presence of precipitated carbides inhibit grain growth, and fine austenite grains, substructure, and dislocations assist the formation of a refined ferritic or bainitic structure, depending on the cooling conditions [4, 7]. Because of the low-temperature rolling, diffusional phenomena are limited, and the deformed microstructure carries strong crystallographic textures, which lead to anisotropy and possibly a decrease of mechanical properties [4, 5, 8]. As such, numerous investigations have been performed recently to understand texture formation in TMCP steels and its correlation with mechanical properties, especially impact toughness behavior (Charpy tests) [5, 6, 8–10].

Fracture toughness and how crack propagation occurs in steels, depend on their chemical composition [4, 5, 11–13], resultant microstructures [4, 5, 10–12, 14], inclusions [4, 5, 11, 12], grain morphology, e.g., pancaked or elongated [4, 12], crystallographic textures [4, 5, 10–14] and residual stresses produced after the TMCP process [15]. Moreover, many studies in the literature point out the crystallographic orientation as the major cause of delamination, i.e., the presence of 001 plane more specifically [5, 8, 11, 15–18]. Most of the literature presents impact toughness results from Charpy tests. Charpy tests are recommended for qualitative estimation of toughness, with samples that can be machined with low-cost, tests are conducted rapidly, and results are easily processed [19]. For accurate measurements of toughness, crack-tip opening displacement (CTOD) tests are recommended [20]. Also, the crack-tip constraint of Charpy samples changes due to the dynamic loading [21], however, a pipeline under operative conditions do not suffer impact loads, but rather a quasi-static evolution of pressure and internal forces. CTOD tests, with samples designed to guarantee a constant crack-tip triaxiality [21], which represents a crack propagation on opening mode I in quasi-static conditions, has not been well documented in the literature related to the fracture toughness measurement of pipelines.

Delamination is a brittle fracture behavior reported in TMCP steels [9, 17, 22–25], which occurs at the weakest interface, usually near the crack tip. There are two types of delamination based on its geometry: (i) crack divider and (ii) crack arrester. The divider branches the crack into a series of cracks traveling a narrower path [22, 23]. The arrester delamination does not result in crack branching, maintaining the same width of propagation. However, it reallocates the crack at a region with no plastic zone ahead of the crack, triggering the re-initiation of the crack under conditions of nearly uniaxial tension, resulting in high absorption of energy [22, 23]. There are several reports of delaminations of both types in Charpy tests in the literature [9, 17, 23–25] and few reports of delaminations during CTOD tests in the literature [8].

Zong et al. studied the influence of crystallographic orientation upon impact toughness through Charpy impact tests on an API X100 steel [17]. The influence of microstructure on the toughness results was excluded by using the same steel plate. The influence of crystallography orientation was assessed by milling out samples from the different orientation, 0, 30, 45, 60 and 90° tilted from rolling direction. The best condition was found at 0° and then at 90° [17], where the fracture orientation factor, a factor used to characterize the anisotropy of the fracture strength based on $\langle 100 \rangle$, presented lower values compared to 45° to RD, the direction in which maximum fracture orientation factor was obtained. Bakshi et al. [5] studied

the influence of the TMCP, microstructure and crystallography on an X70 also varying the orientation of the machined samples for Charpy impact tests. As many cited works, Bakshi et al. [5] also reported that the presence of 001 plane induces delamination.

Pyshmintsev et al. [26] suggested that the clustering of (001) cleavage plane parallel to the crack plane does not lead to delamination and splitting phenomena, but that microstructure plays the major role. It was reported that prior austenite grain boundary with cube rotation texture lying parallel to crack plane propagation causes severe splitting [26]. Another study [27], reported that the anisotropy in Charpy tests results could be correlated to factors as the spatial grain distribution, grain shape, and the distribution of the phases and microconstituents, mainly the hardening ones. Kimura et al. reported that grain size was the main key to control yield strength and delamination. By applying a TMCP, ultra-fined grain was obtained, increasing the yield strength and triggering delaminations of crack-arrest type, increasing toughness as well [23].

In this work, we aim to determine the causes of the occurrence of delamination occurring during and after fracture toughness tests. The present investigation was conducted using crystallographic textures, microstructures analysis by light optical microscopy (LOM), scanning electron microscopy (SEM) coupled with energy-dispersive x-ray spectroscopy (EDS), electron back-scattered diffraction (EBSD), X-ray diffraction (XRD), and mechanical assessment with tensile tests and fracture toughness test, specifically crack-tip opening displacement (CTOD) tests, in two steel plates of X80 fabricated by TMCP. In addition, a complete fractographic analysis was conducted. The first steel was air-cooled after the last rolling pass in the intercritical region, referred in the text as the AIR-steel. It presented a banded microstructure and segregation in the mid-thickness of the plate, with elongated manganese sulfide particles and pearlite colonies. The second steel, hereafter designated as ACC-steel, underwent accelerated-cooling after finish rolling and exhibited a bainitic matrix with equiaxed bainite packages.

2. Materials and methods

Two plates of X80 grade TMCP steels, produced elsewhere using different cooling conditions, air-cooling (AIR-steel) and accelerated-cooling (ACC-steel) after finish rolling in the intercritical range, were used in the present study. The chemical composition of both steel plates is shown in **Table 1**, which is in good agreement with the ISO 3183 standard [28] requirements.

The fracture toughness assessment was conducted using CTOD tests, with experimental testing according to the ASTM 1820-13 standard [29]. Rectangular

Steel	C	Mn	V	Nb	Ti	Si	Mo	Ni	P*	S*
ISO 3183 standard [28]	0.18	1.9	*	*	*	0.45	0.5	1	250	150
ACC-steel	0.05	1.73	0.01	0.04	0.01	0.26	0.18	0.25	90	4
AIR-steel	0.08	2.07	0.04	0.07	0.01	0.22	0.18	0.01	50	22

*ISO 3183 standard [28] was used for comparisons purpose (*ppm).*

Table 1.
Chemical composition of the ACC-steel and AIR steel (wt.%).

(Bx2B) single edge bending notched samples with different thicknesses (B) of 7 and 15 mm were assessed. First, the 7-mm-thick samples were tested at 25°C to analyze the effect of the crack propagation direction in fracture toughness; therefore notches were located through the transverse (L-T) and longitudinal (T-L) direction (more details about crack orientation the ASTM E1823 standard [30]). After that, the direction of best fracture toughness result of the 7-mm-thick samples in each steel was chosen to conduct tests in thicker plates (15 mm), to increase the constraint of the crack-tip and assess the effect of temperature. 15-mm-thick samples were assessed at 0, -20 and -40°C, using the L-T direction in the AIR-steel and T-L direction in the ACC-steel. Notice that ACC-steel CTOD results were previously reported by Avila et al. [31]. Side grooves were machined on 15-mm-thick samples after pre-cracking to increase triaxiality state at the crack-tip, with straight crack-tip fronts during the CTOD tests.

Tensile tests were conducted in cylindrical samples with a diameter of 6 mm in the reduced area, following ASTM E8 standard [32]. Tensile samples were machined in rolling and transverse directions. The tensile tests were also conducted at temperatures 25, 0, -20 and -40°C.

X-ray Diffraction (XRD) was conducted to assess crystallographic texture along the normal and transverse directions (ND-TD). CuK α radiation with wavelength $\lambda = 1.54059 \text{ \AA}$, a continuous scanning speed of 0.14°/min, 0.02° per step and 2 θ range of 40 to 100° were used during the X-ray measuring. Experimental pole figures were determined by varying azimuthal angle phi (ϕ) 0 to 360° in 3° steps and tilting angle chi (χ) from 0 to 87° in 3° steps. Orientation distribution functions (ODFs) were obtained from independent measurements of the (110), (200) and (211) planes.

For metallographic purposes, samples were ground from 100-grit up to 1200-grit SiC paper. Polishing was performed with diamond pastes of 3 and 1 μm and final polishing was performed in a silica suspension with 0.06 μm particle size.

Microstructural characterization was carried out on all three planes: rolling, transverse, and normal, where the rolling plane is perpendicular to the rolling direction (RD), likewise the transverse plane to TD and normal plane to ND. LOM, SEM coupled with an EDS and EBSD detectors, and Vickers hardness measurements were performed. The EBSD measurements were conducted on non-etched samples and two different magnifications were used. Areas of 1500x1300 μm^2 with a step size of 2.5 μm and 75 x 65 μm^2 with step sizes of 0.1 μm were used. Misorientation above 15° was used to considered grain boundaries. Then the effective grain size was determined using the area method. Grain size measured by the linear intercept technique, was carried out on LOM images. Samples were etched with 2% Nital.

3. Results

3.1 Microstructure

Figure 1a–c shows the microstructure of both steel plates. Microstructural misorientation cubes in **Figure 1d, e** present the microstructure morphology and distribution near the mid-thickness. The fine secondary phases and constituents (SP) presence between ferrite grains in steels depends on the alloying elements and their effect on the transformation kinetics during cooling [33]. The air-cooling after the finishing rolling pass provides enough time at elevated temperature, enabling diffusion and resulting in a variety of incomplete transformations and microconstituents classified into martensite-austenite (M-A), degenerated pearlite (DP), bainite and martensite [33–35]. The AIR-steel exhibited, in **Figure 1a, b**, a banded

microstructure composed by polygonal ferrite, some quasi-polygonal ferrite, pancake grains evidencing a finishing rolling pass at an intercritical temperature, with the formation of banding of fine phases and constituents. A macrosegregation band in the mid-plane induced by solidification is visible on the transverse plane.

The ACC-steel presented a homogenous microstructure, as shown in **Figure 1c, d**, over the transverse and rolling planes composed by granular bainite, with more equiaxed shape, some elongated grains, and SP. Grain size measurements using EBSD data and conventional optical procedure showed similar values, around 1.2 μm , as shown in **Table 2**. However, based on the standard deviation, the grain sizes can be considered similar in both steel plates.

The ACC-steel presented a chemical composition with lower alloying elements content than AIR-steel, resulting in less MA and microconstituents dispersed on a bainitic matrix. The ACC-steel depicted a fine ferrite and bainite matrix with dispersed SP. In addition, the accelerated-cooling suppressed diffusion and favored the formation of bainite products, as packets of bainite and granular bainite [33, 36]. According to Bhadeshia et al. [37], bainite formation takes place first by the growth of one single crystal and formation of clusters, known as packet sheaves, by the cooperative growth of other crystals, with low misorientation angles between the sub-units. As ACC steel had a bainitic microstructure, it presented a higher content

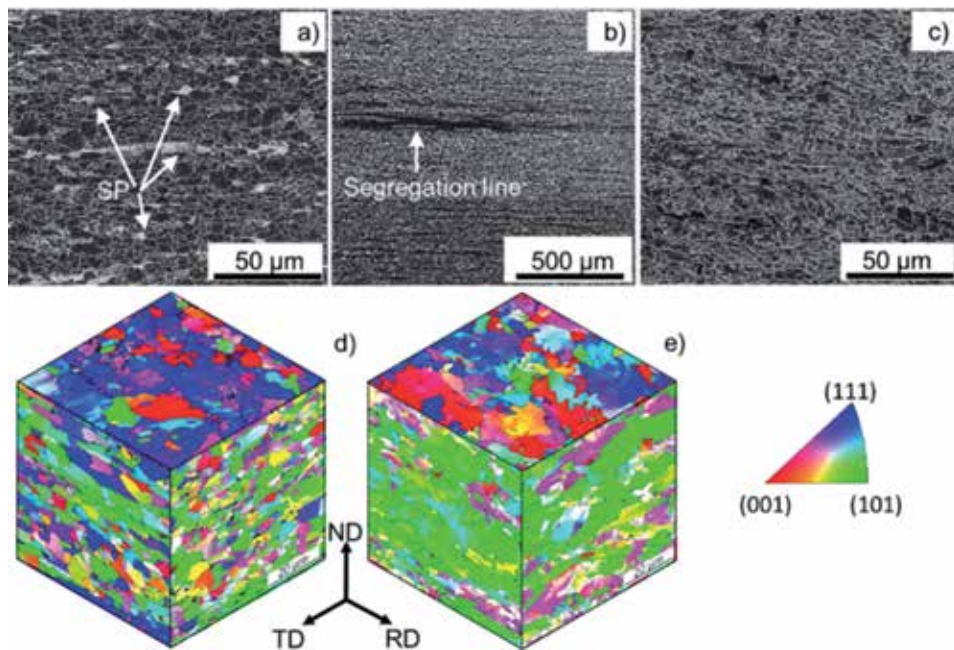


Figure 1. SEM micrographs of the rolling plane of the plates: (a, b) AIR-steel presenting segregation and secondary phases (SP), (c) ACC-steel showing a homogeneous microstructure. Misorientation angle distribution cubes of (d) AIR-steel and (e) ACC-steel. Grain boundary misorientation $>10^\circ$.

Steel	EBSD	Optical measurements
AIR	1.2 \pm 0.05	1.0 \pm 0.03
ACC	1.4 \pm 0.05	1.2 \pm 0.03

Measurements in μm .

Table 2. Grain size values of the studied steels.

of low angle misorientation, between 5 and 15°, than the AIR-steel. The ACC steel presented similar morphology on both planes, rolling and transverse, as shown in **Figure 1e** since the accelerated-cooling resulted in a larger ferrite//bainite nucleation rate. Furthermore, the microstructure did not present elongated ferrite, evidencing a finishing rolling pass at a full austenitization temperature.

SP were observed in both plates of steel distributed around the ferritic matrix, as shown in **Figure 2a, b**. However, the AIR-steel presented a higher number of constituents within the light contrast bands, such as SP bands depicted in **Figure 2a** and zoomed-in in **Figure 2b**. The SP was composed of elongated and massive shapes of DP and M-A, and manganese sulfide (MnS), as detailed in **Figure 3**.

EDS analysis conducted at the mid-thickness on a specific region confirms the presence of MnS in the AIR-steel. These elongated MnS particles also depict silicon and titanium presence, as shown in **Figure 4**. ACC-steel did not show segregation in the mid-thickness.

3.2 Hardness

The average hardness of the steel plates in the through-thickness direction was 238 ± 4 HV for the ACC-steel and 220 ± 4 HV for AIR-steel. There was no significant difference in hardness between rolling and transverse planes of each plate of steel considered separately, as shown in the hardness profiles presented in **Figure 4**.

3.3 Crystallographic texture

ODFs were constructed from the XRD and EBSD data and plotted in colored intensities diagrams using Bunge notation in Euler space, as depicted in **Figure 5**. The crystallographic representation for rolled steels is composed of a plane $\{hkl\}$ which lies parallel to the normal plane and a direction $\langle uvw \rangle$, which is parallel to the rolling direction [38] as schematically shown in **Figure 5e**. The reference system is based on RD, TD and ND, where their related planes are rolling, transversal and normal planes which lies perpendicular to their respective directions. The development of texture produced during hot-rolling at full austenitic region causes

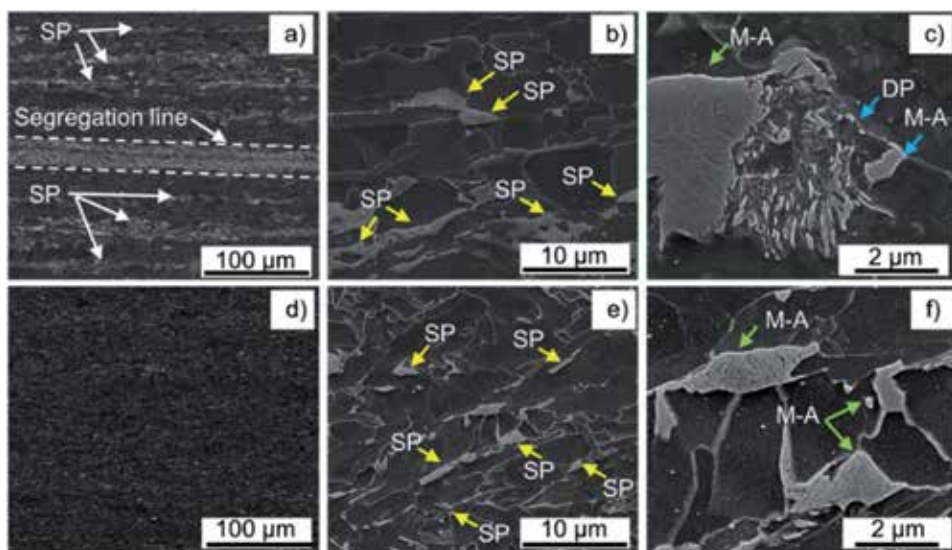


Figure 2.
SEM micrographs of (a)–(c) AIR-steel and (d)–(f) ACC-steel.

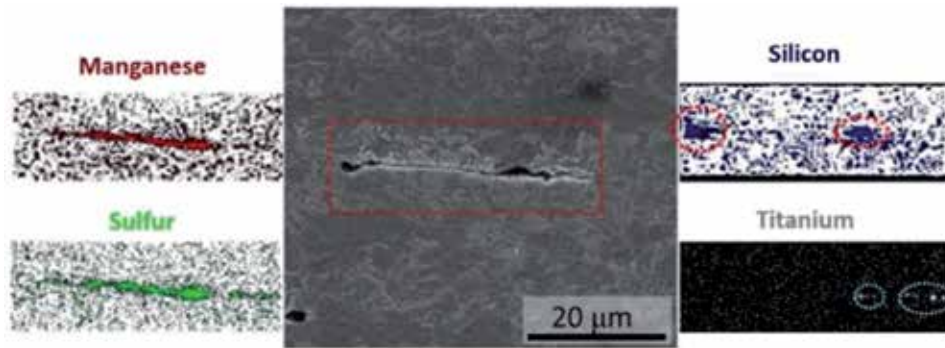


Figure 3.
 EDS analysis of MnS elongated particles in the AIR-steel.

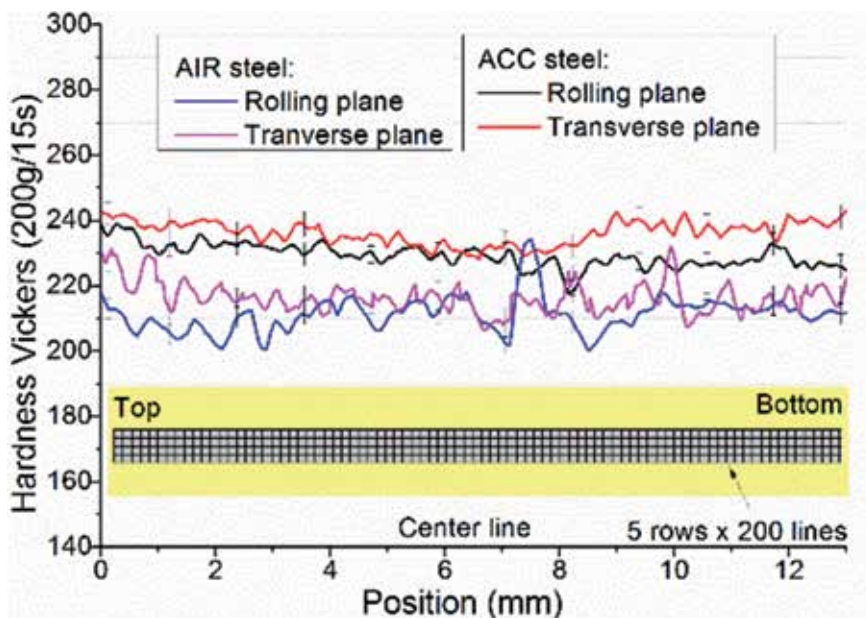


Figure 4.
 Through-thickness hardness profiles in the rolling and transverse planes of the steel of ACC-steel and AIR-steel.

strong alpha-fiber development, which consists of $\{001\} \langle 110 \rangle$ to $\{110\} \langle 110 \rangle$ in $\phi_2 = 45^\circ$, $\phi_1 = 0^\circ$, $\phi = 0-90^\circ$ [38]. It is a rotation on the $\{110\}$ direction axis, being a fiber parallel to RD. As temperature decreases and cold-work increases, there is an increase of gamma-fiber, which consists of $\{111\} \langle 110 \rangle$ to $\{111\} \langle 112 \rangle$ in $\phi_2 = 45^\circ$, $\phi_1 = 0-90^\circ$, $\phi = 55^\circ$ [38]. It is a rotation around the $\{111\}$ plane, i.e., around the perpendicular direction of the plane, which is $[111]$, being a parallel fiber to ND. In **Figure 5a–d** are retrieved the ODFs colored intensities, showing the presence of alpha-fiber and gamma-fiber. Both steels presented low gamma-fiber intensity compared to alpha-fiber. Comparing crystallographic textures in both steels, AIR-steel presented higher alpha-fiber and higher crystallographic intensity in XRD and EBSD measurements than ACC-steel as depicted in **Figure 5a–f**. Another component that plays an important role is the cube side lattice $\{100\}$ since it is the cleavage plane on body-centered cubic (BCC) steels. The family plane $\{100\}$ is likely to have a relationship to the occurrence of delaminations, as is described further in the present work.

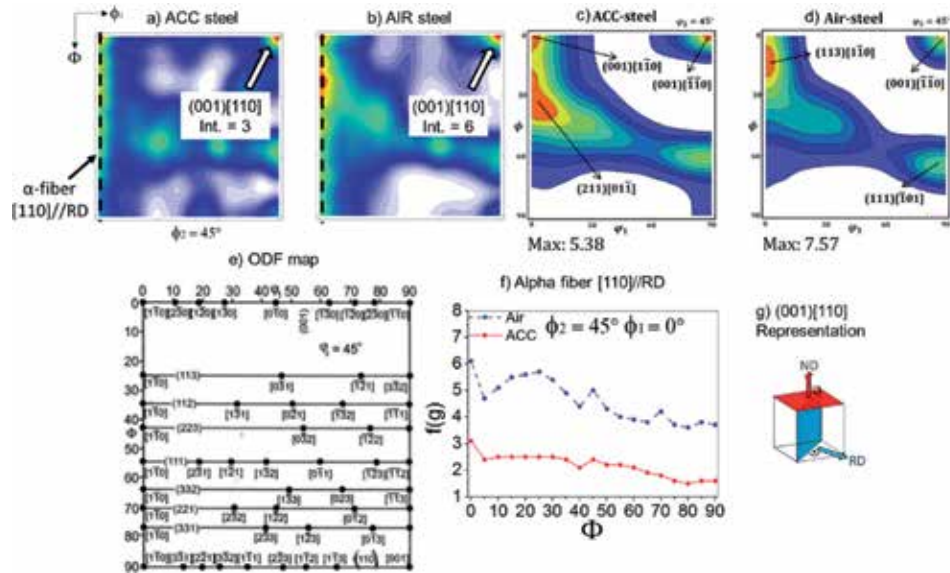


Figure 5.

ODF plots at $\phi_2 = 45^\circ$ highlighting alpha-fiber presence, location and high intensity of $(001)[110]$: (a, b) XRD ODF analysis: (a) ACC-steel, (b) AIR-steel; (c, d) EBSD ODF analysis: (c) ACC-steel, (d) AIR-steel; (e) ODF map [39], (f) quantification of alpha-fiber intensity by XRD, showing higher values for AIR-steel, and (g) schematic representation of crystallographic (001) planes perpendicular to ND and $[110]$ direction parallel to RD.

The crystallographic orientation distribution from EBSD analyses was performed to compare and validate that of XRD. The EBSD analyses were carried on rolling plane of both investigated samples out at areas of $1500 \times 1300 \mu\text{m}^2$ with a step size of $2.5 \mu\text{m}$ containing about 1500 grains. Their related ODFs were calculated using the statistical method of kernel density estimation and presented in **Figure 5**. The results obtained by EBSD are similar to previous ODF results calculated by XRD. A certain difference between these methods could be attributed with a high statistical symmetry at each pole figure (XRD) and local grain orientation (EBSD). Overall texture intensity of AIR-steel was higher rather than ACC-steel due to the formation of $\{110\}$ //RD grains accompanied by banded microstructure. Suikkanen et al. [40] characterized a $\{110\}$ plane of the carbide-free bainitic ferrite similar to the martensitic transformation originated from close-packed $\{111\}$ austenite plane because of the accommodation of transformation strains, enhancing the bainitic transformation. The formation of $(211)[011]$ component could be explained by Shackleton and Kelly works which reported that the habit plane of cementite in lower bainitic ferrite is corresponding to $\{001\}_\alpha/\{211\}_\gamma$ [41]. In other words, the proeutectoid cementite habit induced large shear deformations because of stereological effects to form a displacive bainite structure.

In order to investigate the role of local crystal orientations and boundary types, detailed EBSD measurements were carried out in rolling transversal planes of both AIR and ACC steels. Orientation image (OI) map, Kernel average misorientation (KAM) map, grain boundary (GB) map, Taylor factor (TF) maps, and normal direction pole figure (IPF) maps of each measurement were presented in **Figure 6** for AIR-steel and **Figure 7** for ACC-steel.

The orientation data collected with EBSD displayed by OIM or Euler colored maps, provides a basic presentation of the measured orientation. Grain boundaries are considered as crystal lattice defects, which can be identified by the point-to-point misorientation between neighboring data points, **Figures 6a** and **7a**. Grain

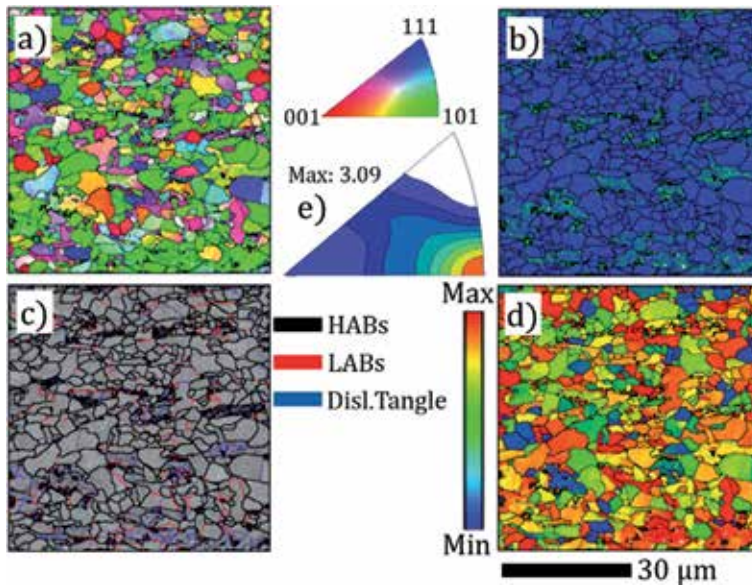


Figure 6. (a) OI map, (b) KAM map, (c) GB map, (d) TF maps, and (e) normal direction IPF maps of the rolling plane of AIR-steel.

boundary energy is attributed by the interfacial region geometry between two adjacent crystals with different orientations. For example, the high angle boundaries (HABs), greater than 15° , are determined by point-to-point misorientation analysis [42, 43]. Low angle boundaries (LABs) and dislocation tangles were characterized from their misorientation angle ($5\text{--}15^\circ$ and $2\text{--}5^\circ$, respectively), **Figures 6c** and **7c**. Also, coincident site lattice (CSL) boundaries with HABs with low stored energy due to good atomic fit between neighboring crystals can act as crack arrester.

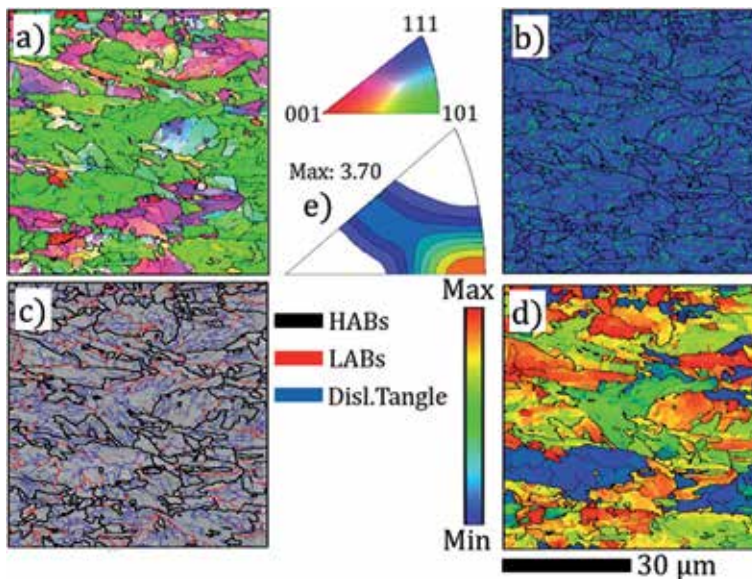


Figure 7. (a) OI map, (b) KAM map, (c) GB map, (d) TF maps, and (e) normal direction IPF maps of the rolling plane of ACC-steel.

KAM map indicates the local plastic strain variations measured between the central point and its nearest neighbors when the misorientation between them exceeds 5° in eliminating the effect of grain boundaries [44, 45]. The high KAM angles appear cumulative build-up of misorientation inside the grain or the presence of sub-grain boundaries, **Figures 6b** and **7b**.

Pencil glide occurs on {110}, {112}, {123} slip planes along the slip direction <111>, in BCC materials such as steel. The external stress imposed during deformation leads to activate the potential activated slip systems for each grain individually according to the crystal rotation axis method based on their Schmid factors [46–48]. Polycrystalline deformation is determined through all possible combinations of the potential slip systems compared with the imposed macroscopic stress state. Then, the yield response of individual grain is predicted based on favorably and unfavorably oriented for easier slip activation according to the geometrical lattice rotation axes. For instance, soft grains with low Taylor factor value (in blue color) have the least resistance to slip, while red-colored grains represent hard grains with highest Taylor factor, i.e., highest resistance to slip [46, 47], **Figures 6d** and **7d**. Also, the corresponding rolling direction IPF obtained from each EBSD data is shown in **Figures 6e** and **7e**, which can quantify the volume fraction of the crystallographic orientation of the grains.

3.4 Tensile tests

Elongation measured at tensile tests superior to 10% and yield strength above 400 MPa for all the evaluated conditions were found. Yield strength (YS) and ultimate tensile strength (UTS) are summarized in **Figure 8**, according to the tested temperature. As shown in **Figure 8a** and considering the results at room temperature, the ACC-steel fulfills the API standard requirement for the minimum yield strength (555 MPa) [28], in the rolling and transverse planes, to be classified as X80. The AIR-steel reaches the X80 grade specification requirement in the transverse plane, but not in the rolling plane, in which it reaches only the X70 specification requirement. Considering the ultimate tensile strength at room temperature (25°C), as shown in **Figure 8b**, both plates of steel fit into the X80 grade requirement.

Regarding the results presented in **Figure 8**, it is possible to state that anisotropy was found in both plates of steel, being more intense in the AIR-steel than in the ACC-steel, which presented a smaller difference in tensile results between the rolling and transverse planes. In addition, the AIR-steel tensile test results varied considerably between temperatures due to the heterogeneity of the microstructure.

AIR-steel fails the API X80 criterion for yield stress. The ACC-steel plates were machined from a pipe, a finished product, while AIR-steel plates came directly from TMCP plate production. For AIR-steel, a further U-O-E process would be necessary to transform plates into tubes, which would promote enough work-hardening to reach the yield stress of X80-grade specification [24]. Also, the YS/UTS ratio was not the predominant factor affecting the fracture toughness, where usually high YS/UTS ratios lead to low toughness, however, in this study high YS/UTS lead to high toughness.

3.5 Fracture toughness tests

Fracture toughness results, measured by the CTOD parameter in mm, are summarized in **Figure 9**. For 7-mm-thick samples, AIR-steel presented lower average CTOD than ACC-steel, as shown in **Figure 9a**. AIR-steel presented difference of CTOD value between L-T and T-L geometries: L-T presented higher values than T-L. ACC-steel presented statistically equal results for both L-T and T-L. Therefore, ACC-steel presented higher toughness and less crystallographic texture effect than AIR-steel.

For 15-mm-thick samples, both steels presented a CTOD decreasing trend lowering temperatures, as depicted in **Figure 9b**. The ACC-steel depicted a better toughness behavior at 0 and -20°C than AIR-steel; however, at -40°C , both steels showed similar CTOD. CTOD results obtained at 0°C were similar to those from 7-mm-thick samples at 25°C . Below 0°C , the drop in temperature caused a partial shift of biaxial tension state towards triaxial tension state, increasing the triaxiality state at the crack-tip and reducing the material ductility [23].

To analyze the fracture surfaces, samples were submerged in liquid nitrogen and then broken by impact to separate samples into two halves. Thus, fracture surfaces of 7-mm-thick samples in **Figure 10** and 15-mm-thick samples in **Figure 11** can be observed. Fatigue pre-cracking region, crack propagation region during the CTOD test and final fracture caused by impact are also shown. The crack opening displacement (COD) and the applied force figure has been added to show the behavior of the material during the CTOD test.

For 15-mm thick samples, the AIR-steel and ACC-steel specimens were tested in L-T and T-L geometries, respectively, due to the best CTOD results of 7-mm thick samples. For AIR-steel CTOD samples, all cases tested at -20 and -40°C presented delamination during CTOD test, totalizing 6 cases. Samples tested at 0°C presented no delamination occurrence. Most of the occurred delaminations manifested as pop-ins in the CTOD test curves and four cases the delamination were considered

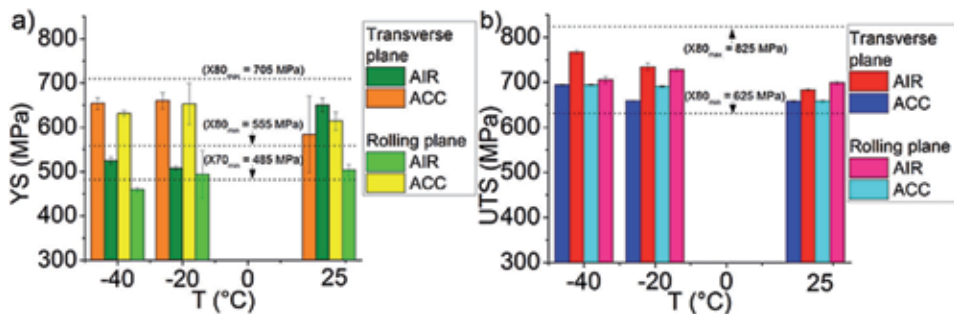


Figure 8. Summary of the tensile tests results of the AIR-steel and ACC-steel: (a) yield strength (YS) and (b) ultimate strength (UTS). Tests were conducted in the transverse and parallel directions relative to the rolling direction.

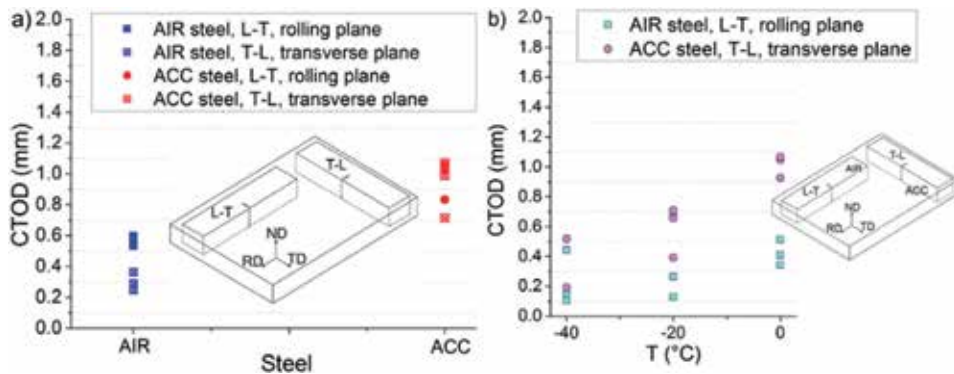


Figure 9. Fracture toughness using CTOD parameter for ACC-steel and AIR-steel: (a) 7-mm-thick samples tested at 25°C ; (b) 15-mm-thick samples tested at 0 , -20 and -40°C . The L-T and T-L correspond to the ASTM E1823 [30] notches nomenclature. Tests were performed in the L-T and T-L direction in SE(B) samples. Results from ACC-steel with 15-mm-thick were published at [31].

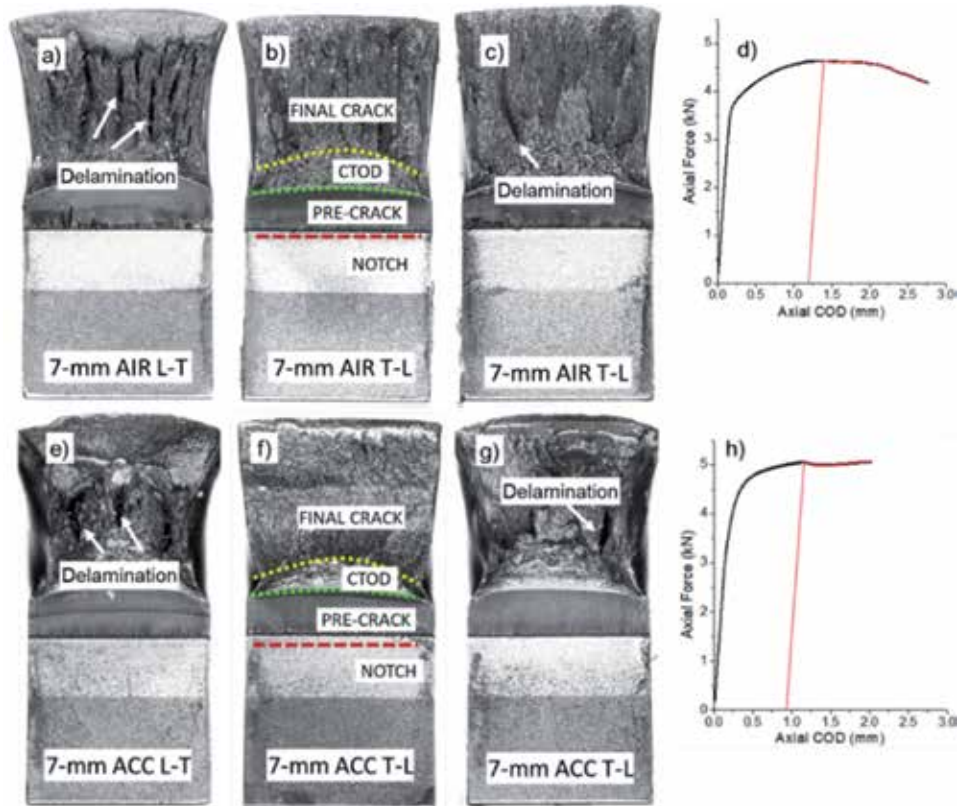


Figure 10.

Fractured surfaces of the toughness of 7-mm thick samples tested at room temperature. AIR-steel: (a) L-T geometry, plastic behavior and occurrence of delamination during sample break; (b) T-L geometry, plastic behavior on CTOD zone and flat and brittle like behavior during sample break; (c) T-L geometry, occurrence of delamination during sample break; (d) force vs. COD experimental graph during CTOD test of the sample shown in (c), displaying red line at maximum achieved force. ACC-steel: (e) L-T geometry, plastic behavior and occurrence of delamination during sample break; (f) T-L geometry, plastic behavior on CTOD zone and flat and brittle like behavior during sample break; (g) T-L geometry, plastic behavior during CTOD and final fracture, with occurrence of delamination during sample break; (h) force vs. COD experimental graph during CTOD test of the sample shown in (g), displaying red line at maximum achieved force. COD: crack open displacement at the crack mouth.

significant according to the ASTM 1820 standard [29], two at -20°C and the other two at -40°C , out of a total of 6 cases of delaminations. Notice that a pop-in event does not mean the start of brittle crack propagation, it is just a disparity of the stable crack propagation and is recommended to calculate CTOD values when they appear; however, the crack propagation continues stably until the end of the test.

Moreover, when the crack front suffers delamination, it is divided into several fronts with specific stress state in each one. Each condition is not considered in the equations to calculate CTOD by the ASTM 1820 standard [29]. This observation was previously reported by [24].

For 7-mm-thick samples, all L-T samples presented a plastic fracture aspect, with lateral deformation and a large crack propagation region during CTOD, with no delaminations, but rather after the CTOD test, during sample break, as shown in **Figure 10a, e**. For T-L configuration, the surface fracture presented less plastic deformation aspect in comparison to L-T, with a flatter surface. The CTOD tests did not present any abrupt drop in force, but due to high plasticity, only a gradual drop of force was presented on CTOD graphic, as depicted in **Figure 10d, h**.

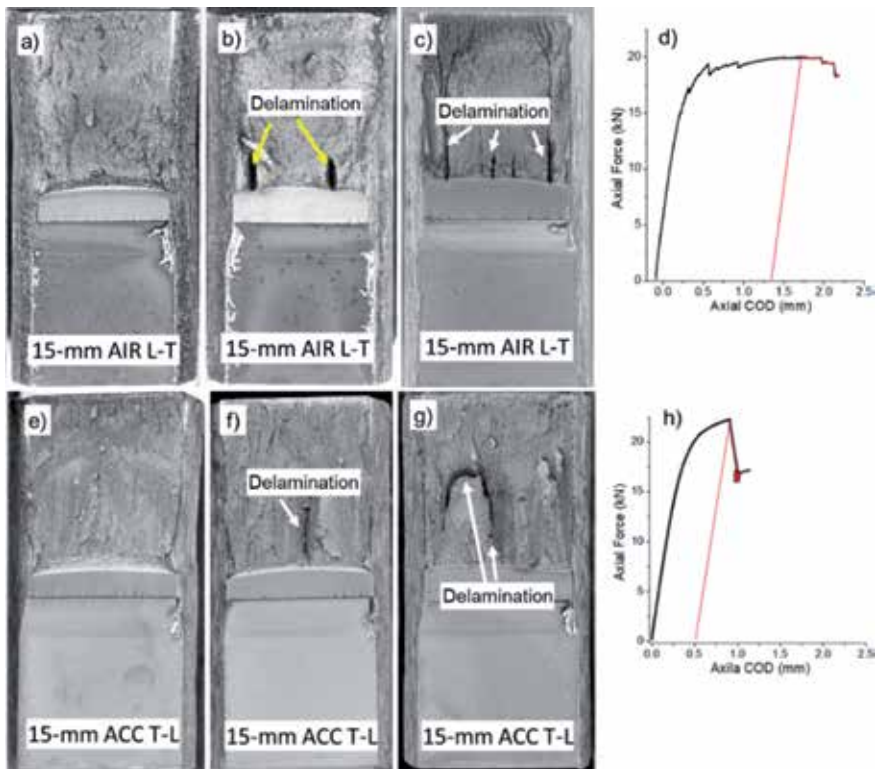


Figure 11.

Fractured surface of API X80 15-mm thick samples tested at different temperatures. AIR-steel in L-T geometry: (a) 0°C, plastic behavior only in CTOD zone, and no occurrence of delamination during CTOD; (b) -20°C, low plastic behavior in CTOD zone and next to delaminations. Delaminations occurred during CTOD test, causing pop-in; (c) brittle behavior with the occurrence of delamination during CTOD test; (d) force vs. COD experimental graph during CTOD test of the sample shown in (c), displaying early delaminations but not significant to end the test, and a red line at maximum achieved force. ACC-steel in T-L geometry: (e) 0°C, plastic behavior in CTOD zone; (f) low plastic behavior in CTOD zone and occurrence of delamination during CTOD test; (g) -40°C, brittle behavior during CTOD and final fracture, with occurrence of delamination during CTOD; (h) force vs. COD experimental graph during CTOD test of the sample shown in (g), displaying red line at occurred delamination, ending the test.

For ACC-steel, 4 cases tested at -20 and -40°C presented delamination during CTOD test. Samples tested at 0°C presented no delamination occurrence. All the occurred delaminations in ACC-steel were considered significant according to the ASTM 1820 standard, two at -20°C and two at -40°C.

Some fracture surfaces of 15-mm samples are presented in **Figure 11**. In general, all delaminations occurred in AIR-steel that was not considered to be significant, presented a high zone of plastic deformation near it, as in **Figure 11b**. Strain hardening is followed by pop-ins in CTOD curve, presenting a drop on CTOD force with subsequent increase of force.

4. Discussion

This study presents two TMCP X80 plates of steel with different characteristics to assess fracture of toughness and mechanisms of crack propagation and delamination of the steels. Microstructural features, such as precipitates, phase boundaries, and grain boundaries, play an important role in determining the crack

propagation by offering a weak path ahead of the crack tip. However, phase or grain boundaries can act as strong crack arrester when a crack propagates across grain boundary. Crack propagation rate inside a single-crystal grain is slower compared with the crack propagation rate along a crystal grain boundary. **Figure 12** shows the frequency of dislocation tangle, LABs, HABs and CSL for both steels in order to evaluate the capacity to offer resistance to a crack. The fraction of HABs in all planes of AIR-steel sample is greater than ACC-steel. This behavior could be attributed to the banded microstructure, secondary phases, and segregation, which produces more grain boundaries by the presence of more phases and constituents. The presence of sub-grain boundaries or LABs has indicated the arrangement of dislocation inside a single-crystal grain, retarding the crack growth. The portion of sub-grain boundaries is higher in ACC-steel, decreasing the crack propagation rate by retarding the movement of dislocation. A higher fraction of dislocation tangles of ACC-steel could be related to the more lattice distortion due to bainitic transformation without diffusion and insufficient dynamic recovery, which also decreases crack propagation rate inside a single-crystal grain. Morales-Rivas et al. reported that $\{211\}_a$ habit plane identified in bainitic structure act as a barrier to the dislocation motion inside bainitic ferrite, consequently postponing the crack initiation process [49]. Although low energy CSL boundaries can effectively increase the fracture resistance and block crack propagation, no significant variation of its fraction was observed in investigated samples.

The frequency distribution of main crystallographic orientations such as $\{001\}$, $\{101\}$, and $\{111\}$ with about 15° deviation from ideal planes were calculated from EBSD data of AIR and ACC-steel samples and presented in **Figure 13**. The $\{111\}$ and $\{101\}$ planes were predominant in the transversal and rolling planes, respectively, of the AIR-steel sample with banded ferritic microstructure with the presence of iron carbide of its structure. The $\{001\}$ family of planes were found in similar proportion among the rolling and normal planes. The $\{001\}$ //ND textural components were dominant on a normal plane, and $\{111\}$ //ND and $\{101\}$ //ND were characterized by transversal and rolling planes, respectively, in ACC-steel with bainitic structure. Such orientation-dependent mechanical properties are largely attributed to texture and crystallographic orientation, causing anisotropy of mechanical properties. It is well understood that the formation of grains lying parallel to compact planes in BCC-ferritic steel with low carbon content such as $\{110\}$ and $\{112\}$ enhance ductile fracture by enhancing dislocation movements by adequate activated slip system, while cleavage occurs in non-compact planes such as $\{001\}$ [40, 42, 43, 50]. It is

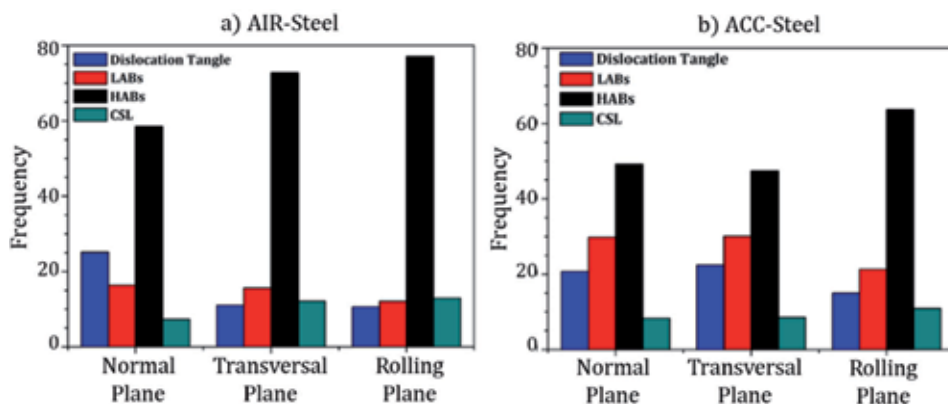


Figure 12. Distribution of boundary types of both steels: (a) AIR and (b) ACC steel.

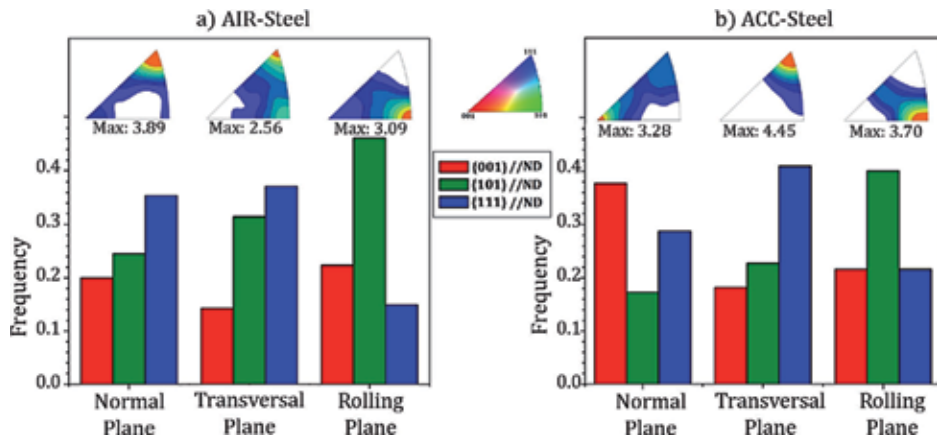


Figure 13. Frequency distribution of main crystallographic orientations of (a) AIR-steel and (b) ACC-steel.

suggested that cleavage fracture in AIR-steel found to be influenced by banded ferrite-pearlite microstructure and formation of segregation zone. The rapid cooling at the surface allowed the formation of finer bainite orientated towards $\{001\} // ND$. Blondé et al. have been discovered that low carbon content austenite grains transform first to martensite/bainite under accelerating cooling. Das Bakshi et al. [5] investigated the Charpy impact toughness of bainitic structure of microalloyed API X70 steels. They also characterized a dominance of a large fraction of $\{111\} // ND$ grains accompanied by the presence of $\{001\}$ and $\{101\}$ because of the less of recrystallized austenite before the bainitic transformation of austenitic grains. However, this bainitic structure has less distortion rather than martensite structure, thereby, exhibited less risk of cleavage fracture.

KAM values indirectly measure the dislocation density and the local plastic strain developed in the steel during rolling processing and were presented in **Figures 6** and **7**. The presence of banded ferrite—pearlite microstructure with the dispersion of secondary particles induced local stress sites concentration that would make AIR-steel sample prone to crack initiation due to the local high elastic energy stored. Inhomogeneous dislocation accumulation at interfaces traps carbon atoms, resulting in brittle carbide precipitates containing high dislocation density, leading to early fracture. It is included that the dislocation piles up concentrated at ferrite grain boundaries increase the risk of microcrack nucleation and crack propagation as well. However, the bainitic packet containing strain localization inside the soft ferrite lath phase decreases the strain gradient between the inside and at boundary region [51], resulting in higher strain hardenability and more fracture resistance.

Full constraint Taylor approach was used to evaluate the potential activated slip systems dependent on the grain orientations (**Figures 6** and **7**). It is found that the AIR-steels had a more distribution of high Taylor factor in comparison with ACC-steel, indicating the higher capability of storage of energy due to the accumulation of larger dislocation densities or dislocation piles-up, due to more active slip systems in a certain direction. ACC-steel with low Taylor Factor bainitic structure limits the deformation ability by not offering adequate slip systems. These assessments agree with the tensile results obtained in **Figure 8** where AIR-steel presented a higher UTS/YS relation in comparison to ACC-steel.

AIR-steel presented higher intensity on $\{001\} \langle 110 \rangle$ to $\{111\} \langle 110 \rangle$ alpha-fiber, and $\{111\} \langle 110 \rangle$ to $\{111\} \langle 112 \rangle$ gamma-fiber than ACC-steel because of a lower finishing rolling temperature. AIR-steel presented stronger $\{100\} \langle 011 \rangle$, known as rotated

cube texture, than ACC-steel, which possess a low Taylor factor, i.e., high strain stored energy, or low further deformation ability. This result indicates intense cold deformation, low finish rolling temperature and low inter-pass rolling time [52, 53].

This non-random distribution of crystal orientations influenced toughness properties, mainly by triggering delamination phenomena. The occurrence of delamination for 7-mm thick samples only occurred out of CTOD zone, after test, during sample break. For 15-mm thick sample, delaminations occurred during CTOD tests, causing pop-in and instant drop on the force.

Crystallographic orientation has been reported to be the major role causing impact toughness anisotropy of the steels [5, 8, 10, 17, 23, 54]. Some atomic planes are more important, as {110}, {112} and {123}, which are the major slip system for BCC steels [5, 8], and the {100}, which is the cleavage plane, the cube side lattice, for BCC steels [5, 8, 10, 17, 23, 54]. Also, it is important to bear in mind that the effect of these planes upon mechanical properties will depend on the volume, distribution and mainly on the position relative to the applied forces and planes presented during crack propagation at the crack-tip. For instance, for cleavage to occur, plane {100} must be presented perpendicular to the applied force, i.e., parallel to the fracture plane. To trigger the {112} slip system, the plane must be placed parallel to the applied force, i.e., perpendicular to the fracture plane.

The alpha-fiber is a parallel fiber to the RD and presents some of the planes mentioned above as {100}, {112} and {113}. It was reported that the sharpening the {112} <110> and {113} <110> components results in improvement of impact toughness [5, 8, 25, 54]. As shown in **Figure 5f**, AIR-steel has a peak intensity at {001} <110>, followed by a dip and then peak at $\phi = 20\text{--}30^\circ$, region of {112} and {113} components. ACC-steel presents a plateau between $\phi = 10\text{--}35^\circ$. Values of intensity are higher for AIR-steel than for ACC-steel. Nonetheless, ACC-steel presented higher CTOD toughness with better isotropy, while AIR-steel presented lower values and anisotropy according to the geometry sample. These results are consistent with another study [8] in which was reported a higher fraction of {112} <110> at L-T than T-L and yet much higher CTOD results were obtained with T-L than L-T, showing no specific correlation of increasing toughness by increasing {112}.

The obtained results show slight crystallographic differences between L-T and T-L configurations, and, for ACC-steel, these differences did not seem to affect toughness. However, it is suggested that the anisotropy displayed by AIR-steel between L-T and T-L geometries relies not only crystallographic orientation discrepancies but the microstructure anisotropy, as also reported [27]. 7-mm AIR-steel presented a higher fracture toughness for L-T configuration than T-L, in which the crack travels on a parallel plane to the rolling plane. Comparing L-T to T-L configurations of AIR-steel, nothing between is different regarding the chemical composition of phases and constituents, but only regarding the distribution and configuration of the microstructure.

For AIR-steel, there is anisotropy of grain morphology and segregation configuration, as depicted schematically in **Figure 14**. Segregation is present on both geometries, but its configuration is different in each case, as for L-T geometry, segregation is transverse to the rolling plane while for T-L, segregation is coincident to the rolling plane as shown in **Figure 14**. Banded regions and the presence of aligned microphases and non-metallic inclusions, such as MnS, create an easy path for crack propagation, influencing toughness according to their volume, morphology and distribution [5, 15]. Ferrite resists the crack propagation better than bands composed of secondary phases and constituents, which act as brittle sites for crack initiation or as a concentrated stress spot, an easy path for the crack propagation [22]. For AIR-steel 7-mm L-T geometry, the fine equiaxed grain is encountered, while for T-L geometry, elongated rolled grains are found. Grain morphology of

7-mm ACC-steel was similar in the transverse and rolling planes, the tensile and toughness values were also similar in both directions.

For 15-mm thick samples, a general decrease is observed with a reduction of temperature. An approximate DBTT is -20°C , once, at this temperature, the values of toughness resulted from CTOD tests were close to a mean value of 0°C with -40°C condition tests. Overall, AIR-steel presented lower toughness than ACC-steel. As the temperature was lowered, the fracture started to present a more brittle-like behavior — this induced delamination occurrence, as well as a dropping tendency on toughness. Many 15-mm thick samples presented delaminations, and all delaminations were of divider type, as shown in **Figure 15**.

For all delaminations not considered significant, posterior plastic deformation and strain-hardening are achieved, increasing the CTOD force during test. These delaminations happen because the divider delamination branches the crack into two or more crack fronts, causing a relaxation of the triaxial tension towards a state of biaxial tension resulting in the decrease of the overall material constraint, promoting strain-hardening [22, 23]. In the cases of significant delamination, little or no

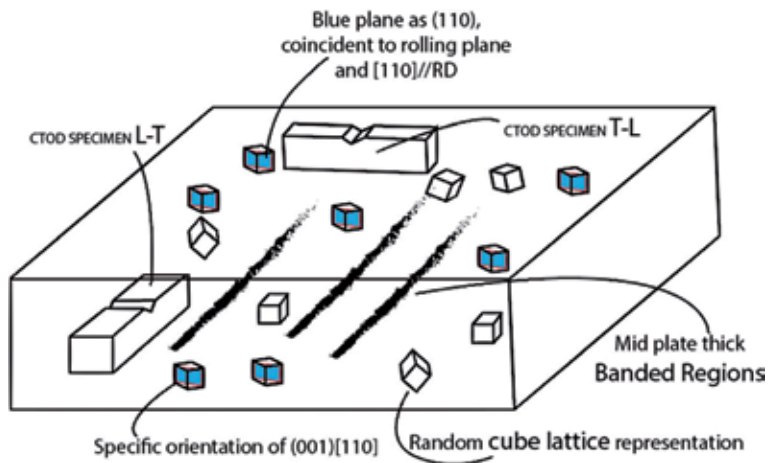


Figure 14. Schematic illustration of the used AIR-steel. CTOD specimens in L-T and T-L configuration shown to better visualize the relationship between the microstructure on the CTOD crack propagation path and global plate microstructure.

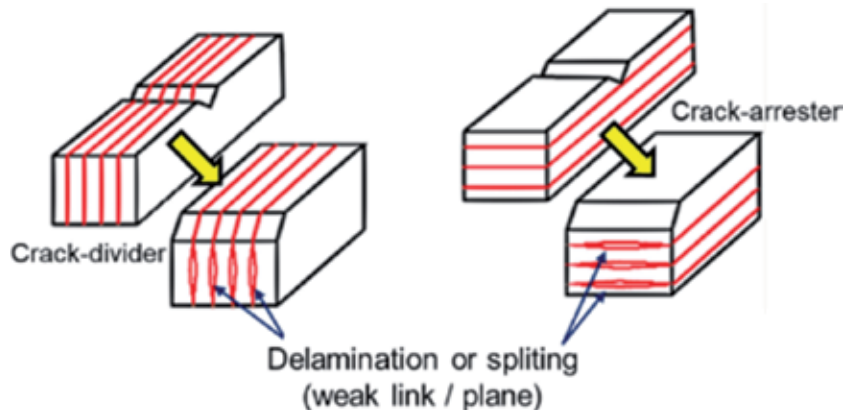


Figure 15. Delamination morphology: divider or arrester.

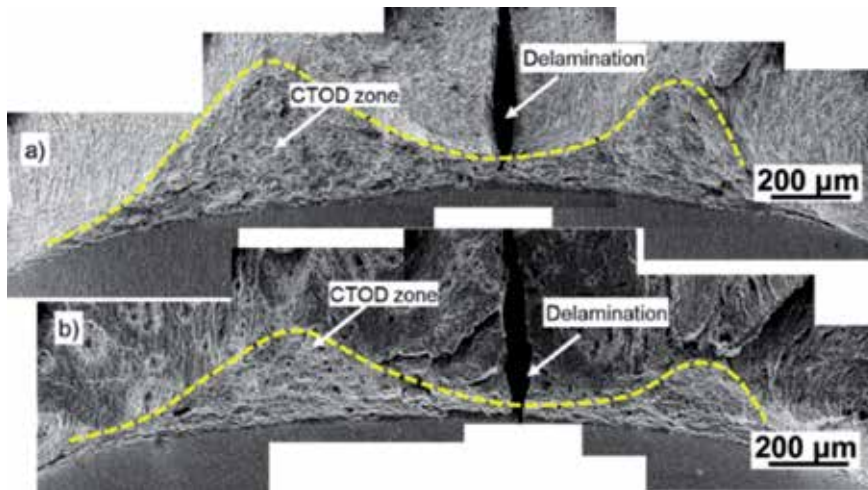


Figure 16. CTOD fracture surface of API X80 AIR-steel samples tested at different temperatures. Condition tested at (a) 25°C, showing a more plastic extension of CTOD zone, and plastic deformation on delamination edges; (b) -40°C, still exhibiting a plastic character in CTOD zone, but for a shorter extension. Yellow pointed line representing CTOD zone delimitation.

strain-hardening ability was promoted. **Figure 16** shows a fracture surface with non-significant and significant delamination, showing an aspect more plastic in the former case.

Many works studied the cause of delamination, assigning it to the presence of $\{100\}$ cleavage plane [5, 8, 10, 23], but without further explanations. Some authors believe that delaminations are consequence mostly of the microstructure [26, 27]. In fact, microstructure exerts an effect on delamination occurrence, since AIR-steel presented more cases of delamination than ACC-steel, but not playing a major role. ACC-steel presented delamination on CTOD for 15-mm and on sample breaking for 7-mm, and yet presented a homogeneous microstructure with no detected inclusions or oxides, and not presenting mid-thickness segregation as AIR-steel.

Delamination phenomena are mainly governed by the crystallographic orientation presented next to the crack propagation path. It is necessary to fulfill embrittlement factors to satisfy the delamination criterion, i.e., many related parameters as temperature, crystallographic planes and orientations and presence of brittle phases. Regarding crystallographic orientation, the many previous works cited above correlated all delamination cases to the presence of $\{001\}$.

The X-ray diffraction results showed low presence of $\{001\}$ parallel to fracture plane in L-T and T-L geometries, and intense $\{001\}$ at 45° to fracture plane. **Figure 17** shows exactly the display of alpha-fiber according to L-T configuration. The delamination takes place traveling the $\{001\}$ cubes face, macroscopically display at 45° to the fracture plane.

Figure 18 illustrates the CTOD sample and the path of crack propagation, containing grains with random crystallographic orientations. The red-colored cube representing the $\{100\} \langle 011 \rangle$, and the presence a possible clustering of $\{100\} \langle 011 \rangle$. If two adjacent grains possess the same orientation, then they belong to the same grain. Therefore, it is assumed the existence of slight misorientation between schematic cubes. During the CTOD test, an external force produces internal stresses, causing transmission of forces in each atom lattice. This force transmission assuming the cubic lattice reaches a maximum shear component exactly when the vertex of the cube is pointing out to the applied force. In other words, a maximum shear in the lattice is achieved when the plane $\langle 011 \rangle$ is parallel to the applied force.

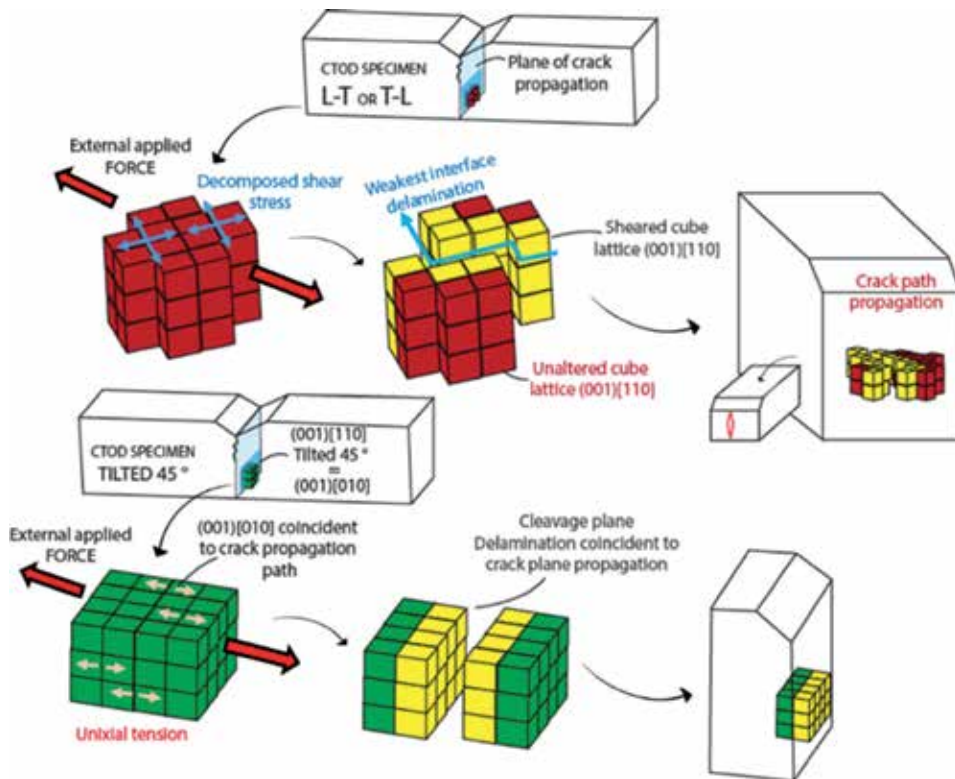


Figure 19. Schematic illustration of CTOD sample in L-T, T-L configurations, and tilted 45° from RD. Explaining how delamination occurs, and why the 45° tilted sample presents the worst toughness according to the literature.

was concluded that the dominant aspect of anisotropy was the crystallographic texture. Furthermore, the anisotropy was enhanced when a near DBTT temperature was used [10]. These cited results are very similar to the obtained result in the present paper.

The microstructure may have affected the delamination occurrence, once AIR-steel presented more delaminations than ACC-steel and showed a macrosegregation in the mid-thickness of the plate and elongated grains. It is also important to highlight that the observed delaminations occurred not only next to the mid-thickness of the samples, showing that microstructure banding is not the major or unique factor to trigger delamination. As expected, testing samples in RD or TD showed little difference for a homogeneous microstructure. Changing from RD to TD results only in slight crystallographic difference for a cubic system. AIR-steel presented a decrease of toughness mainly due to the change of polygonal to elongated microstructure.

Toughness value is mainly controlled by crystallographic feature, and delaminations have a straight relation to the presence of $\{100\}$ specifically on the plane of fracture [5, 8–10, 17, 23, 25, 54]. The alpha-fiber plays an important role because it aligns the $[110]$ direction to RD, as shown in **Figure 17**, and, usually, the rolling process produces strong alpha-fiber, therefore, strong $(100)[011]$. This condition leads to a strong $(100)[010]$ at 45° from RD, resulting in the lowest toughness as reported [10, 25, 54], and it is in agreement with the present work and proposed model in **Figure 19**. However, the 45° to RD configuration is not the cause of low toughness, but the presence of $\{100\}$ on the fracture plane. Bakshi et al. obtained high toughness at 45° and low toughness at RD and ND (0 and 90° to RD) due to low $\{100\}$ at 45° to RD [5].

5. Conclusions

- Delamination is governed by the presence of a specific crystallographic orientation. For the present work and others cited from literature, the $\{100\} \langle 011 \rangle$ is the main orientation that triggers delamination.
- This work presented a schematic model of how the presence of $\{100\}$ on fracture plane causes cleavage. The acting forces became nearly maximum uniaxial as Mohr theory, suppressing plastic deformation and cleavage fracturing.
- The presented model clarifies the reason for generally rolled plates presenting lowest toughness at 45° to RD. Furthermore, the strong alpha-fiber is translated to strong $\{100\}$ 45° to RD according to a cubic lattice system, causing cleavage through $\{100\}$ coincident to the fracture plane.
- The texture is the main factor causing anisotropy that affects toughness.
- Macrosegregation and grain morphology affects the toughness of steel. As similar crystallography is obtained //RD and //ND for a cubic lattice, ACC-steel did not present toughness change for L-T and T-L configuration, while AIR-steel presented lower toughness on the elongated grain plane T-L.
- ACC-steel and AIR-steel plates were produced by TMCP, with accelerated-cooling and air-cooling in the final production stage, respectively. Moreover, both steels presented differences in mechanical properties and fracture toughness due to anisotropy and heterogeneities in the microstructure. ACC-steel exhibited a granular bainitic microstructure, which increased hardness and fracture toughness compared to AIR-steel.

Acknowledgements

We would like to thank Tenaris Confab and Petrobras for the material donation, Brazilian Nanotechnology National Laboratory (LNNano) for the provision of the FEI ® Quanta 650FEG SEM/EBSD microscope, and X-ray Diffractometer. Special thanks are due to Pedro Brito and Eduardo Fonseca for their important review and suggestions of the manuscript. Vanessa da Silva from LNNano and Alberto Cury from USP/EESC are acknowledged for XRD measurements. This study was financed in part by the National Council for Scientific and Technological Development, Brazil CNPq, process 150215/2016-9; also H. Pinto is a CNPq fellow.

Author details

Fabio Faria Conde¹, Haroldo Cavalcanti Pinto¹, Mohammad Masoumi²
and Julian Arnaldo Avila^{3*}

1 USP – University of São Paulo, SP, Brazil

2 Center for Engineering, Modeling and Applied Social Sciences (CECS),
Universidade Federal do ABC (UFABC), SP, Brazil

3 UNESP – São Paulo State University (UNESP), SP, Brazil

*Address all correspondence to: julian.avila@unesp.br

IntechOpen

© 2019 The Author(s). Licensee IntechOpen. This chapter is distributed under the terms of the Creative Commons Attribution License (<http://creativecommons.org/licenses/by/3.0>), which permits unrestricted use, distribution, and reproduction in any medium, provided the original work is properly cited. 

References

- [1] Bai Y, Bai Q, editors. *Subsea Engineering Handbook*. Gulf Professional Publishing; 2010. pp. 919. ISBN: 9781856176897. DOI: 10.1016/B978-1-85617-689-7.10030-5. Available from: <http://www.sciencedirect.com/science/article/pii/B9781856176897100305>
- [2] Bai Y, Bai Q, editors. *Subsea Pipelines and Risers*. Elsevier Science Ltd; 2005. pp. 808. ISBN: 9780080445663. DOI: 10.1016/B978-008044566-3.50043-9. Available from: <http://www.sciencedirect.com/science/article/pii/B9780080445663500439>
- [3] Nishioka K, Ichikawa K. Progress in thermomechanical control of steel plates and their commercialization. *Science and Technology of Advanced Materials*. 2012;**13**(2):023001
- [4] Militzer M. 1.10 - Thermomechanical Processed Steels. In: Saleem H, Gilmar FB, Chester JVT, Bekir Y, editors. *Comprehensive Materials Processing*. Elsevier; 2014. pp. 191-216. ISBN: 9780080965338. DOI: 10.1016/B978-0-08-096532-1.00115-1. Available from: <http://www.sciencedirect.com/science/article/pii/B9780080965321001151>
- [5] Das Bakshi S, Dhande T, Javed N, Sasidhar KN, Sharma V, Mukherjee M, et al. Effect of hot deformation and crystallographic texture on toughness anisotropy and fracture behavior of Nb+V microalloyed API X70 steel. *International Journal of Pressure Vessels and Piping*. 2019;**171**:162-172. Available from: <https://linkinghub.elsevier.com/retrieve/pii/S0308016118302217>
- [6] Sung HK, Lee S, Shin SY. Effects of start and finish cooling temperatures on microstructure and mechanical properties of low-carbon high-strength and low-yield ratio bainitic steels. *Metallurgical and Materials Transactions A, Physical Metallurgy and Materials Science*. 2014;**45**(4):2004-2013
- [7] Gervasyev A, Carretero Olalla V, Sidor J, Sanchez Mouriño N, Kestens LAI, Petrov RH. An approach to microstructure quantification in terms of impact properties of HSLA pipeline steels. *Materials Science and Engineering A*. 2016;**677**:163-170
- [8] Chatterjee S, Koley S, Das Bakshi S, Shome M. Role of crystallographic texture, delamination and constraint on anisotropy in fracture toughness of API X70 line pipe steels. *Materials Science and Engineering A*. 2017;**708**:254-266. DOI: 10.1016/j.msea.2017.09.104
- [9] Joo MS, Suh DW-W, Bae JH, Bhadeshia HKDH. Role of delamination and crystallography on anisotropy of Charpy toughness in API-X80 steel. *Materials Science and Engineering A*. 2012;**546**:314-322. DOI: 10.1016/j.msea.2012.03.079
- [10] Joo MS, Suh DW, Bae JH, Sanchez Mouriño N, Petrov R, Kestens LAI, et al. Experiments to separate the effect of texture on anisotropy of pipeline steel. *Materials Science and Engineering A*. 2012;**556**:601-606
- [11] Joo MS, Suh DW, Bhadeshia HKDH. Mechanical anisotropy in steels for pipelines. *ISIJ International*. 2013;**53**(8):1305-1314. Available from: <http://jlc.jst.go.jp/DN/JST/JSTAGE/isijinternational/53.1305?lang=en&from=CrossRef&type=abstract>
- [12] Mintz B, Morrison WB, Morris PP, Davies GJ. The influence of texture on the tensile and impact properties of controlled steels. In: Davies GJ, editor. *Texture and Properties of Materials*. London, UK: The Metal Society; 1976. pp. 224-234

- [13] Inagaki H, Kurihara K, Kozasu I. Influence of crystallographic texture on the strength and toughness of control-rolled high tensile strength steel. *ISIJ International*. 1977;**17**:75-81
- [14] Sung HK, Sohn SS, Shin SY, Lee S, Kim NJ, Chon SH, et al. Effects of finish rolling temperature on inverse fracture occurring during drop weight tear test of API X80 pipeline steels. *Materials Science and Engineering A*. 2012;**541**:181-189. DOI: 10.1016/j.msea.2012.02.019
- [15] Ghosh A, Modak P, Dutta R, Chakrabarti D. Effect of MnS inclusion and crystallographic texture on anisotropy in Charpy impact toughness of low carbon ferritic steel. *Materials Science and Engineering A*. 2016;**654**:298-308. DOI: 10.1016/j.msea.2015.12.047
- [16] Ghosh A, Kundu S, Chakrabarti D. Effect of crystallographic texture on the cleavage fracture mechanism and effective grain size of ferritic steel. *Scripta Materialia*. 2014;**81**:8-11. DOI: 10.1016/j.scriptamat.2014.02.007
- [17] Zong C, Zhu G, Mao W. Effect of crystallographic texture on the anisotropy of Charpy impact behavior in pipeline steel. *Materials Science and Engineering A*. 2013;**563**:1-7. DOI: 10.1016/j.msea.2012.11.055
- [18] Mineur M, Villechaise P, Mendez J. Influence of the crystalline texture on the fatigue behavior of a 316L austenitic stainless steel. *Materials Science and Engineering A*. 2000;**286**(2):257-268
- [19] Avila JA, Lucon E, Sowards J, Mei PR, Ramirez AJ. Assessment of ductile-to-brittle transition behavior of localized microstructural regions in a friction-stir welded X80 pipeline steel with miniaturized Charpy V-notch testing. *Metallurgical and Materials Transactions A, Physical Metallurgy and Materials Science*. 2016;**47**(6):2855-2865
- [20] Lucon E. Testing of Small-Sized Specimens. In: *Comprehensive Materials Processing* [Internet]. Elsevier; 2014. p. 135-163. Available from: <https://linkinghub.elsevier.com/retrieve/pii/B9780080965321001102>
- [21] Tunncliffe MC. The Fracture Toughness of Low Carbon Steels; The Effects of Grain Size and Temperature. PhD thesis. University of Canterbury; 1991
- [22] Joo MS, Suh D-W, Bhadeshia DH. Anisotropy of Charpy properties in linepipe steels. *ISIJ International*. 2013;**53**:1305-1314
- [23] Kimura Y, Inoue T, Fuxing YIN, Tsuzaki K. Delamination toughening of ultrafine grain structure steels processed through tempforming at elevated temperatures. *ISIJ International*. 2010;**50**(1):152-161. Available from: <http://www.scopus.com/inward/record.url?eid=2-s2.0-77949815730&partnerID=40&md5=e3206b9cc9b2a4b7ca5866e292637020>
- [24] Ávila JAD, Ruchert COFT, Mei PR, Reppold RM, Piza MTP, Ramirez AJ. Fracture toughness assessment at different temperatures and regions within a friction stirred API 5L X80 steel welded plates. *Engineering Fracture Mechanics*. 2015;**147**:176-186
- [25] Yang XL, Xu YB, Tan XD, Wu D. Relationships among crystallographic texture, fracture behavior and Charpy impact toughness in API X100 pipeline steel. *Materials Science and Engineering A*. 2015;**641**:96-106
- [26] Pyshmintsev I, Gervasyev A, Petrov RH, Carretero Olalla V, Kestens L. Crystallographic texture as a factor enabling ductile fracture arrest in high strength pipeline steel. *Materials Science Forum*. 2011;**702-703**:770-773. Available from: <https://www.scientific.net/MSF.702-703.770>

- [27] Petrov RH, García OL, Mouriño NS, Kestens L, Bae JH, Kang KB. Microstructure - texture related toughness anisotropy of API-X80 pipeline steel characterized by means of 3D-EBSD technique. *Materials Science Forum*. 2007;**558-559**:1429-1434
- [28] Specification for Line Pipe. ISO 3183:2007 (Modified). American Petroleum Institute; 2009. p. 176
- [29] ASTM F1820-13. Standard Test Method for Determining the Forces for Disassembly of Modular Acetabular Devices. West Conshohocken, PA: ASTM International; 2013. www.astm.org
- [30] ASTM E1823-13. Standard Terminology Relating to Fatigue and Fracture Testing. West Conshohocken, PA: ASTM International; 2013. www.astm.org
- [31] Avila JA, Rodriguez J, Mei PR, Ramirez AJ. Microstructure and fracture toughness of multipass friction stir welded joints of API-5L-X80 steel plates. *Materials Science and Engineering A*. 2016;**673**:257-265
- [32] ASTM E8 / E8M-16a. Standard Test Methods for Tension Testing of Metallic Materials. West Conshohocken, PA: ASTM International; 2016. www.astm.org
- [33] Zajac S, Schwinn V, Tacke KH. Characterisation and quantification of complex bainitic microstructures in high and ultra-high strength linepipe steels. *Materials Science Forum*. 2005;**500-501**:387-394
- [34] Cizek P. Transformation behaviour and microstructure of an API X80 linepipe steel subjected to simulated thermomechanical processing. *Metal*. 2001;**15**:1-8
- [35] Silva RDA, Souza LFG, Morales EV, Rios PR, Bott IDS. Formation of microphases and constituents from remaining austenite decomposition in API X80 steel under different processing conditions. *Materials Research*. 2015;**18**(5):908-917
- [36] Yan P, Bhadeshia HKDH. Mechanism and kinetics of solid-state transformation in high-temperature processed linepipe steel. *Metallurgical and Materials Transactions A: Physical Metallurgy and Materials Science*. 2013;**44**:5468-5477
- [37] Bhadeshia HKDH, Honeycombe RWK. In: Lecomte-Beckers J, Schubert F, Ennis PJ, editors. *Steels: Microstructure and Properties*. 3rd ed. Vol. 3. Oxford: Elsevier Ltd; 2006. p. 357
- [38] Suwas S, Gurao NP. Crystallographic texture in Materials. *Journal of the Indian Institute of Science*. 2008;**88**:151-177
- [39] Bunge HJ. *Texture Analysis in Materials Science*. Butterworth-Heinemann; 1982. pp. 593. ISBN: 9780408106429. DOI: 10.1016/B978-0-408-10642-9.50002-7. Available from: <http://www.sciencedirect.com/science/article/pii/B9780408106429500027>
- [40] Suikkanen PP, Cayron C, Deardo AJ, Karjalainen LP, Oy RM, Box PO, et al. Crystallographic analysis of isothermally transformed bainite in 0.2C-2.0Mn-1.5Si-0.6Cr steel using EBSD. *Journal of Materials Science and Technology*. 2013;**29**(4):359-366
- [41] Yan J, Zhang W, Borgenstam A. Observations of surface relief of proeutectoid widmansta cementite plates in a hypereutectoid carbon steel. *Metallurgical and Materials Transactions A: Physical Metallurgy and Materials Science*. 2013;**44**:4143-4149
- [42] Masoumi M, Silva CC, Ferreira H, Abreu, De G. Effect of crystallographic orientations on the hydrogen-induced cracking resistance improvement of API 5L X70 pipeline steel under

various thermomechanical processing. *Corrosion Science*. 2016;**111**:121-131

[43] Mohtadi-bonab MA, Eskandari M, Sanayei M, Das S. Microstructural aspects of intergranular and transgranular crack propagation in an API X65 steel pipeline related to fatigue failure. *Engineering Failure Analysis*. 2018;**94**:214-225

[44] Zhang X, Matsuura K, Ohno M. Misorientation/local plastic strain manifestations in chemical etching color. *Micron*. 2014;**59**:28-32

[45] Chen Y, Tsai Y, Tung P, Tsai S, Chen C, Wang S. Phase quantification in low carbon Nb-Mo bearing steel by electron backscatter diffraction technique coupled with kernel average misorientation. *Materials Characterization*. 2018;**139**:49-58

[46] Kocks UF, Chandra H. Slip geometry in partially constrained deformation. *Acta Metallurgica*. 1982;**30**:695-709

[47] Zheng X, Zhang H. Experimental determination of deformation induced lattice rotation by EBSD technique for slip system analysis. *Journal of Materials Science and Technology*. 2017;**33**:90-98

[48] Taylor GI. Plastic Strain in Metals. *Journal of the Institute of Metals*. 1938;**62**:307-324

[49] Morales-rivas L, Archie F, Zaefferer S, Benito-alfonso M, Tsai S, Yang J, et al. Crystallographic examination of the interaction between texture evolution , mechanically induced martensitic transformation and twinning in nanostructured bainite. *Journal of Alloys and Compounds*. 2018;**752**:505-519

[50] Masoumi M, Echeverri EAA, Silva CC, Aguiar WM, de Abreu HFG. Improvement of formability and tensile mechanical

properties of SAE 970X steel by controlled rolling process. *Journal of Materials Research and Technology*. 2018;**8**(1):1353-1365

[51] Ishikawa N, Yasuda K, Sueyoshi H, Endo S, Ikeda H, Morikawa T, et al. Microscopic deformation and strain hardening analysis of ferrite—Bainite dual-phase steels using micro-grid method. *Acta Materialia*. 2015;**97**:257-268

[52] Chang SK, Il LS, Lee DN. Change of rotated cube texture through multi-processing in 3% Si-steels. *ISIJ International*. 2009;**49**(1):105-108

[53] Takajo S, Vogel SC, Hayakawa Y. Strongly developed texture components near rotated cube orientation during recrystallization in a severely cold rolled low carbon steel. *ISIJ International*. 2019;**59**(3):541-550

[54] Mouriño NS, Petrov R, Bae JH, Kim K, Kestens LAI. Texture dependent mechanical anisotropy of X80 pipeline steel. *Advanced Engineering Materials*. 2010;**12**(10):973-980

Contact Strength of Material

Xiaofeng Qin

Abstract

Contact is one of the common positions for relationship existing between surfaces of mechanical components with line or point shape, which lead to different stress condition between them. Classic Hertz theory solved the stress distribution of two components with different contact form. The different stress form of contact components will result in different failure modes, and different strength requirement is needed in design. For those works under conditions like classic Hertz contact, obvious plastic deformation should be avoided and the maximum stress should be smaller than the allowed limit stress which is usually equal to yield stress of material. While for the ones enduring load by extrusion of two contact surface, the crushing of two contact surface should be avoided and the maximum contact stress should be smaller than the ultimate strength of the material. But for those works under varying stresses, fatigue and wear are common failure modes. The typical failure form resulted from contact fatigue is pitting and spalling; the previous one usually results in small peeling of materials from surface and lots of small shallow pits will formed, while the spalling usually leads to larger part of material drop off from the surface and scrap of mechanical components. Wear is another failure form of components works under contact conditions, which is actually can be seen as the accumulation of pitting of asperities. Comparing the classic static strength theory and fatigue strength theory of material, the static contact strength is actually the limit condition of contact fatigue strength with the one circle stress loaded in the whole life. With the development of fatigue theory, lots of models were proposed to study the contact strength of material from the fracture mechanics view. The most popular ones are critical plane method and Dang Van multi-axial fatigue criterion, which are used to assess the crack initiation of materials works under contact load.

Keywords: mechanical component, static contact strength, contact fatigue strength, fracture mechanics, multi-axial fatigue

1. Introduction

Usually, strength reveals the mechanical properties of a kind of material or a component to resistant to fracture and over deformation. Based on the variation characteristics of stress endured by the material or components, the strength can be classified into static strength and variable stress intensity [1, 2]. In the real application, different materials are used for manufacturing mechanical components that work under contact load. According to the contact form and stress level induced by the load, the contact form can be classified into line contact as shown in

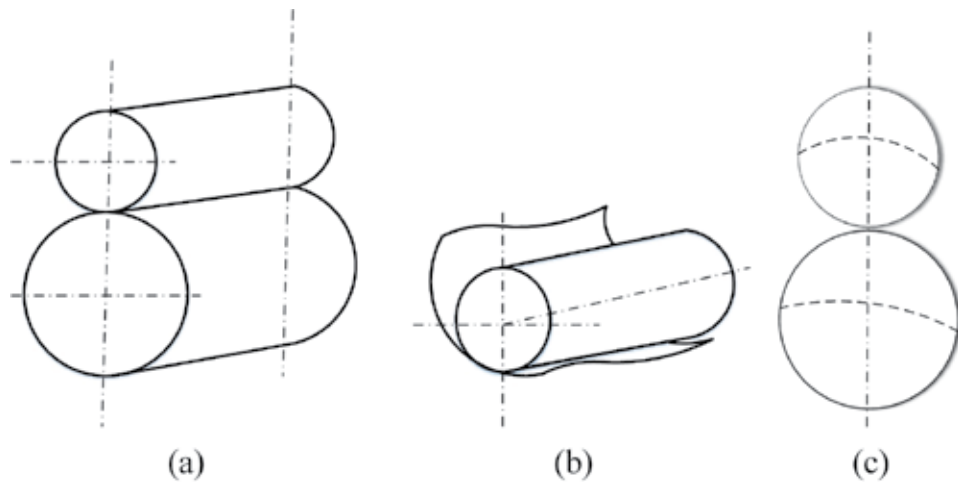


Figure 1.
Diagram for different contact forms of mechanical parts.

Figure 1(a) and **(b)** and point contact as shown in **Figure 1(c)** [1–3]. The contact line or point will be transformed to load-bearing area [3, 4]. For actual application, the contact between gears, rolls in mill, rail/wheel, roller bearing and contact of bolt and holes are all under line contact form; while the ball and ring in bearing are under the point contact form [1–4].

As the strength is the capability of material enduring the load or stress, failure will occur if the load or stress is beyond the level that it can bear [4, 5]. The failure modes of material working under contact load show different forms with the different stress vibration characteristics such as plastic deformation, surface pitting, surface wear and crushing of contact surface. Typically, the plastic deformation and crushing of contact surface are both resulted from the stress which is exceeding the yield limit of the material. The surface pitting and wear usually are considered to be formed by the accumulation effect induced by varying stress. For ensuring the strength of material working under stress with different variation characteristics, different manner should be used to assess the safety of the material.

2. Static contact strength

2.1 Static contact stress

According to the classical elasticity theory, the deformation of material can be divided into three mechanical states: elastic state, plastic state and fracture. Some materials used for manufacturing the components works under static contact state, are not allowed have plastic deformation due to the requirement of working reliability and transmission accuracy. For the materials used in the manufacturing of the components working under contact state, most of them cannot work properly with obvious plastic deformation.

According to the different contact forms shown in **Figure 1**, the contact stress between two cylinders loaded by force F as shown in **Figure 2(a)** can be expressed as below [1, 3]:

$$\sigma_{H \max} = \frac{4}{\pi} \frac{F}{2ab} = \sqrt{\frac{F \left(\frac{1}{\rho_1} \pm \frac{1}{\rho_2} \right)}{\pi b \frac{1-\mu_1^2}{E_1} + \frac{1-\mu_2^2}{E_2}}} \quad (1)$$

The half-width a of contact area along the circumference is [3]:

$$a = \sqrt{\frac{4F \frac{1-\mu_1^2}{E_1} + \frac{1-\mu_2^2}{E_2}}{\pi b \left(\frac{1}{\rho_1} \pm \frac{1}{\rho_2} \right)}} \quad (2)$$

where ρ_1 and ρ_2 are the curvature radius of contact area of two parts; the plus sign '+' means outer surface contact as shown in **Figure 1(a)**; the minus sign '-' means inner surface contact as shown in **Figure 1(b)**; E_1 and E_2 are the Young's modulus of materials of two components in contact, respectively; μ_1 and μ_2 are the Poisson's ratio of materials of two components in contact, respectively.

The contact stress between two balls loaded by force F shown in **Figure 2(b)** can be expressed as equation below [3]:

$$\sigma_{H \max} = \frac{3}{2} \frac{F}{\pi c^2} = \frac{1}{\pi} \sqrt{6F \left(\frac{\left(\frac{1}{\rho_1} \pm \frac{1}{\rho_2} \right)}{\frac{1-\mu_1^2}{E_1} + \frac{1-\mu_2^2}{E_2}} \right)^2} \quad (3)$$

The radius c of contact area is [3]:

$$c = \left[\frac{3F \frac{1-\mu_1^2}{E_1} + \frac{1-\mu_2^2}{E_2}}{4 \left(\frac{1}{\rho_1} \pm \frac{1}{\rho_2} \right)} \right]^{1/3} \quad (4)$$

where c is the radius of contact area; the meaning of other symbols are same to that mentioned before.

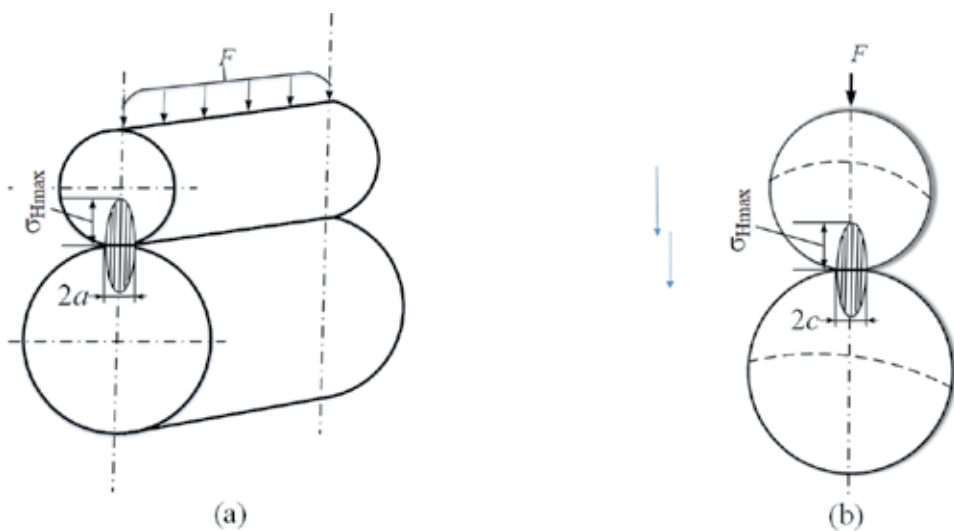


Figure 2.
 Diagram for stress distribution of different contact form.

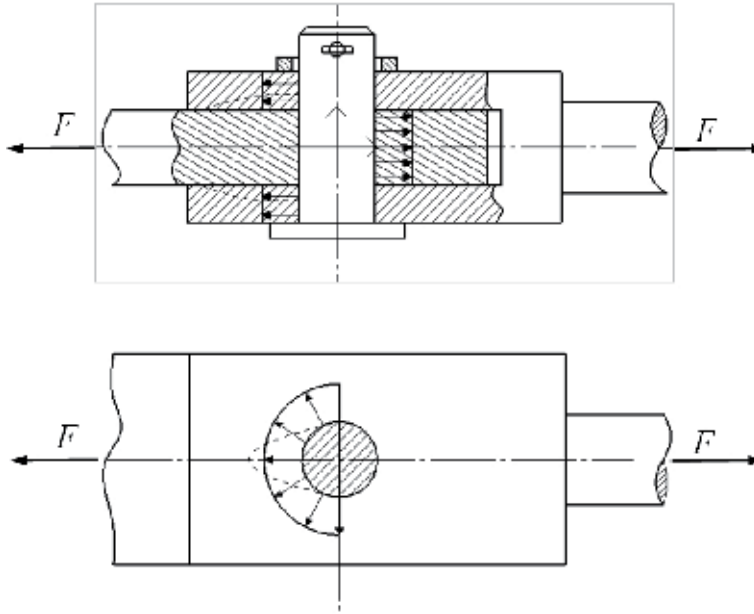


Figure 3.
Diagram of extrusion contact.

2.2 Static extrusion stress

For materials used in bolt connection, pin connection and key connection shown like in **Figure 3** mostly transfer the load by extrusion of match surface. Under contact form like the one shown in **Figure 3**, the main failure mode of the material located in the contact area is crushing. Based on the assumption of the stress distribution in the contact area, the stress between two match surfaces under extrusion load can be expressed as below:

$$\sigma_p = \frac{F}{A} \quad (5)$$

where F is the load acting on the two components and the acting direction of it is perpendicular to the bearing surface. A is the area size of match surface between two components when the bearing surface is flat or the projection area size of match surface between two components when the bearing surface is not flat.

2.3 Condition of static contact strength

For the linear state of stress, the condition of strength can be recorded as the following form:

$$\sigma \leq [\sigma] = \frac{\sigma_{\text{lim}}}{[S]} \quad (6)$$

where σ is the maximum stress active in a part or structure; $[\sigma]$ is the admissible stress level which can be determined by $\sigma_{\text{lim}}/[S]$; σ_{lim} is the ultimate stress of material; and the $[S] > 0$ is termed the strength safety factor.

The materials for manufacturing the components' transmission load usually fails in the form of plastic deforms under static load. So the condition of materials under contact conditions, as shown in **Figure 1(a)** and **(b)** or **Figure 2**, is:

$$\sigma_{H \max} \leq [\sigma_H]_{\max} = \frac{\sigma_{\lim}}{[S]} \quad (7)$$

The condition of strength for the components enduring load by extrusion of match surface is:

$$\sigma_p \leq [\sigma_p] = \frac{\sigma_{\lim}}{[S]} \quad (8)$$

For different types of materials, the ultimate stress σ_{\lim} is different. If a material is not allowing the transition to the plastic state, then $\sigma_{\lim} = \sigma_y$; where σ_y is the yield strength of material. If the material is of brittle type, then the $\sigma_{\lim} = \sigma_b$. Here, σ_b is the ultimate strength of the material, which can be obtained by standard tension test.

The safety factor [S] can be determined based on the safety requirement of components in the actual application conditions.

3. Contact fatigue strength of material

Any materials used in real application exist in the form of mechanical part. There is little mechanical part works under static stresses. For the time and space view, the amplitude of stresses may regularly or irregularly change with time. The fatigue is resulted from changes in the structure and properties of material led by the gradual accumulation of damage under the act of alternating stresses. Mechanically, the form of fatigue of material usually goes through the nucleation and growth of cracks, and ultimately leads to the volume fracture. This phenomenon occurring in the material of components working under contact load is often named pitting and wear.

The detail of the contact fatigue process may vary with the difference of material and load conditions, but in almost all cases, the process can be manifested as the initiation and propagation of cracks. Based on the actual application of different materials under different contact conditions, the initiation of cracks led by the accumulation of contact fatigue damage is from the surface or near-surface layer. The final manifested form of cracks, initiated from different sites of contact components, after propagation until a piece of material detaches itself, will form a pit or spall; while from the point of micro view, the wear is the accumulation process of pit or spall of asperities of contact surface due to contact load.

3.1 Pit and spall

As mentioned before, pitting and spalling are the macro shown of material dropping from the contact surface due to damage accumulation with the cyclic of stresses.

Pitting is generally considered to be caused by the propagation of surface-initiated cracks. **Figure 4** shows the typical form of pitting of a contact surface. The process also includes three stages: crack initiate, crack propagate and material drop from the surface [6].

In the first stage, the cracks will initiate from the site where the damage accumulation reached the damage capacity limit of material. In the second stage, the cracks will propagate under the comprehensive act of tensile stress result from surface friction and traction and squeezing effect of the lubricant into the crack. In the last stage, the material will rupture from the surface if the remaining section between part 1 and the parent surface cannot endure the comprehensive act of

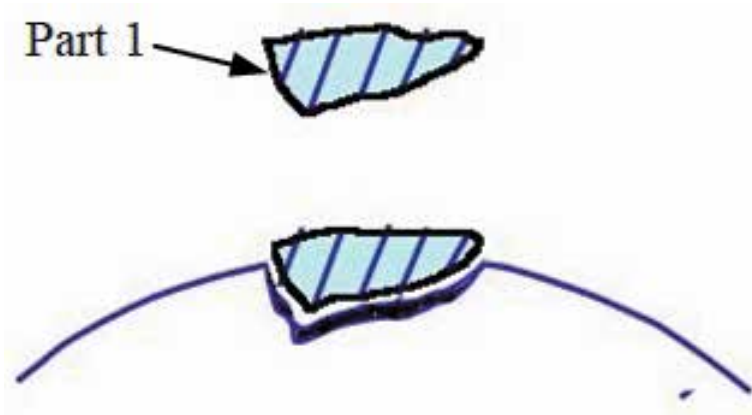


Figure 4.
Diagram for pitting form process.



Figure 5.
Typical morphology of pitting.

stress. Due to the edge of pitting, it will further result in the increase of stress by stress concentration effect; more cracks will initiate around the generated pitting and finally form a pitting surface as shown in **Figure 5**. Usually, the pitting caused by contact fatigue will not result in the loss of function of mechanical components.

Sometimes the cracks initiating from contact surface or subsurface will first propagate along the path which is at an acute angle to the surface. Then it is propagated along the path parallel to the surface which will let the crack to propagate along a relatively long path and eventually leading to large chunks peeled off from the surface. The whole process can be described by the sketch shown in **Figure 6** [7–9].

Figure 7 shows a typical spalling morphology of backup roll used in steel production. Based on the morphology of spalling of roll shown in **Figure 7**, it can be seen that the crack propagates along the peripheral direction of roll and causes extensive surface peeling. Usually, the spalling can cause the complete loss of function of mechanical components.

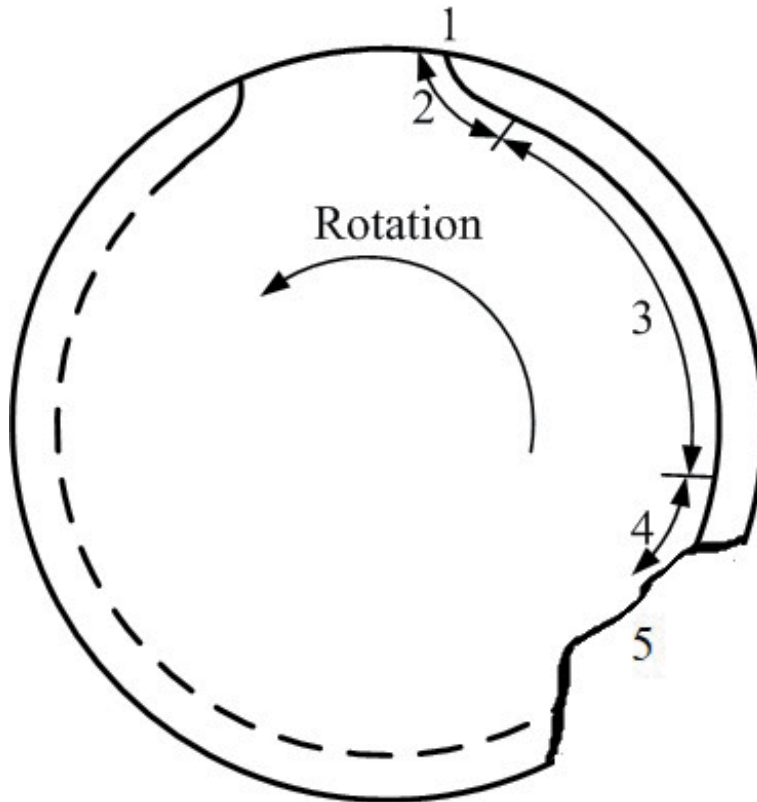


Figure 6.
Spalling failure process of contact components [7].



Figure 7.
Typical spalling of component result from contact fatigue.

3.2 Wear

Wear is a common phenomenon for the mechanical components working under contact and having relative move. The wear resulted from contact fatigue is a more common phenomenon in components with good lubrication. As the machined

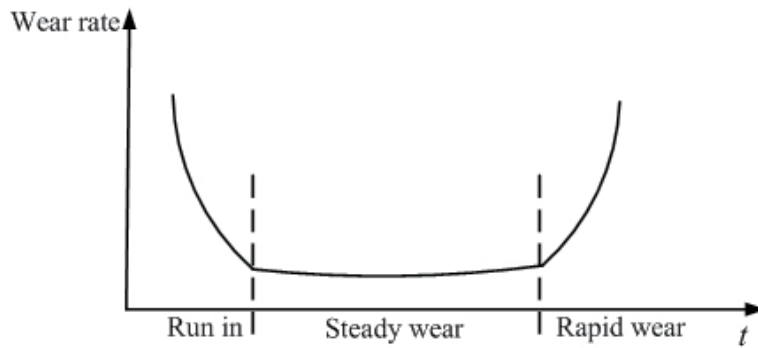


Figure 8.
Wear rate variation line in whole life.

surface of components such as gear, ball and ring of bearing and wheel/rail consists of asperities, the load of two surface contact is supported by contact of lots of asperities and lubricates in micro level [10, 11]. Usually, we considered that the pitting occurs at the surface contact under macro level. If we observe two contact surfaces in micro level, the contact of separate asperities is equivalent to that contact of two surfaces in macro level. The only difference between them is the relative radius of curvature.

So if we considered the contact of asperities as two components contact under micro level, the formation of wear is actually the accumulation of micro pitting between the contacted asperities, and the variation process of wear during the whole life of mechanical components can be described by the formation mechanism of macro pitting. As it is known, the process of wear of mechanical component in its whole life can be divided into three stages including run-in process, steady wear and rapid wear process as shown in **Figure 8**.

In the run-in stage, the contact of two macro surfaces is supported by contact of asperities, which will result in the micro contact fatigue of asperities. The fatigue damage accumulation due to contact of asperities will result in the pitting which occurs on the surface of asperities. The pitting of asperities leading to the equivalent radius of curvature of asperities increase and contact stress between the two asperities decrease, which will decrease the damage during later contact and the wear process enter into steady wear process and last long time. With the further increase of using time, the damage of whole surface will increase and the whole strength of surface will degrade. Then the occurrence of pitting of asperities will speed up and wear rate of surface will sharply increase, which means the arrival of rapid wear.

4. New trend of contact fatigue strength research

With the development of material process technology, the contact strength of it is increased gradually. But the failure caused by contact fatigue and wear cannot be avoided. Lots of models, established based on fracture mechanics and damage accumulation theory, are established to assess the contact fatigue process of material. In these models, the most popular ones are Dang Van criterion and the critical plane method.

4.1 Critical plane model

The critical plane method considered that the crack initiation plane may occur on a plane near the maximum normal stress range for medium to high strength

steels, and the model used for assess on the occurs of critical plane can be expressed as [12, 13]

$$FP = \frac{\Delta\varepsilon}{2} \sigma_{\max} + J\Delta\gamma\Delta\tau \quad (9)$$

where $\Delta\varepsilon$ is the normal strain range, σ_{\max} is the maximum normal stress, $\Delta\gamma$ is the shear strain range, $\Delta\tau$ is the shear stress range and J is material constant.

Based on the above equation, the relationship between the fatigue parameter and life is expressed as

$$(FP - FP_0)^m N_f = \text{constant} \quad (10)$$

where N_f is the fatigue life corresponding to fatigue parameter FP , and m , FP_0 and C are material fatigue properties determined from fatigue life experiments [13].

If the damage accumulates linearly, then the damage per loading cycle is [13]

$$\frac{dD_f}{dN} = \frac{1}{N_f} = \frac{(FP - FP_0)^m}{C} \quad (11)$$

where D_f is the fatigue damage equal or smaller than 1; and N represents the number of load cycles. If $FP \leq FP_0$, there is no damage resulted from the load cycle.

4.2 Dang Van multi-axial fatigue criterion

Dang Van multi-axial fatigue criterion assumes there is elastic shakedown occurs before cracks initiation and considered two scales [14–16]. The first is that often used by engineers who used to analysis the fatigue of point that surrounded by an arbitrary elementary volume in macroscopic scale. The second one is used to subdivide the macroscopic scale element in mesoscopic scale. It thinks that macroscopic stress tension result in the mesoscopic one and the local inelastic deformation lead to the local residual stresses. Based on that assumptions, the model is expressed as an inequality of mesoscopic stresses at all instants t of the cycle to characterize the damage as below [14]:

$$\max_t [\tau(t) + ap(t)] \leq b \quad (12)$$

Where $\tau(t)$ and $p(t)$ are the instantaneous mesoscopic shear stress and hydrostatic stress, a and b are material constants which can be determined by classic bending and twisting fatigue test.

Acknowledgements

This work was supported by the National Natural Science Foundation of China (Grant No. 51805355) and Natural Science Foundation for Young Scientists of Shanxi Province, China (Grant No. 201701D221136). The author is grateful to all the partners of College of Mechanical and Vehicle Engineering, Taiyuan University of Technology, China.

Author details

Xiaofeng Qin
College of Mechanical and Vehicle Engineering, Taiyuan University of Technology,
Taiyuan, P.R. China

*Address all correspondence to: qinxiaofeng@tyut.edu.cn

IntechOpen

© 2019 The Author(s). Licensee IntechOpen. This chapter is distributed under the terms of the Creative Commons Attribution License (<http://creativecommons.org/licenses/by/3.0>), which permits unrestricted use, distribution, and reproduction in any medium, provided the original work is properly cited. 

References

- [1] Ugural AC. Mechanical Design of Machine Components. 2nd ed. Florida: CRC Press; 2015
- [2] Childs P. Mechanical design. London: Butterworth Heinemann; 2003
- [3] Popov VL. Contact Mechanics and Friction. Berlin: Springer Berlin Heidelberg; 2010
- [4] Sosnovskiy LA. Tribo-Fatigue: Wear-Fatigue Damage and its Prediction. Berlin: Springer Science & Business Media; 2010
- [5] Todhunter IA. History of the Theory of Elasticity and of the Strength of Materials. New York: Cambridge University Press; 2014
- [6] Mao K. Gear tooth contact analysis and its application in the reduction of fatigue wear. *Wear*. 2007;262(11–12): 1281-1288
- [7] Frolish MF, Fletcher DI, Beynon JH. A quantitative model for predicting the morphology of surface initiated rolling contact fatigue cracks in back-up roll steels. *Fatigue & Fracture of Engineering Materials & Structures*. 2002;25(11):1073-1086
- [8] Kapadia BM, Marsden KW. Spalling behavior of back-up roll materials. In: 39th Mechanical Working and Steel Processing Conference. 1997. pp. 349-386
- [9] Ohkomori Y, Kitagawa I, Shinozuka K, et al. Study on spalling of hot strip mill backup roll. *Tetsu to Hagane*. 1987;73(6):691-698
- [10] Kato K. Classification of wear mechanisms/models. Proceedings of the Institution of Mechanical Engineers, Part J: Journal of Engineering Tribology. 2002;216(6):349-355
- [11] Martínez FJ, Canales M, Bielsa JM, et al. Relationship between wear rate and mechanical fatigue in sliding TPU–metal contacts. *Wear*. 2010;268(3–4): 388-398
- [12] Jiang Y, Sehitoglu H. A model for rolling contact failure. *Wear*. 1999; 224(1):38-49
- [13] De-Guang S, De-Jun W. A new multiaxial fatigue damage model based on the critical plane approach. *International Journal of Fatigue*. 1998; 20(3):241-245
- [14] Ciavarella M, Monno F, Demelio G. On the dang Van fatigue limit in rolling contact fatigue. *International Journal of Fatigue*. 2006;28(8):852-863
- [15] Ciavarella M, Maitournam H. On the Ekberg, Kabo and Andersson calculation of the dang Van high cycle fatigue limit for rolling contact fatigue. *Fatigue & Fracture of Engineering Materials & Structures*. 2004;27(6):523-526
- [16] Araujo JA, Nowell D, Vivacqua RC. The use of multiaxial fatigue models to predict fretting fatigue life of components subjected to different contact stress fields. *Fatigue & Fracture of Engineering Materials & Structures*. 2004;27(10):967-978

Corrosion Fatigue of Aluminum-Copper-Lithium Alloy 2050-T84 Submitted at Salt Spray and Aqueous Saline Solution

*Maciel Carla Isabel dos Santos,
Bose Filho Waldek Wladimir and
Ruchert Cassius Olívio Figueiredo Terra*

Abstract

Interest in the improvement of the structural performance of aircraft has begun in the substitution of aluminum alloys due to the possibility of reduction of density, an increase of stiffness, high fracture toughness, greater resistance to the propagation of cracks by fatigue and greater resistance to corrosion. In these issues, the aluminum-copper-lithium alloy 2050-T84 is outstanding, which presents excellent mechanical properties even when subjected to aggressive atmospheres. The failure of structural components of aircraft occurs due to several factors that may arise from microstructural defects and/or applied static or cyclic stresses associated with atypical environments such as cryogenic or corrosive. In this sense, the results have evidenced the presence of precipitates that influence in the increase of the mechanical strength, behavior of fracture toughness, fatigue life, and corrosion fatigue, in different temperatures and aggressive means. Tensile and fracture toughness tests at 23 and -60°C the material showed ductility retention without a significant difference in the results. Fatigue crack growth in air and corrosion fatigue with 3.5 and 5% NaCl and aqueous solution with 3.5% NaCl showed a meaning difference in the threshold region; however, for the Paris region at the saline environment, fatigue crack growth (FCG) rates are similar.

Keywords: corrosion fatigue, da/dN , Al-Cu-Li alloy, 2050-T84, mechanical behavior, salt spray, aqueous saline solution

1. Introduction

High strength heat hardening aluminum alloys are relevant for aeronautical applications due to their excellent interaction between chemical, physical and mechanical properties, and weight reduction. Such integration results in structures with maximum efficiency and fuel economy for aircraft in operation, based on this a large number of alloys has been developed in response. The aircraft industry is the symbols of technological generation and has developed improvements in structural

integrity with the replacement of aluminum alloys, safer aircraft, and reduction of the costs of manufacturing, maintenance and operation. Therefore, this technological sector develops research for optimization of projects that result in lighter aircraft with the direct consequence in the fuel consumption and operationally more viable.

Highlighting of the substitution of structural and fuselage materials, the proposal for the manufacture of aluminum-lithium alloys showed up attractive, according to reference [1], the presence of lithium (Li) in aluminum (Al) alloys simultaneously increases the elastic limit and decreases density because every 1% Li the density is reduced by about 3% and the elastic limit increased by 6% thus, the Al-Cu-Li alloy 2050-T84 get up as a substitution attractive aluminum-magnesium-zinc alloy 7050-T7451.

The improvement of aeronautical alloys induces the industry to produce materials with lower density and high strength, in this way the aluminum-copper-lithium alloys. The first generation, designated as 2020, was produced in the United States in the 1950s. The manufacture of these alloys was abandoned due to low ductility and poor fracture toughness. The second generation, composed of 2090, 2091 and 8090 alloys, was created as a proposal to improve the resistance to corrosion and its mechanical properties, however, it resulted in alloys with excessive anisotropy and low resistance to stress corrosion cracking. Recently, alloys of the third generation, composed of 2094, 2097, 2099, 2196, AA2197 and 2050 alloys, have been developed for military and aerospace applications and when compared Al-Li alloys of previous generations present high resistance to static and tolerance to damage [2].

The resistance of corrosion of 2xxx series alloys is dependent on their chemical composition and the effect of their elements on the oxide layer. For practical applications, the presence of alloying elements such as Cu, Mg, Mn, Zn, Li, and Si have the purpose of increasing mechanical strength or specific resistance, however these elements form intermetallic particles or precipitated, which are harmful to the corrosion properties of the material, due to the formation of a thinner and more conductive oxide layer that allows the occurrence of cathodic reactions. Avoiding the appearance of these precipitates would be the most effective measure of preventing corrosion, however, the precipitates are important to increase the mechanical properties of the material [3].

These alloys are fabricated by two processes: heat treatments and mechanical forming. Heat treatments perform considerable influence on the corrosive behavior of aluminum alloys as they may result in localized chemical effects and become the material resistant to localized corrosion. When there is no complete solubilization of the alloying elements, the result is a non-uniform microstructure that favors susceptibility to corrosion. The mechanical forming influences the grain morphology and the distribution of the constituent particles of the alloy. The deformation of the material can generate failures in atomic ordering and weaken the oxide layer, allowing localized corrosion [4].

The common forms of corrosion in aluminum alloys are by pits and intergranular, the latter coming from the process of stress corrosion cracking (SCC) and occurs in the contours of grains resulting in poor mechanical properties and brittle fracture of the component when still subject to mechanical requests. The pitting corrosion occurs in isolated points on the metal surface and growth to the inside, often through the material [5].

There are several researches about the behavior of the Al-Cu-Li 2050-T84 alloy, and the microstructural characteristics are presented using the transmission electron microscopy (TEM) technique that showed the presence of precipitates influencing the increase of the strength mechanical of the alloy, fracture toughness,

fatigue and corrosion fatigue at room temperature (23°C), cryogenic (−60°C) and saline environment [6]. The corrosion evaluation was carried out with the potentiodynamic polarization tests and indicated that the alloy in question has a higher value of corrosion potential and pit, when compared to another Al-Li alloys, favoring the formation and growing of pits become pointed enough to results in stress concentration and a crack nucleation contributing directly to the fatigue life of aluminum alloys used in aircraft structures and can result in accelerated failure. However, the results obtained in air, salt spray at 3.5 and 5% NaCl and aqueous saline solution with 3.5% NaCl showed a clear difference in the region of the threshold, however, for the region of Paris independently of the environment, the FCG rates are quite similar.

1.1 Microstructural features of 2050-T84 alloy

Aluminum alloys (Al) of the 2xxx series have Copper (Cu) and Lithium (Li) as the main alloying elements and require heat treatments of solubilization, precipitation and aging to improve your mechanical properties. Specifically, the Al-Cu-Li 2050 ternary alloy has density of 2.71 g/cm³ [7] and presents precipitates responsible for the increase of mechanical strength as S' (Al₂CuMg), T_1 (Al₂CuLi), and formation of small particles of MnAl₆, Al₂₀Cu₂Mn₃, Al₁₂Mg₂Cr, presented by reference [8] through the technique of scanning electron microscopy (SEM) as shown in **Figure 1**. The authors evidenced the formation of precipitates rich in Mg, Zn, Cu and Mn in the grain boundary, which promote reducing of mechanical properties and fracture toughness.

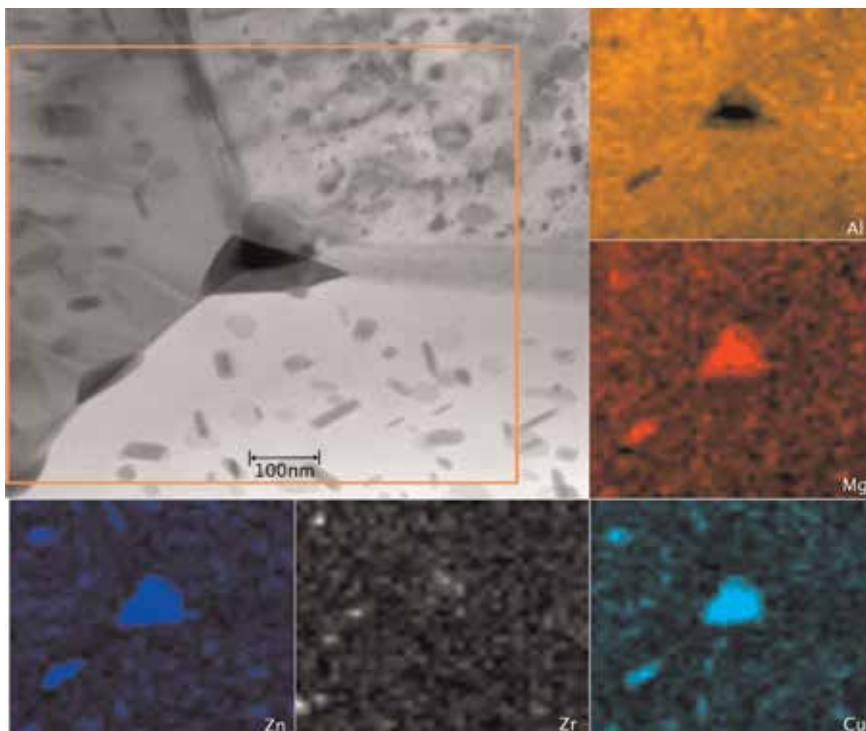


Figure 1. Bright field STEM micrograph and respective (EDS) elemental mapping of Al-K, Mn-K, Mg-K, Cu-K and Zn-K in 2050-T84 alloy, showing the composition of precipitates at the grain boundaries (larger) and inside the grain (smaller) on a nanometric scale; bright field TEM micrograph [8].

The presence of S' in the metal matrix restrains the movements of dislocations and promotes a homogeneous deformation and increases the strength of the alloy. According to Deng et al. [9], the presence of lithium (Li) favors the formation of free zones precipitate (FZP) in the grain boundary, **Figure 2**, which affects fracture properties, increasing the ductility of the material.

Evaluating from corrosion, these properties are not suitable as other aluminum alloys, because under certain conditions they may favor intergranular corrosion and resulting of the embrittlement the material [10].

1.2 Effects of corrosion on alloy 2050-T84

By exposing aluminum alloys to the presence of alkaline factors or acidic factors such as chemical ions composed of chlorides or fluorides, e.g., their alumina oxide layer (Al_2O_3) can be broken and its degradation accelerated. In 2xxx series alloys, the presence of precipitates containing Cu creates a potential difference between the precipitate and the aluminum matrix resulting in a galvanic cell that makes these materials highly susceptible to corrosion, so that second phase precipitates as $CuAl_2$ can influence the intergranular corrosion.

Presence of precipitates such as $Al_6(Cu, Fe, Mn)$ and T_1 in the 2050-T84 alloy may cause pitting corrosion which are cavities that have the bottom in an angular shape and depth generally greater than its diameter. This phenomenon affects corrosion rates, the structural integrity of the component and it is processed in points or in small areas located in the metallic surface in three stages [3]:

- i. Nucleation: is tiny, rapid and leads to the formation of metastable pits due to adsorption of the aggressive ions on the metal surface followed by the rupture of the alumina oxide layer in the most susceptible regions;
- ii. Meta-stable formation: the growth is not fully established, however, is determined by the exposure of the free surface of the metal and by the geometry of the boundary defined during the breakage of the film passive oxide;

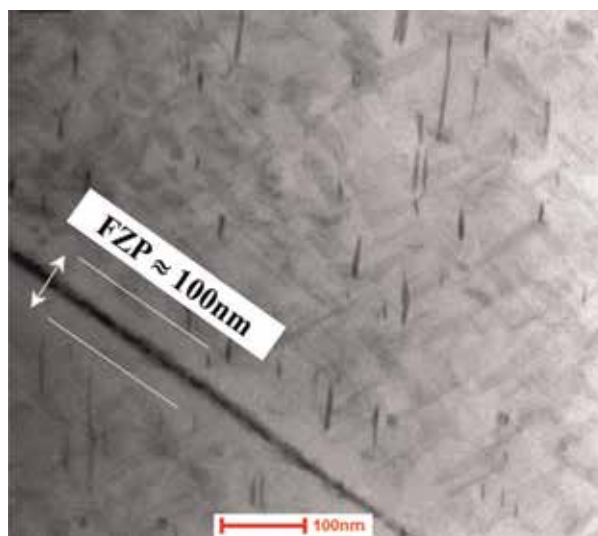


Figure 2.
Imagem de MET evidenciando a zona livre de precipitados da liga de alumio-lítio 2050-T84 [8].

- iii. Stabilization: occurs after the formation of corrosion products at the entrance of the pits that holds the ions and after several days of exposure, they stop growing and are again passivated. However, if exposed to the medium again the growth of new pitting nucleation sites.

Figure 3 shows images obtained by SEM reveal the presence of pitting corrosion sites in 2050-T84 alloy when exposed to saline solution. This corrosion process occurred near precipitates and salt crystals deposited on the surface of a sample analyzed by the potentiodynamic polarization tests.

With corrosion evaluation criteria, the addition of lithium is very harmful because this element is highly reactive and additions of about 3% in aluminum causes changes in pitting potential (E_{pit}) leaving the material more vulnerable when exposed to corrosive conditions [3]. With a short time of exposure to the corrosive environment some alloys already have a large number of pits, varying according to the alloy and the environment to which inserted.

This corrosive behavior can be investigated by Evans diagram, obtained through potentiodynamic polarization tests, which provides values for potential corrosion (E_{corr}), pitting potential (E_{pit}) and corrosion current density (j_{corr}) [11]. The corrosion potential is that the anode current process equals the cathode current process. If the anode overvoltage curve is characteristic of a passive metal, at a given potential the pitting nucleation occurs with a sudden surge of current, then the intersection with the cathode overvoltage curve will occur exactly at this potential [12].

1.3 Corrosion fatigue in aluminum-copper-lithium alloy 2050-T84

Corrosion fatigue is the term used to denote the damage and failure of components subjected to cyclic loading in a brittle environment resulting from the interaction between plastic deformation and localized chemical or electrochemical reactions [3–5]. Aluminum alloys have relatively low corrosion resistance if exposed to NaCl salt spray due to the presence of precipitates from heat treatments, which have less corrosion resistance than the matrix. When there is remaking of these precipitates in the grain boundaries there is an increase in susceptibility to intergranular corrosion. Avoiding the emergence of these precipitates would be the

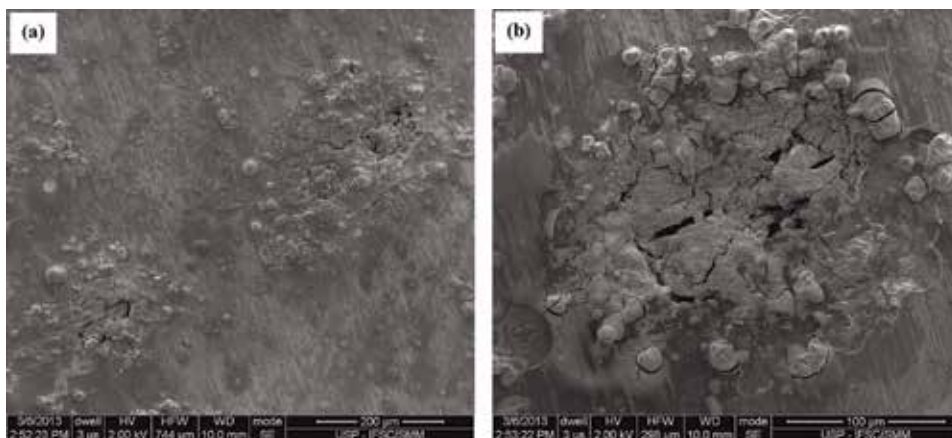


Figure 3. Images of 2050-T84 surface alloy by scanning electron microscopy after the potentiodynamic polarization tests. In (a) shows pits and salt crystals in corrosion process, in (b) detail of pit.

most effective measure of preventing corrosion, however, they are important in enhancing the monotonic mechanical properties of the material [3]. For the reduction of damage caused by the environment, materials less susceptible to corrosion of the environment or the application of surface protection processes such as paints and galvanizing should be used.

In addition to the development complexity of the corrosion fatigue testing methodology, the fatigue crack growth presents adverse behavior in some moments. The crack increases rapidly and in others, cases remain at the same length for hours or even days [3–13]. Interpretation for the fast growth crack, due to the embrittlement of metal alloys subjected to corrosion fatigue, is based on the mechanism of hydrogen embrittlement. Such mechanisms occur due to the reduction of hydrogen particles and the adsorption of atoms at critical locations such as pits, voids between the crack walls and towards the crack tip. Hydrogen atoms, even at room temperature, may be interstitially lodged in the metal crystal or even in grain boundaries, resulting in drastically reducing the toughness and ductility of the material [13].

According to the reference [14] hydrogen induces the appearance of delayed fractures as a consequence of the appearance of numerous surface cracks, which are nucleated throughout the process of leaving hydrogen in the gaseous form of the material. Thus, the FCG rate is accelerated due to the action of hydrogen embrittlement and the presence of oxides that alter the crack closure mechanism.

The plastic deformation at the crack tip causes the oxide layer to break down by exposing the free surface to the corrosive environments and allows for pit. The interior of the pit is more anodic than the rest of the material and in this way the corrosion proceeds to the interior making the pit pointed enough to produce intense

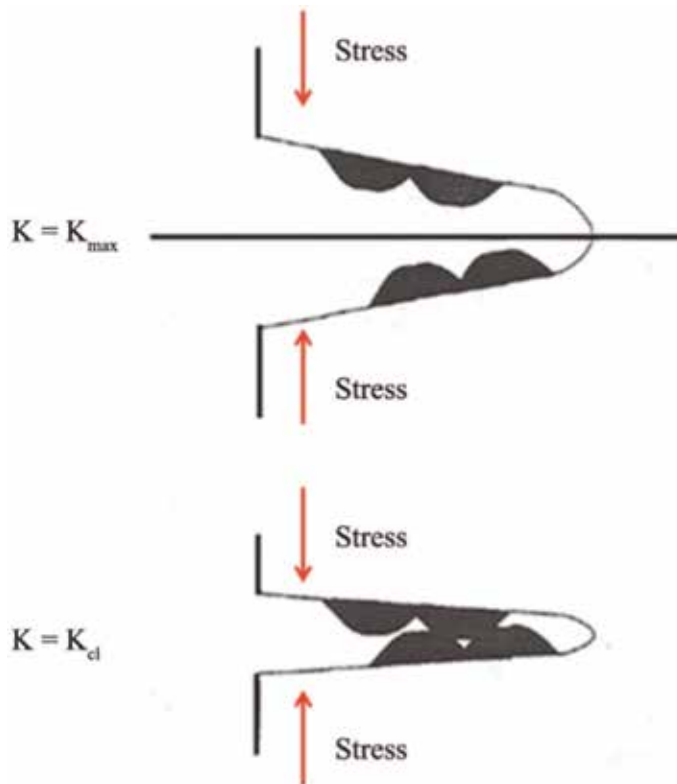


Figure 4. Schematic illustration of the wedging effect mechanism induced by corrosion products [6].

concentration of tension and to initiate a crack. If the layer of the repassivation reaction does not occur, the propagation of the crack is continuous [15].

Adversely, there is a possibility that some oxide residue caused by corrosion or salt crystals deposited in front of the crack will deform plasticize the crack tip [16] and with the decrease of the cyclic load the crack tip will not move, it is very thin and closed with a very small radius, as shown in **Figure 4**, and with increased static loading the crack opens elastically and becomes blunting. Under these conditions if the stress at the crack tip is less than or equal to the fracture stress, the crack will not propagate. The final result of the crack propagation rate is due to competition among all of these factors discussed [6].

During the fatigue corrosion tests, the crack growth is controlled by the maximum stress intensity factor K_{max} and the load ratio (R). Since the corrosive action is a time-dependent phenomenon, corrosion is most evident at low frequencies due to the greater integration between the environment and the material, increasing the embrittlement of the crack. Jones et al. [17], investigated the effect of corrosion on crack nucleation of the 2024-T3 alloy at various levels of fatigue crack growth and identified nucleation from pits that emerged during the corrosion process and concluded that the aggressive condition accelerates nucleation and crack growth in regions close to the threshold.

The action of chemical elements at the crack tip was studied by Wang [16] in corrosion fatigue tests with 3.5% NaCl in aluminum alloys. The authors verified there was a variation of the stress intensity factor at the threshold and increase in the fatigue crack growth rate (da/dN) and also concluded that the ratio between stresses has an influence in the region close to the threshold and as the ratio increases, the variation of the factor of intensity decreases.

2. Methods and materials

The material of this study is an aluminum-lithium alloy 2050 with the T84 heat treatment indicates that it was obtained through the solubilization steps with the temperature between 480 and 540°C, cold rolling, stress relief and natural aging hardening as shown in Ref. [7] and the chemical composition described in **Table 1**.

This material it was provided as plate with 800 × 550 × 50 mm from which they were extracted specimens for potentiodynamic polarization, tensile, toughness, fatigue and corrosion fatigue tests. Potentiodynamic polarization performed in triplicate followed the ASTM G61 [18] standard and the measurements were made in the range -1.2 to -0.2 V with a potential sweep rate of 0.5 mV s⁻¹ using a GAMRY reference 600 potentiostat/galvanostat, with 3.5% NaCl, aerated at 23°C resulted in the values of E_{corr} and j_{corr} obtained by the curve.

Tensile tests were carried out according to the ASTM E8/E8M [19] standard, using 05 specimens removed longitudinally to the sheet rolling direction, see **Figure 5**. The fracture toughness were carried out according to the ASTM E399 [20] standard in in MTS servo-hydraulic testing machine, with the clip gage to measure the crack size using the compliance technique and specimens with C(T)

Li	Cu	Mg	Mn	Zr	Ag	Si	Ti	Cr	Fe	Ni	Zn	Al
0.87	3.54	0.31	0.37	0.08	0.37	0.03	0.03	0.06	30*	0.02	<1*	Base

*ppm – part per million

Table 1.
 Nominal chemical composition of aluminum-lithium alloy 2050-T84 (wt%) [7].

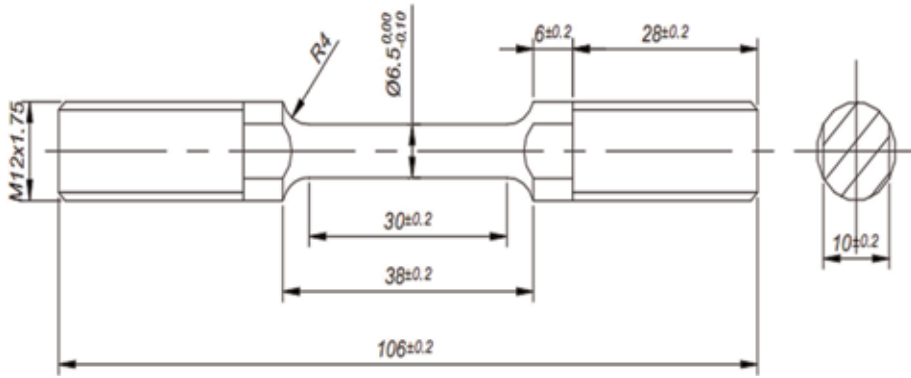


Figure 5.
Dimensions in millimeter of specimens to tensile test at room and cryogenics temperatures.

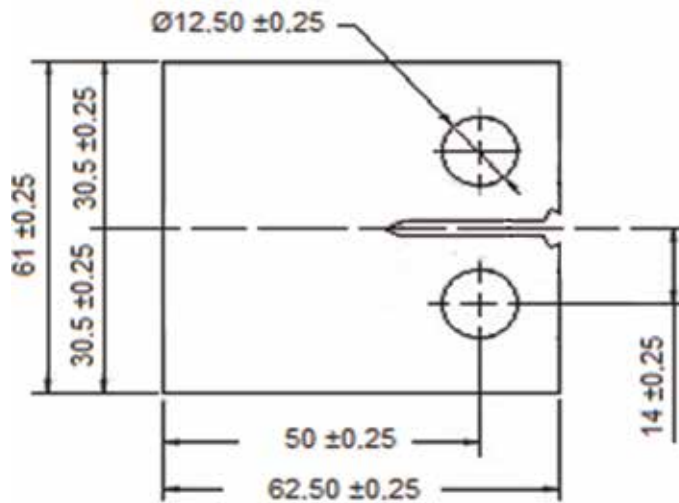


Figure 6.
Geometry and dimensions of specimens to fracture toughness tests at room and cryogenics temperatures (thickness (B) 25.4 mm).

geometry removed at direction TL and LT, thickness (B) 25.4 mm and geometry and dimensions shown in **Figure 6**. Both tests were conducted at 23 and -60°C at a chamber with liquid nitrogen.

Fatigue crack growth and corrosion fatigue were performed in air with a frequency of 15 Hz, 3.5 and 5% NaCl salt spray and with 3.5% NaCl aqueous saline solution. Specimens with C(T) geometry and extracts in the LT direction according to the specifications of ASTM E399 [20], thickness (B) 12.5 mm were tested in a MTS servo-hydraulic machine, according to the specifications of ASTM E647 [21], with sinusoidal waveform, extensometry and load ratio $R(K_{\min}/K_{\max})$, Poisson's coefficient if $\nu = 0.33$ and intensity gradient $C = -0.787$. From the region II of curves, the coefficient (m) of the linear regression line of the equation proposed by de Paris and Edorgan (Eq. (1)) was determined and the coefficient found by the extension of the straight line.

$$\frac{da}{dN} = C(\Delta K)^m, \quad (1)$$

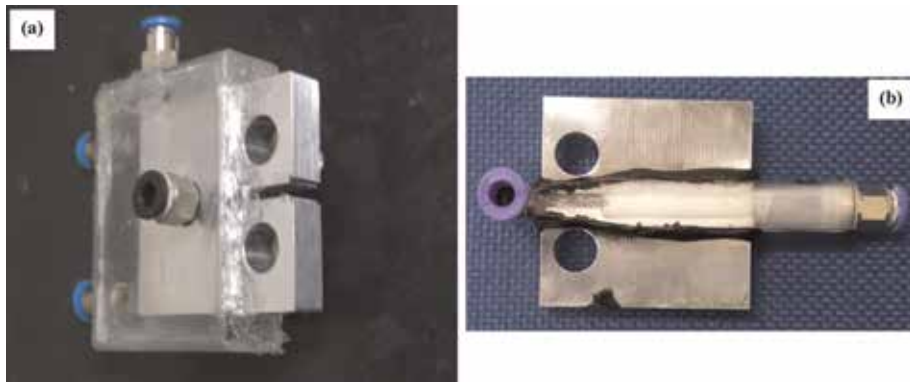


Figure 7. Fatigue crack growth specimens mounted for testing. In (a) for tests in salt spray with 3.5 and 5% NaCl (thickness (B) 12.5 mm). In (b) for tests in aqueous solution with 3.5% NaCl (thickness (B) 6 mm).

Where da/dN : fatigue crack growth rates, C: constant, ΔK : variation of the stress intensity factor, m : coefficient of the linear regression line of the equation proposed by de Paris and Edorgan.

The corrosion fatigue tests in 3.5 and 5% salt spray were conducted with C(T) specimens, see **Figure 6**, mounted inside fog cell coupled to a salt spray generation and conditioning device consisting of an air compressor, a reservoir of saline solution and nebulizer. **Figure 7(a)** shows the test specimen whose flow rate was 0.084 ml/s. The threshold values for air and salt spray tests were estimated from a linear regression of the fatigue crack growth rate as a function of the variation of the stress intensity factor ($da/dN \times \Delta K$), using at least 5 points between 10^{-6} and 10^{-7} mm/ciclo rates of and therefore, this procedure was adopted. A curve in the propagation stage II was obtained for the tests in aqueous saline solution, conducted with 1 Hz and a flow rate of 14.70 ml/s. The fog cell was positioned in such a way that integrity and the free circulation of saline solution were guaranteed by the inlet and outlet of the system as shown in **Figure 7(b)**.

3. Results

3.1 Potentiodynamic polarization

Results of potentiodynamic polarization shown in **Figure 8(a)** and from the curve shown in **Figure 8(b)** the E_{pit} . These results were listed and compared with the Al-Cu-Li-Mg 2198-T851 alloy as shown in **Table 2**.

Evaluating the results of E_{corr} , close values between both alloys, however, the j_{corr} of the 2050-T84 alloy is larger indicating that this material has a higher dissolution rate. As seen in **Figure 8(b)**, E_{pit} has been determined when the current value increases abruptly due to breakage of the insulating and passivating film, changing the orientation of the curve. When comparing two alloys, ensure that the 2050-T84 alloy has a slightly more negative volt than the 2198-T851 alloy, indicating that the alloy requires more energy yielded to begin the corrosion process and that although the alloy 2050-T84 require less amount of energy yielded, once the process is started the material is corroded with higher speed.

Presence of precipitates T_1 and T_2 and results in an inversion of the corrosion mechanism. First, these precipitates are anodic, resulting in the dissolution thereof

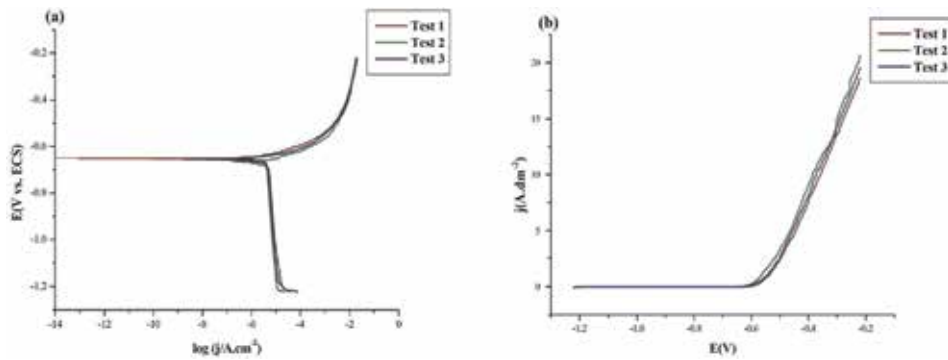


Figure 8. Potentiodynamic polarization plots obtained for aluminum-lithium in (a) corrosion potential; in (b) pitting potential.

Alloy	E (V)	Log J	E (pit)
2050-T84	-0.6581	-3.963	-0.601
2198-T851	-0.667	-2.711	-0.587

Table 2. Results obtained of potentiodynamic polarization for aluminum-lithium alloys 2198 T851 and 2050 T84.

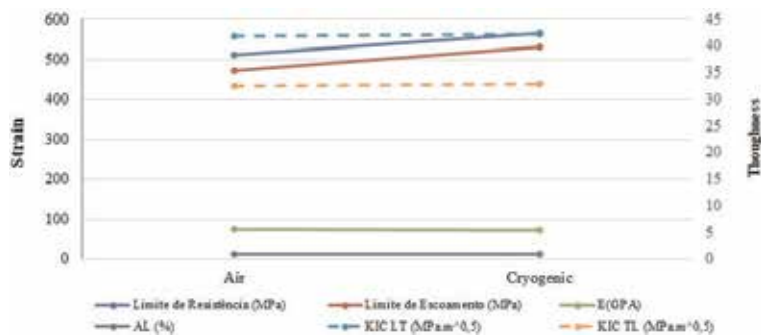


Figure 9. Tensile and toughness properties of alloy 2050-T84.

however, during the corrosion process, the Li is preferably dissolved, resulting in an increase in the amount of Cu on the surface. Consequently, the corrosion potential increases to more positive values, causing matrix dissolution [6].

3.2 Mechanical behavior and toughness of 2050-T84 alloy

Evaluation of the mechanical and tenacity behavior of high strength aluminum alloys is performed according to the types of stresses requested and operating temperature because they are materials used in structures of vehicles, pipelines, pressure vessels, aircraft fuselage and reservoir of storage hydrogen and oxygen liquids that are mechanically requested at ambient and/or cryogenic temperatures as described by reference [11]. Such applications are possible because of their low density, high specific strength, non-magnetism, stable microstructure, high elastic limit, and ductility retention.

Mechanical behavior and fracture toughness of the 2050-T84 alloy at the air at 23°C and cryogenic at -60°C are shown in **Figure 9**. Results showed no significant difference with temperature variation and can be attributed to the retention of ductility at cryogenic temperatures due to the face-centered cubic crystal structure (FCC) and the and the freezing of impurities with low melting point and rich in hydrogen (H), sodium (Na) and potassium (K), dispersed in the Al matrix [15].

Influence of temperature on fracture toughness K_{IC} was evaluated with specimens for analysis machined in TL and LT orientation. The values of the LT orientation are higher and reveal anisotropy of the material related to the characteristics of the recrystallized grains. Another important point that explains this concept is the crystallographic and morphological texture produced by the rolling, associated with the FZP and the distribution of the constituent particles in the material. These factors determine a preferred sense for the of intergranular crack growing and intrinsic plastic anisotropy of the material [16]. Additionally, when the stresses at the crack tip are high, the resistance to deformation is lower and provides the intergranular fracture. With lower ductility and high loading, the crack growing rapidly and the fracture toughness of the material decreases.

3.3 Fatigue crack growth and corrosion-fatigue

The plots are shown in **Figure 10** and was determined the coefficient found by the extension of the straight line as shown **Table 3**. Evaluating the threshold (ΔK_0) results for tests conducted in air and 3.5 and 5% salt spray where can be verified in the tests conducted in salt spray, the corrosive action is the most influential variable

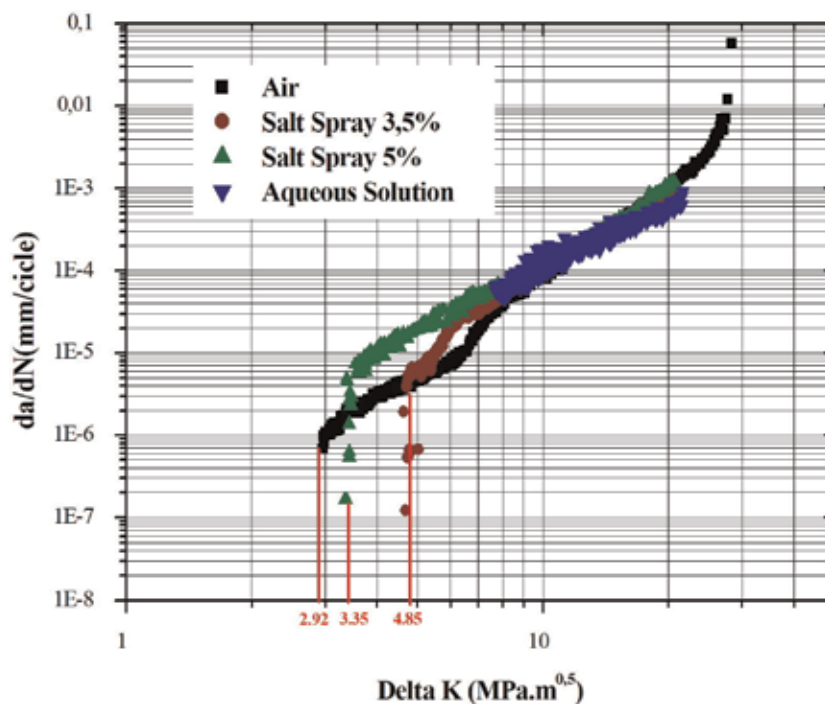


Figure 10. da/dN and ΔK curves for the 2050-T84 in air, salt spray at 3.5 and 5% of NaCl and aqueous solution with $R = 0.1$.

Condition	Paris	R ²	$\Delta K_0(MPa\sqrt{m})$
Air	$da/dN = 5.04E - 08(\Delta K)^{2.89}$	0.99	2.92
Salt spray 3.5%	$da/dN = 2.14E - 08(\Delta K)^{2.97}$	0.99	4.85
Salt spray 5%	$da/dN = 3.22E - 08(\Delta K)^{3.02}$	0.99	3.35
Aqueous solution	$da/dN = 7.19E - 08(\Delta K)^{2.41}$	0.97	—

Table 3.

Aluminum-lithium's constant C and m for the Paris-Erdogan equation and threshold.

due to the action of the environment the loading action overlaps and may increase or reduce the crack growth rate and the propagation rate. Observed that there is an acceleration of the propagation rate and as this value increases, the behavior in salt spray is similar to that of the behavior in air with a slight influence on the FCG of the test carried out in aqueous saline solution that presents a tendency to increase the critical stress intensity factor indicating improvement of the fracture toughness to the increase of the plastic zone at the crack tip.

Lowest threshold value was found with the test conducted in air. This is due to the common factors influencing the crack closure, such as the induction of plasticity, the formation of oxides in front of the crack and/or the roughness generated on the fracture surface, due to the severity of the loading. The curve obtained with a salt spray of 3.5% NaCl presented a higher threshold indicating a significant influence of the action of the oxides residues or salt crystals deposited on the surface of the crack that possibly induced the plastic deformation and avoided the embrittlement action of the fog. Considering that the 5% NaCl test curve accelerates discretely from the region close to the threshold, is possible that hydrogen embrittlement and anodic dissolution acted preferentially in the crack growth process, forming surface oxides and increasing the fatigue crack growth rate in the Paris region by reducing the threshold values.

In these conditions the fracture micromechanism occurred due to the movement of the slip bands that favored the rupture of the oxide layer and the surface of the metal was exposed to the saline solution making it anodic, whereas the regions adjacent to the sliding became cathodic forming an electrochemistry heaped load that, together with hydrogen embrittlement, accelerated crack growth and resulted in a lower threshold. Although no threshold result was obtained with tests conducted in aqueous saline solution, the final result of the crack propagation rate in this region is due to the competition between hydrogen embrittlement and the plasticity induced by crystals of salt and oxides, therefore it is a very complex micromechanism.

According to Wang [16], when the corrosion occurs simultaneously with fatigue loading, is expected to result in reduced material properties due to slip bands on the material, grain handling, free surface corrosion at the crack tip and crack closure, however, this did not occur with the 2050-T84 alloy. These results show that there is a clear difference of the threshold region when the tests were conducted in salt spray, however, for the Paris region regardless of the environment, the rates of FCG are quite similar. For Moreto et al. [6] this behavior occurs for two reasons, the first is related to the process of crack growth being purely mechanical because, a short time of interaction with the environment and the second reason is based on the concepts of crack closure, which when fully opened, the corrosion products formed within the crack lead to contact between the surfaces by raising the crack closing tension intensity factor.

4. Discussion

The 2050-T84 alloy with additional lithium was developed to have improved mechanical properties to be applied to aircraft structural components. The results of potentiodynamic potential shows that this alloy requires less amount of energy yielded for rupture of the oxide layer, however, once corrosion is started its evolution is rapid. Corrosion process occurred near precipitates T_1 and T_2 that increases to more positive values, causing matrix dissolution. However, the presence of the lithium to weight reduction and increase of mechanical resistance due to the appearance of precipitate T_1 and free zones precipitate. In cryogenic conditions, this material presents retention of ductility and fracture toughness, due to the face-centered cubic crystal structure (FCC) and the and the freezing of impurities with low melting point and rich in hydrogen (H), sodium (Na) and potassium (K), dispersed in the Al matrix.

Fatigue corrosion behavior of this material indicates that the competition between hydrogen embrittlement and the plasticity induced by salt crystals and cracking tip oxides are beneficial for FCG. This behavior occurs for to process of crack growth being purely mechanical and the corrosion products formed within the crack lead to contact between the surfaces by raising the crack closing tension intensity factor.

Acknowledgements

The authors would like to thanks CAPES for the financial support, EMBRAER supply the material and the Department of Materials, São Carlos School of Engineering, University of São Paulo for the use of the experimental facilities.

Author details

Maciel Carla Isabel dos Santos^{1*}, Bose Filho Waldek Wladimir²
and Ruchert Cassius Olívio Figueiredo Terra³

1 Paulista State University “Júlio de Mesquita Filho”, Bauru, SP, Brazil

2 São Carlos Engineering School, University of Sao Paulo, São Carlos, SP, Brazil

3 Lorena Engineering School, University of Sao Paulo, Lorena, SP, Brazil

*Address all correspondence to: carla.ism@usp.br

IntechOpen

© 2019 The Author(s). Licensee IntechOpen. This chapter is distributed under the terms of the Creative Commons Attribution License (<http://creativecommons.org/licenses/by/3.0>), which permits unrestricted use, distribution, and reproduction in any medium, provided the original work is properly cited. 

References

- [1] Fendoni A. The effect of post weld heat treatment on the corrosion behaviour of a Aa2050T34-Fsw [thesis]. Birmingham: University of Birmingham; 2009
- [2] Starke EA. Historical Development and Present Status of Aluminum-Lithium Alloys. Amsterdam: Elsevier Inc.; 2013
- [3] Ghali E. Corrosion Resistance of Aluminum and Magnesium Alloys: Understanding, Performance, and Testing. Hoboken: John Wiley & Sons; 2010
- [4] Jagan Reddy G, Wanhill RJH, Gokhale AA. Mechanical Working of Aluminum-Lithium Alloys. Amsterdam: Elsevier Inc.; 2013
- [5] Piascik RS, Gangloff RP. Environmental fatigue of an Al-Li-Cu alloy: Part I. Intrinsic crack propagation kinetics in hydrogenous environments. *Metallurgical Transactions A*. 1991; 22(10):2415-2428
- [6] Moreto JA et al. Environmentally-assisted fatigue crack growth in AA7050-T73511 al alloy and AA2050-T84 Al-Cu-Li alloy. *Materials Research*. 2015;18(6):1291-1297
- [7] Aerospace Material Specification. SAE AMS 4413—Aluminum alloy plate—3.5Cu-1.0Li-.40Mg-.35Mn-.012Zr (2050-T84) . West Conshohocken: SAE Aerospace International Group; 2007. pp. 1-5
- [8] Chemin AEA, Afonso CM, Pascoal FA, Maciel CI dos S, Ruchert COFT, et al. Characterization of phases, tensile properties, and fracture toughness in aircraft-grade aluminum alloys. *Material Design & Processing Communications*. 2019;1(4):1-13
- [9] Deng YL, Yang JL, Li SY, Zhang J, Zhang XM. Influence of Li addition on mechanical property and aging precipitation behavior of Al-3.5Cu-1.5Mg alloy. *Transactions of Nonferrous Metals Society of China (English Edition)*. 2014;24(6):1653-1658
- [10] ASM International. Handbook Committee. Properties and Selection: Nonferrous Alloys and Special-Purpose Materials. Vol. 2. Ohio: ASM International; 2001
- [11] Hafley RA, Domack MS, Hales SJ, Shenoy RN. Evaluation of Aluminum Alloy 2050-T84 Microstructure and Mechanical Properties as Ambient and Cryogenic Temperatures. Hampton, Virginia: National Aeronautics and Space Administration. Nasa Center for Aerospace Information; 2011. p. 81
- [12] Anderson TL. Fracture Mechanics Fundamentals and Applications. 3rd ed. New York: Taylor & Francis Group; 2005
- [13] Perng TP, Altstetter CJ. Hydrogen effects in austenitic stainless steels. *Materials Science and Engineering A*. 1990;129(1):99-107
- [14] Samui AB, Patankar AS, Rangarajan J, Deb PC. Study of polyaniline containing paint for corrosion prevention. *Progress in Organic Coatings*. 2003;47(1):1-7
- [15] Moreto JA, Gamboni OC, Marino CEB, Bose Filho W, Fernandes JCS, Rocha LA. Corrosion behavior of Al and Al-Li alloys used as aircraft materials. *Corrosion and Protection of Materials*. 2012;31(34):60-64
- [16] Wang R. A fracture model of corrosion fatigue crack propagation of aluminum alloys based on the material elements fracture ahead of a crack tip. *International Journal of Fatigue*. 2008; 30(8):1376-1386

[17] Jones K, Shinde SR, Clark PN, Hoepfner DW. Effect of prior corrosion on short crack behavior in 2024-T3 aluminum alloy. *Corrosion Science*. 2008;**50**(9):2588-2595

[18] ASTM. ASTM G61-Standard Test Method for Conducting Cyclic Potentiodynamic Polarization Measurements for Localized Corrosion Susceptibility of Iron, Nickel or Cobalt Based Alloys. West Conshohocken: ASTM International; 2010

[19] ASTM Standard. E8/E8M—16a Standard Test Methods for Tension Testing of Metallic Materials. West Conshohocken: ASTM International; 2016

[20] ASTM E399-12. Standard Test Method for Linear-Elastic Plane-Strain Fracture Toughness K_{Ic} of Metallic Materials. West Conshohocken: ASTM International; 2013

[21] ASTM International. ASTM E647—Standard Test Method for Measurement of Fatigue Crack Growth Rates. Finland: University of Oulu; 2015. pp. 1-49

Dynamic Effect in Fatigue on High-Deflection Structures

Raphael Paulino Goncalves

Abstract

There are a few kinds of structures that are created to fill in as a system, for example, springs, torsion bars, and axles, among others. They are structures, since they comprise of one single body, with no movement joints, however, with degrees of freedom, allowed by the mechanical compliance of the body. This aspect is extremely difficult to represent in durability assessment, since these structures-mechanisms are highly sensitive to dynamic effect of the system and the traditional method to predict fatigue (load history) is static and does not consider how the structure responds dynamically to the loading. In this chapter, we will study the fatigue behavior of two generic components, a classical structure and a structure-mechanism, using three different methods of calculation: load history (static), transient modal superposition (dynamic), and frequency domain modal superposition (dynamic). The objective is to demonstrate the differences between each calculation methodology due to the different ways each considers the dynamic effect.

Keywords: fatigue, structure, mechanism, deflection, dynamic, static, modal, superposition, transient, frequency, domain

1. Introduction

A mechanism is a system of multiple bodies assembled by one or many joints, with the objective to change a given input set of forces and moments to a desired output set of forces and moments. In a traditional mechanism, joints or kinematic pairs interface these bodies, giving relative movement between them. The combination between all bodies and joints produces the degrees of freedom of the component.

However, it is possible to design mechanisms with the desired degrees of freedom, without relying on joints and kinematic pairs. Compliant structures can produce relative movement depending on its design shape and the elastic characteristic of the material it consisted, by high mechanical strains.

A high mechanical strain implies that the absolute deflection of a body is “huge” when contrasted with its original form (without any deflection). Although there is no standard to characterize what is “huge,” it is very much acknowledged and broadly received as strains higher than 5% [1].

However, even with “huge” strains, the material of the structure must always be inside the elastic region; otherwise, the mechanical work can cause failure. This can be achieved by tuning the design accordingly to the material used. For example, rubbers in simple prismatic rectangles can achieve “huge” deflections in axial directions, while steel must be in a different shape as a coil spring.

The utilization of components dependent on mechanical strain rather than kinematic sets is basic in the industry. Torsion axles, coil springs, leaf springs, and stabilizer bars are a few models broadly embraced in business applications, for example, trains, planes, and vehicles.

Due to its larger compliance and, therefore, natural degrees of freedom, the mechanism-structures respond differently to dynamic inputs, usually presenting lower natural modes. This characteristic has an important influence in fatigue performance when the loading input is dynamic.

To measure this influence, we will study in this chapter the fatigue performance using three different approaches: static load history, transient modal superposition, and frequency domain modal superposition.

2. Methods and materials

2.1 Dynamic and static loading

An important definition to establish is the difference between static and dynamic loading. In theory, a load is static when time is not considered at its application and, therefore, inertial reaction of bodies is not part of the calculation. In practice, pure static load does not exist, since the load will require an amount of time to be applied at a body. In physical environment, a load can be considered static when not producing relevant inertial effects to the system.

Figure 1 shows two beams with the same length and section. The beams are constrained at the left extremity and have an actuator applying force at the right extremity. The actuators are applying the same F force in both beams; however, the actuator on the left is applying the F force in a large amount of time, which is not enough to produce any relevant inertial effect to the system and therefore can be considered static. The actuator on the right is applying the F force but in a small amount of time, which creates relevant inertial effects to the system and therefore can be considered dynamic.

2.2 The chosen structures and the method for analysis

The structure-mechanism chosen for our study in this chapter is a torsion axle and the pure structure a sub-frame. Both are structures of the same system, a commercial vehicle. The system “vehicle” was chosen here for a reason, to submit the two structures to the same loading condition. The geometries in this chapter are simplified

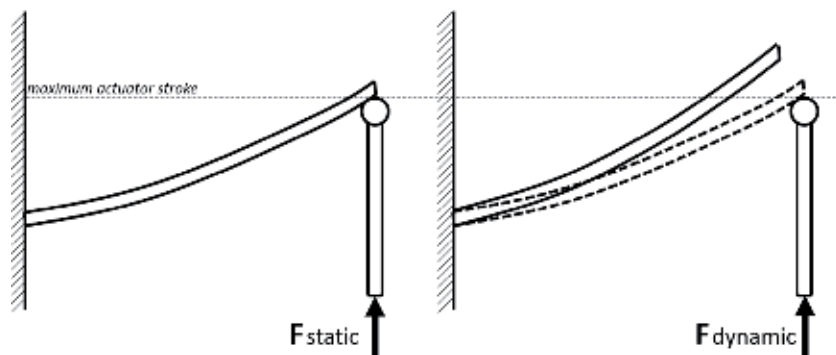


Figure 1. Comparison between two beams under a force with the same magnitude but different duration of application.



Figure 2.
Torsion axle—High displacement structure. The geometry was conceived using a topology optimization algorithm just for this study.



Figure 3.
Sub-frame—Pure structure. The geometry was also conceived using a topology optimization algorithm just for this study.

models created only for academic purposes, based on the same characteristics of the original models. They have the same mass, stiffness, and normal modes of the real torsion axle and sub-frame. The geometries were developed using topology optimization algorithms in order to maintain the same mentioned physical and mechanical properties. The models are conceived in finite element shell based (CQUAD4 elements) on structural analysis required in this chapter (stress/strain for fatigue and modal). The material considered for the structures is common steel, both with the same fatigue properties in order to make the comparisons of this study consistent (**Figure 2**).

The torsion axle is a common component present in commercial vehicles, used to support the entire suspension system (usually the rear suspension), since all suspension parts are attached to it, such as springs, shocks, and wheels. It performs also as a stabilizer beam, linking the left side to the right.

The sub-frame (**Figure 3**), also known as cradle, is a part of the vehicle used to attach the entire front suspension framework. It transmits all forces that came from the road from suspension to the body of the vehicle, and it has no relative movement between its points of interface. Uniquely in contrast to the torsion axle, it does not act as a stabilizer bar; in fact, in many vehicle designs, the sub-frame supports a stabilizer bar.

2.3 The load inputs

The loading conditions were obtained using a multi-body dynamic model (**Figure 4**) of the vehicle. This multi-body vehicle runs a rough road track made of Belgian blocks as the same way of a physical vehicle [2].

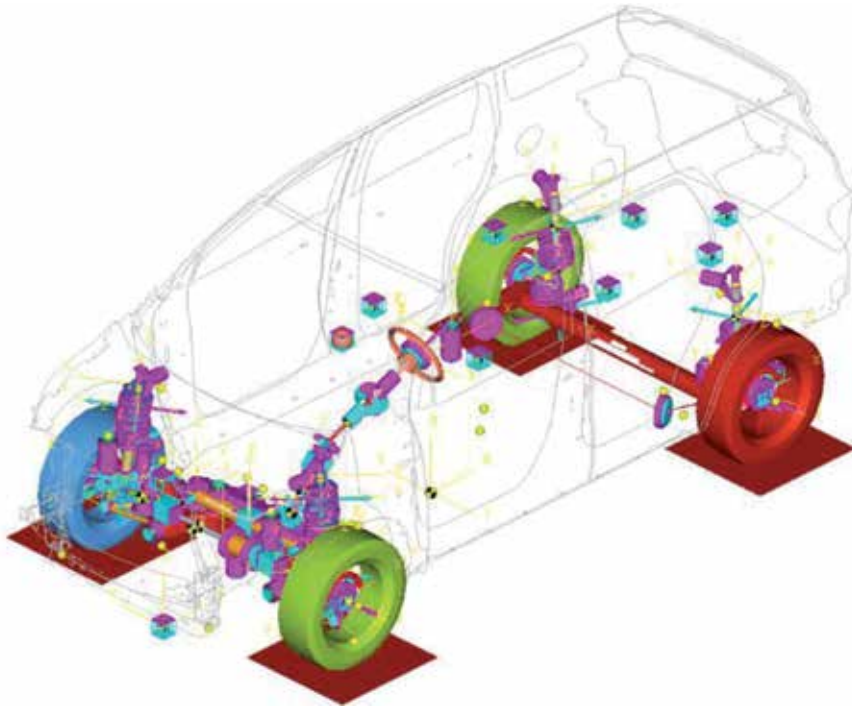


Figure 4.
Multi-body vehicle model used for loads acquisition.

The reason for using rough road Belgian blocks track is to submit both structures to a high-cycle fatigue, instead of a high-load low cycle. Also, this kind of track can produce dynamic loads as we already defined previously.

2.4 The dynamic effect

Before examining the durability behavior of the two structures, it is imperative to understand how they react dynamically to any set of loads. The study in this chapter proposes simply to contrast the distinctions of these two structures in a dynamic domain. For this reason, the modal analysis can, in a roundabout way, show how each structure reacts to dynamic conditions. The lower the mode, the



Figure 5.
Torsion axle: First normal mode of 33 Hz.

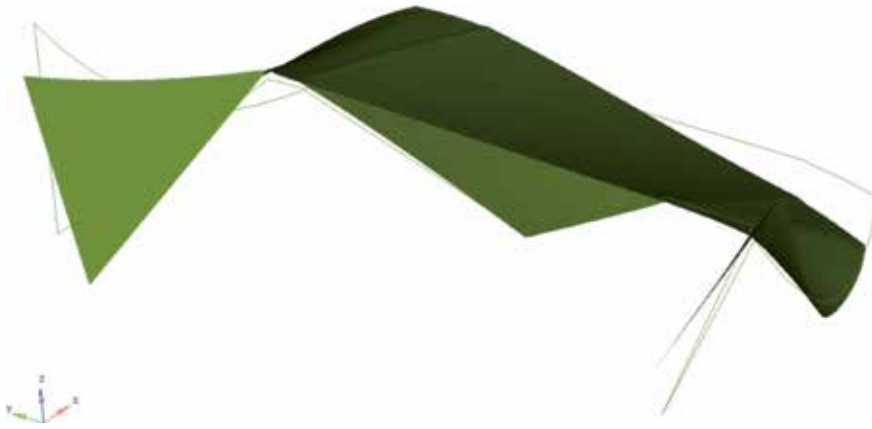


Figure 6.
Sub-frame: First normal mode of 283 Hz.

more probable the structure may enter in resonance during a given random load input. When this happens, the system starts to store kinetic energy and oscillate in a higher amplitude, affecting the durability performance.

The two structures presented in this chapter, the sub-frame (pure structure) and the torsion axle (mechanism-like structure), were submitted to a simple modal analysis using a standard commercial finite element analysis software. It is possible to see how each of them has different first natural modes (**Figure 5**).

Because of the lower compliance, the sub-frame has a higher first normal frequency than the torsion axle, 283 Hz (**Figure 6**) for the sub-frame and 33 Hz for the torsion axle. Until reaching the first normal frequency of the sub-frame (283 Hz), the torsion axle will have also other seven normal frequencies, representing seven different modes to resonate in a frequency sweep from 0 to 283 Hz, while the sub-frame will have only one mode.

2.5 Fatigue assessment

2.5.1 Process introduction

The fatigue assessment combines the stress/strain results with the repetitions from the event to calculate the damage/life. The stress/strain results in this chapter came from the finite element mode and the load magnitude, and repetitions came from the multi-body model running the Belgian block track.

2.5.2 Static load history approach

The durability analysis utilizing the load history approach is the less difficult and most customary method for computing fatigue of a given event. It is performed by applying a unitary static load to each interface point of the structure and after that, consolidating the results of stress/strain utilizing direct superposition (**Figure 7**).

The models are loaded with linear unit magnitude static loads (forces and moments) in each degree of freedom (6 in total), and the result is the elemental stress.

These stresses are then used by the fatigue solver. The elemental stress result is combined to calculate the fatigue damage of the event, in this case, the Belgian blocks.

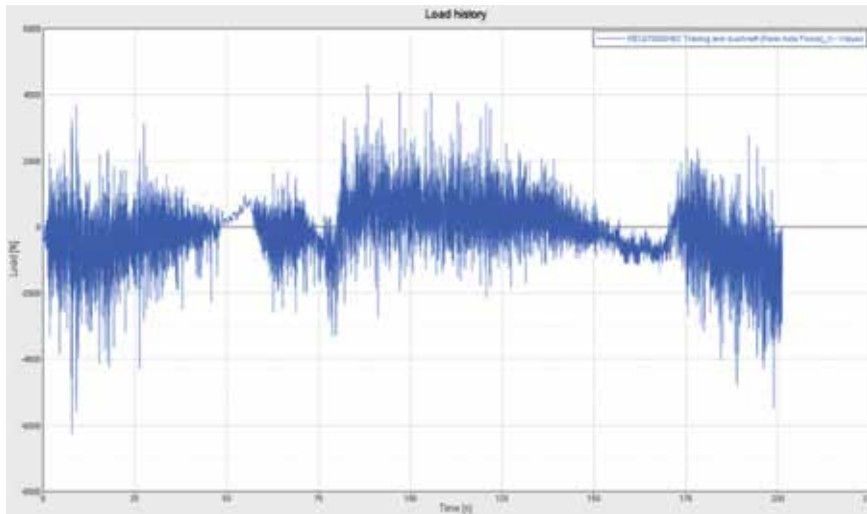


Figure 7.
Load history (load \times time) of one hard point of the torsion axle in the X-axis.

2.5.3 Transient and frequency domain modal superposition

The equation for dynamic motion of a system with linear single degree of freedom is given by the following:

$$M_{mass} \frac{\partial^2 x}{\partial t^2}(t) + C_{damping} \frac{\partial x}{\partial t}(t) + K_{stiffness} x(t) = L_{load}(t) \quad (1)$$

The output of the system is a rotation or displacement, in function of a time t . Eq. (1) is a second-order ordinary differential equation that can describe the motion of the system, by its acceleration (second derivative of displacement in respect of time), velocity (derivative of displacement in respect of time), and displacement.

The Duhamel integral can provide a solution for a given $L_{load}(t)$ for any instant greater than zero, i.e.,

$$x(t) = \int_0^t L_{load}(\tau) h(t - \tau) d\tau \quad (2)$$

Equation (2) can be rewritten, considering that $h(t)$ is the unit impulse (Dirac's delta) response function.

$$x(t) = L_{load}(t) * h(t) \quad (3)$$

Equation (2) will only have solutions in very simple systems. In general conditions, Eq. (2) will only have solutions when using algorithms to perform numerical integrations. These solutions for Eq. (2) should introduce a few volatilities that force the utilization of little steps of time (t). Moreover, the procedure can have a high cost (computational) regarding handling a large amount of time fractions (since the time step is small, a larger number of time fractions will be needed to represent the entire event). For this, two fundamental arrangements are known in general as modal transient response and direct transient response.

On the other hand, by taking the Fourier transform of Eq. (3) and using the concepts of spectral analysis [3–10], it is possible to simplify the time involution integration by multiplying in time domain, i.e.,

taking the Fourier transform of Eq. (3) permits simplifying the solution of the time convolution integration in a simple multiplication in frequency (ω) domain, i.e.,

$$X(\omega_{frequency}) = P(\omega_{frequency})H(\omega_{frequency}) \quad (4)$$

Here, the functions $L_{load}(t)$, $x(t)$, $h(t)$ are replaced by its Fourier transform pair, i.e., if considering $x(t)$,

$$X(\omega_{frequency}) = \frac{1}{2\pi} \int_{-\infty}^{\infty} x(t) e^{-i\omega_{frequency}t} dt \quad (5)$$

$$x(t) = \int_{-\infty}^{\infty} X(\omega_{frequency}) e^{i\omega_{frequency}t} d\omega_{frequency} \quad (6)$$

Here, $\omega_{frequency} = 2\pi f$, where $\omega_{frequency}$ and f are the linear and circular frequency variables, expressed, respectively, in [Hz] and [rad/s].

The last equation, Eq. (6), an inverse Fourier transform, and the normal Fourier transform in Eq. (5) can be numerically evaluated using FFT algorithms (fast Fourier transform) which are well-known and widely used.

The Fourier integrals in Eqs. (6), (5) will be valid, depending on the properties of the function considered. This occurs when the system in Eq. (1) is submitted to random loading inputs.

In the context of processes theory [2, 11–13], Eq. (4) must be used to handle input/output relationships when the system is submitted to random excitations.

A random event can be portrayed in frequency domain using spectral density functions. These functions, also known as power spectral densities (PSDs), along with the correlation functions are related by Fourier transform pairs.

The spectral density function $S_{xx}(\omega)$, for any stationary and ergodic random variable $x(t)$, is given by

$$S_{xx}(\omega_{frequency}) = \frac{1}{2\pi} \int_{-\infty}^{\infty} R_{xx}(\tau) e^{-i\omega_{frequency}\tau} d\tau \quad (7)$$

with

$$R_{xx}(\tau) = \int_{-\infty}^{\infty} S_x(\omega_{frequency}) e^{i\omega_{frequency}\tau} d\omega \quad (8)$$

where $R_{xx}(\tau)$ is the autocorrelation of $x(t)$, or in other words, it is the expected value $E[x(t)x(t + \tau)]$, i.e.,

$$R_{xx}(\tau) = \lim_{T \rightarrow \infty} \frac{1}{T} \int_0^T x(t)x(t + \tau) dt \quad (9)$$

and, Fourier transform is valid to be applied over $R_{xx}(\tau)$, in certain conditions.

Equation (1) can be rewritten in form of a matrix for multiple degrees of freedom (MDOF), i.e.,

$$[M_{mass}] \left\{ \frac{\partial^2 x}{\partial t^2}(t) \right\} + [C_{damping}] \left\{ \frac{\partial x}{\partial t}(t) \right\} + [K_{stiffness}] \{x(t)\} = \{L_{load}(t)\} \quad (10)$$

The multiple load input spectral density also can be expressed in a matrix form given by (where m is the number of load inputs)

$$[S_{pp}(\omega_{frequency})]_{m \times m} = \begin{bmatrix} S_{11}(\omega_{frequency}) & \cdots & S_{1m}(\omega_{frequency}) \\ \vdots & \ddots & \vdots \\ S_{m1}(\omega_{frequency}) & \cdots & S_{mm}(\omega_{frequency}) \end{bmatrix} \quad (11)$$

where the off-diagonal terms $S_{ij}(\omega_{frequency})$ are the spectral densities for the cross-correlation of the load inputs ($L_{load_i}(t)$ and $L_{load_j}(t)$) and the diagonal term $S_{ii}(\omega_{frequency})$ is the auto spectral density of $L_{load_i}(t)$.

Therefore, in the frequency domain, the input/output relation for the matrix system in Eq. (10) is (where n is the number of output response variables)

$$[S]_{n \times n}(\omega_{frequency}) = [H(\omega_{frequency})]_{n \times m} [S_{pp}(\omega_{frequency})]_{m \times m} [H(\omega_{frequency})]_{m \times n}^T \quad (12)$$

The “*” is the complex conjugate and T denotes transpose matrix.

The matrix $[H(\omega_{frequency})]$ is the transfer function matrix between the input loads and output response variables, i.e.,

$$[H(\omega_{frequency})] = \frac{1}{-[M]\omega_{frequency}^2 + i[C]\omega_{frequency} + [K]} \quad (13)$$

that can be calculated by standard FE solutions, as a unit modal frequency response. This transfer function becomes an input to the fatigue solver in frequency domain analysis process.

2.5.4 Conversion of loads from time to frequency domain

The loads needed for the frequency domain analysis must be created using a Fourier transformation. Customarily, the correct interpretation of the frequency domain approach depends upon three premises (stationarity, Gaussian, random) completely met. In any case, some flexibility is conceivable. Besides, there are methodology that can be applied to break down nonstationary (and nonrandom, non-Gaussian) data into shorter subcases that do conform in an adequate manner.

The loading channels on both strictures are comprised of the number of hard points (where the structure interfaces with the environment, like constrains and load inputs) times the degrees of freedom. The torsion axle for example has 48 loading channels, 8 hard points (as can be seen in **Figure 8**, hard points are represented as yellow circles) times 6 degrees of freedom. For the frequency domain approach to deal with the correlation between channels, the purported cross-PSD's are additionally required. Each channel requires a real and imaginary PSD (together they compose the complex cross-PSD), and these are observed in **Figure 9**.



Figure 8.
The hard points of the torsion axle.

	channel 1	channel 2	channel 3	channel 4	channel 5	channel 6	channel 48
channel 1	PSD_1-1	PSD_1-2	PSD_1-3	PSD_1-4	PSD_1-5	PSD_1-6	PSD_1-7	PSD_1-8	PSD_1-9	PSD_1-48
channel 2	PSD_2-1	PSD_2-2	PSD_2-3	PSD_2-4	PSD_2-5	PSD_2-6	PSD_2-7	PSD_2-8	PSD_2-9	PSD_2-48
channel 3	PSD_3-1	PSD_3-2	PSD_3-3	PSD_3-4	PSD_3-5	PSD_3-6	PSD_3-7	PSD_3-8	PSD_3-9	PSD_3-48
channel 4	PSD_4-1	PSD_4-2	PSD_4-3	PSD_4-4	PSD_4-5	PSD_4-6	PSD_4-7	PSD_4-8	PSD_4-9	PSD_4-48
channel 5	PSD_5-1	PSD_5-2	PSD_5-3	PSD_5-4	PSD_5-5	PSD_5-6	PSD_5-7	PSD_5-8	PSD_5-9	PSD_5-48
channel 6	PSD_6-1	PSD_6-2	PSD_6-3	PSD_6-4	PSD_6-5	PSD_6-6	PSD_6-7	PSD_6-8	PSD_6-9	PSD_6-48
channel 7	PSD_7-1	PSD_7-2	PSD_7-3	PSD_7-4	PSD_7-5	PSD_7-6	PSD_7-7	PSD_7-8	PSD_7-9	PSD_7-48
channel 8	PSD_8-1	PSD_8-2	PSD_8-3	PSD_8-4	PSD_8-5	PSD_8-6	PSD_8-7	PSD_8-8	PSD_8-9	PSD_8-48
channel 9	PSD_9-1	PSD_9-2	PSD_9-3	PSD_9-4	PSD_9-5	PSD_9-6	PSD_9-7	PSD_9-8	PSD_9-9	PSD_9-48
...
...
...
channel 48	PSD_48-1	PSD_48-2	PSD_48-3	PSD_48-4	PSD_48-5	PSD_48-6	PSD_48-48

Figure 9.
 Torsion axle. PSD matrix for event 1.

3. Results

As can be observed in durability results plotted (damage) on the sub-frame, the performances were practically indistinguishable among the three techniques. Because of the low compliance of the structure, the dynamic impact of the loading input is low, and accordingly, all techniques merged to an akin answer, as far as damage magnitude, yet additionally, damaged regions.

For the torsion axle, there was a bigger contrast, because of the dynamic influence. Its mechanism-like characteristic has a higher structural compliance, presenting higher deflections and relative movements between the interface points when submitted to loading. Also, its lower stiffness properties induce it to be more susceptible to dynamic influence as already explained. Due to that, a contrast between the static and dynamic durability assessment can be observed. It is usually hard to decide the significance of variations in fatigue results, for instance, if we accept we are managing a material that has a correspondent stress/strain-life slant of around 10, then we can convert the life or damage differences into stress/strain difference. In other words, we can assume the following relationship:

$$\text{Damage variation} = (\text{damage to be compared} / \text{damage baseline})^{-1}$$

For instance, for the torsion axle, the static damage result is 38, and transient in frequency domain is 68, and in transient time domain is 198. If we consider the static as a baseline (since it is the lowest value), we can expect the following damage variation: 6% increase of damage for transient frequency domain and 11% increase of damage for transient time domain when compared to static.



Figure 10.
Static load history damage result plot. Maximum damage = 38.



Figure 11.
Time domain modal superposition damage result plot. Maximum damage = 198.



Figure 12.
Frequency domain modal superposition damage result plot. Maximum damage = 68.

When calculating damage using the static method, the dynamic effects are not considered, and accordingly, the result is the lowest among the other methods introduced. The transient method in time domain shows the higher damage.



Figure 13.
Static load history damage result plot. Maximum damage = 119.



Figure 14.
Time domain modal superposition damage result plot. Maximum damage = 116.



Figure 15.
Frequency domain modal superposition damage result plot. Maximum damage = 92.

The most damaged regions are also different among the three approaches on the torsion axle. It is possible to observe that the center was the most damaged region in all methodologies; however, the most critical elements are different. This suggests that these various approaches can point various conclusions as far as magnitude as well as most damaged regions (**Figures 10–15**).

4. Discussion

This chapter does not propose to conclude which methodology is the best. The static approach is the easiest method to numerically foresee the durability of a model; if the loading history is simple (cyclic with frequency below the first natural mode) or the structure is stiff (non-compliant, like the sub-frame), the static technique can achieve results with a similar quality as the two other dynamic approaches. But, if the loading history is complex (random, like the one utilized in this examination) or the structure is compliant (like the torsion axle), the static approach may not be enough to correctly calculate the durability of the structure, since it does not consider the dynamic effects.

However, during the development of any structure, it is common to find scenarios where it is difficult to determine if a signal is simple enough or a structure is stiff enough to rely only to the static methodology. In this chapter, the structures adopted as examples were previously known how to behave, but this may not be the case in most practical applications, since there is no formula or rule to guarantee the use of a specific approach. A modal analysis of the structure and a deep analysis of the signal may help to point a direction of which methodology to choose, static or dynamic, but still cannot conclude by its own.


When comparing the two dynamic methods, the transient modal superposition approach gave more conservative results in the example presented in this chapter. However, the underlying change in stress to cause the contrast is only 11%, and this could be by statistical scatter in the underlying random process. In this way, it is not conclusive which approach is more appropriate for this sort of structure. It has been reported that the frequency domain approach can be performed with considerably less computational resources and so could be preferred for large models [14].

Author details

Raphael Paulino Goncalves
General Motors, São Caetano do Sul, Brazil

*Address all correspondence to: raphael.p.goncalves@gmail.com

IntechOpen

© 2019 The Author(s). Licensee IntechOpen. This chapter is distributed under the terms of the Creative Commons Attribution License (<http://creativecommons.org/licenses/by/3.0>), which permits unrestricted use, distribution, and reproduction in any medium, provided the original work is properly cited. 

References

- [1] Altair University, Introduction to Nonlinear Finite Element Analysis using OptiStruct, Altair; 2018
- [2] Zhang Y, Stawiarski T, Subramanian M, Yung D, Farahani AD, Zhang X. Full Vehicle Finite Element Model 4-Post Durability Analysis. SAE Technical Paper 2005-01-1402. General Motors Corporation, Engineering Technology Associates, Inc. 2005. <https://www.sae.org/publications/technical-papers/content/2005-01-1402/>
- [3] Leistein P. Frequency Domain Fatigue Analysis of Exhaust Systems. SAE; 2018
- [4] Thesing T, Bishop N. Modern Methods for Random Fatigue of Automotive Parts. SAE Technical Paper 2016-01-0372; Hella KGaA Hueck and Co., CAEfatigue, Ltd; 2016. DOI: 10.4271/2016-01-0372
- [5] Newland D. An Introduction to Random Vibrations, Spectral & Wavelet Analysis. 3rd ed. Dover Publications; 2005
- [6] Maymon G. Structural Dynamics and Probabilistic Analysis for Engineers. Butterworth-Heinemann; 2008
- [7] Karadeniz H. Stochastic Analysis of Offshore Steel Structures. Springer Series in Reliability Engineering. London: Springer-Verlag; 2013
- [8] Ferreira W, Meehan T, Cardoso V, Bishop N. Comparative Study of Automotive System Fatigue Models Processed in the Time and Frequency Domain. SAE Technical Paper 2016-01-0377. Ford Motor Company, Valdir Cardoso, CAEfatigue, Ltd.; 2016. <https://doi.org/10.4271/2016-01-0377>
- [9] Bishop, Neil WM, Sherratt F. Finite Element Based Fatigue Calculations. Glasgow: NAFEMS Ltd; 2000
- [10] Bishop N, Murthy P, Sweitzer K, Kerr S. Time vs Frequency Domain Analysis For Large Automotive Systems. SAE Technical Paper 2015-01-0535. Booz Allen Hamilton Inc., CAEfatigue, Ltd; 2016. DOI: 10.4271/2015-01-0535
- [11] Bishop NSF. Fatigue life prediction from power spectral density data. Part 1, traditional approaches and part 2, recent developments. *Env. Eng.* 1989;2:2-11
- [12] Bishop N, Kerr S, Murthy P, Sweitzer K. Advances Relating to Fatigue Calculations for Combined Random and Deterministic Loads. SAE International Paper 2014-01-0725; 2014. <https://doi.org/10.4271/2014-01-0725>
- [13] Bishop N, Kerr S, Murthy P, Sweitzer K. Advances relating to fatigue calculations for combined random and deterministic loads. In: 13th International ASTM/ESIS Symposium on Fatigue and Fracture Mechanics (39th National Symposium on Fatigue and Fracture Mechanics). Jacksonville; 2013
- [14] CAEfatigue VIBRATION (CFV) User Guide & Verification Manual (Release 3.0), UK: CAEfatigue Limited; 2016

Modeling of Creep Deformation and Creep Fracture

Qiang Xu and Zhongyu Lu

Abstract

This chapter reports the recent progresses in (1) the development of a modified hyperbolic sine law able to depict the minimum creep strain rate over a wider range of stress levels; (2) the development of the creep fracture criterion and model based on the cavity area fraction along grain boundary calibrated with the most representative and comprehensive cavitation data obtained from X-ray synchrotron investigation; and (3) the development of mesoscopic composite approach modeling of creep deformation and creep damage. The first progress facilitates to overcome the difficulty in creep deformation modeling caused by stress breakdown phenomenon; the second progress is of a really scientifically sound and fundamental new approach, first in the world; the third progress provides the concept and tool, at the appropriate size scale, for the modeling of the creep deformation and creep fracture. They all contribute to the specific knowledge and new methodology to the topic area. Furthermore, it is expected that cavitation fracture modeling methodology reported here will find use in the analysis and modeling of other types of failure such as ductile and fatigue failure. This chapter presents an excellent example of interdisciplinary collaborative research and it advocates further such collaboration in its conclusion.

Keywords: creep stress breakdown, creep strain and stress law, Xu's modified hyperbolic sine law, creep cavitation damage and fracture model, X-ray synchrotron cavitation; mesoscopic composite type modeling

1. Introduction

1.1 General

Creep damage is one of the life-limiting factors for high-temperature components. A sound scientific understanding and an accurate mathematical description of the creep deformation and creep fracture are of great interest to and a challenge for the materials and structural integrity research communities and high-temperature industries.

It is generally understood and accepted that for the majority of metals and alloys, creep cavitation at grain boundary is the cause for the creep fracture [1, 2].

Creep continuum damage mechanics (CDM) has been developed to model creep deformation and creep fracture, where internal variables were introduced to depict the macroscopic behavior and the cavitation is incorporated in an average, smeared-out manner.

High Cr alloys is one of the alloys developed for and utilized in power generation industry. So, they have been chosen for the research, and progress made with them will be reported here. Additionally, copper-antimony alloy is used in the illustrative example of the mesoscopic composite modeling of creep deformation and fracture due to the unavailability of the micro-mechanical constitutive equation for high Cr alloys. Although the examples of progress reported here are based on the specific material, the methodology is generic and not material dependent.

1.2 The problem

In the development of and particularly in the characterization of high-temperature structural materials, the accelerated creep testing (short-term) may be conducted; then the result might be extrapolated for long-term service condition (say 100,000 hours). Normally, this approach is not reliable, as this microstructure may progressively degrade with often unexpected consequences for long-term creep performance under lower applied stress. Such phenomenon is called stress breakdown; it profoundly exists in high Cr alloys [3–7].

Ennis et al. [3] found that the Norton stress exponent n was found to be 16 for the stresses of above 150 MPa at 600°C and above 110 MPa for 650°C, and an n value was 6 below these stresses. A selection of quantitative presentation of the dependence of the minimum creep strain rate, creep lifetime, and strain at failure on the stress level can be found in [3]. Furthermore, Lee et al. [4] found (1) the stress exponent for rupture life to be decreased from 17 in short-term creep to 8 in long-term creep for the ASTM grade 92 steel crept at 550–650°C for up to 63,151 h, (2) the change of fracture mechanisms with stress level, and (3) creep cavities nucleated at coarse precipitates of Laves phase along grain boundaries.

It can be seen that (1) a wider range of stresses, particularly the lower stress level, must be considered; (2) there is a change of creep deformation mechanism and possible creep damage mechanism under the different stress level. Currently, there is no adequate and accurate data to characterize the creep cavity nucleation, growth, and coalescence under lower stress.

1.3 Current creep cavity damage modeling

In an attempt to model the long-term creep behavior, Yin et al. [8] have proposed a phenomenological relationship between the creep cavity damage and creep strain, which departed from the firm and well-known mechanism-based relationship of Dyson [9]. The relevant equations are listed below for completeness:

Dyson [9]:

$$\dot{D}_n = \frac{k_N}{\varepsilon_{f_u}} \dot{\varepsilon} \quad (1)$$

Yin et al. [8]:

$$\dot{D}_n = A \varepsilon^{B'} \dot{\varepsilon} \quad (2)$$

where A is the creep cavity damage coefficient, and it is assumed that it does not change with stress, it changes with temperature.

Yin's approach cannot be extrapolated into a lower stress level than it has been calibrated according to Yang et al. [10] as a constant value of A is not able to depict the stress breakdown phenomenon.

Basirat et al. followed Yin's approach but allowed the cavity damage coefficient to be stress level dependent, in the following form [11]:

$$\dot{D}_n = A\dot{\epsilon}\epsilon^{0.9} \quad (3)$$

However, an unexpected abnormal variation of the value of A with stress level occurred which is shown in **Table 1** and graphically in **Figure 1** [12]. Due to the lack of a trend with stress level, it is hard to use them in prediction with confidence. The concept of creep cavity damage coefficient to be stress level dependent had been introduced by the first author in 2003 [13] for low Cr alloy creep damage modeling where no such abnormality occurred.

Hence, the phenomenological modeling of creep cavity damage for high Cr alloy is not satisfactory.

Furthermore, the methodology, based on the isochronous surface concept only, for the generalization of a set of uniaxial creep damage constitutive equations into a set of multiaxial version is conceptually flawed [14–16]. Though the creep deformation consistence has to be included, this has not been very well appreciated by the majority of research community, even in the published review type of articles. Progress can be found only in very limited publications, for example, the original one [16, 17] and the more recent one [18].

1.4 Opportunity and research progress

1. Examination and development of the law of the minimum creep strain rate and a wider range of stress levels. The development and application of Xu's modified hyperbolic sine law will be reported with an illustrative example.
2. Modeling of creep cavity damage and creep cavity fracture.

Parameter	$\sigma = 80\text{MPa}$	$\sigma = 100\text{MPa}$	$\sigma = 150\text{MPa}$	$\sigma = 200\text{MPa}$	Temperatures[°C]
A	57	83	1	112	600
A	57	83	47	145	650
A	57	83	113	145	700

Table 1.
 The variation of cavitation coefficient A [11].

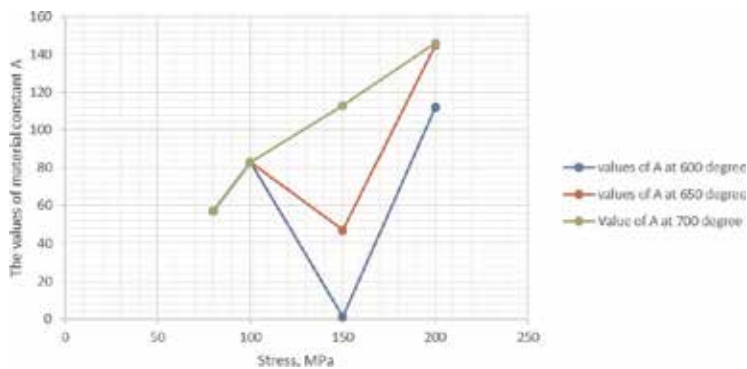


Figure 1.
 The variation of creep cavity damage coefficient A with different stress and temperature [12].

In 2013, the first author noted that the available creep cavitation data is produced with X-ray synchrotron technique by materials scientists. The X-ray synchrotron is a very advanced technique, and it is able to produce a detail and un-destructive, hence more presentative, information over a small volume. This is a very significant advance for the characterization of creep cavitation. Hence, it was the author' view [19] that such information about cavitation should be very valuable for the modeling of creep cavity damage and fracture. Such breakthrough in modeling of creep cavity damage and fracture will be reported with selected examples.

3. The mesoscopic composite approach modeling of creep deformation and damage

Furthermore, the authors [15] have observed that that the current creep continuum damage mechanics operates at macroscopic level is of phenomenological suffering an ambiguity in the depicting of the creep deformation and creep cavity damage and fracture [15], hence, concluded that a mesoscopic composite approach modeling is necessary and better. In this new approach, the grain and grain boundary will be separately presented in space and in property (constitutive equations) to specifically reflect the creep deformation processes and creep damage processes and the ultimate creep fracture. The initial progress will be reported in this chapter.

4. This chapter ends with discussion, conclusion, and suggestion for future work which advocates closer interdisciplinary collaboration.

2. Methods and materials

2.1 The modified hyperbolic sine law for minimum creep strain rate and stress law

Xu's modified hyperbolic sine law is given as [12]:

$$\dot{\epsilon}_{min} = A \sinh(B\sigma^d) \quad (4)$$

It was originally proposed by the first author for low Cr alloy [12], and its application was very successful [12].

Other existing and commonly used laws for high Cr P91 are listed **Table 2**; their suitability was examined first prior to the adoption of Xu's modified law.

The specific material used here is P91 (9Cr-1Mo-V-Nb). The experimental data of the minimum creep strain rate over a range of stress levels was taken from the published creep data [20] produced by the National Institute for Materials Science (NIMS), Japan.

Power law	$\dot{\epsilon}_{min} = A\sigma^n$
Linear + power law	$\dot{\epsilon}_{min} = A\sigma[1 + (B\sigma)^n]$
Hyperbolic sine law	$\dot{\epsilon}_{min} = A \sinh(B\sigma)$
Xu' modified hyperbolic sine law	$\dot{\epsilon}_{min} = A \sinh(B\sigma^d)$

Table 2.
The list of creep laws for the minimum creep strain rate and stress.

2.2 Creep cavity fracture model

2.2.1 Method

The cavitated area fraction, w , along the grain boundaries is given as [1]:

$$w = \int \pi R^2 N(R, t) dR \quad (5)$$

$$w = I(\alpha, \beta, \gamma) A_2 A_1^{\frac{2}{\beta+1}} t^{\alpha+\beta+\frac{(1-\alpha)(\beta+3)}{\beta+1}} \quad (6)$$

where the dimensionless factor $I(\alpha, \beta, \gamma)$ is definite integral

$$I = \pi(1 + \beta)^{(\beta+3)/(\beta+1)} \int_0^U x^{\beta+2} [1 - (1 - \alpha)x^{\beta+1}]^{(\alpha+\beta)/(1-\alpha)} dx \quad (7)$$

and the cavity size distribution function, $N(R, t)$, represents the number of voids with radii between R and $+dR$ in the time interval t and $t + dt$:

$$N(R, t) = \frac{A_2}{A_1} R^\beta t^{\alpha+\gamma} \left(1 - \frac{1 - \alpha}{1 + \beta} \frac{R^{\beta+1}}{A_1 t^{1-\alpha}} \right)^{(\alpha+\gamma)/(1-\alpha)} \quad (8)$$

if the non-station growth rate of the cavity radius and the nucleation rate of cavity are:

$$\dot{R} = A_1 R^{-\beta} t^{-\alpha} \quad (9)$$

$$J^* = A_2 t^\gamma \quad (10)$$

where the unknown constants $A_1, A_2, \alpha, \beta,$ and γ are material cavitation constants.

It is emphasized and concluded here that (1) if the values of creep cavitation constants $A_1, A_2, \alpha, \beta,$ and γ are known, the cavitated area fraction, w , could be determined quantitatively and (2) a critical value for $w_f = \frac{\pi}{4}$ for coalesce could be used as fracture criterion.

2.2.2 Determination of cavitation constants

The method for the determination of the material cavitation constants, $A_1, A_2, \alpha, \beta,$ and γ , depends on the available experimental cavitation data [12].

The nucleation rate and growth rate can be directly determined if such data is directly available.

Based on qualitative analysis for 3D tomographic reconstructions of the distribution voids of E911 and P91 steel, a theoretically derived function of taking into account nucleation and growth of voids [1] was used to evaluate the experimental obtained histograms; the distribution equation (8) proposed by Riedel fitted well with the histogram density functions of void equivalent radius R of E911 and P91 [21], while the identical value of $\beta = 1.95 \pm 0.05$ (closely to 2) is characterized for the constrained diffusional mechanism of void growth and $\alpha = 1$ characterized for continuum cavity nucleation [21, 22].

Cavity histogram is often used by material scientists, and it can be used to determine the values of these five or part of these constants, through either optimization method or trial and error method.

2.2.3 Explicit creep cavity damage fracture model

The explicit creep fracture model can be derived with the given values of creep cavitation constants [12].

For the given values of $\alpha = 1$, $\beta = 2$, and $\gamma = 1$ for P91 [12], Eq. (5), w , is simplified as:

$$w = \pi \times \frac{3}{5} \times 3^{\frac{2}{3}} \times U^5 \times A_1^{2/3} A_2 \times t^{1+\gamma} \quad (11)$$

And further,

$$w = U' \times t^{1+\gamma} \quad (12)$$

where $U' = \pi \times \frac{3}{5} \times 3^{\frac{2}{3}} \times U^5 \times A_1^{2/3} A_2$; it is termed as creep lifetime coefficient. Insert $\gamma = 1$ in Eq. (12); the creep cavity damage function is:

$$w = U' \times t^2 \quad (13)$$

$$w_f = U' \times t_f^2 \quad (14)$$

The creep fracture is assumed to occur when the area coverage attains a critical value, denoted by w_f . The critical value, w_f , will be chosen for as $w_f = \frac{\pi}{4}$, since regularly spaced round cavities touch each other if $w_f = \frac{\pi}{4}$ [1].

2.2.4 Application for lifetime prediction over a wider stress range

This section investigates such dependence on stress. The method is stated as:

1. The creep cavity fracture lifetime is fully described by Eq. (11), where the creep cavitation coefficients are deemed stress level dependent.
2. If the creep cavity coefficients are known at different stress levels, then there is a simple ratio of the two creep cavity fracture lifetimes.
3. Furthermore, if the trend of the values of the creep cavity coefficients with stress is known, then the above simple ratio relationship could be used for lifetime extrapolation.
4. Approximated method for the determination of A_1 and A_2 : If α , β , and γ are known, then the values of A_1 and A_2 can be conveniently obtained by inversely using Eqs. (9) and (10) with known total number of cavity, maximum radius of cavity, and lifetime, assuming that there is no incubation time for the cavity nucleation.

2.3 Mesoscopic composite approach modelling

2.3.1 Concept development: mesoscopic composite model

1. The current creep continuum damage mechanics operates at a macroscopic level with ambiguity in the depicting of the creep deformation and creep damage; hence a mesoscopic level composite model is necessary.

2. In the mesoscopic model, the grain and grain boundary will be separately presented in space and in constitutive equations.
3. The specific creep damage constitutive equations for the grain and grain boundary need to be developed; this, in turn, requires property characterization for grain and grain boundary separately.
4. Grain element: conventional 2d or 3D element can be directly chosen and used here. Grain boundary element: interface type of element, developed for fracture mechanics, can be chosen and used.
5. Micro-mechanics-based grain boundary model [23, 24].

This micro-mechanical-based smeared-out grain boundary element for of copper-antimony alloy [23, 24] has been chosen in the current development, as there is not that much choice. The main contents are:

1. Grain boundary nucleation: Dyson's empirical equation [25] has been consulted.
2. Cavity annihilation: probabilistic description of crack annihilation [26] has been adopted.
3. Cavity growth: constrained cavity growth model [1, 27] adopted.
4. Grain boundary sliding: Ashby viscosity model [28] adopted.
5. Creep fracture criterion when the cavity area fraction along grain boundary reached 0.5, experimentally observed by Cocks and Ashby [29]. In this model, the grain boundary sliding has been considered for the deformation, but not for the cavity nucleation.

2.3.2 Grain boundary element

The GB displacement jump at a normal direction can be obtained by the model which is developed by Markus Vöse [30]. It takes into account nucleation, growth, coalescence, and sintering of multiple cavities and can be written as (**Figure 10**) [30, 31]:

$$\frac{d\beta}{dt} = \frac{3\beta}{2\bar{\rho}} (\dot{\alpha}_p - \dot{\alpha}_a) + \sqrt{\bar{\rho}} \sqrt[3]{36h(\psi)\pi\beta^2} \frac{d\dot{a}}{dt}, \quad (15)$$

$$\frac{d\dot{\rho}}{dt} = \dot{\alpha}_p(1-f) - \dot{\alpha}_a \quad (16)$$

$$\dot{\alpha}_a = x_3 \cdot 8\pi\bar{\rho}^2 \dot{a} \frac{d\dot{a}}{dt}, \quad (17)$$

$$\frac{d\dot{a}}{dt} = x_1 \cdot \frac{2\dot{D}_{gb} [1 - \dot{a}_{tip}(\dot{a}) \cdot (1 - x_2\omega)]}{h(\psi) \dot{a}^2 \cdot q(x_2\omega)}, \quad (18)$$

$$\omega = \sqrt[3]{\frac{9\pi\beta^2}{16h^2(\psi)}}; \dot{a} = \frac{1}{\sqrt{\bar{\rho}}} \sqrt[3]{\frac{3}{4} \frac{\beta}{h(\psi)\pi}}, \quad (19)$$

$$f = \frac{(\eta - 1)\omega}{1 - \omega}, \quad (20)$$

$$\eta = \exp \left(\left[x_4 \cdot 2\pi \dot{D}_{gb} (\dot{a}_{tip}(\dot{a} = 1) - \dot{a}_{tip}(\dot{a})) \dot{\rho} \left(\frac{d\mu^p}{dt} \right)^{-1} \right] \right) \quad (21)$$

$$\frac{d\mu^p}{dt} = \frac{\beta}{\sqrt{\rho^3}} (\dot{\alpha}_p - \dot{\alpha}_a) + \sqrt[3]{36h(\psi)\pi\beta^2} \frac{d\dot{a}}{dt}, \quad (22)$$

where

$$q(\omega) = -2ln\omega - (3 - \omega)(1 - \omega); \dot{a}_{tip}(\dot{a}) = 2\dot{\gamma}_s \sin\psi / \dot{a} \quad (23)$$

In this equation, β is the damage variable, ρ is the cavity density, a is the average radius of the cavity, $\dot{\alpha}_p$ is the stress-dependent nucleation rate, $\dot{\alpha}_a$ is the annihilation rate, ψ is the dihedral angle of the cavity (70°), \dot{D}_{gb} is the GB diffusion coefficient, and ω is the damaged area fraction. The creep degradation of GB is calibrated by three variables: ρ , β and a . These three parameters not only determine the failure degree of GB but also determine the amount of the creep nonlinear deformation. Therefore, ρ , β , and a are the three indicators for the benchmark.

2.3.3 Computational platform development

The well-known displacement-based creep damage algorithm will be adopted here directly [31], which were used and reported, for example, research [32] by Richard Hall.

The main further work is the calculation of the stiffness matrix for the grain boundary element and the integration of the grain boundary element, parallel to that for grain element.

3. Materials

1. P91 high Cr alloy is used in this development of creep cavity fracture model and the associated creep cavity nucleation model and creep cavity growth model [12, 31]. The experimental cavity histogram data was taken from publication [21].
2. ASME Grade 91 (9Cr-1Mo-V-Nb) high Cr alloy is used in the investigation of the trend of creep cavity fracture lifetime coefficient U' . The creep data sheets of creep fracture time under different stress and temperature on this alloy is taken from publication [20].
3. CB8 high Cr alloy is used in the investigation of creep cavity fracture lifetime over a wider stress range. The experimental creep cavitation data and histogram (in the form of graphs) were taken from Ref. [33].
4. Copper-antimony alloy is used for the demonstration of the mesoscopic composite creep cavity damage simulation. The property of copper-antimony alloy at 823 K [24].

The parameters for the grain boundary cavity model is $\tilde{D}_{gb} = 10^{-14} mm^5 N^{-1} s^{-1}$, $a_p = 2 \times 10^2 mm^{-2} s^{-1}$, and $b_p = 1$. The power law creep is used to describe the creep mechanism of the grain part.

The material parameters of copper power law for grain [24] are (400–700°C): $A: 38.8 \text{ MPa}^{-n} \text{ S}^{-m-1}$, $Q: 197 \text{ KJmol}^{-1}$, $n:4.8$, and $m:0$.

A 1 mm^2 squire geometry is chosen, 20 grains and 60 grain boundary were meshed by 909 triangle pane strain element; 152 interface elements, using Neper free software [34]. A finer mesh would be desirable; however, it is a compromise to accept this size to proceed.

A tensile load of 10 MPa was applied uniformly on the top side; and the left side and the bottom side was pinned in X direction and Y direction, respectively.

4. Results

4.1 The minimum creep strain rate over a wide range of stress levels for P91 high Cr alloy

The specific value of $q = 2$ of the modified hyperbolic sine law was obtained through trial and error method. The results are summarily shown in **Figure 2**, where it is clearly shown that the Xu’s modified hyperbolic sine law is the best.

4.2 Creep cavity fracture model

4.2.1 The determination of the creep cavitation coefficients

The obtained creep cavitation coefficients were obtained and shown in **Table 3**, and their application to predict the cavity probability density size distribution is shown in **Figure 3** [12].

Based on the obtained values of creep cavity coefficients, the creep cavity nucleation model, the creep cavity growth model, and creep cavity fracture model

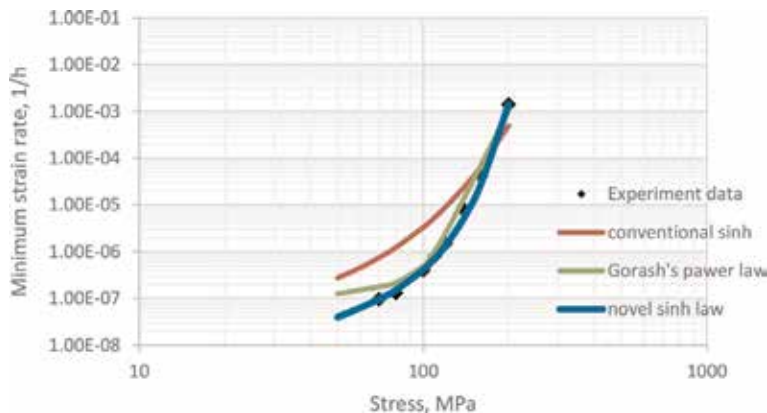


Figure 2.
 The comparison of the modeling of minimum creep strain rate and stress level [12].

A_1	A_2	α	β	γ
6.66E-18	0.019246	1	2	1

Table 3.
 The creep cavitation constants for P91 [12].

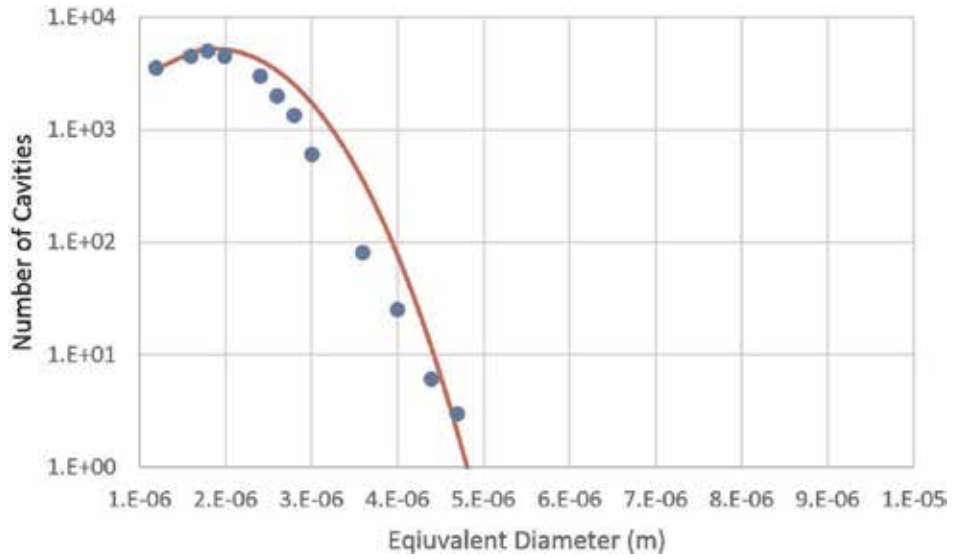


Figure 3.
The comparison of cavity size probability density function for P91, experimental data from ref [22] and only sample points used [12].

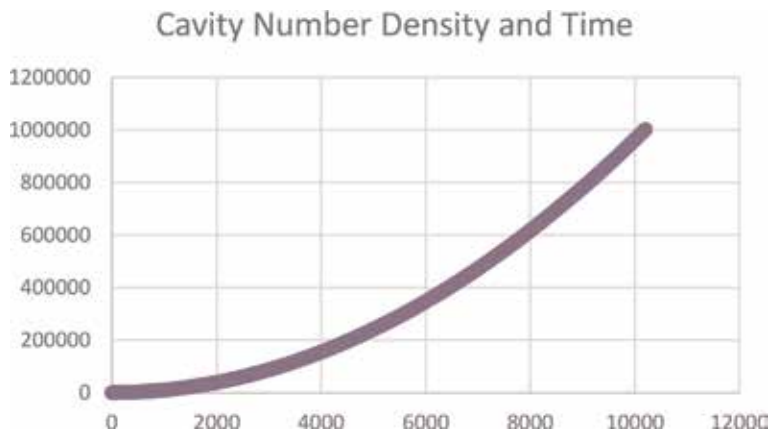


Figure 4.
The predicted number of cavity with time.

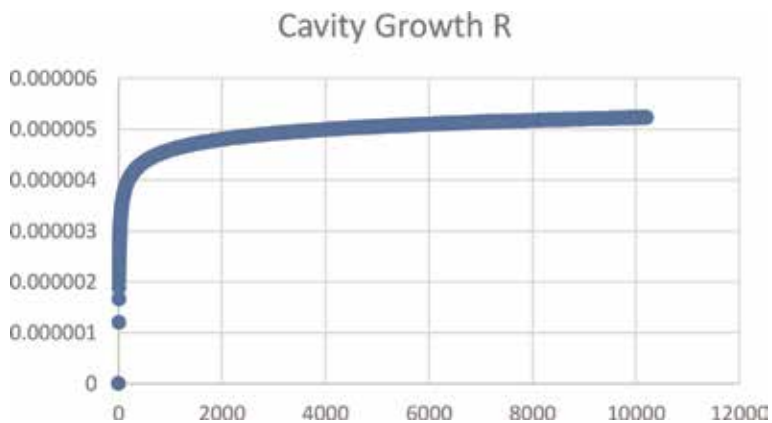


Figure 5.
The predicted cavity growth with time.

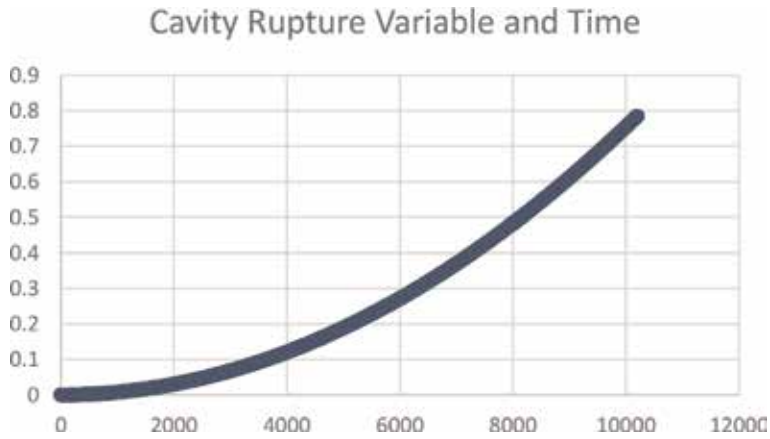


Figure 6.
 The predicted caviated area along grain boundary with time.

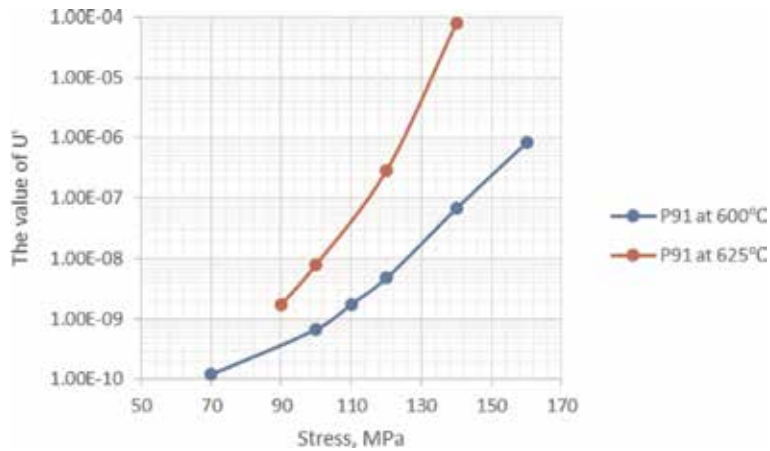


Figure 7.
 The trend of the values of U' under different stresses and temperatures [12].

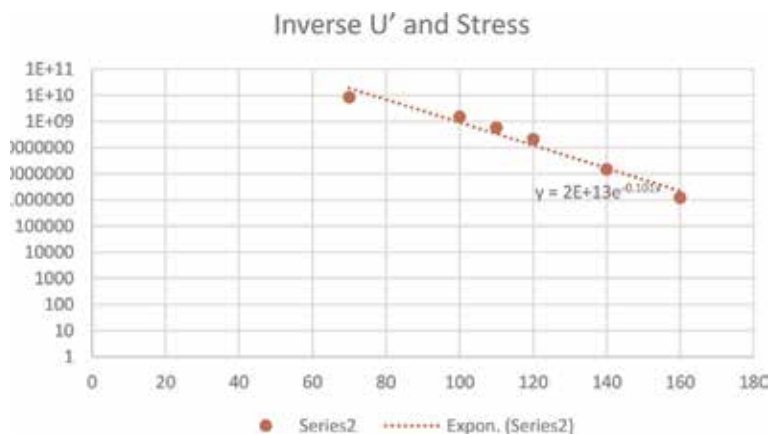


Figure 8.
 Inverse U' and stress level for P91 at 600°C.

are also obtained, respectively. The predicted relationships of the number of cavity, the creep cavity growth, and creep damage variable with time are shown in **Figures 4–6**, respectively.

4.2.2 Trend of creep fracture lifetime coefficient U'

Based creep data sheets of creep fracture time under different stress and temperature on typical ASME Grade 91(9Cr-1Mo-V-Nb) steel [14], the value of U' was calculated and graphically shown in **Figure 7**. Furthermore, the inverse U' and stress level for P91 is obtained and shown in **Figures 8 and 9**, respectively.

4.2.3 Creep cavity fracture lifetime prediction over a stress range

Using the simplified and approximate method described in Section 2.2.3, the obtained values for the cavity nucleation coefficient and cavity growth coefficient are shown in **Table 4**.

Based on Equation (12), the creep lifetime at 120 MPa is predicted to be 44,845 hours, and it is 87% of the actual experimental lifetime of 51,406 (hours).

4.3 Mesoscopic composite model of the simulation of creep cavity damage and fracture

The flow diagram structure is shown in **Figure 10**; the FE model of the polycrystalline case is shown in **Figure 11** [31].

At the time of 78.9 hours, there were seven grain boundary elements that failed. If that is deemed as creep fracture time, then it agrees with the majority of all

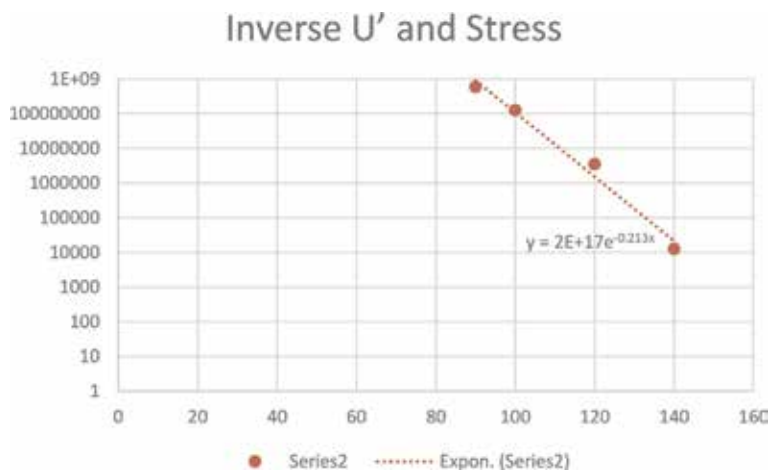


Figure 9.
Inverse U' and stress level for P91 at 625°C.

Stress	A_1	A_2	Lifetime (hours)
180 MPa	1.73E-17	9.397e-8	2825 (experiment)
120 MPa	7.04E-17	8.04e-10	51406 (experiment) 44845 (predicted)

Table 4.
The values of nucleation coefficient and growth coefficient and lifetime prediction.

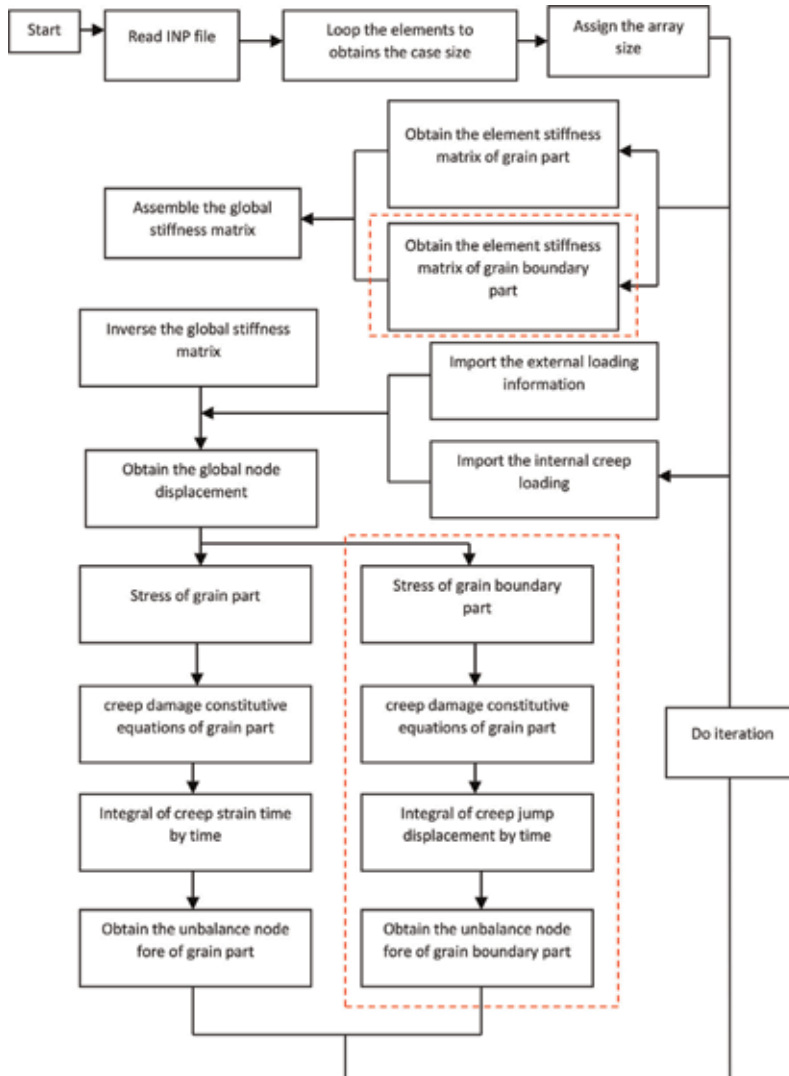


Figure 10.
 The flow diagram structure [31].

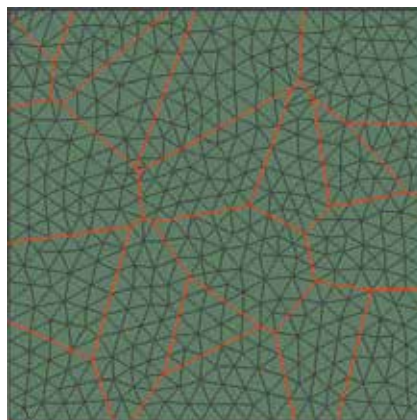


Figure 11.
 The FE model of the polycrystalline case study [31].

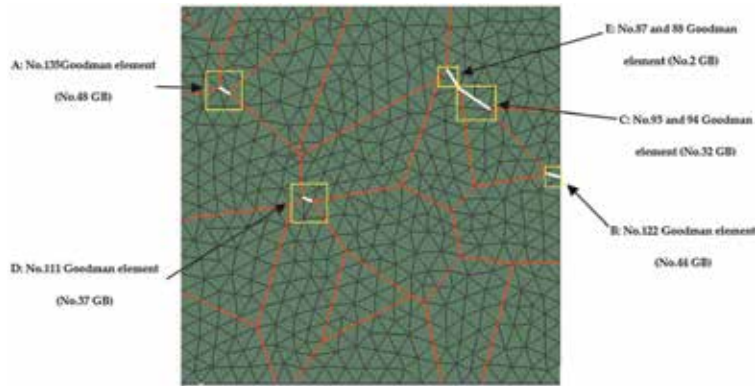


Figure 12.
The location of the first seven failed grain boundary elements [31].

Position	Oritantion Angle (Normal direction)	Element NO.	Time (Unit:hour)	Step
A	65.26084	48	23.55	12003387
B	76.16616	122	65.55	33246192
C	54.01357	93	68.48	34728834
D	54.01357	94	68.48	34728856
E	65.41204	111	70.69	35848560
F	146.3127	87	78.90	39987506
G	146.3128	88	78.90	39987517

Table 5.
The sequence and time of fracture [31].

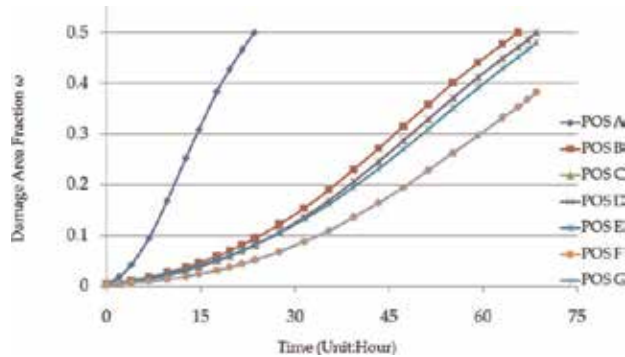


Figure 13.
The damage evolution with time of the seven failed grain boundary elements [31].

uni-axial creep tests conducted [9]: In uniaxial test, one specimen is fractured at 16.6, 17.9, and 58.3 hours, respectively. It is worthy to mention that the simulation was conducted for plane strain case; hence a longer lifetime at the same applied stress is expected.

The location, the sequence of fracture, and the time of fracture of grain boundary element are shown in **Figure 12** and **Table 5**, respectively. The creep cavity damage evolution with time of the first seven failed grain boundary elements is

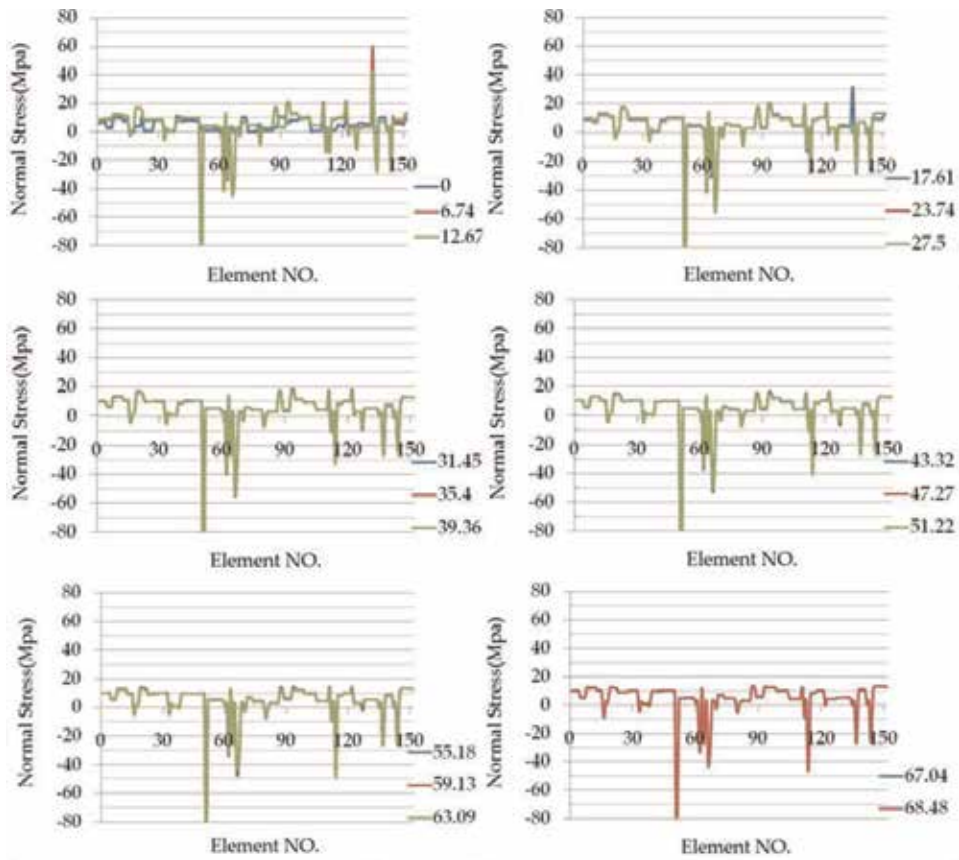


Figure 14.
 The evolution of normal stress with time [31].

shown in **Figure 13**. The whole all normal stress evolution and the creep cavity damage evolution are shown in **Figures 14** and **15**, respectively.

5. Discussion

5.1 The minimum creep strain rate over a wide range of stress levels for P91 high Cr alloy

The results shown in **Figure 2** clearly demonstrated that Xu's modified hyperbolic sine law is the best for the P91 high Cr alloy over a wider range of stress levels.

It is pointed out that the introduction of σ^d into the normal hyperbolic sine function, purposely, offers a capability to depict a wider range of curvatures between the minimum creep strain rate and stress level.

Furthermore, the value $q = 2$ found here for P91 is in similar order to those found for low Cr alloy [12] and for P92 [35]. It is worth to research any profound reason for this similarity.

It is reasonable to propose that, due to generic mathematical property (feature), the application of Xu's modified hyperbolic shin law should be further explored, particularly for a wider range of stress level cases.

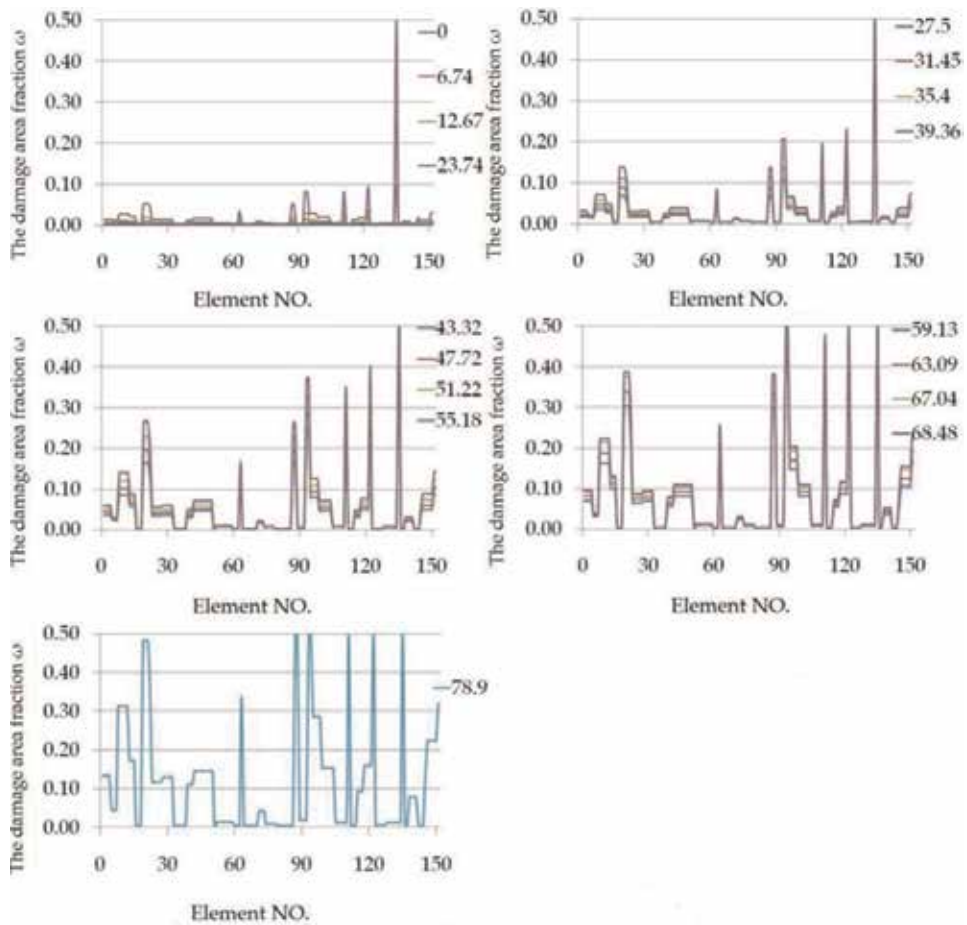


Figure 15.
The damage evolution with time [31].

5.2 Creep cavity fracture model

5.2.1 The determination of the creep cavitation coefficients

A set of creep cavitation model and creep cavity growth model were calibrated using the more representative X-ray synchrotron cavitation data. The predicted cavity size probability density is very close to the experimental measured one, indicated by **Figure 3**, and it can be concluded that the quality of creep cavitation models are good. Hence their application should also be reliable [12].

The predicted relationships of the number of cavity, the creep cavity growth, and creep damage variable with time can provide the insight of the evolution of the complex creep cavity damage process, and its use will lead to a clear and definite answers on (1) how to present creep cavity damage and (2) how to quantify it.

The obtained *explicit creep cavity damage fracture model can be used for creep lifetime prediction and possible extrapolation.*

5.2.2 Trend of creep fracture lifetime coefficient U'

The creep lifetime coefficient U' is introduced in theoretically based cavitation nucleation, growth, and coalescence along the grain boundary. A clear trend shown

from the experimental data, in **Figure 7**, indicated that such creep cavity damage/fracture modeling is scientifically sound and numerically reliable; hence it can be used for creep life time prediction and possible extrapolation.

Furthermore, theoretically, creep lifetime coefficient and lifetime, in log–log scale, is a linear relationship; and the experimental data strongly support that as shown in **Figures 8** and **9**. Hence the trend revealed by experimental data in **Figures 8** and **9** could be used for lifetime prediction and very promising for lifetime extrapolation.

5.2.3 Creep cavity fracture lifetime prediction over a stress range

The excellent agreement (87%) between the predicted creep lifetime and experimental measured one proved the reliability of creep lifetime prediction.

It needs to be reported here [33] that the stress of 180 MPa is of the high stress level and the stress of 120 MPa is of the lower stress level. Hence, the above excellent agreement is actually achieved between two stress levels. There is no stress breakdown phenomenon in this approach; actually, the stress-dependent effects will be taken into account by the values of the creep cavitation coefficients.

The success is underpinned by both the correct mathematical model and the direct using the most presentative cavitation data.

Furthermore, the creep cavitation modeling approach reported here should be generic and can be used for any other cavitation controlled damage and fracture problems such as ductile fracture, fatigue fracture, and creep and fatigue combined fracture.

5.3 Mesoscopic composite model of the simulation of creep cavity damage and fracture

1. The concept of mesoscopic composite-type approach of modeling creep damage model at grain boundary level has been proposed and developed.
2. In this development, in the conventional nonlinear creep damage analysis framework, the only new thing that needs to be added is the grain boundary element.
3. The existing interface element has been chosen and used here.
4. The predicted creep lifetime is in very good agreement with experimental observation.
5. The demonstrative case study reveals its full potential for providing the detailed information at the right size level, and it is anticipated to be widely used in the future.
6. There is an urgent need for the development of creep damage constitutive equations for grain and grain boundary, respectively; in turn, it demands the characterization of the grain and grain boundary separately.
7. Further development work to develop a three-dimensional version.

6. Conclusion

Modeling of creep deformation and creep fracture is very challenging. However, research work report here has made some progress. These progress and suggestions for future work are presented as:

1. A modified hyperbolic sine function was proposed, and suitability for a wider range of stresses is demonstrated. Its successful applications to both low Cr alloy and high Cr alloy merit it to be tried to other alloys. It is worth to research to find any material scientific reasons for the similar magnitude of the q among different alloys.
2. A new creep cavity fracture model was proposed and developed based on the cavity nucleation, growth, and coalesce at grain boundary using the cavitation data from X-ray synchrotron investigation.
3. The creep cavity fracture lifetime coefficient U' can be experimentally produced, and it can be used for lifetime prediction and extrapolation.
4. Creep cavity fracture lifetime prediction works very well over a stress range, and there is no stress breakdown in this model.
5. Research work on the stress state's effect on the cavitation should be pursued in the future.
6. Furthermore, the creep cavitation modeling approach reported here should be generic and can be used for any other cavitation controlled damage and fracture problems such as ductile fracture, fatigue fracture, creep, and fatigue combined fracture.
7. A mesoscopic creep deformation and creep damage model concept was proposed and preliminarily realized in a plane stress version; its potential for providing the right size has been demonstrated.
8. Parallel to the development of 3D computational platform, there is a great need for the development of creep damage constitutive equations for grain and grain boundary separately.

Acknowledgements

QX is grateful for the award of the Santander postgraduate mobility scholarship 2016 and 2017, respectively, which partially funded the field trip of Mr. Xin Yang in 2016 to Japan and Mr. JiaDa Tu in 2018 to China, respectively. It is also acknowledged that some work reported here were taken from previous publications [12, 31] where Dr. Xin Yang and Mr. Jiada Tu did contribute in the original production of these two papers, respectively.

Conflict of interest


The authors declare that there is no conflict interest.

Author details

Qiang Xu* and Zhongyu Lu
School of Computing and Engineering, The University of Huddersfield,
Huddersfield, West Yorkshire, UK

*Address all correspondence to: q.xu2@hud.ac.uk

IntechOpen

© 2019 The Author(s). Licensee IntechOpen. This chapter is distributed under the terms of the Creative Commons Attribution License (<http://creativecommons.org/licenses/by/3.0>), which permits unrestricted use, distribution, and reproduction in any medium, provided the original work is properly cited. 

References

- [1] Riedel H. Fracture at High Temperatures. Springer Verlag; 1987
- [2] Kassner ME, Hayes TA. Creep cavitation in metals. *International Journal of Plasticity*. 2003;**19**:1715-1748
- [3] Ennis PJ, Zielinska-lipiec A, Wachter O, Czyrska-filemonowicz A. Microstructural stability and creep rupture strength of the martensitic steel P92 for advanced power plant. *Acta Materialia*. 1997;**45**(12):4901-4907
- [4] Lee JS, Armakia HG, Maruyama K, Murakic T, Asahic H. Causes of breakdown of creep strength in 9Cr–1.8W–0.5Mo–VNb steel. *Materials Science and Engineering*. 2006;**428**:270-275
- [5] Grades EA. Development of a creep-damage model for non-isothermal long-term strength analysis of high-temperature components operating in a wide stress range, Zentrum für Ingenieurwissenschaften der Martin-Luther-Universität at Halle-Wittenberg; 2008
- [6] Parker J. In-service behavior of creep strength enhanced ferritic steels grade 91 and grade 92 – Part 1 parent metal. *International Journal of Pressure Vessels and Piping*. 2013;**101**:30-36
- [7] Miannay D. Time-Dependent Fracture Mechanics. France: Springer; 2001
- [8] Dyson B. Use of CDM in materials modelling and component creep life prediction. *International Journal of Pressure Vessels and Piping*. 1983;**122**: 281-296
- [9] Yin Y, Faulkner RG, Morris PF, Clarke PD. Modelling and experimental studies of alternative heat treatments in steel 92 to optimise long term stress rupture properties. *Energy Materials*. 2008;**3**:232-242
- [10] Yang X, Xu Q, Lu ZY. The development and validation of the creep damage constitutive equations for P91 alloy. In: *Proceedings of the 2013 World congress in computer science and computer engineering and application*. CSREA Press; 2013. pp. 121–127. ISBN: 1-60132-238-0
- [11] Basirat M, Shrestha T, Potirniche GP, Charit I, Rink K. A study of the creep behavior of modified 9Cr-1Mo steel using continuum-damage modeling. *International Journal of Plasticity*. 2012;**37**:95-107
- [12] Xu Q, Yang X, Lu ZY. On the development of creep damage constitutive equations: a modified hyperbolic sine law for minimum creep strain rate and stress and creep fracture criteria based on cavity area fraction along grain boundaries. *Materials at High temperatures*; **34**(5–6):323-332. DOI: 10.1080/09693409.2017.1388603
- [13] Xu Q, Hayhurst DR. The evaluation of high-stress creep ductility for 316 stainless steel at 550 °C by extrapolation of constitutive equations derived for lower stress levels. *International Journal of Pressure Vessels and Piping*. 2003; **80**(10):689-694. ISSN: 0308-0161
- [14] Xu Q. Development of constitutive equations for creep damage behaviour under multi-axial states of stress. In: *Advances in Mechanical Behaviour, Plasticity and Damage*. London, UK: Elsevier; 2000. pp. 1375-1382. ISBN: 978-0-08-042815-4
- [15] Xu Q. Creep damage constitutive equations for multi-axial states of stress for 0.5Cr0.5Mo0.25V ferritic steel at 590°C. *Theoretical and Applied Fracture Mechanics*. 2001;**36**(2):99-107. ISSN: 0167-8442
- [16] Xu Q. The development of phenomenological multi-axial isotropic

- creep damage constitutive equations. In: *Mechanics and Material Engineering for Science and Experiments*. London, UK: Science Press; 2001. pp. 457-460. ISBN: 1-880132-79-6
- [17] Xu Q. The development of validation methodology of multi-axial creep damage constitutive equations and its application to 0.5Cr0.5Mo0.25V ferritic steel at 590°C. *Nuclear Engineering and Design*. 2004;**228**(1-3): 97-106. ISSN: 0029-5493
- [18] Wen JF, Tu SD. A multiaxial creep-damage model for creep crack growth considering cavity growth and microcrack interaction. *Engineering Fracture Mechanics*. 2014;**123**:197-210
- [19] Xu Q, Lu ZY, Wang X. Damage modelling: The current state and the latest progress on the developing of creep damage constitutive equations for high Cr steels. In: 6th International 'HIDA' Conference: Life/Defect Assessment & Failures in High Temperature Plant; 2-4 December 2013, Nagasaki, Japan. Surrey, UK: European Technology Development Limited; 2013
- [20] Creep and rupture data of heat resistant steels, National Institute for Materials Science (NIMS). Available from: http://smds.nims.go.jp/creep/index_en.html
- [21] Sket F, Dzieciol K, Borbely A, Kaysser-Pyzalla AR, Maile K, Scheck R. Microtomography investigation of damage in E911 steel after long-term creep. *Materials Science and Engineering A*. 2010;**528**:103-111
- [22] Renversade L, Ruoff H, Maile K, Sket F, Borbely A. Microtomographic assessment of damage in P91 and E911 after long-term creep. *International Journal of Materials Research*. 2014;**105**: 621-627
- [23] Vöse M, Otto F, Fedelich B, Eggeler G. Micromechanical investigations and modeling of a copper-antimony-alloy under creep conditions. *Mechanics of Materials*. 2014;**69**(1):41-62
- [24] Vöse M, Fedelich B, Otto F, Eggeler G. Micromechanical modeling of creep damage in a copper-antimony alloy. *Procedia Materials Science*. 2014;**3**:21-26
- [25] Dyson BF. Continuous cavity nucleation and creep fracture. *Scripta Metallurgica*. 1983;**17**:31-37
- [26] Bower AF. *Applied Mechanics of Solids*. Oxford, UK: Taylor & Francis Group, LLC; 2010
- [27] Dyson BF. Constraints on diffusional cavity growth rates. *Metal Science*. 1976;**10**:349-353
- [28] Ashby MF. Boundary defects and atomistic aspects of boundary sliding and diffusional creep. *Surface Science*. 1972;**31**:498-542
- [29] Cocks ACF, Ashby MF. On creep fracture by void growth. *Progress in Materials Science*. 1982;**27**:189-244
- [30] Vöse M, Fedelich B, Otto F, Owen J. A simplified model for creep induced grain boundary cavitation validated by multiple cavity growth simulations. *Computational Materials Science*. 2012;**58**:201-213
- [31] Xu Q, Tu JD, Lu ZY. Development of the FE In-house procedure for creep damage simulation at grain boundary level. *Metals*. 2019;**9**(6):656. DOI: 10.3390/met9060656
- [32] Hall R. Development of continuum damage mechanics models to predict the creep deformation and failure of high temperature structures [PhD thesis]. The University of Sheffield; 1990
- [33] Gupta C, Toda H, Schlacher C, Adachi Y, Mayr P, Sommitsch C, et al.

Study of creep cavitation behavior in tempered martensitic steel using synchrotron micro-tomography and serial sectioning techniques. *Materials Science and Engineering A*. 2013;**564**: 525-538

[34] Quey RP, Dawson P, Barbe B. Large scale 3D random polycrystals for the finite element method: Generation, meshing and remeshing. *Computer Methods in Applied Mechanics and Engineering*. 2011;**200**(2011):1729-1745

[35] Zheng XM, Xu Q, Lu ZY. The development of creep damage constitutive equations for high Cr steel: Further application of the modified hyperbolic sine law for the minimum creep strain rate over a wider range of stress level and the creep cavity fracture model based on the cavity area fraction along grain boundaries. *Materials at High Temperatures*. 2019

Section 2

Sustainable Materials

Structural Evaluation of Bamboo Bike Frames: Experimental and Numerical Analysis

*Juan P. Arango Fierro, Jose L. Arango Fierro
and Héctor E. Jaramillo Suárez*

Abstract

Construction of bicycles with bamboo frames has become an alternative to improve the quality of life of some communities, be friendly with the environment and be ecologically sustainable. However, the production of bike frames is made in an artisanal way and there are few antecedents that have proven their reliability. This work presents the evaluation and simulation of the mechanical behavior of bike frames made in bamboo. Three-points bending tests were performed using bamboo bars with similar dimensions to bike frames, and an equivalent elasticity modulus was determined and used as the input datum of a finite element model. A linear model material and beam elements were used to model the bike frame. Tests were performed using bike frames of bamboo applying loads greater than 7000 N, and the displacements were measured. The experimental displacements were used to calibrate the model, which consisted of modifying the rigidity of the connections until the displacements of the model fit near to 90%. The calibrated model was used for a fatigue simulation in order to predict the lifespan of the bike frame. Some technical values of bamboo bike frames were obtained so that these will allow them to define the technical characteristics of the product and guarantee their operating conditions.

Keywords: bicycle, bike frame, bamboo, fatigue, three-point bending tests, finite element analysis

1. Introduction

Bicycles offer a cost-effective transportation alternative primarily for low-income communities [1]. Additionally, bikes have other advantages, such as zero greenhouse gas emissions, low-cost maintenance, quick displacement in high traffic zones, and physical fitness promotion for the users.

Conventional bike frames, using materials, such as steel [2], aluminum [2, 3], carbon fiber [4, 5], and titanium, have been studied via numerical model analyses and experimental tests. The numerical studies generally use the finite element method, and the tests generally obtain the static load carrying capacity; in this direction, the researches' focus has been oriented to improving the relationship between the weight and the strength. However, the new research trends are focused on the replacement of the bike frame material using a low-cost alternative, like

environmentally friendly materials, low weight and very attractive esthetically [6]. In this direction, the bamboo can become a good alternative.

There are more than 1000 species of bamboo around the world of which 70 are abundant in South America and Asia [7]. Bamboo is a natural fiber species that belongs to grass Poaceae family and subfamily Bambusoideae and grows in diverse types of climate. Compared to other trees, the bamboo has significant low density, high strength, and stiffness [8], most high growth rate (30–100 cm per day). Also, the bamboo plays an important environmental role by preventing ground erosion and landslides in mountainous zones and retaining significant amounts of water that restore ground conditions where it grows [9].

Currently, some companies and foundations have been building a bike frame using bamboo [10–12]. Locally, the bike frames are being manufactured using bamboo and their joints with a composite that uses an epoxy matrix reinforced with natural fibers (fique). However, the composite material joints are highly dependent on the geometric and material characteristics; for this reason, the testing of the actual bamboo bike frame is imperative. Some information can be found in the literature about the experimental strength of bamboo bike frame, although some analyses have been made using the finite element method [2, 13–15]. Once experimental data has been obtained, sensitivity and fatigue studies can be performed in order for the useful life of the bamboo bikes to be assessed.

In this direction, this work pretends to estimate the maximum allowable distance traveled by bikes made using bamboo frames. The general structural performance of the bike frames was evaluated under static and dynamic loads using experimental tests and the finite element method. Also, the mechanical strength of the joints was evaluated.

2. Methods and materials

Several steps were defined in order to perform the research (**Figure 1**). The first step was to determine the experimental properties of bamboo using a three-point bending test, measuring the displacement of some points of the bike under to external load and experimental modal analysis. The next step was to perform a static analysis of the bamboo bike frame using the finite element method. Using the experimental displacements, the finite element model was calibrated (step 3). The model calibrated was validated using the natural frequencies obtained experimentally (step 4). Finally, a fatigue analysis using the finite element method was performed using S-N curves reported and an estimation of the maximum distance that the bike can travel under the load conditions defined.

2.1 Geometry

The bamboo bike frames were made of bamboo tubes joined with a composite material, a resin as a matrix reinforced with fique (**Figure 2**).

A bamboo frame size M was used to perform the experiments and finite element analysis (**Figure 3**).

2.2 Experimental tests

2.2.1 Three-point bending tests

Three-point bending tests were performed in order to characterize the structural behavior of bamboo. The load was applied perpendicularly at midspan of a simply

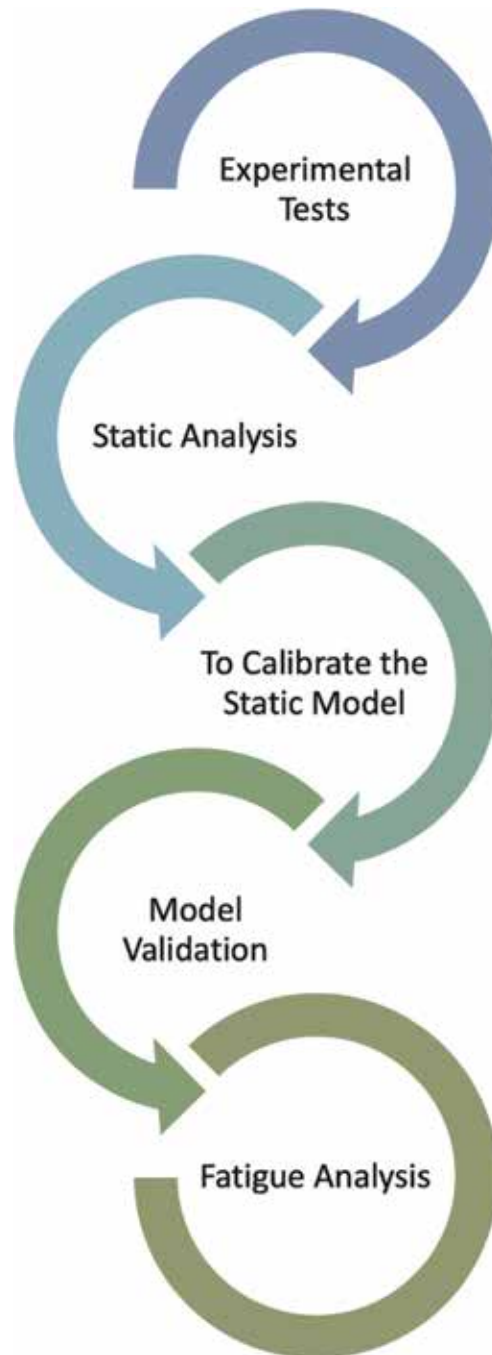


Figure 1.
Steps followed.

supported beam according to ASTM D790-17 standards [16]; from this test Young's modulus was obtained. Bending tests were performed using a universal test machine UTS 200.3. Wood blocks were placed on load application points in order to avoid the load concentration effects (**Figure 4**).

Sixteen bamboo specimens with two sets of radii were tested, eight samples with 15.5 mm of outer radius and 10.5 of inner radius and another eight samples with

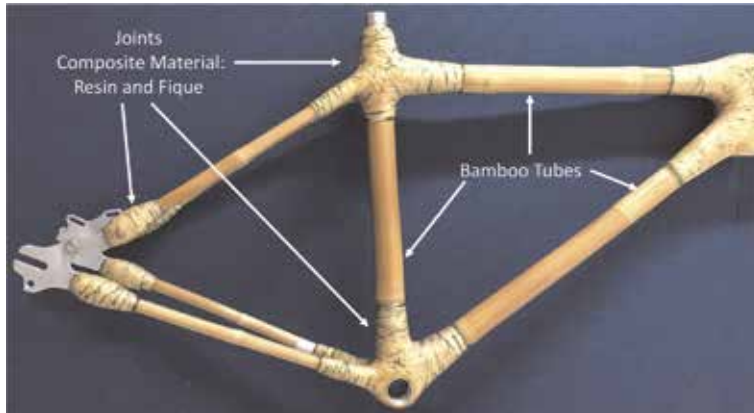


Figure 2.
Bamboo bike-frame.

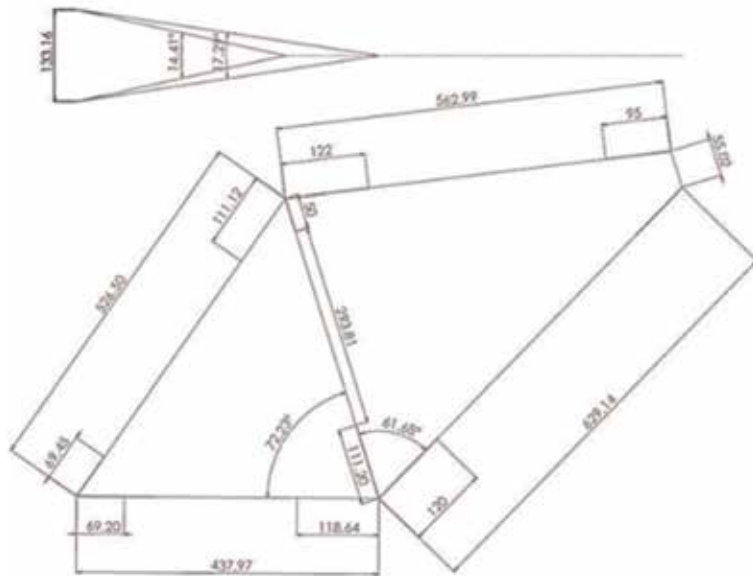


Figure 3.
Bamboo bike-frame dimensions (in mm).

10.5 mm of outer radius and 10.25 mm of inner radius, approximately. A monotonically increasing load was applied to bamboo specimens until fracture and load versus displacement curves were obtained. The Young's modulus was calculated as explained below.

The Y displacement of the midspan of the specimen is:

$$Y = \frac{PL^3}{48EI} \quad (1)$$

Knowing the applied load (P) and the displacement (Y), the Young's modulus (E) must be obtained as:

$$E = \frac{PL^3}{48YI} \quad (2)$$



Figure 4.
Setup of three-point bending test.

where L is the distance between supports and I the inertia of the cross section. The inertia can be calculated as:

$$I = \frac{\pi}{64} (D_{outer}^4 - D_{inner}^4) \quad (3)$$

where D_{outer} is the outer diameter and D_{inner} is the inner diameter.

2.2.2 Experimental displacements

A universal test machine UTS 200.3 was used to obtain the experimental displacements of the A, B, and C points (**Figures 5 and 6**). Three load ramps were applied (2000, 3500, and 6500 N) on the seat tube (**Figure 7**) of the bike frame, and the displacements were measured. The experimental displacements of the bike frame were used to calibrate the numerical model.

2.2.3 Experimental natural frequencies

To validate the finite analysis model of the bike, experimental modal analysis of the frame was performed to obtain their natural frequencies and compare it to the results of the finite element model.

The experimental frequencies were obtained via a mobile application VibSensor [17], loaded on cell phones. The software provides the natural frequency on the system and its direction as responses to impulse loads are induced on the frame by tapping the frame several times at different locations with different intensities. The planes were defined by the phone (Z direction is normal to the screen of the phone).

In order to prove the accuracy of the mobile application, a simple model was used. The simple model consisted of a steel plate. The plate was fixed on both ends and the cell phone placed on the mid-length; then a load was applied to excite the plate, and their experimental natural frequencies were obtained. The first experimental natural frequencies were 19 Hz (**Figure 8**) and 19.95 Hz from the finite element model (**Figure 9**). In this direction, the accuracy of the mobile application was near to 5%. For this reason, the results obtained from the mobile application can be considered acceptable, and it can be used to the bamboo bike frame.

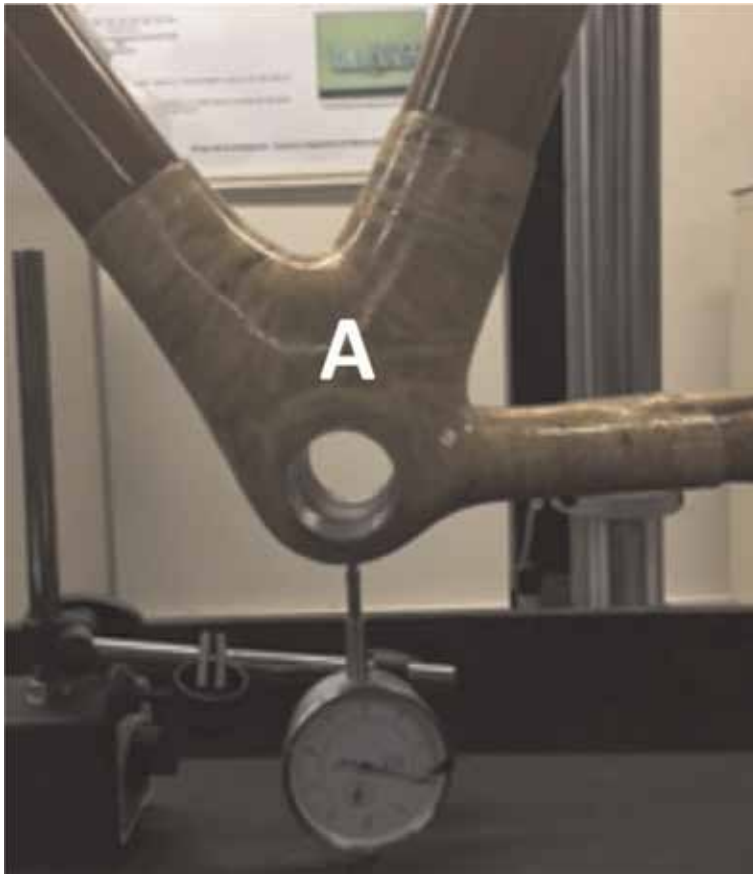


Figure 5.
Setup to measure the vertical displacement in bottom bracket joint, point A.

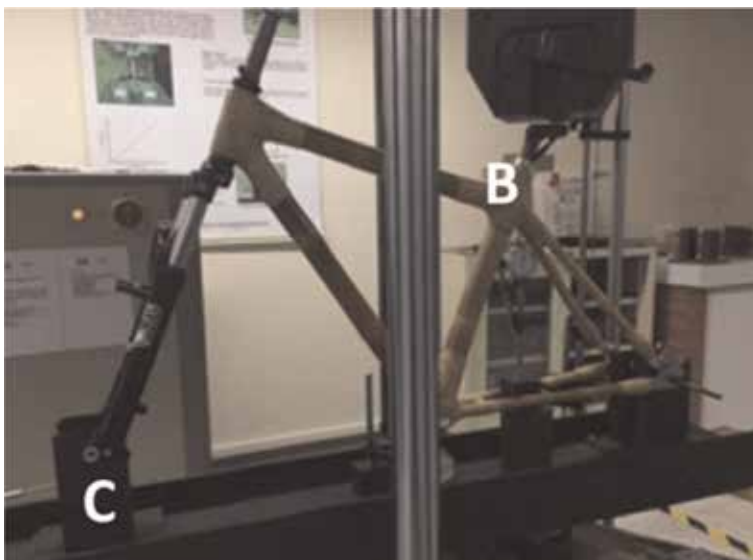


Figure 6.
Setup to measure the vertical displacement, points B and C.

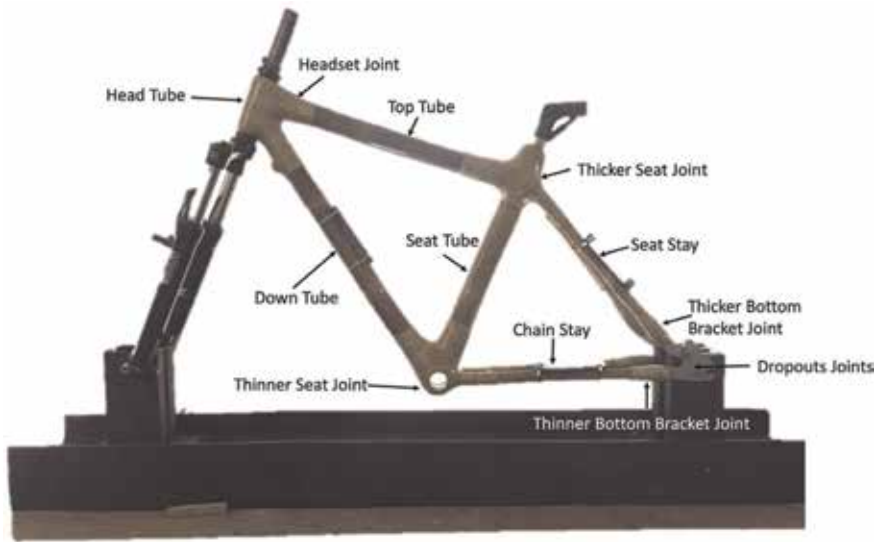


Figure 7.
 Names of parts and joints of the bike.

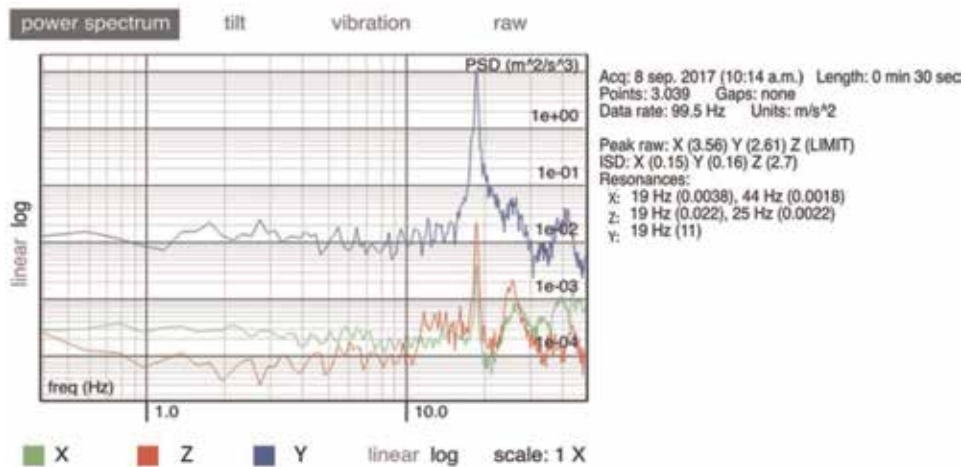


Figure 8.
 Experimental natural frequencies of the plate using Vibsensor software.

A setup was designed to obtain the natural frequencies of the bamboo bike frame (**Figure 10**). Cell phones were placed on three tubes: seat stay, chain stay, and down tube.

The bike frame was supported simulating the real conditions: the rear dropouts were fixed along x - and y -axes, and the front dropouts were fixed along y -axis and free along x -axis. The bike frame was excited using a load, and the cell phones registered the accelerations from which modal frequencies were processed, via a mobile application VibSensor.

2.3 Finite element model

The finite element analysis was performed using Abaqus 6.14-3 [18]. A static load of 3500 N and a moment of 350,000 N-mm were applied to the frame at the

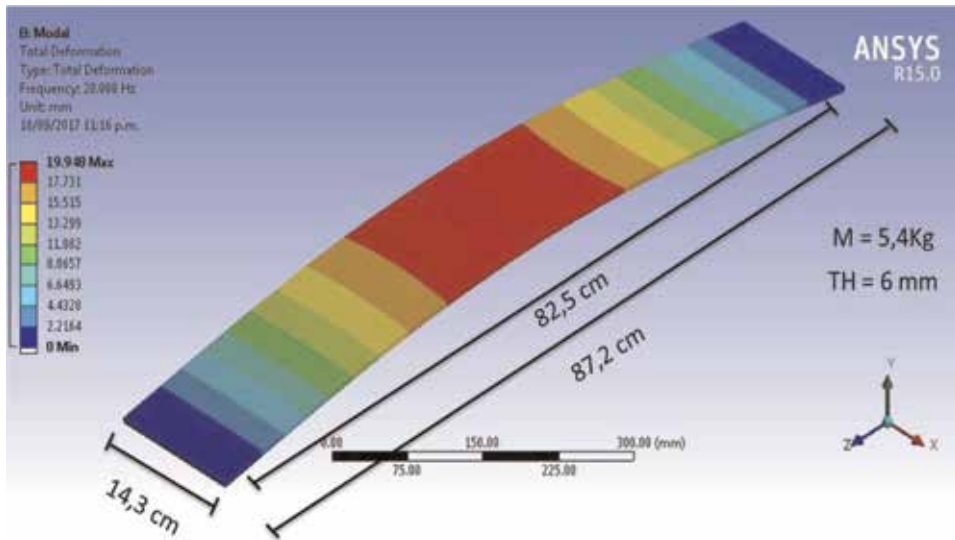


Figure 9.
Natural frequencies of the plate using finite element model.



Figure 10.
Setup of modal test.

saddle. The boundary conditions were defined as the rear dropouts were fixed along x- and y-axes, and the front dropouts were fixed along y-axis and free along x-axis (**Figure 11**). The elastic modulus was taken from the three-point bending tests.

The geometry was represented using straight bars and beam elements. A standard mesh was used in the model with an approximate global size of 60 mm per element. The cross section of each beam elements is shown in **Table 1**.

2.3.1 Model calibration

A SimFlow was created using iSight [19] and Abaqus software [18] in order to fit the displacement of the finite element model (A, B, and C points) with experimental values. The elastic module of the joints was considered as input, and the displacements of points A, B, and C were considered as output data.

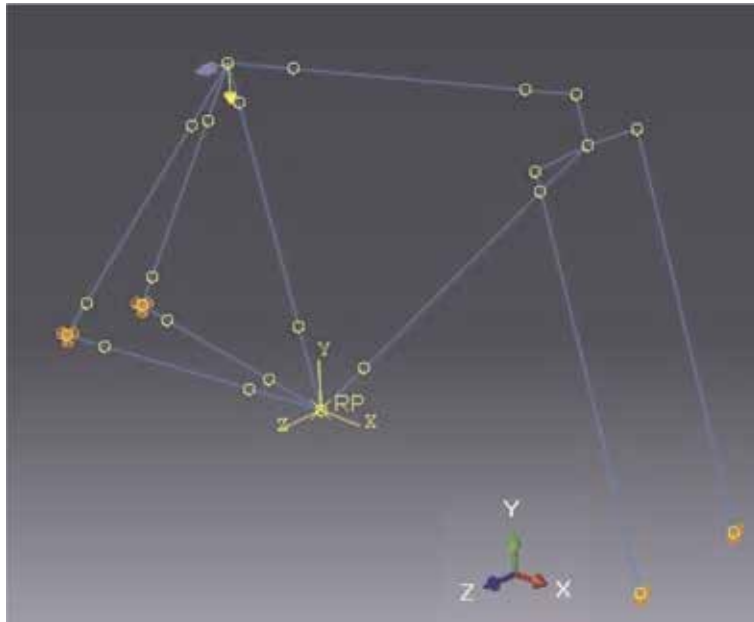


Figure 11.
 Bike-frame finite element model.

Name part	Outer radius (mm)	Thickness (mm)
Down tube	15.5	5.0
Top tube	15.5	5.0
Seat tube	15.5	5.0
Seat stay	10.25	3.5
Chain stay	10.25	3.5
Thicker seat joint	25.0	10.5
Thinner seat joint	13.0	3.25
Headset joint	23.0	7.5
Thicker bottom bracket joint	25.0	10.5
Thinner bottom bracket joint	12.2	1.95
Dropouts joints	10.5	0.25

Table 1.
 Cross sectional of the bike frame parts.

2.3.2 Model validation

The finite element model was validated comparing the experimental natural frequencies obtained in the 2.2.3 item with the modal analysis performed using Workbench/Ansys 19.0 software [20].

2.3.3 Fatigue analysis

Due to the bicycle moving on the irregular road, this induces loads dependent on the time on the bike frame. The fatigue strength is generally represented using alternative stress versus the number of cycles diagram, called the S-N curve.

The structural performance of the bike is important to corroborate the quality of products and to assign warranties. Some standards were found as ASTM F2711-08 [21], F2043-13 [22] and EN 14766 [23]. The standards to evaluate the fatigue performance of bicycle frames require a test setup where the frame is positioned at its normal attitude with the rear dropouts is free to rotate but without translation, while the front axle is free to translate and rotate. In this way, the whole frame is free to bend as it is the case when used on a road.

Fatigue analysis was performed using Workbench/Ansys software [20]. A bar is used to simulate the seat-stem, and it is inserted at 70 mm of distance from the top of the seat tube. The load at the bar simulates the weight of the rider (**Figure 11**). Then 50,000 test cycles load between 0 and 1200 N are applied vertically downward using a 25 Hz of frequency. From a practical standpoint, this cyclic load regime seems arbitrary and not related to any particular road the bicycle may be traveling.

Due to the impossibility of performing experiments to obtain the S-N curve of the bamboo, the S-N curve reported by Song et al. [24] was used to perform the finite element analysis.

Applying the Palmgren-Miner's [25] ratio to the bamboo bike frame, it was possible to determine their life in years:

$$Damage = \left(\frac{N_{applied}}{N_{allowed}} \right) \quad (4)$$

where $N_{applied}$ is obtained from the dynamic simulation obtained from the finite element analysis of the bicycle traveling a given distance, at a given speed, over a road of given characteristics, whereas $N_{allowed}$ is defined by the S-N curve. Where $N_{applied}$ is in cycles per kilometer.

2.3.4 Dynamic analysis

A dynamic analysis of the bike frame was performed. A displacement vs. time function was applied (**Figure 12**) at the front and rear dropout nodes and spring elements used to simulate the tires and fork stiffness (**Figure 13**).

The displacement prescription was obtained from the technical specification of the speed reducer, 6 cm of height and 37 cm of width (**Figure 12**); also we used a bicycle speed of 25 km/h.

Using the road profile and knowing that the wavelength $\lambda = 0.74 \text{ m}$, the frequency $f = 9.57 \text{ Hz}$ and the angular velocity $\omega = 9.57 \text{ Hz}$; the movement equation is:

$$y = 0.06 \sin 58.92t \quad (5)$$

The spring constant (**Figure 13**) was calculated using the vertical deflection of the tire of the bicycle measured at the laboratory under applying a weight. As results were obtained, $K = 15.5 \text{ N/mm}$ for the rear tire and $K = 56.93 \text{ N/mm}$ for the front tire. The model was restricted to all translation degrees on dropouts and fixed the displacement in the Z-axis on the fork.



Figure 12.
Road profile (distances in mm).

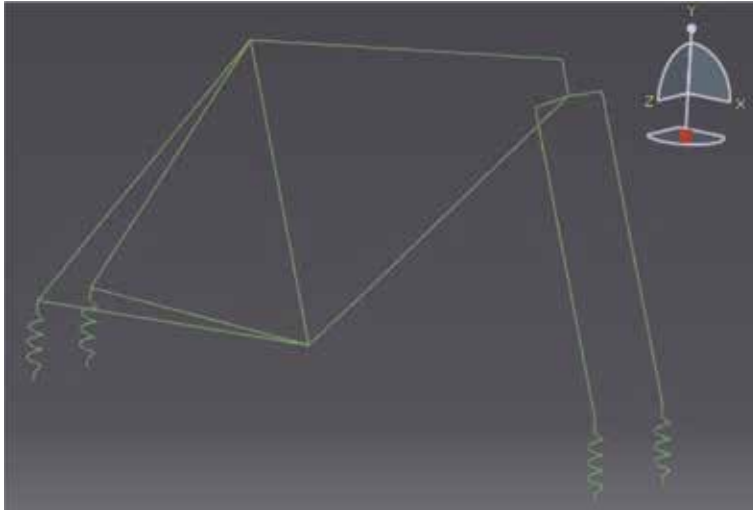


Figure 13.
Finite element model of the bike.

3. Results

3.1 Three-point bending tests

The Young's module was calculated using Eq. (2), and the displacements obtained from three-point bending tests (**Figure 14**). The average values were 9420.8 MPa for the large diameter bamboo and 12610.3 MPa for the small diameter (**Table 2**).

Additionally, the coefficient of variation for a thicker bamboo was good (4.9) considering the variability of the bamboo as a biological material; instead, for thinner bamboo, the variability was 2.7 times higher (**Table 2**).

3.2 Experimental displacements

The maximum displacements were obtained on C point followed by B point and A point (**Table 3**). The behavior of the displacement versus load was lineal, to all points.

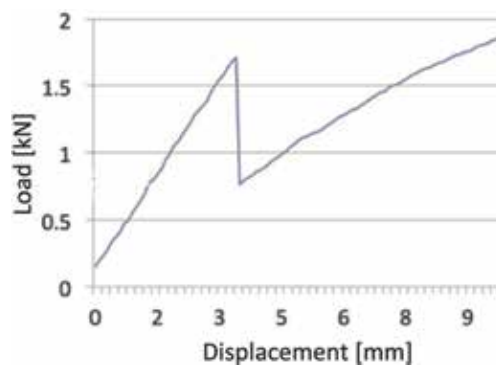


Figure 14.
Typical load vs. displacement curve of bamboo specimen, three-point bending test.

	Thicker bamboo	Thinner bamboo
Average [MPa]	9420.8	12610.3
Standard deviation [MPa]	459.4	1668.9
Coefficient of variation (%)	4.9	13.3
Minimum [MPa]	8589.3	10015.0
Maximum [MPa]	10551.2	14764.8

Table 2.
Longitudinal Young's module for bamboo.

Load	Points displacement (mm)		
	A	B	C
2000 N	-0.06	-2.19	5.09
3500 N	-2.89	-4.14	9.36
6000 N	-5.17	-7.43	16.34

Table 3.
Average of vertical (A and B) and horizontal (C) displacements.

3.3 Finite element model

3.3.1 Model calibration

To calibrate the finite element model, a load of 3500 N and a moment of 35,000 N-mm were used. The target of the model was to fit the displacement of A point near to the experimental displacement, -2.89 mm along y -direction (**Table 3**). The range of Young's modulus used to the joints was 6000–200,000 MPa. The solution converged for a range of Young's modulus between 6000 and 9880 MPa (**Table 4**).

3.3.2 Model validation

Young's modulus obtained from the calibration process (**Table 4**) was used to define the rigidity of the joints. The model was validated using the experimental natural frequency (**Figure 15**), and the first modal shape of the bike frame was out of the plane (Z) with a natural frequency of 38.0 Hz (**Figure 15**). For the finite element model, the first natural frequency was 35.0 Hz (**Figure 16**). The difference between the experimental result and the finite element model was 7.9%.

This difference may be due to the difficulty of exactly modeling the supports and material properties, specifically at the fork and the joints. These results show

Zone	E (MPa)
Bottom bracket	8061
Dropouts joint	6000
Headset	9880
Seat joint	6000

Table 4.
Young's modulus from model calibration.

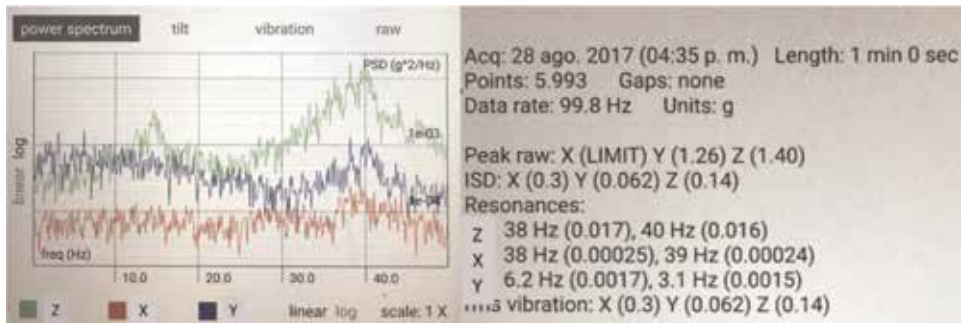


Figure 15.
 Experimental first modal mode.

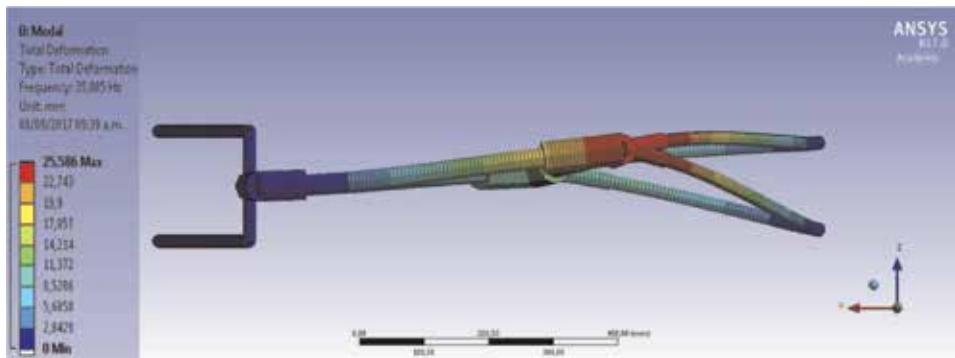


Figure 16.
 First modal mode using finite element analysis modal.

that the model represents satisfactorily the real bike frame. Then, these results can be used to fatigue analysis using the finite element method.

3.4 Dynamic response of the finite element model

Using the finite element model calibrated and validated, a dynamic response analysis was performed. The maximum reaction force at dropout joint zone was 114 N (**Figure 17**), the maximum stress was 114.6 MPa at the dropout, and the maximum displacement was 70.6 mm at the seat joint (**Figure 18, Table 5**). The

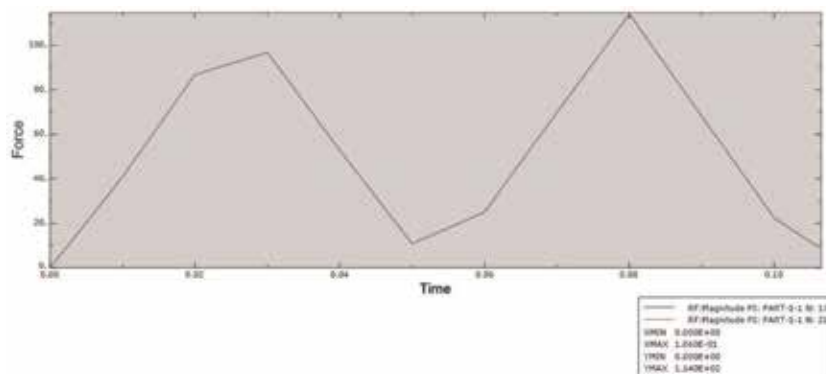


Figure 17.
 Reaction force profile at dropout joint zone.

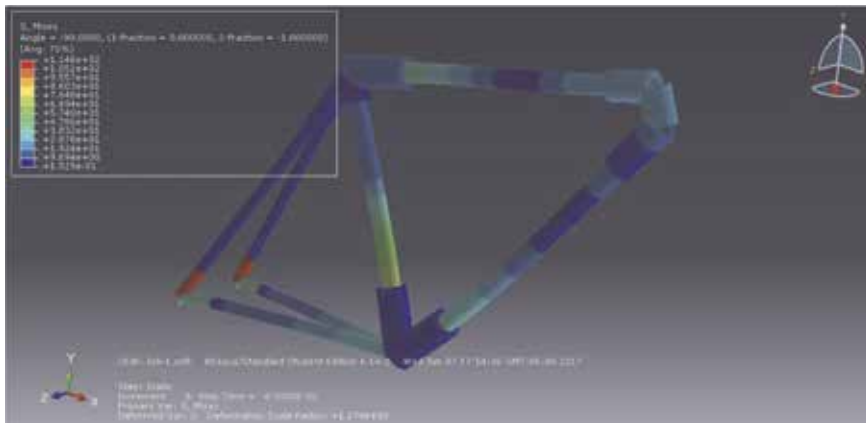


Figure 18.
Results of dynamical analysis simulation.

Control points	Maximum stress (MPa)	Maximum displacement (mm)
Seat joint	15.6	70.6
Bottom bracket	34.3	59.8
Fork	19.6	34.0
Dropout	114.6	0.0

Table 5.
Maximum stress and displacements at control points.

results show that the maximum stress occurs at dropout joints; hereby, this joint requires special attention.

From on the dynamic simulation of bike frame and assuming that the bike travel at 25 km/h, with a rider of 100 kg, and a road with contiguous bumps of 6 cm in height and 34 cm in length. The mechanical response at the intersection between the seat stay and the rear dropout was 114 MPa. Using a rate of application of 1351 cycles/km, 90 km is the distance a rider rides per week. Then, for a year the distance is 4680 km, and assuming a life of the bike of 10 years, the bike works:

$$N_{\text{applied}} = \left(4680 \frac{\text{kilometer}}{\text{year}} \right) \times (10 \text{ years}) \times \left(1351 \frac{N}{\text{kilometer}} \right) \quad (6)$$

$$N_{\text{applied}} = 6.3 \times 10^7 \text{ cycles} \quad (7)$$

Using the bamboo fatigue S-N curve reported by Song [24] and the stress profile obtained from the dynamic analysis (**Figure 19**), a fatigue analysis was performed. The life obtained was 1.7×10^9 cycles, the damage ratio, $N_{\text{applied}}/N_{\text{allowed}} = 0.037$; this indicates that the bike frame would last 26 times longer than its intended use; then the fatigue life of the frame will be more than 100 years, for these work conditions.

4. Discussion and conclusions

The relatively large scatter obtained for the elastic moduli can be explained by the non-exactly replicated nature of the bamboo material from plant to plant [25]. The differences of Young's moduli between thicker and thinner diameter bamboo

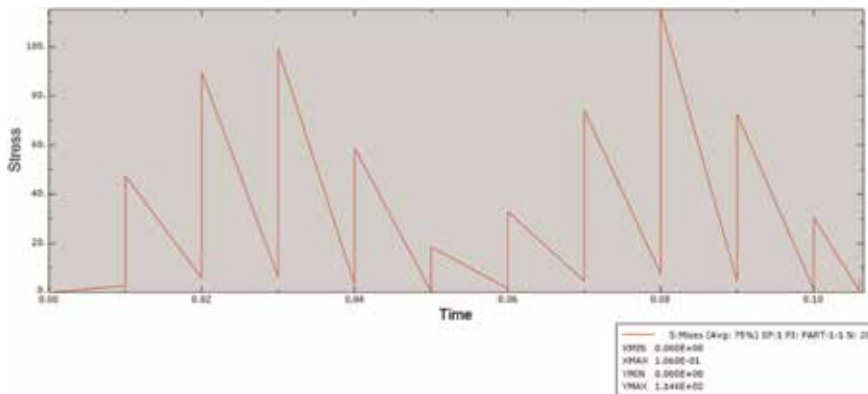


Figure 19.
Stress vs. time profile from dynamical response of the frame.

specimens may be explained by the differences between the compaction of the bamboo structure or the relation between the thickness and diameter of the bamboo samples, depending on the zone of the stem where the specimens were extracted.

In general, bamboo is thicker at the top than at the base of the culms [25]. Comparing the structures for the different diameters, the thinner diameter bamboo (**Figure 20**) has a structure more compact than the thicker diameter bamboo (**Figure 21**) and consequently higher Young's modulus [26].

The vascular bundle is a small longitudinal interstice of the bamboo stem (**Figures 20** and **21**). It affects directly the mechanical properties of the specimen due to these pores that act as stress concentrations. Kanzawa et al. [27] proposed to measure the maximum width and length of the vascular bundles (**Figure 22**). In this work, an average of 0.45 mm length and 0.38 mm width for thicker bamboo and 0.19 mm length and 0.14 mm width for thinner bamboo. Because the gap in the thinner bamboo is smaller than the thicker bamboo, the Young's modulus in the thinner is going to be higher making it more rigid.

In addition, a dynamic simulation of the bamboo frame was performed to obtain the acting forces at the bike frame and thus the stresses, at the most critical joint entering the rear dropout. With this information, the generic specimen representative of this joint was prepared to generate additional fatigue data to evaluate the useful life of the frame in future works (**Figure 23**).



Figure 20.
Microscopical section view for thinner bamboo specimen (1×).

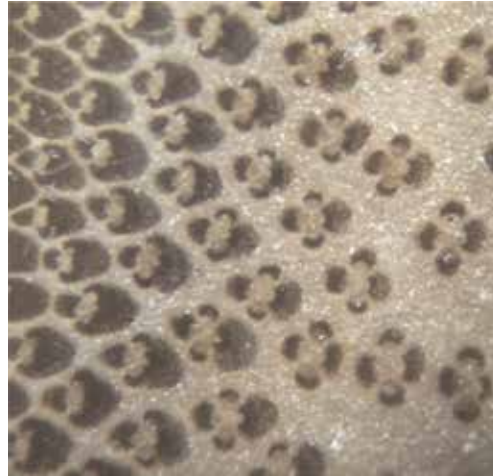


Figure 21.
Microscopical section view for thicker bamboo specimen (1×).

Finally, a methodology was proposed to evaluate the fatigue life of the bamboo bike frame from the experimental data reported for bamboo samples. However, the results should be taken as an approximation because the fatigue life of the bamboo bike frame has a high dependency on their joints. In this direction and in future works, it is necessary to perform fatigue experiments using the whole bike frame or at least to test the joints separated. This can be explained as there are substantial differences between the fatigue life of base material and the fatigue life of the final product. Also, some technical values of bamboo bike frames were obtained, so that

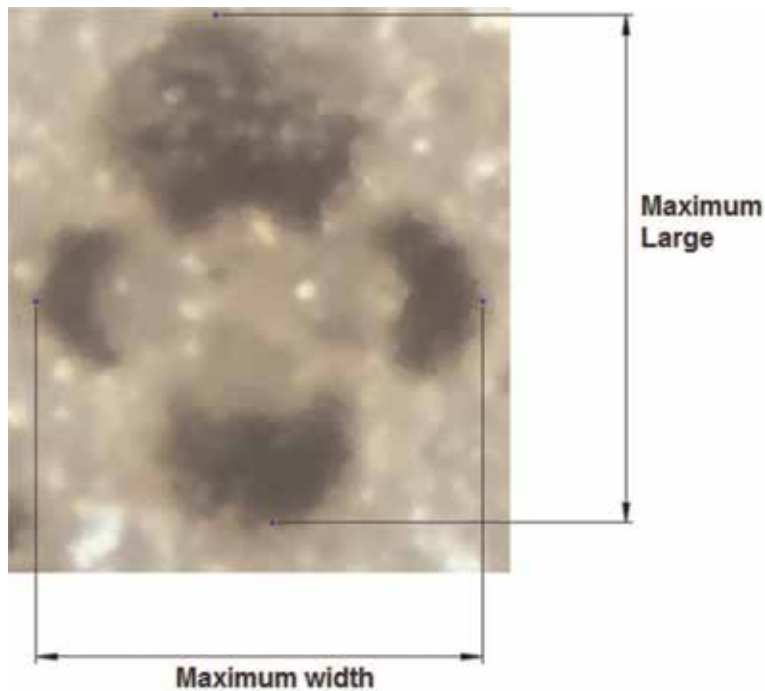


Figure 22.
Vascular bundle scheme in a section view of a bamboo specimen.



Figure 23.
Generic specimen representative of the rear dropout joint.

these will allow them to define the technical characteristics of the product and guarantee their operating conditions.

Acknowledgements

The author appreciates the support of the Universidad Autónoma de Occidente (Cali-Colombia).

Conflict of interest

The author declares that there is no conflict of interest regarding the publication of this chapter.

Author details

Juan P. Arango Fierro¹, Jose L. Arango Fierro¹ and Héctor E. Jaramillo Suárez^{2*}

¹ Mechanical Engineering Program, Autónoma de Occidente University (UAO), Cali, Colombia

² Energetic and Mechanical Department, Autónoma de Occidente University (UAO), Cali, Colombia

*Address all correspondence to: hjsuarez@uao.edu.co

IntechOpen

© 2019 The Author(s). Licensee IntechOpen. This chapter is distributed under the terms of the Creative Commons Attribution License (<http://creativecommons.org/licenses/by/3.0>), which permits unrestricted use, distribution, and reproduction in any medium, provided the original work is properly cited. 

References

- [1] Tai S-YTT, Veraart F, Davids M. How the Netherlands became a bicycle nation: Users, firms and intermediaries, 1860–1940. *Business History*. 2015;**57**: 257–289. DOI: 10.1080/00076791.2014.928695
- [2] Peterson LA, Londry KJ. Finite Element Structural Analysis: A New Tool for Bicycle Frame Design, (n.d.). <https://www.sheldonbrown.com/rinard/fea.htm> [Accessed: 26 April 2019]
- [3] Cicero S, Lacalle R, Cicero R, Fernández D, Méndez D. Analysis of the cracking causes in an aluminium alloy bike frame. *Engineering Failure Analysis*. 2011;**18**:36–46. DOI: 10.1016/j.engfailanal.2010.08.001
- [4] Liu TJ-C, Wu H-C. Fiber direction and stacking sequence design for bicycle frame made of carbon/epoxy composite laminate. *Materials & Design*. 2010;**31**: 1971–1980. DOI: 10.1016/j.matdes.2009.10.036
- [5] Lessard LB, Nemes JA, Lizotte PL. Utilization of FEA in the design of composite bicycle frames. *Composites*. 1995;**26**:72–74. DOI: 10.1016/0010-4361(94)P3633-C
- [6] Alves ME, Pereira TVC, Gomes O, Silva F, Toledo RD. The effect of fiber morphology on the tensile strength of natural fibers. *Journal of Materials Research and Technology*. 2013;**2**: 149–157. DOI: 10.1016/j.jmrt.2013.02.003
- [7] Zakikhani P, Zahari R, Sultan MTH, Majid DL. Extraction and preparation of bamboo fibre-reinforced composites. *Materials & Design*. 2014;**63**:820–828. DOI: 10.1016/j.matdes.2014.06.058
- [8] Osorio L, Trujillo E, Van Vuure AW, Verpoest I. Morphological aspects and mechanical properties of single bamboo fibers and flexural characterization of bamboo/epoxy composites. *Journal of Reinforced Plastics and Composites*. 2011;**30**:396–408. DOI: 10.1177/0731684410397683
- [9] Ben-Zhi Z, Mao-Yi F, Jin-Zhong X, Xiao-Sheng Y, Zheng-Cai L. Ecological functions of bamboo forest: Research and application. *Journal of Forestry Research*. 2005;**16**:143–147. DOI: 10.1007/BF02857909
- [10] BambooCo Bikes Project. EcoCultura. n.d. Available at: <https://ecoculturablog.wordpress.com/about-bambooco-bikes/> [Accessed: 26 April 2019]
- [11] Porque el diseño tiene sentido—talleres ambientales. Corporación Laboratorio de Diseño Sostenible, Coladisos—talleres de sensibilización ambiental, (n.d.). Available at: <https://coladisos.jimdo.com/> [Accessed: 26 April 2019]
- [12] Calfee Design—Bicycles and Components, Carbon Repair, DIY Bamboo Kits. n.d. <https://calfeedesign.com/> [Accessed: 26 April 2019]
- [13] Kingsley U, Imoisili PE, Adgidzi D. Finite element analysis of bamboo bicycle frame. *British Journal of Mathematics & Computer Science*. 2014;**5**:583–594
- [14] Covill D, Begg S, Elton E, Milne M, Morris R, Katz T. Parametric finite element analysis of bicycle frame geometries. *Procedia Engineering*. 2014;**72**:441–446. DOI: 10.1016/j.proeng.2014.06.077
- [15] Cheng Y-C, Lee C-K, Tsai M-T. Multi-objective optimization of an on-road bicycle frame by uniform design and compromise programming. *Advances in Mechanical Engineering*. 2016;**8**. DOI: 10.1177/1687814016632985

- [16] ASTM D790-17. Standard Test Methods for Flexural Properties of Unreinforced and Reinforced Plastics and Electrical Insulating Materials. ASTM International. 2017
- [17] VibSensor 2.1.1 Free Download. n.d. Available at: <https://vibsensor.soft112.com/> [Accessed: 30 April 2019]
- [18] SIMULIA. Software de simulación 3D-Dassault Systèmes®. n.d. <https://www.3ds.com/es/productos-y-servicios/simulia/> [Accessed: 30 April 2019]
- [19] Isight y SIMULIA™ Execution Engine - Dassault Systèmes®. n.d. <https://www.3ds.com/es/productos-y-servicios/simulia/productos/isight-y-simulia-execution-engine/> [Accessed: 30 April 2019]
- [20] Engineering Simulation & 3D Design Software. ANSYS. (n.d.). Available at: <https://www.ansys.com/> [Accessed: 30 April 2019]
- [21] ASTM F2711-08. Standard Test Methods for Bicycle Frames. ASTM International. 2012
- [22] ASTM F2043-13. Standard Classification for Bicycle Usage. ASTM International. 2015
- [23] UNE-EN 14766. Mountain-bicycles—Safety requirements and test methods. Asociación Española de Normalización. 2006
- [24] Song J, Utama J, Hu D, Lu Y. Fatigue characterization of structural bamboo materials under flexural bending. *International Journal of Fatigue*. 2017;**100**:126-135. DOI: 10.1016/j.ijfatigue.2017.03.016
- [25] Zhang Y, Yu W. Effects of thermal treatment on surface color, dimensional stability and mechanical properties of bamboo-based fiber composites. In: *Proceedings of 2012 International Conference on Biobase Material Science and Engineering*. 2012. pp. 132-136. DOI: 10.1109/BMSE.2012.6466197
- [26] Habibi MK, Lu Y. Crack propagation in bamboo's hierarchical cellular structure. *Scientific Reports*. 2014;**4**:5598. DOI: 10.1038/srep05598
- [27] Kanzawa E, Aoyagi S, Nakano T. Vascular bundle shape in cross-section and relaxation properties of Moso bamboo (*Phyllostachys pubescens*). *Materials Science and Engineering: C*. 2011;**31**:1050-1054. DOI: 10.1016/j.msec.2011.03.004

Use of Sustainable Materials in Self-Healing Concrete

*Busari Ayobami Adebola, Kupolati Williams Kehinde,
Loto Tolulope Roland, Sadiku Rotimi Emmanuel,
Jacques Snyman and Ndambuki Julius*

Abstract

Vulnerability to cracks is one of the major flaws of concrete infrastructure. The need to reduce the repair cost of this defect birthed the need for self-healing concrete. The incidence of cracks on concrete structures is a big threat to the stability of bridges, concrete roads, and other concrete infrastructures. This review assessed the use of self-healing technology on concrete using sustainable material as an active method of healing crack. This was done with the view of improving the stability, strength, and sustainability of infrastructure for national growth. The outcome of the review showed three prominent methods used in self-healing technology, which include autogenous healing, encapsulation of polymeric material, and microbial production of calcium-carbonate (biotechnological approaches). The review also revealed that calcium carbonate is a versatile material that can be used in crack healing for the filling of voids and improves the porosity of the concrete. The success of using the autogenous healing method depends on the diameter of the crack induced in the concrete structure. Additionally, this method can operate independently in different conditions regardless of the crack position. Correspondingly, lowering the water-cement ratio improves the autogenous healing process. The use of encapsulation of polymeric material and microbial production of calcium-carbonate methods showed that the presence of water and humidity is a critical factor to be considered. However, biotechnology using microbial action is prone to the production of ammonium ions (NH_4^+) through ureolytic activity, which results in nitrogen oxide emission into the atmosphere. Congruently, this may affect the durability of the concrete. Based on the uniqueness of this technology, it is recommended for the construction of sustainable infrastructure now and in the foreseeable future.

Keywords: self-healing, sustainability, concrete, asphalt, infrastructure

1. Introduction

The concept of self-healing concrete came from the principle of the self-healing properties of the skin, a form of natural defense mechanism. Nature plays an active role in this process by the development of clots to seal the break. This is the first process of skin healing. Self-healing technology is a novel branch of engineering aimed at the protection of concrete infrastructure from developing minor and major cracks. In a bid to improve the strength and durability of concrete

which, is one of the most pervasive material in the world in terms of infrastructural construction, self-healing technology was adopted. The use of concrete has been adopted in the design and construction of major infrastructure for national growth. Globally, concrete is widely used for the construction of structural and pavement elements [1]. The first usage of concrete in the world was in the Roman Empire, for the construction of the Pantheon, which is a very great structure and still in a functional state till date [2]. Concrete microstructure consists of a multiphase nanostructured material in the composite form which ages over time. The structural strength of concrete to a large extent depends on the micro- and nanoscale structural properties of the constituent element.

Despite the uniqueness of concrete infrastructures using these innovative materials, they are still prone to cracks. The research of [3] as reported in [4] revealed that concrete crack is a result of shrinkage, weather action, thermal stresses, and so on. Using self-healing technology, the strength and durability of concrete can be improved using biotechnological method by adopting the calcite precipitation principle. Self-healing technology seems to be very effective if the crack size is not more than 0.8 mm at the early age. However, the research of [4] revealed that hydro-gel encapsulation, vascular systems, and capsules are also good methods of self-healing concrete structures. Recent research focuses on the use of biotechnology and nanomaterial and the use of autogenous principle in self-healing technology which is espoused in this review.

1.1 Self-healing technology

The concept of self-healing was birthed some few decades due to the crack induced in some water retaining structures [5]. One of the major causes of concrete structural failure is the crack that can occur both in the plastic and hardened states [6–9]. The effect of crack may not be pronounced at the early stage, but it affects the mechanical strength at the late age which involves a lot of money for repair. The research of [7] showed that the active treatment of cracks seems to be an effective method as compared with the passive method of crack treatment.

The main concept was to make sure that this concrete structure affected by crack regained its mechanical strength by the hydration of the cement particles present in it [10, 11]. The concept of autogenic healing was used in this approach. According to [11], autogenous healing is a procedure where materials self-heal by nature. The same author avowed that this self-healing may be due to the formation of the carbonate or the hydroxide of carbon (calcium carbonate and calcium hydroxide). Additionally, the sedimentation of particles and swelling of the cement matrix in the concrete proved to be likely causative factors [12]. Asserted the problem of sedimentation and swelling can be averted and corrected using the self-healing capacity of the material composition of concrete.

Self-healing is an example of the active process of crack treatment. This method can operate independently in different conditions regardless of the crack position. The design of materials with healing properties is now gaining acceptance in concrete technology due to its numerous advantages.

1.2 Sustainable materials used in self-healing concrete

Sustainable structures provide environmentally friendly infrastructure, add long-term value to facilities, and improve the structural stability of structures. In concrete technology, different materials have been used in self-healing technology through three main strategies as shown in **Table 1**.

- i. Autogenous healing
- ii. Encapsulation of polymeric material
- iii. Microbial production of calcium-carbonate (biotechnological approaches)

1.2.1 Autogenous healing

This process of healing occurs when the continuity of two sides of cracks is restored without any external repair [25]. The same author avowed that water passing through concrete dissolve the calcium present in the cement mortar of concrete. The passage of water oftentimes is through the presence of cracks either in the hardened or plastic state. The calcium is transported in the insoluble form in the voids which eventually seal the crack without any external approach. The cracks did not only heal, but the mechanical properties were also restored. Additionally, the healed concrete becomes impermeable to water, thereby improving the mechanical strength. The principle of sealing cracks with calcium carbonate crystals from carbon dioxide in the surrounding soil, air, or water is the autogenous healing process. This reaction with the free calcium oxide and calcium hydroxide from the hydration of tricalcium silicate of the cement helps in crack healing also. However the main product that fills the void is the calcium carbonate [25].

Furthermore, the research of [26] showed that calcium carbonate is a versatile material that can be used in crack healing for the filling of voids and improved porosity. The research of [13, 14] showed that the presence of unhydrated cement in the concrete composition can affect autogenous healing. Additionally, the presence of water and humidity are also critical factors. The improvement of this approach of crack treatment depends on the water-cement ratio used in the concrete design. The lower the water-cement ratio, the better the autogenous healing process. Moreover, the success of this approach depends on the diameter of the crack induced in the concrete structure. The research of [18] showed that only cracks ranging from 0.1 to 0.3 can be filled using this approach.

1.2.2 Encapsulation of polymeric material

This process involves coating of the hydrophobic nanoparticles with an additional polymer layer. This process involves the foaming of the healing agent in the presence of moisture. It also involves the use of fibers in concrete. Encapsulation also uses capsules that can survive in concrete matrix. The addition of this capsule must not interfere with rheology and mechanical properties of the concrete both in the plastic and hardened states [27]; this factor according to the research of [19] as stated in [28] makes this method difficult. The research of [19, 28] stated that encapsulation involves the use of liquid, gas, or fine solid particles incorporating synthetic polymer in concrete technology. The research of [19] stated that to provide

Item	Material	Authors
1	Autogenous healing	[13–18]
2	Encapsulation of polymeric material	[19]
3	Biotechnological approaches	[20–24]

Table 1.
Self-healing methods.

protection to the constituents of the healing agent, the healing process begins when the capsule is opened to crack and the applied load breaks the capsule which invariably opens the healing agent [4]. This method can be categorized into the following:

1. Bacterial precipitation
2. Encapsulated chemical healing agents

The materials used in this method are as shown in **Table 2**.

The drawback of this approach is the tendency to repeat itself over time, and this invariably leads to repeated healing. Moreover, the moisture content required is high to make the healing process effective. Research of [42–44] showed that insufficient capillary action could render the method ineffective. The cost of production is another shortcoming of adopting this method.

1.3 Biotechnological approaches

Biotechnology involves the use of biomineralization in concrete technology. It is a process of mineral formation by living organism in nature. According to the same author, the process can be accomplished by inducing biological mineralization in an open environment as a result of uncontrolled microbial metabolic activity [21]. This process occurs in an anaerobic environment or at toxic-anoxic boundary as avowed by [22]. This is as a result of photosynthesis from bicarbonate solutions which results in carbonate production [45]. Besides, the use of this method is feasible when carbon dioxide is present in the surrounding. It can be inferred from this that photosynthesis pathway can be applied when concrete infrastructure is exposed to carbon dioxide in the presence of light.

Furthermore, the heterotrophic growth of different types of bacteria such as *Arthrobacter*, *Bacillus*, and *Rhodococcus* leads to the production of organic salt and carbonate minerals through urea analysis [46–48]. It also results in the increase in the pH consequently increasing the concentration of carbonate. This process is achieved by the conversion of carbon dioxide to carbonate [13, 49, 50]. Invariably, this aids the calcium carbonate precipitation which plays an active role in the blockage of cracks [51, 52]. Other bacteria used in self-healing technology are shown in **Table 3**.

The major drawback of this approach is the production of ammonium ions (NH_4^+) through ureolytic activity which results in nitrogen oxide emission into the atmosphere. It is estimated that the remediation of 1 m^2 of concrete needs 10 g/L

S/N	Material used	Authors
1	The use of hydrophobic solution adopting sonication technique	[29–31]
2	Melamine-based and polyurethane (PU) capsule material	[32, 33]
3	Perspex cast acrylic tubes and glass tubes	[34, 35]
4	Glass and ceramic cylindrical capsules	[36, 37]
5	Spherical capsules using sodium silicate solution	[32, 38]
6	The use of encapsulated epoxy in polystyrene-divinylbenzene microcapsules	[39]
7	Isocyanate prepolymer encapsulated in hollow cylindrical glass tubes	[34, 35]
8	Microcapsules to hold bisphenol F epoxy resin (Cailleux and Pollet)	[19]
9	Microcapsules made of silica gel with oil core were used	[41]

Table 2.
Materials used in encapsulation method of self-healing.

	Type of bacteria	Cement replacement	Importance	Source
1	<i>Bacillus aerius</i>	Rice husk	Strength, durability	[53]
2	<i>Bacillus megaterium</i>	No replacement	Compressive strength	[54]
3	<i>Bacillus sphaericus</i>	Normal concrete	Durability	[14, 55]
4	<i>Sporosarcina pasteurii</i>	Fly ash concrete	Strength, durability	
5	<i>Sporosarcina pasteurii</i>	Silica fume	Improvement in strength and durability	[56]
6	<i>Bacillus sphaericus</i>	No replacement	Alternative surface treatment for concrete	[52]
7	<i>Shewanella</i> species	No replacement	Compressive strength	[52, 57–59]
8	<i>Bacillus subtilis</i>		Compressive strength	[59]

Table 3.
Bacteria used in self-healing technology.

Item	Self-healing materials	Authors
1	Encapsulated sealants and adhesive	[19]
2	The adhesives can be stored in short fiber	[39, 40]
3	The adhesives can be stored in long fiber	[43, 60–62]
4	Expansive component in the concrete	[61, 62]
5	Bacteria to stimulate the self-healing mechanism	[63–65]

Table 4.
Self-healing materials.

of urea which produces 4.7 g of nitrogen. This amount is about one third of the nitrogen that is produced by each person everyday [52]. Furthermore, the presence of excessive ammonium in the concrete matrix increases the risk of salt damage by converting to nitric acid. Hence, an optimization to find the required amount of urea is beneficial to avoid excessive ammonium emission.

For cement-based materials, different methods can be found in literature (Table 4); the first breakthrough involves the use of encapsulated sealant or adhesive [19]. These are stored in fibers [39, 40] or in longer tubes [60]. Filling of the voids and cracks with expansive material can propel carbonation when water percolates [61, 62]. The use of bacteria to stimulate the self-healing mechanism is also a promising alternative [63–65]. Nanotechnology is a unique branch of science that uses nanomaterial in the design, construction, repair, and protection of infrastructures. It deals with the application of the physical world in a small scale by assessing the atom, molar molecule, and similar molecule of material [66–68]. With the increasing development of nanotechnology, the use of tiny nanoparticles and nanomaterial also increased in modern technologies [69].

2. Conclusions

This review assessed the use of self-healing technology for sustainable infrastructural development. Relevant literatures on the use of self-healing technology in concrete technology were assessed. The main concept was to make sure that concrete structure affected by crack regained its mechanical strength by the hydration of the cement particles present in it. Self-healing mechanism using the

autogenous healing, encapsulation of polymeric material, and microbial production of calcium carbonate (biotechnological approaches) was studied. The review revealed that:

- i. The major shortcoming using capsulation method is its repeatability over a long time which can also lead to repeated healing over a long time.
- ii. Capsulation method requires high amount of moisture to make it effective.
- iii. The cost of production of capsules for large concrete structures is also a major flaw of this approach.
- iv. Insufficient capillary force of the crack causes lower than expected amount of healing agent being released into the matrix using capsulation method.
- v. Heterotrophic growth of different genera of bacteria results in the production of carbonate minerals; invariably, this aids the calcium carbonate precipitation which plays an active role in the blockage of cracks.
- vi. The activities of these bacteria lead to an increase in the pH of the medium, thereby increasing the carbonate concentration.
- vii. Excessive production of ammonium in the concrete matrix using biotechnological approach increases the risk of salt damage by conversion to nitric acid.
- viii. The effectiveness of autogenous healing of crack depends on the water-cement ratio used in the concrete design. The success of this approach depends on the diameter of the crack induced in the concrete structure.

3. Recommendations

- i. Future studies should focus on the production of some of these self-healing materials in large quantity.
- ii. Future studies should also focus on the effect of this technology on corrosion considering the versatile usage of reinforced concrete for infrastructural construction.
- iii. It is also recommended that the use of biotechnology in self-healing should be done with caution and the right technology should be used because of its effect on durability.

Acknowledgements

The authors are grateful to the management of Covenant University for the access to the articles used for this review.

Conflict of interest

The authors declare that there is no conflict of interest.

Author details

Busari Ayobami Adebola^{1,2*}, Kupolati Williams Kehinde², Loto Tolulope Roland³,
Sadiku Rotimi Emmanuel^{2,4}, Jacques Snyman² and Ndambuki Julius²

1 Department of Civil Engineering, Covenant University, Ota, Ogun State, Nigeria

2 Department of Civil Engineering, Tshwane University of Technology, Pretoria,
South Africa

3 Department of Mechanical Engineering, Covenant University, Ota, Ogun State,
Nigeria

4 Institute of Nano Engineering Research (INER) and Department of Chemical,
Metallurgical and Materials Engineering, Tshwane University of Technology,
Pretoria, South Africa

*Address all correspondence to: ayobami.busari@covenantuniversity.edu.ng

IntechOpen

© 2020 The Author(s). Licensee IntechOpen. This chapter is distributed under the terms of the Creative Commons Attribution License (<http://creativecommons.org/licenses/by/3.0>), which permits unrestricted use, distribution, and reproduction in any medium, provided the original work is properly cited. 

References

- [1] Oloyede SA. Tackling causes of frequent building collapse in Nigeria. *Journal of Sustainable Development*. 2010;**7**(3):127-132
- [2] Delatte NJ. Lessons from roman cement and concrete. *ASCE Journal of Professional Issues in Engineering Education and Practice*. 2008;**127**(3):109-115
- [3] ACI (American Concrete Institute). *Causes, Evaluation, and Repair of Cracks in Concrete Structures*. Farmington Hills, MI; 2007
- [4] Souradeep G, Kua HW. Encapsulation technology and techniques in self-healing concrete. *Journal of Materials in Civil Engineering*. 2016;**28**(12):04016165. DOI: 10.1061/(ASCE)MT.1943-5533.0001687
- [5] Edvardsen C. Water permeability and autogenous healing of cracks in concrete. *ACI Materials Journal*. 1999;**96**(4):448-454
- [6] Le Métayer-Levrel G, Castanier S, Oriol G, Loubière JF, Perthuisot JP. Applications of bacterial carbonatogenesis to the protection and regeneration of limestones in buildings and historic patrimony. *Sedimentary Geology*. 1999;**126**:25-34. Available from: https://www.researchgate.net/publication/292208328_Bioconcrete_next_generation_of_self-healing_concrete [Accessed: 26 March 2019]
- [7] Warscheid T, Braams J. Biodeterioration of stone: A review. *International Biodeterioration & Biodegradation*. 2000;**46**:343-368
- [8] Achal V, Mukherjee A, Sudhakara Reddy M. Microbial concrete: Way to enhance the durability of building structures. *Journal of Materials in Civil Engineering*. 2011;**23**:730-734
- [9] Achal V, Mukerjee A, Sudhakara Reddy M. Biogenic treatment improves the durability and remediates the cracks of concrete structures. *Construction and Building Materials*. 2013;**48**:1-5
- [10] Ter Heide N. Crack healing in hydrating concrete [MSc-thesis]. The Netherlands: Delft University of Technology; 2005
- [11] Granger S, Loukili A, Pijaudier-Cabot G, Behloul M. Self-healing of cracks in concrete: From a model material to usual concretes. In: *Proceedings of the 2nd International Symposium on Advances in Concrete Through Science and Engineering*; Quebec City, Canada; 2006
- [12] Schlangen E, Joseph C. Self-healing processes in concrete. In: Ghosh SK, editor. *Self-Healing Materials: Fundamentals, Design Strategies and Applications*. Weinheim: Wiley-VCH; 2008. pp. 141-182
- [13] Van Tittelboom K et al. Comparison of different approaches for self-healing concrete in a large-scale lab test. *Construction and Building Materials*. 2016;**107**:125-137
- [14] Wang J, Dewanckele J, Cnudde V, Van Vlierberghe S, Verstraete W, De Belie N. X-ray computed tomography proof of bacterial-based self-healing in concrete. *Cement and Concrete Composites*. 2014;**53**:289-304
- [15] Clear CA. *Effects of Autogenous Healing upon the Leakage of Water through Cracks in Concrete*. USA: Cement and Concrete Association; 1985
- [16] Reinhardt HW, Joos M. Permeability and self-healing of cracked concrete as a function of temperature and crack width. *Cement and Concrete Research*. 2003;**33**(7):981-985

- [17] Şahmaran M, Keskin SB, Ozerkan G, Yaman IO. Self-healing of mechanically-loaded self-consolidating concretes with high volumes of fly ash. *Cement and Concrete Composites*. 2008;**30**:872-887
- [18] Ahn TH, Kishi T. The effect of geo-materials on the autogenous healing behavior of cracked concrete. In: ICCRRR II; Cape Town, South Africa; 2009. pp. 125-126
- [19] Dry C. Matrix cracking repair and filling using active and passive modes for smart timed release of chemicals from fibers into cement matrices. *Smart Materials and Structures*. 1994;**3**:118-123
- [20] Tebo BM, Johnson HA, McCarthy JK, Templeton AS. Geomicrobiology of manganese (II) oxidation. *Trends in Microbiology*. 2005;**13**:421-428
- [21] Ramachandran SK, Ramakrishnan V, Bang SS. Remediation of concrete using micro-organisms. *ACI Materials Journal*. 2001;**98**:3-9
- [22] Hammes F, Verstraete W. Key roles of pH and calcium metabolism in microbial carbonate precipitation. *Reviews in Environmental Science and Biotechnology*. 2002;**1**:3-7
- [23] Barton LL, Northup DE. *Microbial Ecology*. United State: Wiley-Blackwell; 2011
- [24] Wu M, Johannesson B, Geiker M. A review: Self-healing in cementitious materials and engineered cementitious composite as a self-healing material. *Construction and Building Materials*. 2012;**28**:571-583
- [25] Neville AM, Brooks JJ. *Concrete Technology*. United Kingdom: Pearson; 2010
- [26] Hearn N. Self-sealing, autogenous healing and continued hydration: What is the difference? *Materials and Structures*. 1998;**31**:563-567
- [27] Seifan M, Samani AK, Berenjian A. Bioconcrete: Next generation of self-healing concrete. *Applied Microbiology and Biotechnology*. 2006;**100**(6):2591-2602. DOI: 10.1007/s00253-016-7316-z
- [28] Dragostin I, Dragostin O, Pelin A-M, Grigore C, Zamfir CL. The importance of polymers for encapsulation process and for enhanced cellular functions. *Journal of Macromolecular Science. Part A*. 2017;**54**(7):489-493
- [29] Kessler M, Sottos N, White S. Self-healing structural composite materials. *Composites Part A: Applied Science and Manufacturing*. 2003;**34**(8):743-753
- [30] Brown EN, White SR, Sottos NR. Retardation and repair of fatigue cracks in a microcapsule toughened epoxycomposite. Part II: In situ self-healing. *Composites Science and Technology*. 2005;**65**(15):2474-2480
- [31] Feng X, et al. Self-healing mechanism of a novel cementitious composite using microcapsules. In: *Proceedings, International Conference on Durability of Concrete Structures*; Hangzhou, China: Zhejiang University; 2008
- [32] Pelletier M, Brown R, Shukla A, Bose A. Self-healing concrete with a microencapsulated healing agent. Technical Report; Kingston, RI: University of Rhode Island; 2011
- [33] Liu H, et al. Self-healing of concrete cracks using hollow plant fibres. In: *Proceedings, 2nd International Conference on Self-Healing Materials*; Chicago; 2009a
- [34] Thao TDP. Quasi-brittle self-healing materials: Numerical modelling and applications in civil engineering [Ph.D. dissertation]. Singapore: National University of Singapore; 2011

- [35] Thao TDP, Johnson TJS, Tong QS, Dai PS. Implementation of self-healing in concrete-proof of concept. *The IES Journal Part A: Civil & Structural Engineering*. 2009;2(2):116-125
- [36] Van Tittelboom K, Adesanya K, Dubruel P, Van Puyvelde P, DeBelie N. Methyl methacrylate as healing agent for self-healing cementitious materials. *Smart Materials and Structures*. 2011a;20(12):125016
- [37] Van Tittelboom K, De Belie N. Self-healing concrete: Suitability of different healing agents. *International Journal of 3 R's*. 2010;1(1):12-21
- [38] Huang H, Ye G, Leung C, Wan K. Application of sodium silicate solution as self-healing agent in cementitious materials. In: *Proceedings, International RILEM Conference on Advances in Construction Materials Through Science and Engineering*; Bagnaux, France: RILEM Publications SARL; 2011. pp. 530-536
- [39] Li W, Jiang Z, Yang Z, Zhao N, Yuan W. Self-healing efficiency of cementitious materials containing microcapsules filled with healing adhesive: Mechanical restoration and healing process monitored by water absorption. *PLoS ONE*. 2013;8(11):1-8
- [40] Qian SZ, Zhou J, Schlangen E. Influence of curing condition and pre-cracking time on the self-healing behavior of engineered cementitious composites. *Cement and Concrete Composites*. 2010b;32:686-693
- [41] Yang Z, Hollar J, He X, Shi X. A self-healing cementitious composite using oil core/silica gel shell microcapsules. *Cement and Concrete Composites*. 2011;33(4):506-512
- [42] Dong B, Wang Y, Fang G, Han N, Xing F, Lu Y. Smart releasing behavior of a chemical self-healing microcapsule in the stimulated concrete pore solution. *Cement and Concrete Composites*. 2015;56:46-50
- [43] Joseph C, Jefferson A, Cantoni M. Issues relating to the autonomic healing of cementitious materials. In: *Proceedings 1st International Conference on Self-Healing Materials*; Netherlands: Springer; 2007. p. 1
- [44] Sun L, Yu WY, Ge Q. Experimental research on the self-healing performance of micro-cracks in concrete bridge. *Advanced Materials Research*. 2011;250:28-32
- [45] Mann S. *Biom mineralization: Principles and Concepts in Bioinorganic Materials Chemistry*. New York: Oxford University Press; 2001
- [46] De Muynck W, Cox K, De Belie N, Verstraete W. Bacterial carbonate precipitation as an alternative surface treatment for concrete. *Construction and Building Materials*. 2008;22(5):875-885
- [47] Jonkers HM, Thijssen A, Muyzer G, Copuroglu O, Schlangen E. Application of bacteria as self-healing agent for the development of sustainable concrete. *Ecological Engineering*. 2010;36:230-235
- [48] Wiktor V, Jonkers HM. Quantification of crack-healing in novel bacteria-based self-healing concrete. *Cement and Concrete Composites*. 2011;33:763-770
- [49] Stocks-Fischer S, Galinat JK, Bang SS. Microbiological precipitation of CaCO₃. *Soil Biology and Biochemistry*. 1999;31:1563-1571
- [50] Pacheco-Torgal F, Labrincha JA. Biotech cementitious materials: Some aspects of an innovative approach for concrete with enhanced durability. *Construction and Building Materials*. 2013;40:1136-1141

- [51] Dick J, De Windt W, De Graef B, Saveyn H, Van Der Meeren P, Belie N D, et al. Bio-deposition of a calcium carbonate layer on degraded limestone by *Bacillus* species. *Biodegradation*. 2006;**17**:357-367
- [52] Muynck W, Belie N, Verstraete W. Improvement of concrete durability with the aid of bacteria. In: *Proceedings of the First International Conference on Self Healing Materials*; Noordwijk aan zee, The Netherlands; 2007
- [53] Siddique R, Singh K, Kunal M, Corinaldesi Singh V, Rajor A. Properties of bacterial rice husk ash concrete. *Construction and Building Materials*. 2016;**121**:112-119
- [54] Andalib R, Majid MZA, Hussin MW, Ponraj M, Keyvanfar A, Mirza J. et al. Optimum concentration of *Bacillus megaterium* for strengthening structural concrete. *Construction and Building Materials*. 2016;**118**:180-193
- [55] Chahal N, Siddique R, Rajor A. Influence of bacteria on the compressive strength, water absorption and rapid chloride permeability of fly ash concrete. *Construction and Building Materials*. 2012;**28**:351-356
- [56] Chahal N, Siddique R, Rajor A. Influence of bacteria on the compressive strength, water absorption and rapid chloride permeability of concrete incorporating silica fume. *Construction and Building Materials*. 2012;**37**(1):645-651
- [57] Siddique R, Kaur N. Effect of ureolytic bacteria on concrete properties. *Construction and Building Materials*. 2011;**25**(10):3791-3801
- [58] Gosh SK, editor. *Self-Healing Materials; Fundamentals, Design Strategies and Applications*. USA: Wiley Blackwell; 2008
- [59] Khaliq W, Ehsan MB. Crack healing in concrete using various bio influenced self-healing techniques. *Construction and Building Materials*. 2016;**102**:349-357
- [60] Nishiwaki T, Mihashi H, Jang B-K, Miura K. Development of self-healing system for concrete with selective heating around crack. *Journal of Advanced Concrete Technology*. 2006;**4**(2):267-275
- [61] Hosoda A, Kishi T, Arita H, Takakuwa Y. Self healing of crack and water permeability of expansive concrete. In: *1st International Conference on Self-Healing Materials*; Noordwijk, Holland; 2007
- [62] Sisomphon K, Çopuroğlu O, Fraaij ALA. Durability of blast-furnace slag mortars subjected to sodium monofluorophosphate solution curing. In: *Proceedings 4th International Conference on Construction Materials: Performance, Innovations and Structural Implications*; (24) (PDF) *Autogenous self-healing of cement with expansive minerals-I: Impact in early age crack healing*; Nagoya, Japan; 2009
- [63] Bang SS, Galinat JK, Ramakrishnan V. Calcite precipitation induced by polyurethane-immobilized *Bacillus pasteurii*. *Enzyme and Microbial Technology*. 2001;**28**:404-409
- [64] Jonkers H, Schlangen E. In: Schmets AJM, van der Zwaag S. editors, *Proceedings of the First International Conference on Self Healing Materials*; 18-20 April 2007; Noordwijk aan Zee, The Netherlands: Springer; 2007
- [65] De Muynck W, Debrouwer D, De Belie N, Verstraete W. Bacterial carbonate precipitation improves the durability of cementitious materials. *Cement and Concrete Research*. 2008;**38**:1005-1014
- [66] Mansour NM, Zohre D. Nanotechnology's role in

optimization of energy consumption in buildings. In: 5th Conference of Fuel Consumption Optimization of the Country; 2006

[67] Khandve PV. Nanotechnology for building material. *International Journal of Basic and Applied Research*. 2014;**4**:146-151

[68] BASF. Nanotechnology for Simple, Successful Concrete Repair—A Specifiers' Guide. Germany: BASF Company; 2008. pp. 1-24

[69] Seaton A. Nanotechnology and the occupational physician. *Occupational Medicine*. 2006;**56**:312-316

Nano-Modification of Building Composite Structures

Evgeny Chernishov, Olga Artamonova and Galina Slavcheva

Abstract

The paper reviews the theoretical framework of nano-modification principles of building composites and experimental verification of these principles. The concepts of nano-modification of building composite structures are studied. The paper also suggests the conceptual model of the nano-modification from the point of view of the evolutionary model of a solid-phase formation depending on the kinetics of heterogeneous processes. The technological tools of nano-modification of building composites are substantiated. Cement-based materials are shown as an object of nano-modification. Their hydration kinetics, phase composition, microstructure, and strength characteristics are investigated. The results are analyzed based on the special performance criteria which confirm that the efficiency of cement-based materials technological cycle can be improved by nano-modification.

Keywords: cement system, nano-additives, hydration, hardening, structure, strength

1. Introduction

The scientific substantiation of the principles of structure management at the nanoscale level is the key point in the development of high-performance and ultra-high-performance concrete [1, 2]. It is the class of materials, which includes the nanostructured elements as part of their structure. Moreover, to regulate their structure and properties, it seems logical to use nanoscale various types of particles. Nowadays, the problems of synthesis and construction of high-performance and ultra-high-performance concrete structures in building technologies more actively rely on nano-concepts and nano-approaches. It is relevant to identify the potential possibilities and limitations of the application of nanotechnological approaches in solving specific problems of the technology of building materials.

2. Theoretical framework

While applying the technologies of building materials and stages of transitions in the processes of forming the structures of their solid-phase state, it is necessary to keep in mind hydration (lime, gypsum, cement), hydrothermal-synthesis (silicate autoclave) hardening systems, and thermal-synthesis (ceramics, glass) composites (**Table 1**) [1].

The fixed assets of the “nano tool,” implemented in construction material technologies, include the influence and effect of “**top-down**” and “**bottom-up**” nanotechnological approaches.

Type of HS	Hydration synthesis		Hydrothermal synthesis	Thermal synthesis
Form of HS	Monomineral	Polymineral	Polymineral	Monomineral
Synthesis technology	Sol gel	Sol gel	Hydrothermal synthesis	Thermal synthesis
Precursors for the synthesis of HS	Lime	Portland cement	Basic and acid oxide	Basic oxide
The composition of the hardening systems	Portlandite	Hydrosilicates and hydroaluminates of calcium, hydrogrenades, calcium hydrosulfoaluminates	Hydrosilicates and hydroaluminates of calcium, hydrogrenades, calcium hydrosulfoaluminates	Solid solutions based on individual oxides
The resulting building composite	Portland-calcium-calcium and portland-alum-silicate	Cement concrete	Dense and cellular silicate concrete	Constructional and functional nanoceramics

Table 1.
Hardening systems (HS) for design and synthesis structures of building composites.

The “nano” “top-down” approach is based on the use of the phenomenon of changes in the energy state of the structure and, accordingly, the physical and/or physicochemical activity of surface and internal volumes of particles of a solid as they are crushed by mechanical or physical methods.

The effectiveness of the principle is determined not only by the nano- and micro-size of particles but also by the measure of the amorphization of their surface volumes. Amorphization is expressed in the “saturation” of volumes with structural defects of the nano-size range. The principle is the basis of the mechanochemical activation of the components of raw mixtures in the technologies of building materials.

The “nano” “bottom-up” principle is based on the management of condensation phenomena in the evolutionary route of the formation of a solid-phase state of a substance in hydration, hydrothermal-synthesis, and thermal-synthesis hardening systems. The effectiveness of the principle is determined by the possibilities of influencing the development of stages, transitions, selections in the evolutionary route, and, in general, the kinetics of heterogeneous processes of hydration, colloidation, and crystallization in systems (mixtures) of basic and acid oxides upon receipt of building materials.

“Nano tool,” based on “top-down” principles, includes mechanochemical activation of the substance during the dispersion of the initial components of the raw mixes, physical and chemical activations during the high-temperature processing of the mixture components, compulsory compaction of particles of components of a mixture, etc. “Nano tool,” implemented in the principles of “bottom-up,” includes the means of controlling the solubility of components and the degree of saturation of the system with cations and anions; methods of changing the rate of condensation and crystallization through thermal or other physical effects; methods of changing the spatial and geometric environment in the system by introducing additives of nano-modifiers, for example, nanoparticles with both related and non-related crystal-chemical structure of the synthesized compounds; and techniques for changing the state of the surface of solid particles when using additives of surface-active substances, etc.

The “top-down” and “bottom-up” principles act in a systemic unity, and their presence in nanotechnology of building materials is an objective fact. The principles operate within the framework of their own laws. However, it happens within the single process of structure formation and the formation of a solid state of materials. The effects of the above principles in nanotechnology are articulated and super-imposed based on the principle of “top-down,” which is expressed in the role and influence of the phenomenon of mechanochemical metamorphism of the structure of the initial components (according to Avvakumov, Hodakov, etc.) and from the “bottom-up” principle (the phenomenon of stereochemical and topochemical memory according to Bokiy, Belov, Mamedov, Oleinikov, etc.). The principle of “top-down” has a precursor (preparatory) role, ensuring the activation of the initial components of raw mixes in nanotechnology. The evolutionary route of the formation of the nanostructure of the solid phase on the principle of “bottom-up” is developed in the framework of the action of this role.

In the compositional structure of conglomerate building materials, two types of structures are distinguished according to their origin (“genesis”). The first, related to macro-, meso- and microstructure, is the result of the addition of ready-made granular particles. The second one, related to the micro-, submicro-, and nanostructure, is the result of the synthesis of particles in the evolutionary route of their formation. Both types of structures in their genesis are integrated in the composite. The genesis (formation) of the first type of the structure is carried out according to the concept and bases of the mechanics of granular media; at the same time, the nanotechnological top-down principle with the corresponding nano-modifying effects can be realized at the same time. The genesis of the second type of structure is carried out according to the concepts and bases of the condensation mechanisms, which is implemented in the framework of the action of the nanotechnological principle “bottom-up,” which predetermines the effects of nano-modification in the evolutionary route of the formation of a solid state. Thus, the development of the technology of nano-modification of the hardening system structures and construction composites should proceed from the systemic unity of the “top-down” and “bottom-up” principles.

2.1 Evolutionary route of solid formation

Heterogeneity is the main feature of all hardening systems; therefore, when analyzing an evolutionary model, one should consider a heterogeneous composition consisting of different dispersion of solid particles placed in a liquid or gaseous medium (internal medium of the system) and in contact with the external environment space from which matter, thermal, mechanical energy, etc. can be introduced into the hardening system. When considering the processes of evolution of a solid substance in a heterogeneous system, a microvolume can be distinguished at a certain homogeneity. In this conditionally homogeneous system, the nucleation of a solid phase occurs.

In the chemical technology of homogeneous system substances, three determining methods for the synthesis and nucleation of solid particles (including nanoparticles) are distinguished: the ones leading to the formation of a new phase; the method based on the high-temperature reactions of interaction of two or more substances, leading to the formation of an insoluble product; and the method of condensation from the gas phase, when, as a result of redox reactions or hydrolysis reactions occurring in the gas phase, the solid phase is released.

In disclosing and analyzing a general evolutionary model of the formation of a solid, one can follow the interpretations of Melikhova [3]. In accordance with modern concepts applicable to systems of any composition, the following main stages

in the evolution of a substance can be distinguished in the formation of a solid: the nucleation of a solid phase, particle growth, agglomeration, and spontaneous transformation in time (Figure 1). In this case, it is necessary to speak of three evolutionary transitions between the stages and, accordingly, the phenomena of molecular, topological, and morphological selection. In the evolution of solids, two branches of the process development could be implemented: the left, corresponding to small (pre-foreign) supersaturations, and the right, corresponding to large (super-foreign) supersaturations of the phase-forming macrocomponent.

It is important to emphasize that each stage corresponds to a certain range of sizes of solid particles based on them. The size scale shown in Figure 1 illustrates dimensional and geometric boundaries and limits. It is clear that we can use the “arsenal of nano” most significantly at the stages of nucleation of the phase and growth of particles; at other stages, other physicochemical methods of technological impact, affecting the micro- and macroscale of the evolutionary process, become priorities. This should be taken into account when developing methods of influence on each of the considered stages and transitions of the evolutionary route. Based on this, a detailed discussion of the determining stages of the evolutionary route and transitions between them should be carried out, bearing in mind the rationale and formation of “nanotools” but not only “nano” in the technology of building materials, if we take into account the problem of modifying the structure on all its scale levels.

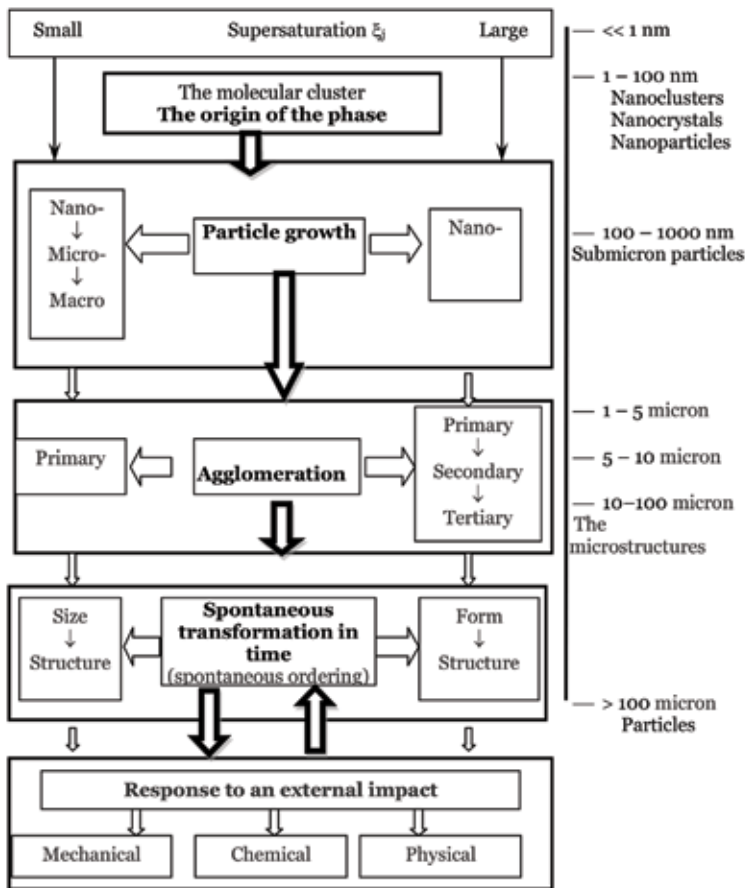


Figure 1. The evolutionary path of formation of solid substances and “dimensional scale” of their structural components.

2.2 The “nucleation of the solid-phase” stage

According to the Gibbs-Volmer thermodynamic theory, the formation of a new phase is possible with a certain critical degree of supersaturation, which depends both on the nature of the starting materials and on the presence of condensation nuclei that can be introduced into the system from the outside. The formation of nuclei becomes possible when a certain (critical) degree of supersaturation of a solution is reached by the substance whose molecules are involved in the formation of a new phase.

Thus, bearing in mind the possibilities of nanotechnological influence on the stage of particle nucleation, first of all, one should speak about such control factors as the creation of supersaturation and the introduction of condensation nuclei (nuclei) from outside. The supersaturation can be created in two ways: by increasing the concentration of the substance molecules in the medium and (or) by decreasing its solubility.

2.3 “Growth of particles of phase-forming substance” stage

Each nucleated particle, being in supersaturated media, attaches to itself the molecules of the medium more often than their separation from the particles. In order to join a particle, the molecule moves from the volume of the medium to the surface of the particle, is adsorbed on it, and then, migrating along the surface, takes the place where its connection with the particle becomes energetically favorable and in this sense strong enough to fix on its place. The probability of fixing a molecule depends on its size, shape, and electronic structure. In fact, controlled molecular selection occurs on the surface of the growing particle.

Considering the decrease in the free energy of the system, a phenomenon of *molecular selection*, which develops in it, results in the following process: nuclei become clusters of molecules containing only slightly different in structure and size of the molecule.

From a nanotechnological point of view, it is possible to keep in mind the tasks of changing the concentration conditions of crystallization as well as the use of nano-additives with a crystal-chemical structure similar to the germ of the phase and providing targeted acceleration of the particles’ growth processes of the phase-forming substance [4–6] and their morphological structure—finification. In connection with the three global transitions indicated by us during the evolution of a solid substance, it is expedient to refine the classification of additives, dividing them according to the size attribute into nanoscale, ultrafine, and microdisperse (Table 2). In the general case, the structure-forming participation and the modifying influence of nanoscale modifiers can be the result of interrelated mechanisms.

2.4 “Agglomeration” stage

After the accumulation of a sufficient number of particles in the system, when the probability of particles meeting and growing together becomes co-measurable with the probability of their molecular growth, the process of agglomeration begins.

There comes a second evolutionary transition “particle growth agglomeration.” In this case, the main phenomenon is the topological selection of ordered aggregates, which consists in the fact that the medium destroys and eliminates disordered aggregates and contributes to the formation of ordered forms consisting of particles with similar morphological parameters.

№	Type systems	The name and the chemical composition	Particle size and morphology	The mechanism of action
1	The nano-sized	Nano-sized silica $\text{SiO}_2 \cdot n\text{H}_2\text{O}$	$\varnothing = 5\text{--}10$ nm, spherical particles	(1) Direct chemical involvement of nanoparticles (NP) in heterogeneous processes of phase formation of hydrated compounds; (2) the catalytic role NP as nucleation (growth of a new phase)
2		Sol.Fe(OH)_3	$\varnothing = 5\text{--}10$ nm, spherical particles	
3		Sol.Al(OH)_3	$\varnothing = 30\text{--}50$ nm, spherical particles	
4		Montmorillonite, a synthetic $(\text{Na, Ca})_{0.3}(\text{Al, Mg})_2\text{Si}_4\text{O}_{10}(\text{OH})_2 \cdot n\text{H}_2\text{O}$	$\sim 5\text{--}10$ nm, hexagonal plates	
5		Chrysotile nanotubes $[\text{Mg}_3\text{Si}_2\text{O}_5(\text{OH})_4]$	$\varnothing = 25\text{--}50$ nm, $l = 100\text{--}700$ nm, a tubular structure	
6	The zeolite sol-type zeolite NaX, ratio $\text{Si/Al} = 1.3\text{--}1.5$	Carbon nanotubes fulleroid-type carbon content $\sim 99\%$	$\varnothing = 2$ nm; $l = 200$ nm, tubes of graphite cloth	Increased packing density of particulate addition, changing the porosity of the material structure
7			$\varnothing = 0.8\text{--}1.2$ nm reticular structure	
8		Ultradispersed	“Astralen—S” water-soluble fullerene analogue carbon content $\sim 99\%$	
9		Micro silica $\text{SiO}_2 \cdot n\text{H}_2\text{O}$	$\sim 100\text{--}300$ nm	
10	Microdispersed	Montmorillonite—natural $(\text{Na, Ca})_{0.3}(\text{Al, Mg})_2\text{Si}_4\text{O}_{10}(\text{OH})_2 \cdot n\text{H}_2\text{O}$	< 1 μm layered, leaf structure	Zoning structure hardening
11		Shungite—C 60–70%; ash 30–40%; SiO_2 –35–50%; Al_2O_3 –10–25%	0.1–10 μm , graphite-like globules	
12		Bergmeal— SiO_2 –70–85%; Al_2O_3 –5–13%; Fe_2O_3 –2–5% и др	0.01–0.001 mm, spherical rounded opaline globules of silica	

Table 2.
Modifiers of nano-, ultra-, and micro-sized levels of dispersion and their mechanism of action.

In real technologies of materials, the stage of agglomeration can be regulated by the addition of additives of surface-active substances (surfactants), widely used plasticizers, and superplasticizers (SP) [7–10].

2.5 “Spontaneous structure formation” stage

The evolutionary changes of the hardening system are objectively related to the third evolutionary transition “agglomeration → spontaneous structure formation.” At the end of the growth stage and the agglomeration stage, the state of the system is far from the equilibrium state, therefore at a certain period inside. Systems of substance and energy redistribution develop simultaneously, which leads to spontaneous ordering of the system. The phenomenon of morphological selection is observed, and a “change in the geometry of the system” takes place; ordered aggregates of a certain shape and size are formed instead of less ordered shapes.

Technologically, the management of the spontaneous structure formation stage can be based on different temperature processing, on the use of various types of forced compaction by pressing, on the introduction of additives of microparticles, etc. (Table 3).

Stage of the process	Transition phenomenon	Driving force	Management factors	Management techniques	Modifying mechanism	Modification result
Origin of the phase	Molecular selection	Reducing the chemical potential of the system	(1) The radius of the nucleus phase; (2) the degree of supersaturation of the solution (concentration and solubility of the phase-forming substance)	(1) Methods of synthesis, depending on the type of the nascent phase; (2) the introduction of nano-sized additives	(1) Direct physicochemical interaction; (2) the catalytic role of nanoscale particles	(1) The formation of a molecular cluster; (2) a decrease in the activation energy of the process; (3) crystallization centers of the hardening structure
Agglomeration	Topological selection	Reducing the surface energy of the system	(1) The type of physical and chemical adsorption; (2) the degree of dispersion; (3) formation of a fractal grid of solvent	(1) The introduction of plasticizers and SP; (2) the introduction of nano- and ultrafine carbon particles	(1) Electrostatic interaction and dispersion of the system; (2) changes in the reaction surface and system morphology	(1) Change in thermodynamics and kinetics of the hardening process; (2) changes in the composition, structure, and properties of solids
	Morphological selection	Reducing the total energy of the system	(1) The change in the intergranular surface of the system; (2) the formation of additional boundaries	Heat treatment, pressing, the introduction of additives of microparticles	(1) Zoning structure of hardening; (2) implementation of topochemical memory additives	(1) An increase in the area of intergranular contacts; (2) dispersed reinforcement of the structure; (3) formation of ordered hardening structures with dense packing of crystals

Table 3. Systematics of structural modification mechanisms on the main transitions of the evolutionary route solid substance formation.

The stage of spontaneous structure formation is completed by the formation of coagulation (thixotropically reversible) and condensation-crystallization (irreversible-decaying) structures that are capable of further evolutionary transformation when interacting with the external environment, which is associated with an evolutionary transition “spontaneous structure → response to external influence. In this case, the principle of equalization and equal distribution of substances and energies in the volume of each phase is implemented.

Summarizing the analysis of the evolutionary route of the solid state and the related analysis of engineering and technological methods and means of nano-modifying the structure, it is possibly reasonable to present a systematics of the main phenomena and driving forces of structural transitions between the stages of the route, factors controlling these transitions, and their mechanism effects on the hardening system (**Table 3**).

Using the method of introducing nanoscale particles, effects of structure formation control are being implemented. Those associated with the nano-size particles are playing the role of (a) structure-forming nuclei, (b) substrates for crystallization, (c) centers of new formation zoning in the matrix substance of the material, and (d) nano-reinforcing matrix element. In all of these cases, the essential point is the lowering of the energy threshold for activating the processes of synthesizing hardening systems and accelerating hardening. Another important point is the spatial geometric modification of the structure, which, as was noted, is its zoning and the corresponding effect on the characteristics of homogeneity-inhomogeneity and, as a result, on the mechanical properties of the material [11, 12]. Finally, we should also keep in mind the effects of disperse reinforcement [13, 14].

The effects of structure formation control could be observed when the method of introducing nanoscale particles is applied. These are associated with the nano-size particles playing the role of (a) structure-forming nuclei, (b) substrates for crystallization, (c) centers of new formation zoning in the matrix substance of the material, and (d) nano-reinforcing matrix element. In all these cases, the essential point is the lowering of the energy threshold for activating the processes of synthesizing hardening systems and accelerating hardening.

Another important point is the spatial geometric modification of the structure, which, as was noted, is its zoning and the corresponding effect on the characteristics of homogeneity-inhomogeneity and, as a result, on the mechanical properties of the material [11, 12]. Finally, one should also keep in mind the effects of disperse reinforcement [13, 14].

3. Materials and methods

In the course of our experimental studies, we considered the possibility and efficiency of using 12 additives attributable [15, 16] to three groups on the basis of size: (1) the group of nano-sized ones are specially synthesized particles $\text{SiO}_2 \cdot n\text{H}_2\text{O}$, sols of aluminum hydroxide particles and iron hydroxide, montmorillonite, NaX type zeolite, chrysotile nanotubes, and fulleroid-type carbon nanotubes; (2) the group of ultrafine silica fume (waste of ferroalloy production), carbon pipes of the type “Astralen—C,” and a departure from the combustion of high-energy fuel; and (3) the group of microdisperse natural montmorillonite, tripoli, and shungite.

These additives were monitored by the effect of their type, dosage, and methods of introduction into the cement-water suspension on the structure formation processes [16–20]. In experiments with changes in W/C, the introduction in some cases of superplasticizers (C-3 based on naphthalene lignosulfonate; GLENIUM® ACE 30 и Sika® ViscoCrete® 20HE based on polycarboxylate esters; Sikament FF

based on melamine sulfonate) fixed the degree of hydration in time and the kinetics of cement strength. The study of the hydration kinetics and strength of the modified cement stone was carried out based on the comparison of the reference cement system without additives.

When varying the dosage of nano-additives from 1 to 0.0001% of the mass of cement, it was shown that its optimal value corresponds to hundredths of a percent [16, 18]. Based on the monitoring, a different measure of the effect of the studied additives was revealed, and it was found that the most effective of them can be considered as a complex additive of SiO₂ nanoparticles in combination with Sika®ViscoCrete®20HE (additive CND) as well as individual addition of chrysotile or carbon nanotubes.

Below are experimental data on the use of this complex (additive CND) and the addition of carbon nanotubes of the fulleroid type of the brand “Nanocyl-7000,” treated with ultrasound (additive CNT in the accepted designation) for the nano-modifying structure of the cement stone.

Portland cement CEM I 42.5 and these nano-additives with a dosage of 0.01% were used in the experiments for the production of cement paste with a W/C = 0.33. Studies of the parameters of the kinetics of the cement hydration process were carried out under thermostatic conditions at temperatures of 0, 20, 40, and 60°C (with, respectively, 273, 293, 313, 333 K), with the duration of the process implementation for 1, 3, 7, 12 hours and 1, 3, 7, 14, 28 days. The phase composition of the reference and nano-modified cement paste was monitored by an X-ray method (CuK α radiation, $\lambda = 1.541788 \text{ \AA}$, ARL X'TRA diffractometer). The processing of diffractometric data was carried out automatically using the PDWin 4.0 computer program. The hydration degree D_h (C₃S) was calculated [21–23] by the formula:

$$D_h(C_3S) = \left(1 - \frac{I_m}{I_0}\right) \cdot 100\%, \quad (1)$$

where I_m is the diffraction intensity of 3CaO·SiO₂ (C₃S) ($d = 2.75 \text{ \AA}$) phase for hardening cement paste samples and I_0 is the diffraction intensity of 3CaO·SiO₂ (C₃S) ($d = 2.75 \text{ \AA}$) for cement.

The hydration kinetics was formally described by the kinetic equation [24, 25]:

$$D_h(C_3S) = (k \cdot \tau)^n, \quad (2)$$

where $D_h(C_3S)$ is the *cement hydration degree* (g/g) to the point in time τ (hour), k is the *hydration rate constant*, and n is the *exponent of the kinetic equation*.

Taking into account Eq. (2), for all the above conditions, isotherms of the hydration degree were obtained and, on their basis, n_{cp} was calculated considering this quantity based on the logarithmic equation

$$\ln(D_h) = \bar{n} \cdot \ln(\bar{k}) + \bar{n} \cdot \ln(\tau) \quad (3)$$

We also determined $\ln(\bar{k})$ for each of the temperatures and then considered the Arrhenius dependence $\ln\bar{k} = f(1/T)$, by which the calculation found the effective activation energy (EEA) as an indicator characterizing the energetics of hydration process development in terms of the use of structure formation nano-modifiers. To draw a conclusion about the limiting kinetic or diffusion components of the cement hydration process, the temperature coefficients of its speed were determined. In this case, the calculation was carried out according to the van't Hoff rule using the kinetic dependences of the cement hydration degree on temperature obtained for different compositions.

The compressive strength of the hardened cement paste was determined after 1, 3, 7, 14, and 28 days in water-curing conditions; tests of samples with a size of “5 × 5 × 5 cm” were conducted on an INSTRON Sates 1500HDS test system; to ensure the statistical reliability of the results of physical and mechanical tests, the number of samples in the series ranged from 9 to 12. It was determined that the intra-serial coefficient of variability of the results of the strength assessment did not exceed 7–10%.

4. Results and discussions

The main problem of ensuring the conditions for the effective development of the process of cement hydration according to the criteria E and τ . in the case of nano-modification in the determining measure consists in the optimal combination of the kinetic and diffusion components of structure formation [26]. The kinetic component controls the evolutionary route of the formation of the solid phase during the hydration of cement as far as possible the realization of all the phenomena (stages, transitions, etc.) of the nucleation of particles of the new phase and their development; the diffusion component acting as opposed to the kinetic one controls the dynamics of the evolutionary route phenomena. With the optimal combination of these types of control, it is possible to ensure minimization of the energy intensity of the formation of the cementing bond and the duration of the hardening process.

The following conclusions about the energy efficiency of nano-modification are based on the results we obtained on speed change, temperature coefficient of speed, effective activation energy of cement hydration process under the influence of factors of introducing nano-additives, and changes in temperature conditions presented in **Tables 4** and **5** and in **Figure 2**.

The generalization of the experimental data shows that in systems with nano-modifying additives, the cement hydration process is substantially (**Table 4**) accelerated: to the daily duration of hardening at 20°C (293 K), the degree of hydration reaches at least 70–75%.

Such a result for the control “additive-free” system is recorded only by 28 days. And thus, in this example, hydration is accelerated by criterion τ . almost 30 times.

The effect of the accelerating action of additives is valid for all variants of the composition and temperature conditions of hydration, differing, however, in the magnitude and timing of the achievement of the limiting values of the hydration degree. For the options of low temperatures (0°C, 273 K), the hydration degree of 70–75% is reached by 7 days, if the additive of pressure coefficient is used, and by 14 days, if the additive of CNT is used. At the same time, in the “additive-free” system, such a hydration degree is not achieved at all. By the 28th day, it makes only 50% of the possible maximum value.

For elevated temperatures (40–60°C, 303–333 K), in systems with the considered nano-additives CND, the degree of hydration already reaches 80–85% by the hardening for 1 h; by 7 h it is 90%, and by the first day up to 95%. Based on this data, it can be concluded that, firstly, in the presence of nano-additives, the main part of the evolutionary route of cement hydration takes place almost within the first hour and, secondly, that the hydration of cement can be completed within the first day.

The effects of such acceleration of hydration are explained by the achieved decrease in the effective activation energy of the process under the conditions of nano-modification: the effective activation energy required for the process “start” decreases 2.3–2.8 times as compared with the control “additive-free” system.

Specimen ID	The cement hydration degree (mass%) for the process duration									
	Hour					Day				
	1	3	7	12	24	3	7	14	28	
Curing temperature 273 K										
C + W	11	12	15	18	20	40	45	48	51	
C + W + CND	37	42	54	57	62	67	72	75	78	
C + W + CNT	28	33	37	42	49	55	64	69	73	
Curing temperature 293 K										
C + W	39	41	49	53	55	61	65	68	75	
C + W + CND	60	63	69	71	75	81	92	93	93	
C + W + CNT	55	60	65	68	70	78	87	88	89	
Curing temperature 313 K										
C + W	42	48	51	59	68	75	81	83	89	
C + W + CND	81	85	88	91	93	95	96	96	97	
C + W + CNT	78	79	83	88	91	94	95	96	96	
Curing temperature 333 K										
C + W	71	75	79	85	91	92	93	95	95	
C + W + CND	84	88	91	93	96	96	97	97	98	
C + W + CNT	85	87	92	93	95	96	97	97	97	

Table 4.
 The hydration degree of cement depending on temperature for cement paste modified by nano-additives (0.01% mass cement).

Specimen ID	Hydration rate constant \bar{k} in curing temperature				\bar{n}	EEA, kJ/mol
	273 K	293 K	313 K	333 K		
C + W	17.53	25.40	27.72	31.68	0.13	173.4
C + W + CND	46.53	54.19	56.71	57.19	0.08	61.7
C + W + CNT	42.84	53.55	56.00	57.29	0.08	76.2

Table 5.
 Kinetic parameters of hydration process of cement paste modified by nano-additives (0.01% mass cement).

It is worth emphasizing that the experimentally obtained lowest EEA value (61.7 kJ/mol) corresponds to the use of a complex modifying additive based on nano-sized SiO₂ particles in combination with a superplasticizer. This is explained by the fact that, unlike carbon nanotubes, SiO₂ nanoparticles are related to the mineral phases of hardening cement neoplastms with a crystal-chemical structure that facilitates the formation of molecular clusters and nuclei on SiO₂ nanoparticles as active crystallization centers. We draw attention here to the fact that the accelerating role of the additive takes place, despite the fact that the surfactant present in the complex additive slows down the hydration processes.

Analyzing the results of kinetic studies, it is necessary to address the question of the feasibility of combining the factor of introducing additives of nano-modifiers with the temperature factor accelerating the process of cement hydration. And in this regard, we will review the data obtained on the values of the temperature coefficient of the reaction rate ($\alpha(T)$) (see **Figure 2**).

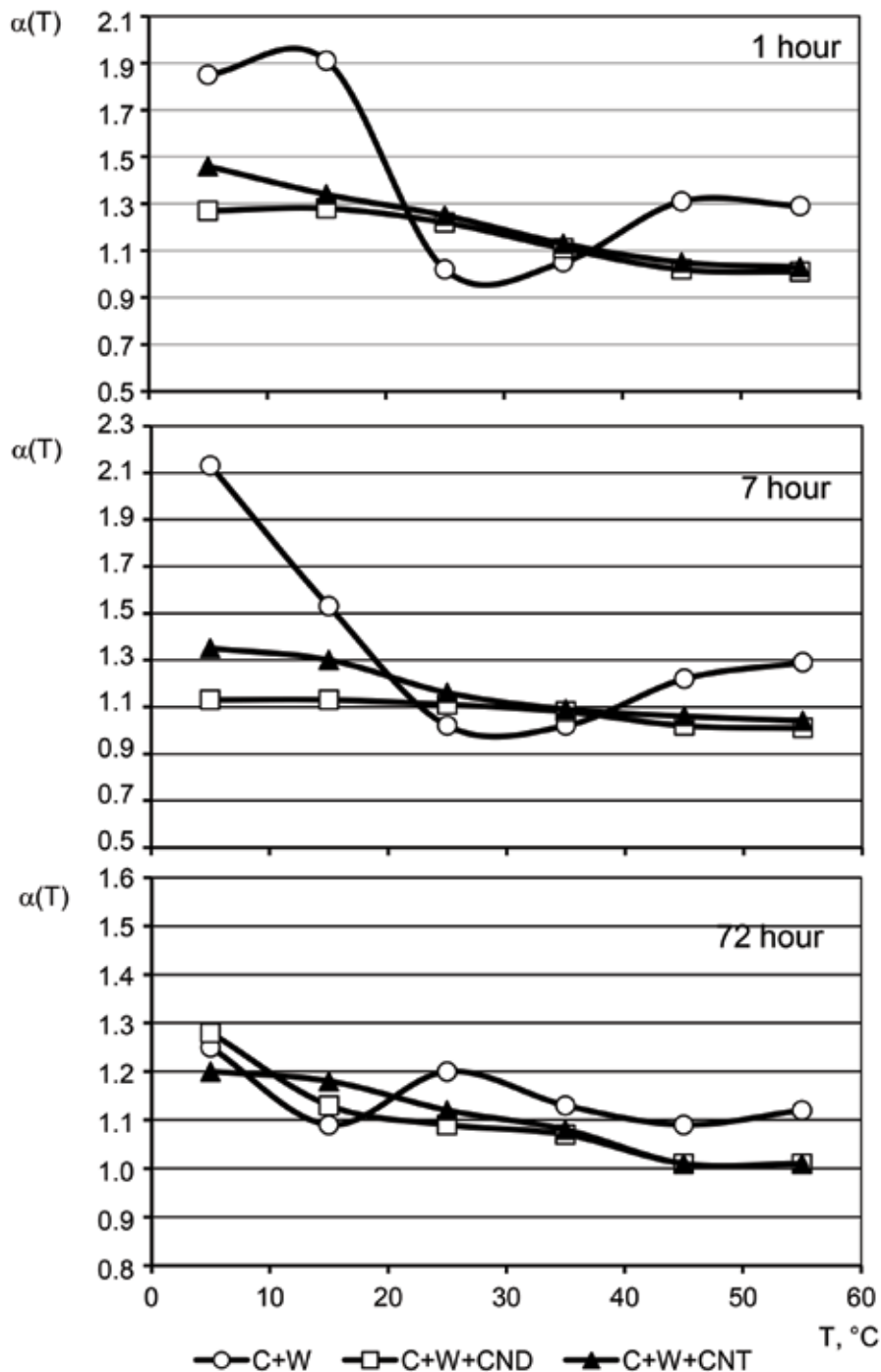


Figure 2.
The temperature coefficient of the reaction rate.

First of all, we note that only for the control “additive-free” system at lower temperatures of the hydration process, the situation of its kinetic control is realized. Indeed, the temperature coefficient of the reaction rate, up to the duration of hydration of 1 day, has a value close to 2 m ($\alpha(T) = 1.85\text{--}2.25$). However, already after the 3 days, the coefficient $\alpha(T)$ decreases to values of 1.25 and subsequently (for durations

of 7, 14, and 28 days) remains at the indicated level. This indicates the transition of the process to the area of the diffusion control, which explains the relatively low (in the limit of about 50%) values of the degree of hydration, which are fixed for the standard system (see **Table 4**).

The use of nano-modifying additives fundamentally changes the kinetic picture of the process. It accelerates so much that even at low temperatures, in the first hour, it goes (see **Figure 2**) to the mixed (for the CNT $\alpha(T) = 1.46$) and diffusion (for the CND $\alpha(T) = 1.27$) control. The transition of the process kinetics from the kinetic control region to the diffusion region in systems with nano-additives is observed at a much earlier time than in the reference system.

In the cumulative effect of the introduction of nano-additives and temperature conditions, the manifestation of the first factor is much stronger. Therefore, the use of technologies that provide for raising the temperature of cement hardening above 30°C is not relevant but more unacceptable. Indeed, for all systems with additives, an increase in temperature leads to a decrease in the $\alpha(T)$ coefficient to values of 1.0–1.1, that is, to the transition of the hydration process to the region of strict diffusion control.

In contrast, for the reference “additive-free” system, the temperature increase is a positive factor for the kinetics of the process. In this case, we can speak about the phenomenon of the so-called “temperature breakdown,” when the diffusion of anions and cations in the “inter-grain” volume through the “subsurface” volume is accelerated, with a layer of shielding surface of the cement grains. For this reason, at lower temperatures, the development of the process from the diffusion control region can pass into the mixed control region (the coefficient $\alpha(T)$ increases from 1.0–1.05 to 1.3).

Thus, it is clear that the use of nano-additives is accompanied by the change in the parameters of the development of the cement hydration process in terms of its kinetics and energy. The result of a possible reduction in the hydration time t is a consequence of the acceleration of the reactions due to a significant decrease in their effective activation energy. On the contrary, in the field of lower and possibly negative temperatures, the use of nano-additives seems to be very effective, providing a high temperature coefficient of the reaction rate, characteristic of the development of the hydration process in the kinetic region.

When modifying the structure of cement paste with nano-additives, the change in the parameters and indicators of the strength kinetics is decisive in terms of raising efficiency. These include the speed of curing, the duration of reaching the “tempering,” and the achievable limit values of the strength of the hardened cement paste. Due to this fact, it was important to analyze the strength kinetics in relation to the type and dosage of nano-additives.

In the course of experiments, when *assessing the effect* of nano-modification of the structure on the strength, the above two additives in dosages of 0.01–1% by weight of cement were studied.

Figures 3 and **4** reflect the effect of these additives on the strength kinetics; a conclusion is drawn about the acceleration of the curing of the hardened cement paste using the minimum and maximum doses of additives. In the case of the use of the complex additive of nanoparticles SiO₂ in combination with a superplasticizer (CND), close to the limiting strength, values are achieved for compositions with different dosages by the third day of hardening. The use of CND allows you to provide 70% of the strength of the values achieved by 28 days, for 1 day. For the option of dosing an additive of 0.01%, an increase in the limiting values of strength up to 90 MPa against 50 MPa in the control “additive-free” system is noted. Such a difference is explained by the modifying effect of the additive on the dispersed and morphological composition of the cement stone neoplasms, which acquire a nano-dispersed and cryptocrystalline state. This is precisely in accordance with the

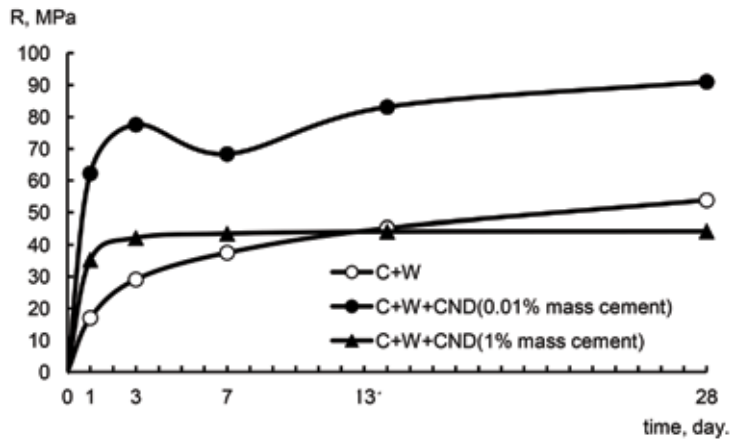


Figure 3.
Strength kinetics curves of cement pastes modifying by CND.

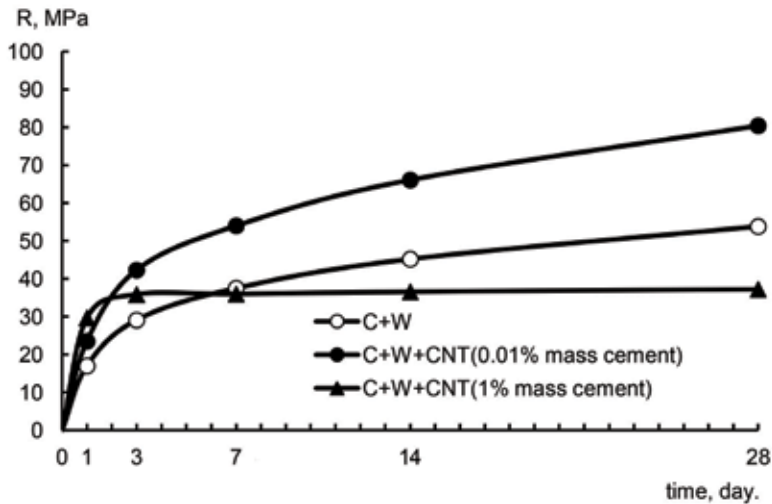


Figure 4.
Strength kinetics curves of cement pastes modifying by CNT.

well-known theory of “fine grain” of Rebinder P.A. and the pattern of Hall–Petch and determines the higher resistance of the modified structure to destruction.

A similar situation occurs when the carbon nanotube additives at a dosage of 0.01% are applied. However, the strength kinetics in this type of nano-modification is noticeably different in that in the early periods of hardening, strength is slower: achieving 70% strength from its values at 28 days old is provided in this variant for 7 days, and for 1 day cement stone gains only 20%. Another difference concerns the maximum achievable strength value, which is 80 MPa.

Based on this data, it can be observed that the introduction of an additive to carbon nanotubes is less effective in comparison with the addition of nanoscale particles of SiO_2 and above all in terms of the kinetic parameters of hardening strength.

Based on the results of the experiments, we should specifically dwell on the question of the strength kinetics for the variants with the dosage of additives of 1% by weight of cement. With this dosage, an accelerated increase in strength in the initial (1–3 days) hardening periods is also noted; however, no increase in strength is noted in the subsequent periods, and it remains at 35–40 MPa, which is lower than the

values for the control “additive-free” composition. It can be assumed that, at an elevated dosage, the so-called poisoning of the system occurs, when excessively accelerated hydration of cement and crystallization of new growths lead to the development of self-destructive crystallization pressure. This is true: in our experiments, which involved the introduction of a 5% dose of the additive of nano-particles SiO_2 , self-destruction of cement paste samples was observed after the first day of hardening in normal temperature and humidity conditions. These experimental facts confirm the urgency of the problem of optimizing the dosages of additives recommended in the technology of nano-modification of the structure of cement stone.

Thus, it has been shown that the effect of nano-modification of cement paste in relation to R is that it hardens faster in the early stages of structure formation and becomes more durable when the curing process is completed. And this is the basis for a reduction in overall terms of hardening and refusal of heat treatment of hardening cement paste.

The criterion assessment of nano-modification effectiveness was made using comparative indicators, which allowed showing the measure of its action on the kinetic parameters of the hydration and hardening processes of cement paste (Table 6).

It has been established that the introduction of nano-modifying additives into the “cement + water” system changes the kinetic parameters of the evolutionary route development and accelerates cement hydration by 10–30 times, which is explained by a decrease in the activation energy of the process by 2–3 times.

Modification of the hardened cement paste structure according to the dispersion and morphology of the neoplasms is accompanied by an increase in the strength value at 28 days old by 45–65%, depending on the type of additive (at their dosage 0.01% by weight of cement).

The use of additives based on SiO_2 nanoparticles, which are related in their crystal-chemical structure to the minerals of the cement stone neoplasms, ensures the completion of the hardening process almost on the first day. The efficiency coefficient of nano-modification to increase the specific strength of hardened cement paste (that is, in terms of the effectiveness of the realization of the potential of the activity of cement in the synthesis of strength under the conditions of nano-additives) in the first days of hardening is 2.5 times higher for additive CND compared to adding CNT.

Criteria and efficiency ratios	Specimen ID		
	C + W	C + W + CND	C + W + CNT
EEA, kJ/mol	173.4	61.7	76.2
Required time to reach 75% cement hydration degree, day	28	1	3
Speedup cement hydration degree ratio	—	28–30	9–10
Relative strength hardened cement paste, $R(\tau)/D_i(\tau)$, MPa			
in 1 day	31	83	71
in 7 day	58	74	62
in 28 days	72	98	90
Strength hardened cement paste, $R(\tau = 28 \text{ day})$, MPa	55	90	80
Increase strength ratio, $R(\tau = 28 \text{ day})$	—	1.64	1.45
Required time to reach 75% of strength hardened cement paste, day	7	1	7

Table 6.
 Criteria and efficiency ratios of cement paste nano-modification by the additives CND and CNT.

By reaching the “mature” 28-day-old age, the magnitude of the efficiency coefficient of nano-modifying increases the specific strength of hardened cement paste which is 1.36 for the additive of CND and 1.25 for the addition of CNT, and this shows that the effect of nano-modifying with the introduction of additives is not just in the first periods, when their accelerating effect is manifested on the parameters of hydration kinetics and, accordingly, on quantitative accumulations of the neoplasm phase but also in regulatory terms (28 days), when the quality begins to manifest itself of the cement hydration products.

5. Conclusions

Based on the theoretical analysis of the basic models of the kinetics of heterogeneous processes of structure formation of cement-based materials, we proved that they are the subject and purpose of nanotechnological control. The possibilities of regulating the evolutionary route of formation of a solid substance for cement-based materials at the stages of phase nucleation, particle growth, their agglomeration, and spontaneous and self-organized structure formation are revealed. It is shown that in the evolution of the structure of cement-based materials at the nanoscale level, its nano-modification is determined by a set of controls. In this complex, one of the effective means is the use of nanoscale additives, which determine the direct nano-modification of structural elements at the level of individual crystals and crystalline intergrowth, in the zoning and clusterization of the microstructure.


It was experimentally shown that the use of nano-modifiers based on nanoscale SiO₂ particles and carbon nanotubes determines the acceleration of hydration, hardening by 3–10 times, increasing the maximum values of the strength of cement-based materials by 1.5–2 times.

Author details

Evgeny Chernishov*, Olga Artamonova and Galina Slavcheva
Voronezh State Technical University, Voronezh, Russia

*Address all correspondence to: gslavcheva@yandex.ru

IntechOpen

© 2020 The Author(s). Licensee IntechOpen. This chapter is distributed under the terms of the Creative Commons Attribution License (<http://creativecommons.org/licenses/by/3.0>), which permits unrestricted use, distribution, and reproduction in any medium, provided the original work is properly cited. 

References

- [1] Artamonova O, Chernyshov E. Concepts and bases of technology nano-modification of structures of building composites. Part 1: General problems of fundamentality, the main directions of research and development. *Construction Materials*. 2013;**9**:82-95
- [2] Bazhenov Yu V, Chernyshov E, Korotkikh D. Construction of modern concrete structures: Defining principles and technological platforms. *Construction Materials*. 2014;**3**:6-14
- [3] Melikhov I. *Physico-Chemical Evolution of Solids*. Moscow: BINOM, Laboratory of Knowledge; 2009. p. 309
- [4] Xu R, Xu Y. *Modern Inorganic Synthetic Chemistry*. New York: Elsevier; 2011. p. 588
- [5] Klabunde KJ. *Nanoscale Materials in Chemistry*. New York: A John. Wiley & Sons Inc; 2001. p. 292
- [6] Gudilin E, Eliseev A. *Crystallization Processes in Chemical Materials Science*. Moscow: Moscow State University; 2006. p. 90
- [7] Mendoza O, Sierra G, Tobon JI. Influence of super plasticizer and $\text{Ca}(\text{OH})_2$ on the stability of functionalized multi-walled carbon nanotubes dispersions for cement composites applications. *Construction and Building Materials*. 2013;**47**:771-778
- [8] Strokova V, Nelyubova D, Serenkov I. Properties of composite binder based on nanostructured suspension. *Construction Materials*. 2017;**1-2**:50-54
- [9] Jennings H, Thomas J, Gevrenov J, Constantinides G, Ulm F-J. A multitechnique investigation of the nanoporosity of cement paste. *Cement and Concrete Research*. 2007;**37**(3):329-336
- [10] Korolev E. Nanotechnology in construction materials. Analysis of the status and achievements. Ways of development. *Construction Materials*. 2014;**11**:47-79
- [11] Bullard J, Livingston J, et al. Mechanisms of cement hydration. *Cement and Concrete Research*. 2011;**41**:1208-1223
- [12] Mendes T, Hotza D, Repette W. Nanoparticles in cement based materials: A review. *Reviews on Advanced Materials Science*. 2015;**40**:89-96
- [13] Chernyshov E, Artamonova O, Slavcheva G. Concepts and understanding of the technology of nano-modification of the structures of building composites. Part 3. Effective nano-modification of hardening systems for cement and cement stone structure (criteria and conditions). *Construction Materials*. 2015;**10**: 54-64
- [14] Chernyshov E, Slavcheva G, Artamonova O. Conceptual models for controlling the fracture resistance of nano-modified structures of conglomerate building composites. *News Kasan State University of Architecture and Civil Engineering*. 2014;**3**(29):156-161
- [15] Artamonova O, Sergutkina O, Ostankova I, Shvedova M. Synthesis of SiO_2 -based nanodispersed modifier for cement composites. *Condensed Matter and Interphase Boundaries*. 2014;**16**(1):152-162
- [16] Artamonova O. *Synthesis of Nano-Modifying Additives for Construction Composites Technology: A Monograph*. Voronezh: Voronezh GASU; 2016. p. 100
- [17] Quercia G, Hüsken G, Brouwers HJH. Water demand of amorphous nanosilica and its impact on the

workability of cement paste. *Cement and Concrete Research*. 2012;**42**:344-357

[18] Singh L, Agarwal S, Bhattacharya S. Preparation of silica nanoparticles and its beneficial role in cementitious materials. *Nanomaterials, Nanotechnology*. 2011;**1**(1):44-51

[19] Kalinichev A, Wang J, Kirkpatrick R. Molecular dynamics modeling of the structure, dynamics and energetics of mineral—Water interfaces: Application to cement materials. *Cement and Concrete Research*. 2007;**37**(3): 337-347

[20] Gaitero J, Campillo I, Guerrero A. Reduction of the calcium leaching rate of cement paste by addition of silica nanoparticles. *Cement and Concrete Research*. 2008;**38**(8-9):1112-1118

[21] Skibsted J, Hall C. Characterization of cement minerals, cements and their reaction products at the atomic and nanoscale. *Cement and Concrete Research*. 2008;**38**(2):205-225

[22] Li H, Xiao H-G, Yuan J, Ou J. Microstructure of cement mortar with nanoparticles. *Composites Engineering B*. 2004;**35**(2):185-189

[23] Mondal P, Shah S, Marks L. Nanoscale characterization of cementitious materials. *ACI Materials Journal*. 2008;**105**:174-179

[24] Skibsted J, Hall C. Characterization of cement minerals, cements and their reaction products at the atomic and nanoscale. *Cement and Concrete Research*. 2008;**38**(2):205-225

[25] Wua M, Johannesson B, Geiker M. A review: Self-healing in cementitious materials and engineered cementitious composite as a self-healing material. *Construction and Building Materials*. 2012;**28**:571-583

[26] Artamonova O, Slavcheva G. Structure of cement systems as objects of nanomodification. *Scientific Herald of the Voronezh State University of Architecture and Civil Engineering, Construction and Architecture*. 2016;**1**(29):13-26

Bioconc-Based Green Concrete Quality Treatment for Mass Concrete's Low Heat Concrete

Makno Basoeki

Abstract

Thermal cracking in concrete members having large sections, namely *mass concrete*, continues to be a concern for designers and specifiers of concrete. These issues are common to both large structural components in buildings and in civil engineering infrastructure projects. The common issues is based on the large scale of concreting dimension; mean large cement content cause more thermal hydration of concrete extremely. There is often a conflict for concrete specifier or concrete structural designer, between requirement to form high strength concrete for structural durability and structural bearing load capacity, which needs higher binder content versus higher heat of hydration characteristic of concretes. The potential problem that may be occurred is concrete thermal crack. The reaction of cement with water is exothermic, therefore it produces heat. The more Portland cement in the mix, the greater is the heat produced. To control the thermal crack means to control the concrete hydration thermal. The research started by laboratory scale trial mix Fc'25 Low Heat Concrete Bioconc-based concrete Job Mix, from cement content reduction 20, 25, 30, and 40%. The attached result shows optimum jobmix is Fc'25 Low Heat Concrete Bioconc-based concrete Job Mix on 40% cement as binder content reduction, was chosen as Low Heat Concrete Mix Mock Up. Later on, based on the optimum concrete jobmix Fc'25 R = 40%, cement content reduction 40%, above mentioned trial mixed, the research developed to project scale on mock up for sampling mass concrete dimension 1000 × 1000 × 2500 mm³ compared with similar two mock-up of mass concrete thermal hydration control, i.e., Fc'25 + FA.20% + Ice Block (Pre-cooling with crushed ice block Mass Concrete Fc'25 with fly ash 20%) and Fc'25 + FA.40% (Low Heat Concrete Fc'25 with Fly Ash 40%). The attached Graph Thermal Monitoring Low Heat Concrete shows that the peak temperature occurred 63.5°C in 29.5 h after pouring and maximum thermal differential between LHC layers is 19.5°C. Another two Low Heat Concrete Method Statement, i.e.: Pre-cooling and Low Heat Concrete with Fly Ash 40%, Mock Up Graph Thermal Monitoring also attached for comparison study. The observation and analysis proof that, "Low Heat Concrete Hydration Thermal Reduction with Bioconc" is work simplifier and economically, for mass pouring. The most essential thing is that, the basic concept of Bioconc's Low Heat Concrete on reducing the mass concrete cement-binder content means reducing CO₂ emission in every concrete production, without any hazard impact to the environment. Its mean Bioconc based Low Heat Concrete contribute to develop the green technology and eco-friendly technology on the concrete industry as sustainable green technology.

Keywords: mass concrete, concrete hydration thermal control, low heat concrete, pre-cooling, post cooling, Bioconc, green technology, eco-friendly

1. Introduction

The concrete is most common construction material which is use on every construction project. Mostly concrete construction material, especially related to high-rise building structural elements, in large dimension forms mass concrete. Mass concrete is any volume of concrete with dimension large enough to require that measures be taken to cope with the generation of heat from hydration of cement and attendant volume change to minimize cracking. The design of mass concrete structure is generally based on durability, economy, and concrete hydration thermal control, and strength often being secondary concern [1].

Therefore this journal is written the research on how to control the hydration thermal control with Bioconc, in concentration of discussion to observe the engineering feasibility and economical feasibility.

1.1 Reference's discussion

There are several existing method to control the potential concrete thermal cracks on mass concrete, with the following concrete hydration thermal method statements:

1. Pre-cooling Method with Ice, refer <https://www.scribd.com/document/109689638/Mass-Concrete-Method-Statement-comparison-reference> [2].
2. Pre-cooling Method with Liquid Nitrogen, https://www.concreteconstruction.net/how-to/materials/precooling-mass-concrete_o [3].
3. Post-cooling Method, <https://www.forconstructionpros.com/concrete/equipment-products/article/11598829/how-to-plan-and-manage-curing-for-mass-concrete-pours> [4].
4. Low Heat Concrete with Fly Ash 40% Concrete Mix, to reduce the binder as source of hydration heat on acceptable peak temperature and thermal differential not exceed than 20°C, as comparison reference [5].

The first three method statements are costly, since they have to provide ice blocks, liquid nitrogen, and post cooling installation system. The last method statement Low Heat Concrete with Fly Ash 40% is most economically method but facing the environmental and human health issues, based on the following references:

1. <https://www.psr.org/wp-content/uploads/2018/05/coal-ash-hazardous-to-human-health.pdf> [6].
2. ojs.unsw.adfa.edu.au/index.php/juer/article/download/465/300 [7].

This chapter discuss the concrete *hydration thermal control* with the economical and *eco-friendly* Method Statement, based on the basic performance of concrete bio-admixture, Bioconc, which is produce micofiller, reduce the binder content up to 40% as described on sub clause 1.2.

The concrete hydration thermal sources is from the cement as binder, since Bioconc may reduce up to 40% binder content, the concrete hydration thermal can be controlled and worked as *Low Heat Concrete*. The paper limited discuss about the application of the Bioconc, for laboratory scale trial mix, *Low Heat Concrete* mock up modeling test and comparison with another 2 (two) Low Heat Concrete above mentioned [2, 5].

1.2 Research's object

The Object of Research is how to control concrete thermal hydration on mass concrete with bio-admixtures Bioconc, compared with existing common method statement in control mass concrete thermal hydration, of precooling as described previously on reference [2, 5].

Bioconc is a biotechnology product that is a liquid which is made of organic, natural materials, denatured proteins, biopolymer surfactant and organominerals which already fermented by beneficial microbes. Bioconc is an environmentally friendly product, non-toxic, safety use and not harmful to humans and other living things, related to object treated, concrete [8]. Bioconc performed by several microbe, which is one of them produce mycelia, functioned as microfiller for concrete mix, as shown on SEM (Scanned Electronic Microscopy) **Figure 1**

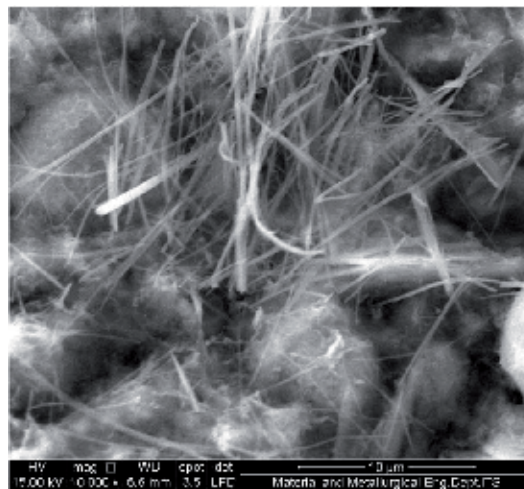


Figure 1.
SEM Bioconc treated concrete.

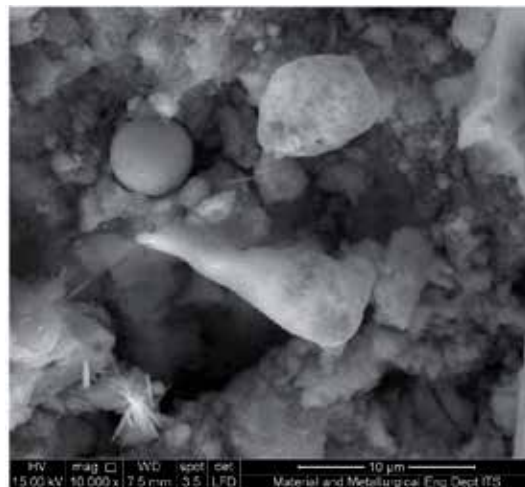


Figure 2.
SEM regular concrete.

and compared with normal concrete mix shown on **Figure 2**. The Physical of this Bioconc mycelia as the following [8]:

- a. Diameter 5 μm s.d. 10 μm
- b. Length 5–30 μm
- c. Growing Speed 10^7 – 125^9 within 1 day (Refer to **Figure 3**).
- d. Alive survival under concrete heat setting 1 hour in 60°C (Refer to **Figure 4**), then “dormant”

1.3 The aim of research

The Research’s Aim is directed to observe the following objects, in controlling the potential thermal crack caused by the differential thermal between mass concrete core hydration thermal rising and mass concrete surface cooling as captured on **Figures 5** and **6**. The objects of the research’s aim are:

1. The engineering effectiveness of concrete bio-admixture, Bioconc on control the concrete thermal hydration, compared with another mass concrete hydration thermal control as reference [2, 5].

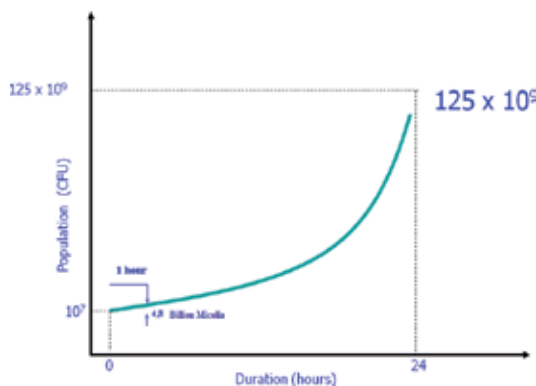


Figure 3. Growing speed 10^7 – 125^9 within 1 day.

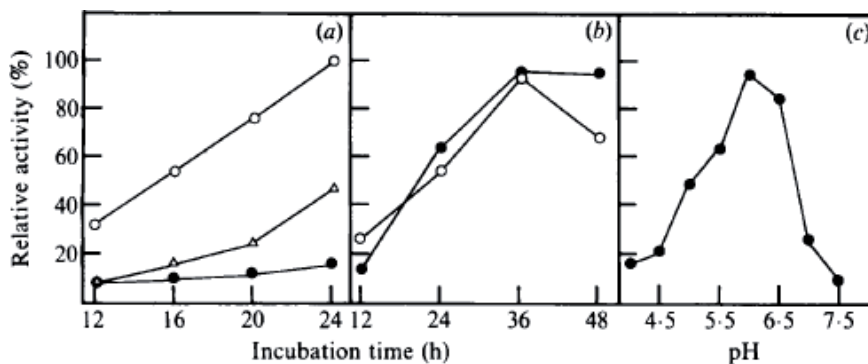


Figure 4. (a) Incubation time of microbe which is life in Bioconc 24°C, 28°C, 34°C. (b) Mycelium age from microbe which is life in Bioconc 18°C and 24°C. (c) Mycelium age from microbe which is life in Bioconc on various pH.

2. The effectiveness of concrete bio-admixture, Bioconc on increase the mass concrete quality, compared with another mass concrete hydration thermal control as reference [2, 5].
3. The economical effectiveness of the application of concrete bio-admixture, Bioconc on control the concrete thermal hydration on Low Heat Mass Concrete compared with another mass concrete hydration thermal control as reference [2, 5] (**Figure 7**).

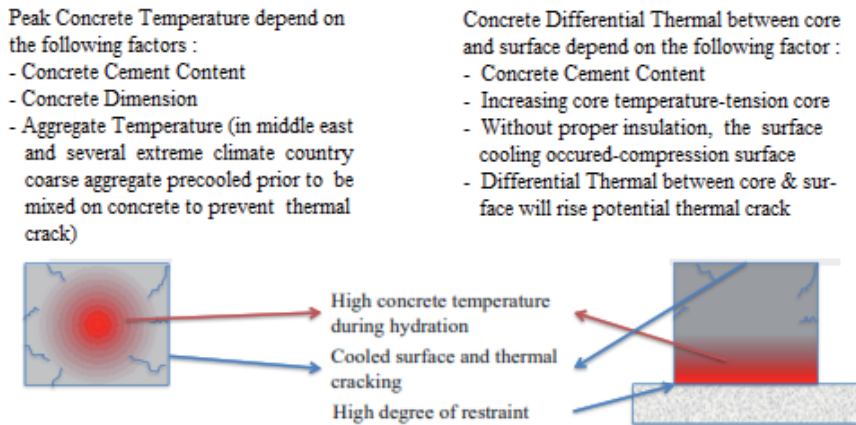


Figure 5.
 Potential thermal crack of mass concrete caused by differential thermal core and surface.

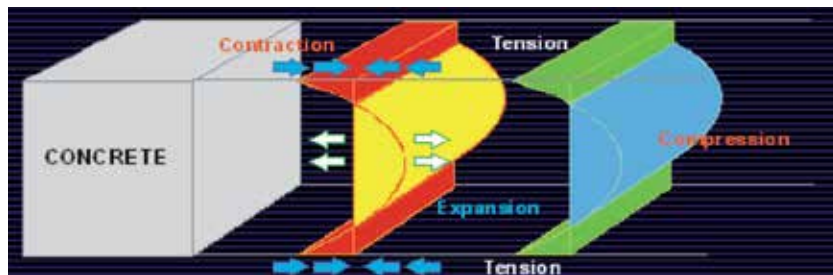


Figure 6.
 Mass concrete core hydration thermal rise up expansion vs. surface tension potential crack.

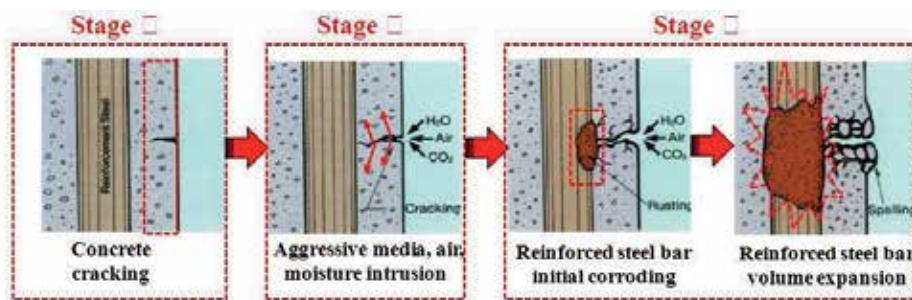


Figure 7.
 Mass concrete potential crack defect and potential rebar corroding.

1.4 Scope of discussion

The discussion scope is directed on the following object:

1. Laboratory scale trial mix, directed to observe the optimum Bioconc’s Low Heat Concrete Jobmix.
2. The mass concrete modeling or mock up scale of Bioconc based, Low Heat Concrete $1000 \times 1000 \times 2500 \text{ mm}^3$ dimension, observation to discover the peak temperature on the observed peak time.
3. Simply economical calculation of the Bioconc-based Low Heat Concrete application.

Those scopes of discussion are compared with another mass concrete hydration thermal control reference [2, 5].

2. Method statement

The bio-admixture Bioconc treatment concrete job mix modification from original job mix (non-fly ash job mix) is describe on the following **Table 1**:

Material mix	NFA mix	Bioconc Jobmix modification
Cement	A	A. (1 – R%)
Water	B	B. (1 – R%)
Coarse Ag-1	C	$C + (A + B).R\%.\{C/[C + D + E]\}$
Coarse Ag-2	D	$D + (A + B).R\%.\{D/[C + D + E]\}$
Fine Aggregate	E	$E + (A + B).R\%.\{E/[C + D + E]\}$
Bioconc (cc)		–600 cc [9]
Total weight	A + B + C + D + E	A + B + C + D + E+600 cc

Table 1.
NFA job mix and Bioconc Jobmix modification.



Figure 8.
Concrete job mix between original mix (NFA mix) vs. modified Bioconc-treated concrete mix.

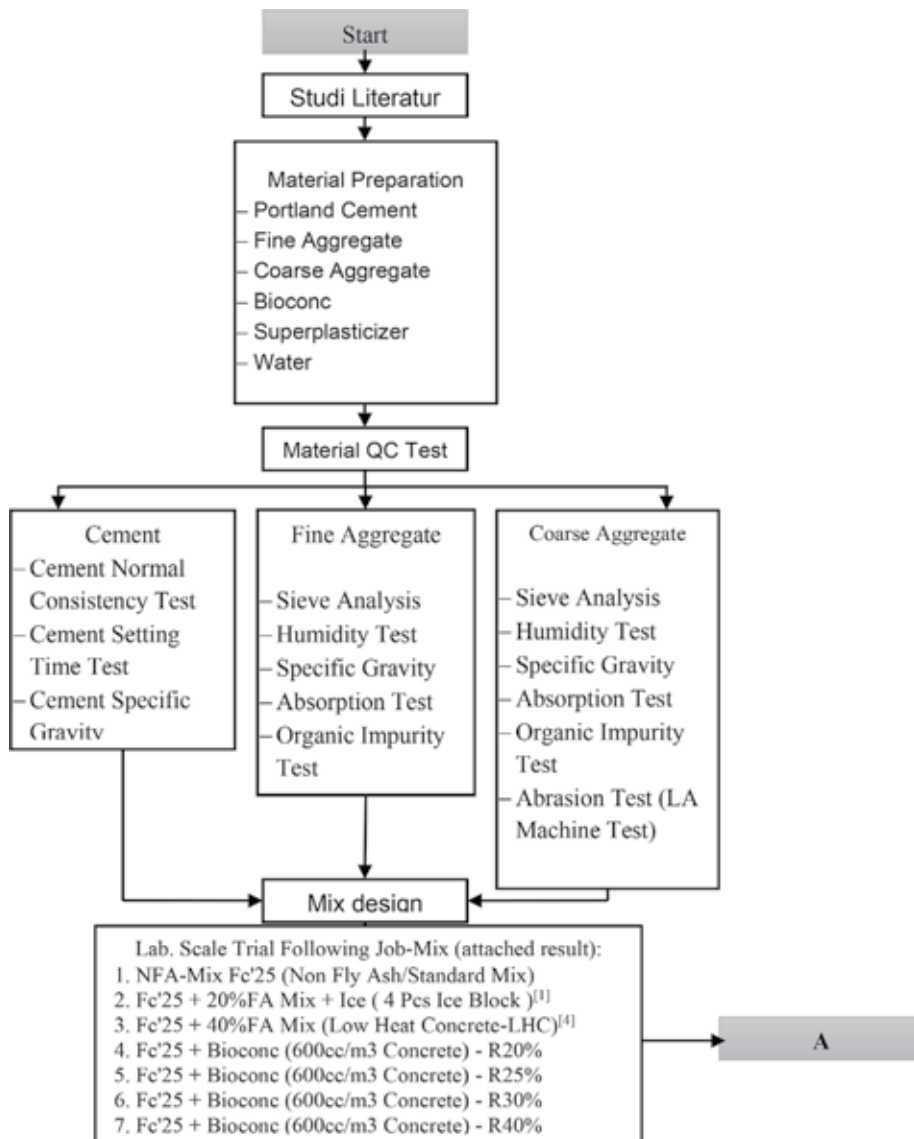


Figure 9.
 Flow chart of lab scale trial mix.

Observed cement content (binder content) reduction = R %.

Concrete Job Mix - Grade (G) = Fc'25 (in this research, but not limited to).

Concrete Volume - standard jobmix reference = 1 m³.

Optimum Bioconc dosage in 1 m³ of Concrete = 600 cc [9].

The Modified Concrete Job Mix, based on the original concrete mix (non-fly ash concrete mix), can be described on the following **Figure 8**.

The sequence OF the research execute as the following method statement, refer to the previous research on reference [9–11], describe on the following flow chart (**Figures 9–11**).

Sequence of Bioconc mock-up and thermocouple monitoring compared to another 2 method concrete hydration thermal control is provided in **Figures 12–18**.

Bioconc Centre Foundation
Low Heat Concrete Fc'25 Trial Mix

Bioconc Treatment Low Heat Concrete Fc'25 Trial Mix Observation
 In Order to Find Out Optimum Low Heat Concrete Job Mix and
 Comparison with another 2 (two) Low Heat Concrete Method



Age (days)	Concrete Strength (Mpa) Compared another 2 LHC-Method		Standard Fc'25 (Mpa)	Trial Mix Low Heat Concrete Fc'25-Trial Bioconc as Microfiller Cement on Various Concrete Mix Cement Content Reduction Strength (Mpa)				Mock-Up LHC Bioconc FAS=0.45 Fc'25_R=40% (Mpa)	Notes
	Low Heat Concrete Fc'25 - FA=40%	Ice Concrete Fc'25 (4 Ice-Block/m3)		R = 20%	R = 25%	R = 30%	R = 40%		
0	0	0	0	0	0	0	0	0	
3	20.0	12.8	11.5	31.14	27.17	24.73	12.46	12.46	
7	24.5	18.3	17.5	35.61	31.33	31.33	21.89	25.48	
14	30.6	24.7	20.5	40.80	36.80	33.40	25.48	29.44	
28	35.3	29.0	25	43.1	40.7	39.3	26.82	30.164	

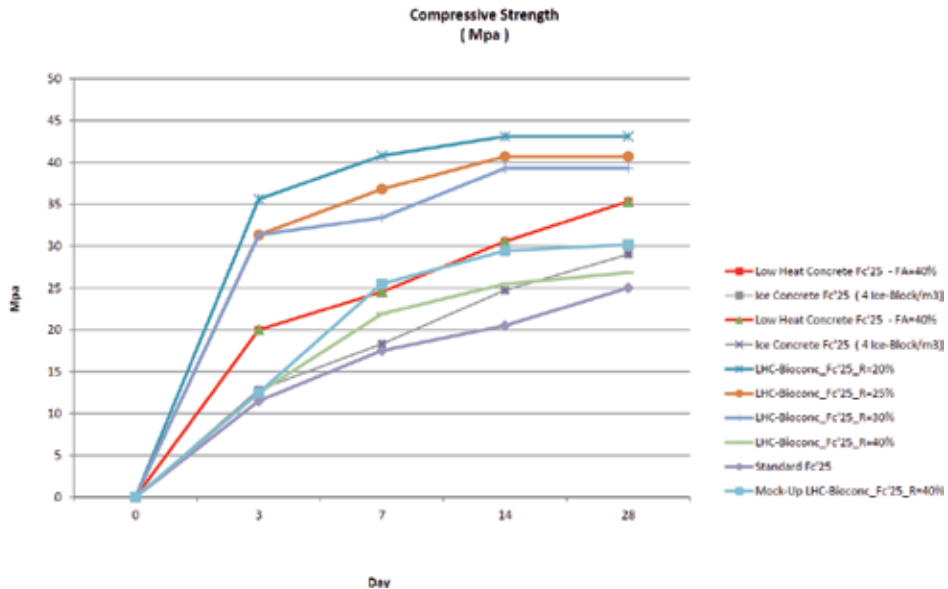


Figure 10.
 Strength test of Cylindrical Samples lab Trial and Site Mock-up Mass Concrete.

3. Concrete hydration thermal control research data result

Based on the above mentioned sequences method of research, the following output data found.

3.1 Bioconc low heat concrete Fc'25, with cement binder content reduction R = 40% research data result

The Mock Up Bioconc Treatment Low Heat Concrete with cement binder content reduction R = 40% to control concrete hydration thermal, on mass concrete modeling 1000 × 1000 × 2500 mm³, Graph thermocouple monitoring output data, figured on the following graph (Figure 19).

3.2 Fc'25 + concrete Fly-ash 20% + 4 pcs ice block/m³ concrete research data result

The Mock Up of Fc'25 + FA20% + 4pcs Ice Block to control concrete hydration heat, on mass concrete modeling 1000 × 1000 × 2500 mm³, Graph thermocouple monitoring output data, figured on the following graph (Figure 20).

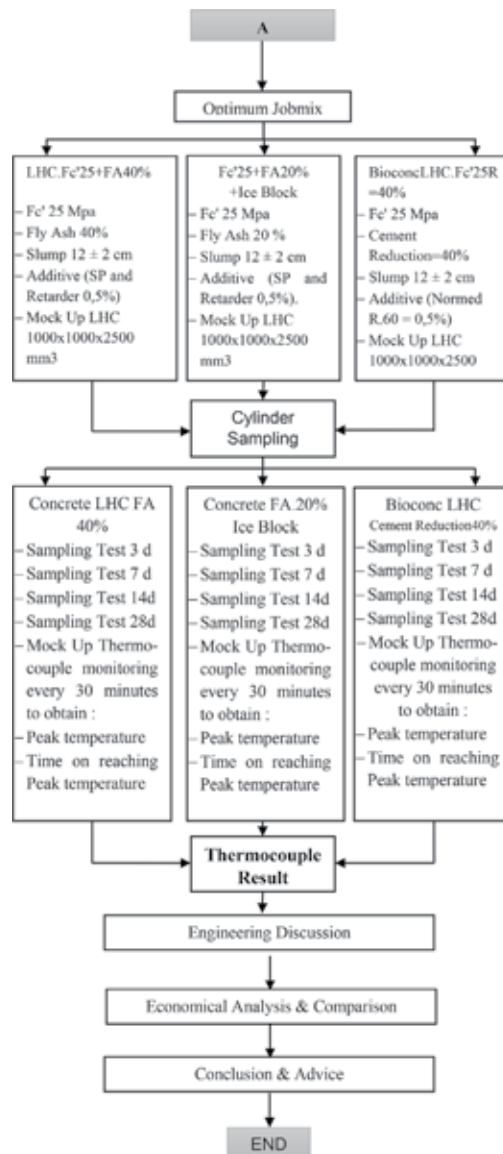


Figure 11.
 Mass concrete mock up 1000 × 1000 × 2500 mm³ and thermocouple monitoring.



Figure 12.
 Bioconc LHC mixing plant.



Figure 13.
Slump test.



Figure 14.
Bioconc LHC concreting.



Figure 15.
Bioconc product packing.



Figure 16.
Fc'25 + FA40% LHC & Fc'25 + ice.

3.3 Fc'25 + concrete Fly-ash 40% low heat concrete research data result

The Mock Up of Fc'25 + FA40% Low Heat Concrete to control concrete hydration heat, on mass concrete modeling $1000 \times 1000 \times 2500 \text{ mm}^3$, Graph thermo-couple monitoring output data, figured on the following graph (**Figure 21**).

4. Engineering discussion

Mainly concern of mass concrete Quality Control is on the Hydration Thermal Control, as the above mentioned research data result (item 3.1, 3.2 and 3.3) can be summarized as following **Table 2**:



Figure 17.
Bioconc LHC mock up.



Figure 18.
Bioconc LHC mock up thermocouple monitoring.

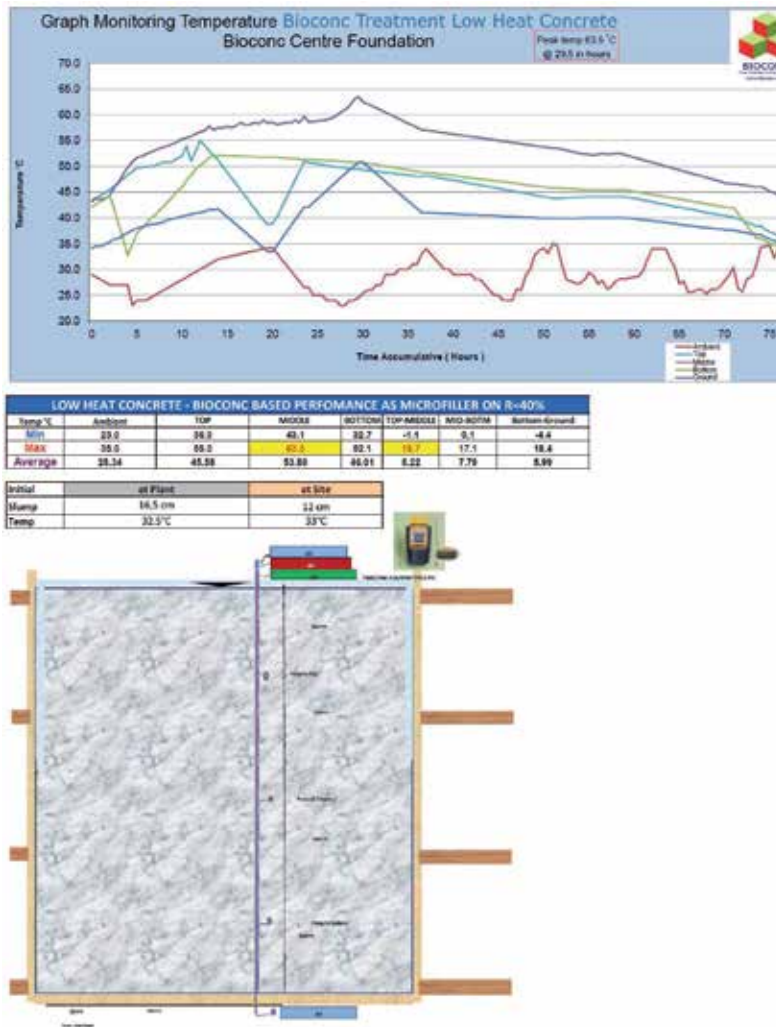


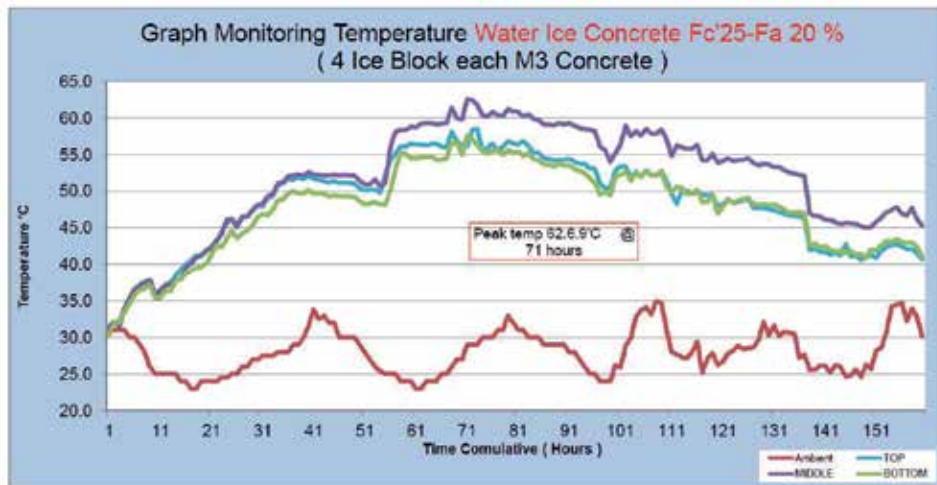
Figure 19. Thermocouple Bioconc-LHC monitoring, Summary data & mock up sketch.

Based on **Table 2**, Bioconc Treatment Low Heat Concrete the faster method to reach the peak time on 29.5 hours from concrete pouring. On construction process, its mean cost advantage, since faster the peak temperature of mass concrete occurred, faster the next step of construction can be execute, also cheaper overhead cost in maintaining the mass concrete, such as rent of mass concrete tends, curing, etc.

Secondly concern of mass concrete Quality Control is on the concrete strength is the concrete cylindrical samples strength test as describe on **Figure 6**, shown that various Concrete Strength Tests are match to the specified.

5. Economic feasibility analysis

Based on the each jobmix material proportion, Low Heat Concrete LHC-Fc'25 + FA40%, Fc'25 + FA20% + Ice block and Bioconc Treatment Low Heat



NORMAL CONCRETE + ICE						
Temp °C	Ambient	TOP	MIDDLE	BOTTOM	TOP-MIDDLE	MIDDLE-BOTTOM
Min	23.0	31.3	31.4	30.3	-1.3	-0.5
Max	35.0	58.5	62.6	57.6	7.9	7.1
Average	27.46	48.39	51.55	47.63	3.16	3.92

Initial	at Plant	at Site
Slump	12 cm	11 cm
Temp	22°C	25°C

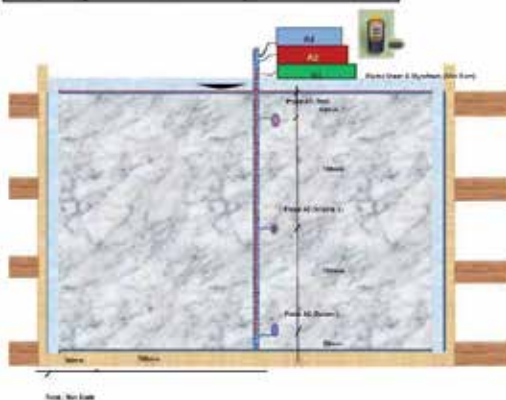


Figure 20. Thermocouple Fc'25 concrete+20%FA + ice, monitoring, Summary Data & Mock up Sketch.

Concrete with cement binder content reduction $R = 40\%$, can be analyzed the initial each cost of production as the following **Table 3**:

Based on **Table 3**, Fc'25-LHC + FA40% is the cheapest one, but considering the risk of environmental hazard and human health [6, 7] the Bioconc Treatment Low Heat Concrete as the mass concrete's hydration thermal control is the wise option to avoid any environmental hazard and human health.

6. Conclusion

1. Considering the eco-friendly, engineering and economical aspect, the Bioconc Treatment Low Heat Concrete satisfy all related condition.

2. Considering the time required to reach peak temperature, the Bioconc Treatment Low Heat Concrete fastest method to control mass concrete's hydration thermal in 29.5 h after pouring. This facts impact to reduce indirect cost of production of the mass concrete, and speed up to execute the next stage of the construction.

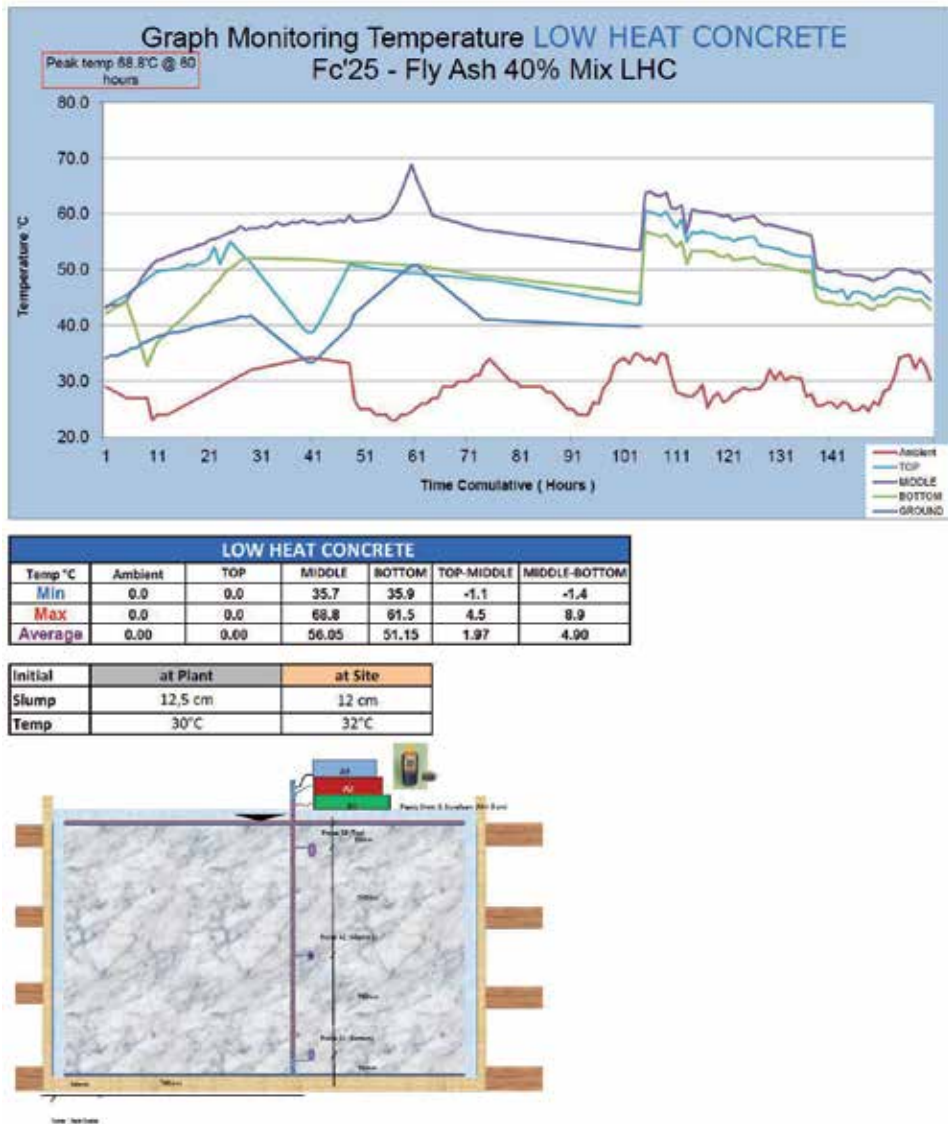


Figure 21. Thermocouple Fc'25 + FA40%-LHC graph monitoring, Summary Data & Mock-up Sketch.

Material mix	Bioconc LHC	FA20% + Ice	LHC-FA40%
Peak thermal (°C)	63.5	62.6	68.8
Peak time (h)	29.5	71	60
Dif. thermal (°C)	19.7	79	8.9

Table 2. Thermocouple monitoring summary.

No.	Material Composition					Cost of LHC FA 40%	Cost of LHC FA 20% + Ice Block	Cost Of LHC Bioconc	Remark
	Material	LHC FA 40	LHC FA 20 + Ice Block	Bioconc LHC+R=40%	Rate @ Rp.	Rp.	Rp.	Rp.	
1	Cement	236.0	315.0	236.0	1,000	236,000	315,000	236,000	
2	Water	158.0	158.0	158.0	100	15,800	15,800	15,800	
3	Fly Ash	158.0	79.0	-	100	15,800	7,900	-	
4	Coarse Agg	1,160.0	1,160.0	1,160.0	250	290,000	290,000	290,000	
5	Fine Agg	760.0	760.0	760.0	175	133,000	133,000	133,000	
6	Ice Block	-	4.0	-	35,000	0	140,000	0	
7	Ice Block Storage System	-	1.0 Lump-sum	-	52,500	-	52,500	-	
8	Bioconc	-	-	0.6	80,000	-	-	48,000	
Total Initial Cost of Production						690,600	954,200	722,800	

Table 3.
Initial cost of production analysis and comparison.

Acknowledgements

First of all, I would like to thank to Alloh SWT, for his blessing on read one of His natural verse, Bioconc, and implementing for the sustainable eco-friendly construction system. Later on, I would like to thanks in advance to all following partners who support on this research:

1. SCG Readymix Indonesia - Surabaya Branch, Mr. Fery Farozdaq and team, who totally support this research of the bioconc's application on reducing the mass concrete hydration heat.
2. Dr. Eng. Januarti Jaya Ekaputri, ST, MT and Prof. Dr. Ir. Triwulan, DEA. Institut Teknologi Sepuluh Nopember (ITS) – Surabaya, which have been collaborated Bioconc Application Research and Development with the Author.
3. KSO Waskita-Darmo Permai, which is give permit to make mock up research, Mr. Ir. M.S. Rishan Kurnia and team, on 88 avenue - Surabaya Project.
4. PT Manajemen Konstruksi Utama – Surabaya, Dr. Andi, ST, M.Eng and Dr. Lie, M. Constr. Mngmt.
5. PT Pulau Intan Baja Perkasa, Mr. Ir. Benyamin and team, who support on making mock up formwork and concreting the mock up mass concrete.
6. My wife and my only daughter, who support me in this research.
7. All partners who support this research, which cannot stated all on this paper.

Author details

Makno Basoeki
CEO Bioconc Centre Foundation, Indonesia

*Address all correspondence to: maknobasoeki@gmail.com;
maknobasoeki@bioconc.com

IntechOpen

© 2020 The Author(s). Licensee IntechOpen. This chapter is distributed under the terms of the Creative Commons Attribution License (<http://creativecommons.org/licenses/by/3.0>), which permits unrestricted use, distribution, and reproduction in any medium, provided the original work is properly cited. 

References

- [1] ACI Committee 207, Guide to Mass Concrete, American Concrete Institute-ACI 207.1R-05. 2006
- [2] <https://www.scribd.com/document/109689638/Mass-Concrete-Method-Statement>
- [3] https://www.concreteconstruction.net/how-to/materials/precooling-mass-concrete_o
- [4] <https://www.forconstructionpros.com/concrete/equipment-products/article/11598829/11598829/how-to-plan-and-manage-curing-for-mass-concrete-pours>
- [5] SCG Readymix Indonesia, Mock Up Trial Low Heat Concrete & Mass Concrete Fc'25+Ice Block, on Avenue88 Project – Surabaya; 2017
- [6] Physicians for Social Responsibility: Coal Ash: Hazardous to Human Health, United States Affiliate of International Physician for Prevention of Nuclear War. 2010
- [7] Juliana Karantonis: The Hazard of Fly Ash, Final Thesis Report, University of New South Wales Australia Defence Force Academy, School of Engineering and Information Technology, Canberra, ACT2600, Australia
- [8] Basoeki M. Hands Out Diskusi Panel Peran Enzyme Mikroba dalam Peningkatan Kualitas Beton dan Produksi Beton dengan Reduksi Emisi CO₂, Bogor; 2000
- [9] Bagio TH, Basoeki M, Pradana SA. Optimum concrete compression strength using bio Enzyme, EACEF 2017. In: The 6th International Conference of Euro Asia Civil Engineering Forum; Seoul-Korea. 2017
- [10] Tappangrara JH, Ekaputri, JJ, Triwulan. Pengaruh Penambahan Silica Fume Sebagai Pengganti Sebagian Semen Pada Kuat Tekan Beton Mutu Tinggi Dengan Tambahan Black Liquor dan Mikrobakteri, Tugas Akhir Fakultas Teknik Sipil dan Perencanaan Institut Teknologi Sepuluh Nopember, Surabaya; 2016
- [11] Annas A, Ekaputri JJ, Triwulan. Pemanfaatan Mikrobakteri Pada Beton Mutu Tinggi Dengan Tambahan Silica Fume. Surabaya: Tugas Akhir Fakultas Teknik Sipil dan Perencanaan Institut Teknologi Sepuluh Nopember; 2016

*Edited by Héctor Jaramillo S.,
Julian Arnaldo Avila and Can Chen*

In materials, their strength is the ability to bear an applied load before their failure. In this direction, the Strength of Materials studies the stresses and deformations that happen in materials as an outcome of loads acting on them. The book contains eleven peer-reviewed chapters organized into two sections. Section 1 is focused on the strength of metals and composites materials, in other words on traditional materials used in engineering projects. Section 2 contains chapters on sustainable materials or non-conventional materials. We sincerely hope that you enjoy this book and the contents will help in the dissemination of knowledge to researchers and students working with materials and their applications.

Published in London, UK

© 2020 IntechOpen
© nd3000 / iStock

IntechOpen

